Simulations of turbulent swirl combustors
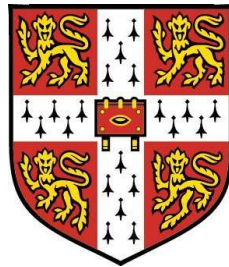
Simon Ayache

Department of Engineering

University of Cambridge

Selwyn College

A thesis submitted for the degree of

Doctor of Philosophy

Tuesday, 20th of December, 2011

À mes parents Laurent et Régine, et mes grands-parents Henri et Simonne.

Dla mojej ukochanej żony, Urszuli.

Declaration

This dissertation is the result of my own work and includes nothing which is the outcome of work done in collaboration except where specifically indicated in the text. The dissertation contains approximately **63,500** words, **138** figures and **5** tables.

Signature	:	
Name	:	Simon Ayache
Date	:	Tuesday, 20th of December, 2011

Acknowledgements

I am very grateful to many people for their support and their help throughout the duration of my PhD.

First and foremost, I would like to thank my supervisor, Prof. Epaminondas Mastorakos, for his guidance throughout my PhD. His continuous availability and insight have contributed towards making my PhD years at Cambridge go very smoothly and pleasantly.

I also express my sincere thanks to Mr Peter Benie (Cambridge) for his help and expertise in Computing Science. Little would be possible in Hopkinson Laboratory without his support. I would also like to thank Dr. Marco Zedda (Rolls-Royce UK) for welcoming me in his CFD team in Derby and for making my stay in Derby a fruitful one, even though the work I conducted there could not be included in this thesis. I also wish to express my gratitude to the European Commission for its financial support granted through the Marie Curie Project MYPLANET.

I would like to thank my friends from Selwyn College as well as my colleagues from the MYPLANET project and the University of Cambridge who created a pleasant atmosphere that lasted all the way through my PhD. In particular, I wish to thank Andrea Maffioli, Alexandre and Carole Neophytou, Camille Letty, Ivan Bahena-Ledezma, Robert Gordon, Theresa Leung, Thibault Pringuey, Frank Yuen, Davide Cavaliere, Peter Schroll, Andrea Pastore and Cheng Tung Chong. I hope to preserve our friendship in the future.

Thanks to my parents who have always believed in me and supported me during my studies.

My final thanks go to Ula, a former Selwyn College mate who recently decided to take my last name. You have been with me all the way through this PhD, and

I am so grateful for that. This thesis would not have been possible without you.

Publications

Journal publications

1. S. Ayache, J.R. Dawson, A. Triantafyllidis, R. Balachandran, E. Mastorakos, Experiments and large-eddy simulations of acoustically-forced bluff-body flows. *International Journal of Heat and Fluid Flow*, 31 (5), pp. 754-766. ISSN 0142-727X, 2010.

2. S. Ayache, E. Mastorakos, Conditional Moment Closure/Large Eddy Simulation of the Delft-III natural gas non-premixed jet flame. *Flow, Turbulence and Combustion*, 88, pp. 207-231. ISSN 1386-6184, 2012.

3. S. Ayache, E. Mastorakos, Investigation of the "TECFLAM" non-premixed flame using Large Eddy Simulation and Proper Orthogonal Decomposition. *Flow, Turbulence and Combustion*, submitted.

Conference publications

1. S. Ayache, J.R. Dawson, A. Triantafyllidis, R. Balachandran, E. Mastorakos, Experiments and large-eddy simulations of acoustically-forced bluff-body flows. *Proceedings of Sixth International Symposium on Turbulence, Heat and Mass Transfer, Rome, Italy*, 14-18 September 2009.

2. S. Ayache, E. Mastorakos, Conditional Moment Closure/Large Eddy Simulation of the Delft-III natural gas non-premixed jet flame. *Proceedings of the Eighth International Symposium on Engineering Turbulence Modelling and Measurements, Marseille, France*, 9-11 June 2010.

3. S. Ayache, E. Mastorakos. LES of the confined swirling non-premixed TECFLAM S09c flame using Conditional Moment Closure, *Proceedings of the Fifth European Combustion Meeting, Cardiff, Wales, UK*, 28 June-1 July 2011.

4. S. Ayache, E. Mastorakos, Investigation of the TECFLAM non-premixed flame using Large Eddy Simulation and Proper Orthogonal Decomposition, *Proceedings of the Seventh Mediterranean Combustion Symposium, Chia Laguna, Cagliari, Sardinia, Italy*, 11-15 September 2011.

Abstract

This thesis aims at improving our knowledge on swirl combustors. The work presented here is based on Large Eddy Simulations (LES) coupled to an advanced combustion model: the Conditional Moment Closure (CMC). Numerical predictions have been systematically compared and validated with detailed experimental datasets. In order to analyze further the physics underlying the large numerical datasets, Proper Orthogonal Decomposition (POD) has also been used throughout the thesis. Various aspects of the aerodynamics of swirling flames are investigated, such as precession or vortex formation caused by flow oscillations, as well as various combustion aspects such as localized extinctions and flame lift-off. All the above affect flame stabilization in different ways and are explored through focused simulations.

The first study investigates isothermal air flows behind an enclosed bluff body, with the incoming flow being pulsated. These flows have strong similarities to flows found in combustors experiencing self-excited oscillations and can therefore be considered as canonical problems. At high enough forcing frequencies, double ring vortices are shed from the air pipe exit. Various harmonics of the pulsating frequency are observed in the spectra and their relation with the vortex shedding is investigated through POD.

The second study explores the structure of the Delft III piloted turbulent non-premixed flame. The simple configuration allows to analyze further key combustion aspects of combustors, with further insights provided on the dynamics of localized extinctions and re-ignition, as well as the pollutants emissions.

The third study presents a comprehensive analysis of the aerodynamics of swirl flows based on the TECFLAM confined non-premixed S09c configuration. A periodic component inside the air inlet pipe and around the central bluff body

is observed, for both the inert and reactive flows. POD shows that these flow oscillations are due to single and double helical vortices, similar to Precessing Vortex Cores (PVC), that develop inside the air inlet pipe and whose axes rotate around the burner. The combustion process is found to affect the swirl flow aerodynamics.

Finally, the fourth study investigates the TECFLAM configuration again, but here attention is given to the flame lift-off evident in experiments and reproduced by the LES-CMC formulation. The stabilization process and the pollutants emission of the flame are investigated in detail.

Contents

List of Figures

List of Tables

Chapter 1

Introduction

1.1 Swirl flows

Swirl flows are present both in nature and in pratical equipment. In nature, they can be found in tornadoes, dust devils or waterspouts, while they have a wide range of applications in engineering. In combustion system, swirling is widely used, due to a variety of advantages like the reduction of the flame length, a better stabilization and a cleaner burning [121]. We can quote some pratical uses of reactive swirl flows such as industrial furnaces, utility boilers, gasoline, diesel engines and of course gas turbines combustors [37; 42; 67; 124], which is the main topic of interest of this thesis.

1.2 Motivation of studying swirl flows

Combustors are designed to achieve a complete chemical reaction in the smallest, lightest and cheapest enclosure possible [42; 52]. Swirl flows allow a better reaction inside the chamber: the swirl creates regions of reverse flows and hence recirculation zones that maintain the reactants inside the combustors and allow a better mixing between oxidizer and fuel. A better reaction is also achieved by mixing hot gases with fresh combustible mixture, which leads to a reduction in pollutants emissions. However the aerodynamics of swirl flows is extremely complex and a strong coupling between the aerodynamics of the swirl flow and

the combustion process arises. Even though swirl flows have been intensively studied due to their industrial applications, several aspects of their aerodynamics and combustion process have to be understood further, as it will become evident from the literature review in Chapter 2. The thesis aims at investigating the aerodynamics of swirl combustors in detail, in particular the aerodynamics of the injector, the combustion process occuring in the combustion chambers, and the coupling between the swirl flow and flame.

1.3 Methods of investigation

The work presented in this thesis is based on Large Eddy Simulations. The choice of this relatively costly numerical method to compute flow fields compared to the cheaper Reynolds-averaged Navier-Stokes simulations is justified by the nature of the computed flows. In LES, the large-scale unsteady motions are explicitly represented while RANS is based on purely statistical approach regarding turbulent viscosity or Reynolds stresses. As a result, computations of bluff body flames and swirling flames, which involve large-scale unsteady motions, are ideal candidates for LES [11]. Besides, the RANS methods using $k - \epsilon$ methods have already been found inadequate to predict the kinematic properties of strongly swirling flows, leading to inaccurate predictions of the stabilization process of turbulent swirl flames [8].

A first-order Conditional Moment Closure (CMC) has been used to model combustion throughout the various reactive simulations presented in this thesis. This model has been developed to study non-premixed combustion [60]. The first order CMC uses the conditional averages of the reactive scalars in the calculation of the reaction rate. This assumption is much better than if the averaging was done in an unconditional manner. The reason is that the fluctuations of species concentrations and temperature are expected to be mostly related to the mixture fraction fluctuations [19]. Many non-premixed problems, including flows with re-circulations behind a bluff-body using RANS [57] or LES [118], and a bluff body swirl-stabilized methane flame using a RANS method [37], have been successfully modelled using first-order CMC. The discepancies observed in the predictions of species in the swirl-stabilized flame were regarded as a consequence of the

2

shortcomings of the fluid-flow model, especially in the mixture fraction prediction. These results seem encouraging and justify the decision to compute swirling reactive flows using a coupled LES/CMC formulation, knowing that the recirculation zone in swirling jets exhibits similarities with those produced by bluff bodies [42].

In order to organize and understand further the large amount of information contained in the LES datasets of the various simulations, the Proper Orthogonal Decomposition (POD) method has been widely used throughout this thesis. POD is used to extract and analyse the structures of the flow and to look for any interaction with the flow aerodynamics and the combustion process.

1.4   Scope of the thesis

In this thesis, various aspects of swirl flame stabilization are investigated from both the aerodynamics and combustion points of view. Chapter 2 presents a review of the different aspects of flows and flames that will be investigated throughout the thesis as well as the challenges that the design of swirl combustors faces. The chapter ends up with a brief presentation of the motivation for the different numerical studies conducted during this PhD work. Chapter 3 presents the numerical tools used to perform this work. In particular, a comprehensive description of the LES-CMC formulation used in this thesis is provided, and the Proper Orthogonal Decomposition method, which has been used throughout this work, is presented.

Chapters 4 and 5 then present works that investigate key aspects of combustors considered separately. Chapter 4 focuses on the study of isothermal forced bluff body flows. The configuration is thought of as a model problem for gas turbine combustors. It allows to understand the aerodynamics of combustors undergoing self-excited oscillations involving recirculation zones and periodicity, and without the extra complexities of a swirl and combustion. The Proper Orthogonal Decomposition method allows a better understanding of the effects of the inlet pulsation on the bluff body flows. In Chapter 5, the focus is put on the combustion process with the study of a piloted non-premixed flame showing significant finite-rate chemistry effects. The study provides more insights on the

dynamics of localized extinctions and re-ignitions.

Chapters 6 and 7 are the central chapters of this thesis. In these two chapters, an academic non-premixed swirl flow is investigated in-depth for both inert and reactive configurations. Chapter 6 provides a comprehensive analysis of the aerodynamics of the burner, by means of spectral analysis, autocorrelations and Proper Orthogonal Decomposition. Chapter 7 is focused on the study of the combustion process of the swirl flame, in particular the reproduction and analysis of extinction and flame lift-off.

Finally, the main findings and conclusions from this PhD work, as well as some guidelines for further research, are summarized in Chapter 8.

Chapter 2

Literature review

In this chapter, we briefly present the different aspects of flows and flames that will be analysed in this thesis. We mainly focus on the study of non-premixed flames.

2.1 The problem of flame stabilization: localized extinction, lift-off and blow-off

Consider first a premixed configuration, where fuel and air have been completely mixed before reaching the combustion chamber. The flame in a combustor is considered to be stable over a range of input parameters, such as the fuel flow rate or the air/fuel ratio, if the flame does not extinguish or flash back with variation in the above input parameters [42]. On one hand, when the flow velocity of a stable flame is decreased until the flame velocity at the burner level exceeds the flow velocity, the flame flashes back into the burner. On the other hand, an increase of the flow velocity until exceeding the flame velocity everywhere in the chamber will lead to either the flame to be extinguished completely or, for fuel-rich mixtures, it will lift above the burner until a new stable position in the fuel stream is reached.

Consider now a non-premixed configuration. In this case, the oxidizer and the fuel are injected through different streams. For a jet flame and for low inlet velocity, the air and fuel mix up due to molecular diffusion. If now the fuel is ignited, a

laminar flame will develop, and the flame front will be located along the stoichiometric mixture fraction. The flame will remain anchored to the burner nozzle. If the jet velocity is slowly increased, the flow and flame will become increasingly turbulent. Turns [109] provides a general description of what happens if we keep on increasing the flow rate. At sufficiently low flow rates, the base of the flame remains quite close to the burner outlet and the flame is attached. As we keep on increasing the flow rate, holes will begin to form in the flame sheet at the base of the flame [109]. With further increase in the flow rate, more and more holes will appear until there is no continuous flame close to the burner exit: the flame has lifted-off [109]. At a sufficiently large flow rate, the flame blows off [109]. Thus, Turns identifies two critical flow conditions related to the flame stability: the lift-off and the blow-off. Masri et al. [73] have investigated several flames approching blow-off. As the flame approaches blow off, the number of locally extinguished samples is found to increase significantly. The start of occurrence of localized extinction depends on the fuel mixture. The flame reignites intermittently further downstream where the mixing rates are more relaxed. Reignition can only occur as long as there are burnt fluid parcels convected from the intense mixing neck.

Therefore, in non-premixed configurations, the problem of flame stabilization consists of maintaining a stable flame at operating conditions, without reaching the blow-off limit. The solutions to delay the occurrence of blow-off are based on the transport of hot combustion products at the root of the flame, where cold reactants are located. This is generally done by using a pilot flame or by creating one or several recirculation zones that will convect the hot products of the flame back to its root. In the next section, a recirculation zone without swirl is considered while the effect of swirl will be investigated in-depth in Section 2.3.
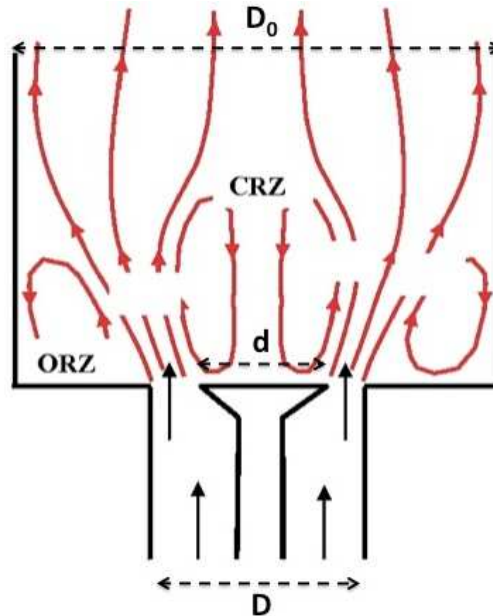
Figure 2.1: Schematic of a bluff-body flow.

2.2 Aerodynamics and stabilization of flames without swirl

2.2.1 Canonical problem for flame stabilization

A bluff body is often introduced in order to create a Central Recirculation Zone (CRZ) behind the air inlet pipe, while a sudden-expansion creates an Outer Recirculation Zone (ORZ), as schematized in Fig. 2.1. There is a re-attachment length associated with the end of the ORZ (X_r) and a forward stagnation point at the downstream end of the bluff body wake (X_s). These recirculation zones are very useful as they behave as flameholders.

In the following, D refers to the diameter of the air flow pipe, d to the axisymmetric bluff body diameter located at the end of the pipe, and D_o will be the diameter of a round enclosure, with $d < D < D_o$ (see Fig. 2.1). The bulk velocity of the flow coming out of the annular passage between the disk and the inner wall of the pipe is refered as U_b.

2.2.2 Bluff body flows

Consider first a flow with a CRZ created by a bluff body and no sudden expansion. When the incoming flow is steady and of almost infinite extent compared to the bluff body (considered here as an infinitely-thin disk), this configuration has been studied extensively for a wide range of Reynolds number:

$$Re = \frac{dU_b}{\nu} \tag{2.1}$$

At very low Reynolds numbers, the separation region behind the disk is stable, with a toroidal vortex forming the recirculation zone. As the Reynolds number increases, various instabilities set in and symmetry is lost [36; 46; 103], similar to what happens to the flow behind a sphere [36; 87], albeit at a different Reynolds number. The review by Kiya et al. [58] mentions a critical Re of about 140 above which the wake becomes unsteady; more recent numerical simulations report a slightly lower value [36; 103]. For Reynolds numbers between this critical value and for values up to $10^3 - 10^5$, helical vortices seem to be formed at a natural frequency f_n corresponding to a natural vortex shedding Strouhal number:

$$St_n = \frac{f_n d}{U_b} \tag{2.2}$$

in the range 0.13-0.15 [58; 77]. Huang and Lin [46] reported that no vortex shedding is found for $Re > 1500$, although no detailed examination of spectra was reported in that paper and hence a relatively mild vortex shedding may have been missed. The helical vortex from the circular disk is a weaker structure compared to the von Kármán vortex street from two-dimensional cylinders. Nevertheless, upon close examination, it can be revealed even at distances as far as $50d$ from the disk and $St_n = 0.135$ has been specifically reported [119].

We should distinguish this helical vortex structure from the Kelvin-Helmholtz instabilities associated with the shear layers surrounding the recirculation zone. This instability gives rise to ring vortices that are convected downstream with the flow. In the wake behind a sphere, the Strouhal number associated with this instability:

$$St_{KH} = f_{KH} d/U_b \tag{2.3}$$

has been measured as a function of Reynolds number. Similar data for the Kelvin-Helmholtz ring vortices for the shear layers around the CRZ of a disk do not seem to be available [58], at least expressed as a function of the Reynolds number based on the disk diameter.

Finally, we mention that the normalized stagnation point location X_s/d increases with Reynolds number for low Reynolds numbers and peaks at about 1.6, but seems to decrease slowly to asymptote to about 1.5 [46; 84; 116] for high Reynolds numbers. Note that the mean length of the recirculation zone is a strong function of the disk shape: for conical bluff bodies, the CRZ is longer than for flat disks [84]. The enclosure also plays a role [116]. Note also that if the incoming flow is turbulent, the CRZ length may be reduced [84].

2.2.3 Flows behind a sudden expansion

Consider now a flow in an axisymmetric sudden expansion, without a centrally-placed bluff body, and consider a steady incoming flow. The flow above a two-dimensional backward-facing step has been studied extensively by experiment and simulation. The separated shear layer from the corner of the sudden expansion eventually turns towards the wall and re-attaches, at a distance that depends on the step height, the Reynolds number, and the boundary layer thickness of the flow before the step (see Ref. [40], Section 9, for a review and Ref. [29], Ref. [34] and Ref. [107] for recent simulations and discussions of the main experimental findings). One important point is that the Kelvin-Helmholtz instabilities of the shear layer interact with a shedding-type instability to cause large fluctuations of the reattachment length. In an axisymmetric sudden expansion, the reattachment length, X_r, depends on the ratio D_o/D [30], with D_o and D defined in Section 2.2.1, and could be as large as 10 step heights $(D_o - D)/2$. Large-eddy and RANS simulations are found to reproduce the major features of the flow [41; 122]. Ref. [24] reported a Strouhal number:

$$St = fD/U_b \tag{2.4}$$

of about 0.3 for the re-attachment length fluctuations, attributed to the vortices from the separated shear layer.

2.2.4   Sudden expansion and bluff body flows

The flows behind a bluff body and over a backward-facing step can be considered as canonical problems for gas turbine combustors. The sudden expansion and the recirculation zone behind an axisymmetric bluff body are commonly studied in the context of flame stabilisation and structure of flames [101]. This flow itself has been studied in Ref. [102], but only for low Reynolds numbers. Due to the use of this configuration for flames, velocity [84; 116] and flame emission [28] measurements have been performed. Both ratios D_o/D and D/d affect the sizes of both CRZ and ORZ.

2.3   Aerodynamics and stabilization of swirl flames

Another solution to create a recirculation zone is by introducing a high swirl at the flow inlet. The aerodynamics of flows with an imposed swirl are very rich and the effects of the swirl on the flow field increase with its strengh. This section presents the main characteristics of the aerodynamics of swirl flows and emphasizes its role on swirl flame stabilization.

2.3.1   Swirl flow characterization

Swirl flows result from the application of a spiraling motion. A swirl (or azimuthal) velocity component is thus imposed to the flow by the use of swirl vanes [124], axial-plus-tangential entry swirl generators [52] or by direct tangential entry into the chamber [42; 96]. Swirl flows, and their effects on the combustion process in the case of reacting flows, are all strongly dependant on the degree of swirl imparted to the flow [42]. This degree of swirl is characterized by the swirl number S. The swirl number is a nondimensional number defined as the ratio of the axial flux of swirl momentum to the product of the axial flux of axial momentum and the injector radius R [42; 52; 120; 121; 124]:

$$S = \frac{\int \rho U_\theta U_x r dA}{R \int \rho U_x{}^2 dA} \tag{2.5}$$

where U_x and U_θ are the axial and the tangential components of the mean velocity respectively, A is the section of the injector and R is a characteristic length, typically the radius of the cross section plane [120] or the equivalent radius in case of a non-cylindrical shape [121].

Other important dimensionless parameters characterizing a swirl flow are the Strouhal number St and the Reynods number Re with:

$$St = \frac{fD}{U} \tag{2.6}$$

and

$$Re = \frac{DU}{\nu} \tag{2.7}$$

with f being the precession frequency, D a characteristic diameter (typically $D = 2R$), U the flow velocity and ν the kinematic viscosity of the fluid [121].

2.3.2 Vortex breakdown and recirculation zone

At low swirl level (Gupta gives $S < 0.4$ [42], while Doherty gives $S < 0.6$ [69]), the centrifugal forces can create significant radial pressure gradients at any axial position compared to axial pressure gradient. This adverse axial pressure gradient is not large enough to cause axial recirculation. There is also no coupling between axial and tangential velocity components [42; 69].

As the swirl number is increased, a strong coupling develops between the axial and tangential velocity components. Both strong axial and radial pressure gradients are set up near the nozzle exit [69]. When there is a change in the cross-sectional area, such as when the flow enters the combustion chamber, the flow expansion results in a decrease of the radial pressure gradient. This leads to an increase in the pressure along the centreline as we go downtream [112]. When the axial momentum of the fluid cannot any longer overcome the axial pressure gradient along the jet axis, a flow reversal occurs and a central toroidal recirculation zone is set-up [69]. The formation of this recirculation zone, through a vortex breakdown process [115; 120], acts as an aerodynamic blockage or like a three dimensional bluff body and helps to stabilize the flame [115] for the same
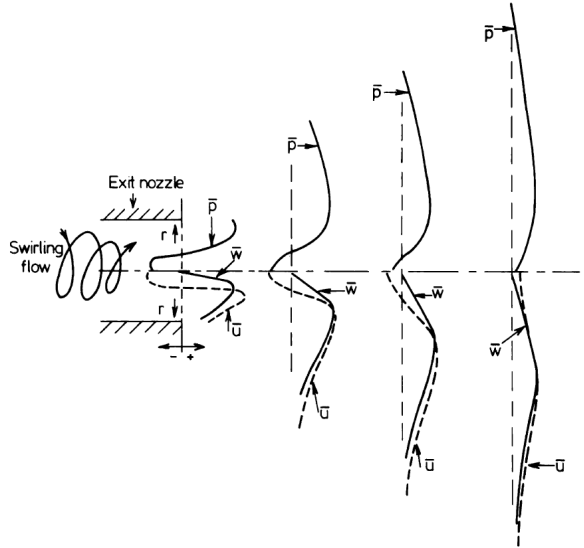
Figure 2.2: Schematic diagram of processes leading to CRZ formation. From Ref. [112].

reasons as in bluff body flames. The formation mechanism of a recirculation zone induced by swirl is summarized in Fig. 2.2. The presence of a confinement affects the vortex breakdown process as it modifies the tangential velocity and thus the pressure gradients [112].

The mechanism of vortex swirl generation by devices such as swirlers is due to strong inertial effects. However, once the vortex flow is generated, the mechanism that leads to vortex breakdown in high-Reynolds number flows is related largely to inviscid (dynamical) effects [120]. Vortex breakdown is a highly unstable and transient flow pattern which occurs due to the instabilities present in swirl flows such as shear-layer instabilities (like Kelvin-Helmholtz instability) similar to axial jets and azimuthal shear-layer instabilities created by the radial gradient in azimuthal velocity. The centrifugal force is another source of instability and leads to a flow profile corresponding to a vortex [52]. Rusak et al. [97] propose criteria to predict the stability and the dynamics of vortex breakdown in high Reynolds number swirl flows. One first defines the inlet swirl ratio as $\Omega = \dot{\theta} R_i / U$ with R_i as the inlet section radius, $\dot{\theta}$ as the rotation rate and U as the uniform axial velocity. Ω represents the swirl number of the swirler at the swirler exit plane.

Two critical swirl ratios, $\Omega_0 < \Omega_1$, are found to exist for a swirl flow in a pipe. For $\Omega < \Omega_0$, a columnar flow is found to develop throughout the pipe, which is the unique solution of the unsteady and axisymmetric Navier-Stokes equations. For $\Omega_0 < \Omega < \Omega_1$ two stable steady-state solutions can develop. One of them describes a columnar swirl flow while the other one is a swirl flow with a stagnation breakdown region. Which solution appears will depend on initial disturbances introduced to the columnar flow inlet. If small perturbations decay in time it is the columnar state which will prevail while large disturbances enforce a transition to the breakdown state. This transition is called the breakdown process. At last, when $\Omega > \Omega_1$, the columnar swirling flow is unstable and the flow always develops a vortex breakdown state [120]. Using the work of Rusak et al. [97], these critical swirl levels can be computed.

2.3.3 Precessing Vortex Core

The vortex breakdown can sometimes display strongly time dependent characteristics, whereby the recirculation zone itself becomes unstable and starts to precess about its own axis. This situation refers to a Precessing Vortex Core (PVC) [113]. In any swirl burner flow where a vortex breakdown has occurred, a large three-dimensional periodic flow structure can appear that is also referred to as a precessing vortex core [42; 121]. PVC (Fig. 2.3) is usually found at the boundary of the reverse flow zone [42; 114]. It forms when the forced vortex region of the flow becomes unstable and the axis of the rotation of the flow inside the swirling recirculation zone starts to precess around the axis of symmetry. As a consequence, the vortex breakdown becomes asymmetric and highly time-dependent [69].

The vortex breakdown can take on several forms, including the appearance of multiple helical vortices formed in the swirl stream shear layer. It has been reported that the unsteady dynamics of these particular features can play an important role in combustion induced oscillations [78; 108].

The combustion process tends to dampen a structure (PVC...) that is present under isothermal conditions, especially in non-premixed configuration (Fig. 2.4 from Ref. [112]). Even when the vortex core precession is suppressed, the result-

<div align="center">(a)   (b)</div>
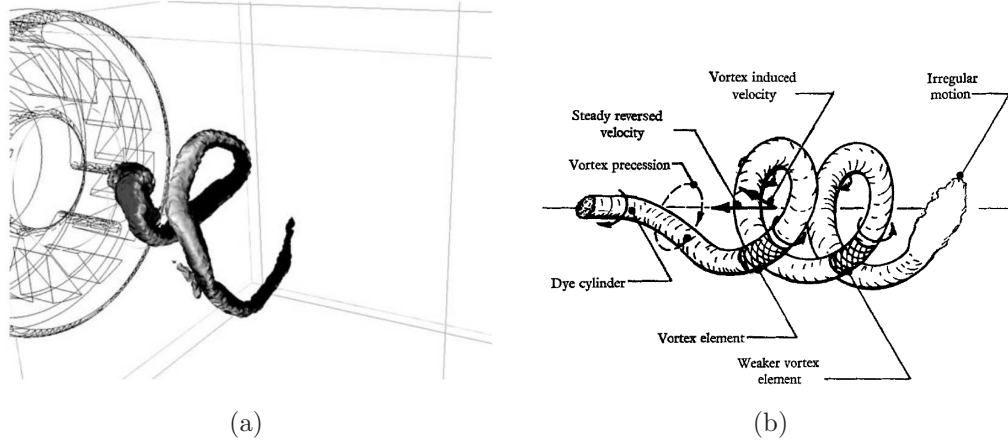
Figure 2.3: (a) Visualization of a PVC structure as predicted by LES at the exit of the swirler using an isosurface of low pressure. From Ref. [96]. (b) A sketch of a PVC. From Ref. [21].

ing swirling flame is unstable and tend to wobble in response to minor perturbations in the flow, most importantly close to the burner exit [112].

Premixed or partially premixed combustion can also produce large PVC similar in structure to that found isothermally. In that case, it has been reported that the Strouhal number associated with the PVC in reactive conditions at equivalence ratios around 0.7 may increase by a factor of 2 compared to isothermal conditions [112].

2.3.4 Stabilization of swirl flames

In order to maintain the flame, a continuous source of ignition must be provided to the fresh reactants located at the root of the flames. At high velocity, blow-off occurs if the heat received by the recirculating eddies from the hot combustion gases is insufficient to maintain a temperature high enough to cause ignition.

As described in the previous section, in jets with high swirl number, when the angular-to-linear-momentum ratio exceeded a critical value, a toroidal vortex type recirculation zone appeared in the central region of the flow and close to the nozzle. This toroidal vortex plays a key role in the stabilization of flames. The high-intensity turbulence that occurs in the vortex region increases the mixing

(a) Diffusion flame

(b) Premixed flame
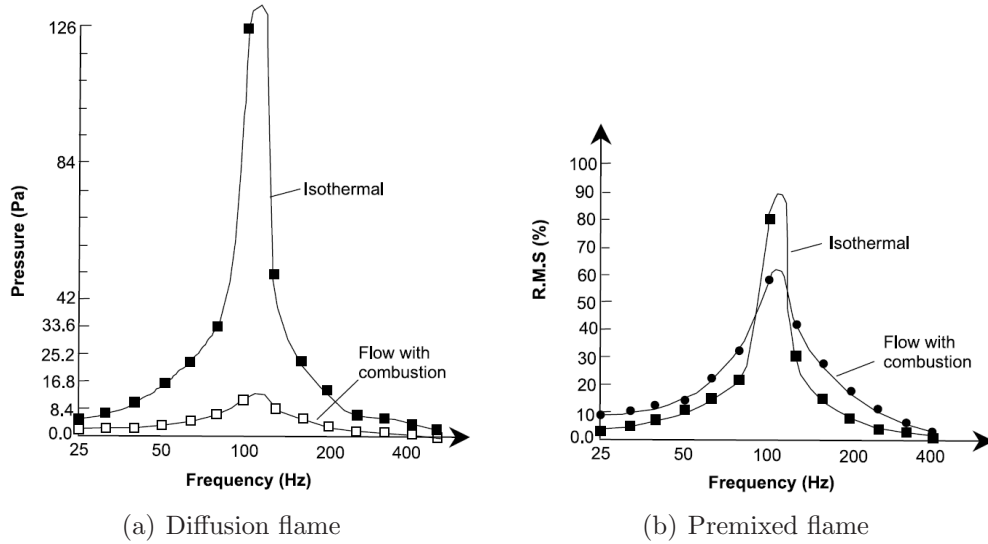
Figure 2.4: Effect of combustion upon the PVC with (a) 100% axial fuel injection
(b) premixing, $S = 1.98$, equivalence ratio 0.89. In Fig. (a), the term "pressure"
refers to the mean pressure, while in Fig. (b) the term "R.M.S" refers to the
R.M.S of the pressure. Figures from Ref. [112].

which can be enhanced by up to a factor of 5 [2; 121]. The hot gases and active
chemical species recirculate back to the burner due to the Central Recirculation
Zone (CRZ). Heat and mass are thus transported effectively from combustion
products to fresh combustible mixture [42]. It has also been reported that the
periodic motion of vortex precession enhances the mixing between fuel and ox-
idiser [52]. The improved mixing allows to push back the blow-out limits of
non-premixed flames and to shorten both the flame length and the distance
from the burner at which the flame is stabilized [121].

The recirculation zone in swirling jets and in bluff body flows exhibits simi-
larities. In the case of bluff body stabilized flames, a region of recirculating flow
appears behind the bluff body. This recirculating system acts as a continuous
source of ignition for the flame that originates behind the bluff-body and spreads
obliquely across the flow: it receives heat from the flame, then carries it back
upstream, and eventually ignites the flow of fuel/air mixture by contact. How-
ever, one of the most important differences is that the blockage in swirling jets
is entirely aerodynamic. There is no need for the presence of a solid surface. In

combustion system, this is a fundamental improvement, as the flame is generally attached to the bluff body that is therefore exposed to high temperature and to effects of soot deposition [42]. Other benefits of using a swirl for flame stabilization come from the compact flame and the high level of mass recirculation that are obtained compared to non-swirling flow. Therefore, all industrial combustors feature a swirl that is intense enough to create a large central recirculation zone.

Several factors influence the size of the recirculation zone, namely the degree of swirl, the blockage ratio of the flame holder in the stream, divergent walls if there is no separation of the flow from the walls and the shape of the flame holder [42]. Changing the amount and nature of fuel injected allows to control the temperature and the gas composition into the reverse flow zone while variations of the degree of swirl controlled by the swirl number allows an aerodynamic control for mixing and reaction [42].

2.4 Combustion instabilities

High amplitude low frequency oscillations in combustors are generally regarded as undesirable as they can cause large pressure fluctuations leading to damage of the combustor structures [15; 42; 55]. Among the different types of instabilities that can affect a combustor, the ones arising from acoustic and fluid dynamic phenomena will be briefly reviewed.

2.4.1 Acoustic instabilities

In the presence of upstream and boundary ductworks, which impose certain acoustic characteristics to the flow, self-excited oscillations may arise in realistic combustors, which cause a strongly-pulsating flow and vortex formation [28, 68]. Acoustic instabilities are characterized by the propagation of acoustic waves in the combustion chamber. Oscillations arise and their frequency is determined by the chamber geometry. Thus, if noise is present inside the chamber, certain frequencies can be selected and amplified by the combustion system. In a combustion chamber, acoustic energy is mainly generated due to variations of the heat release rate: an unsteady source of heat behaves like a source of sound.

Acoustic waves are thus generated and propagate upstream and downstream of the flame location. These waves are then reflected at the inlet and outlet sections of the combustion chamber. The reflected acoustic waves travel back to the flame, increasing their perturbations and affecting again the instantaneous heat release. Therefore a coupling between the acoustic field where chemical reactions occur and the heat release process arises. According to the Rayleigh criterion [92], the acoustic oscillations will amplify themselves when the fluctuations in heat release and acoustic pressure at the flame location are in phase with each other. Another criterion for the system to develop combustion instabilities is that the acoustic energy received from the fluctuating heat release is larger than the energy lost both at the boundaries of the chamber and from the viscous dissipation [15; 42; 64; 99]. The physical mechanisms of the flame response to these acoustic perturbations are strongly dependent on the nature of the flame [15]: partially premixed flames are very sensitive to equivalence ratio fluctuations [100]. In fully premixed flames heat release rate fluctuations are linked to variations in the flame surface area. The pressure fluctuation can be driven by either the oscillation in the flow [31] or the displacement of the flame anchoring point [9].

2.4.2   Hydrodynamic instabilities

The other types of instabilities that can occur in a combustion chamber are developed by fluid dynamic phenomena. They lead to combustion fluctuating periodically inside the combustion chamber. These instabilities are called hydrodynamic instabilities and appear due to the establishment of certain flow patterns.

The development of a vortex shedding can be a source of instabilities [42; 64]. In this context, acoustic and fluid dynamic instabilities can be strongly coupled mechanisms in turbulent, premixed combustion systems. The formation of vortices have thus been identified as a mechanism driving the combustion instabilities [99]. The formation of these ring-vortex structures can always be observed together with the occurence of pressure oscillations in highly turbulent combustors in both non-premixed and premixed systems. They are also thought to be independent of the type of flame as they are encountered in jet, bluff body or swirl stabilized flames. The mechanism by which they sustain combustion
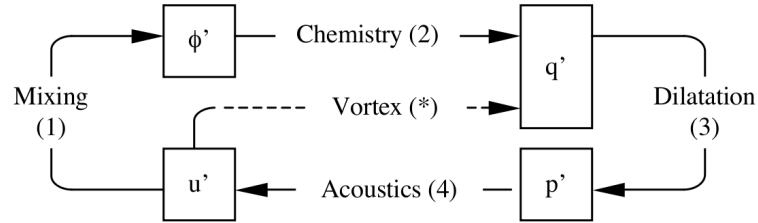
Figure 2.5: Links between different quantities in typical gas turbine combustion instabilities. From Ref. [99].

instabilities is the same as described previously: when toroidal vortices are formed by rolling-up the fuel-air mixture, they change the mixing and reaction fields of the steady-state flame. The heat release rate of the flame is modified, leading to new pressure fluctuations that can create next generations of larger ring-vortex if the Rayleigh's criterion is satisfied. A feedback loop can then arise as explained previously.

The PVC is also responsible for large fluctuations in the velocity and mixing fields. If these fluctuations become coupled with acoustic frequencies of the combustion chamber, combustion-induced oscillations and high pressure pulsations could arise. Figure 2.5 summarizes the interactions between the different mechanisms leading to instability in gas turbine combustion.

2.4.3 Pulsating flows

The previous section has shown that combustion instabilites may lead to self-excited oscillations developing inside the combustor and create a strong pulsating flow. The study of a forced pulsating flow may thus be seen as a canonical problem for combustor experiencing combustion instabilities. In this section, we do not consider the case of a swirl flow and limit the study to flow composed of a bluff body and a sudden-expansion. The interaction between the recirculation zones and the pulsating flow introduces significant complexities compared to the case described in Section 2.2.1.

2.4.3.1 Bluff body flows

When the incoming flow of a bluff body flow is virtually laminar or with very low turbulent intensity but is oscillating in a periodic manner, the flow changes in many respects. Work of this nature for oscillating flow above cylinders has shown that the vortex shedding frequency may lock-on to the frequency of the flow oscillation [62]. The possibility of controlling the von Kármán vortex street for a cylinder or the wake of the sphere by carefully-placed small-amplitude pulsations has been reviewed by Choi et al. [23]. Extrapolating the results from pulsating jets [18], we may expect that ring vortices may be shed from the edge of the disk when the flow is pulsating at an appropriate Strouhal number, given (for a circular jet) in the range 0.7-0.9. We are not aware of a detailed examination of the flow over a disk placed normal to the flow when the flow is oscillating.

2.4.3.2 Flows behind a sudden expansion

A superimposed oscillation above a two-dimensional backward-facing step has been studied extensively in the context of re-attachment length control [29; 40]. Apparently, even small amplitudes of oscillation can affect greatly the re-attachment length due to the interaction with the Kelvin-Helmholtz instability. We are not aware of any simulations or experiments of the flow in an axisymmetric sudden expansion with an oscillation superimposed to the mean flow.

2.4.3.3 Sudden expansion and bluff body flows

When the incoming flow is oscillating, flow visualization and inferences from flame studies show that counter-rotating torroidal vortices may be formed at the edge of the bluff body and at the corner of the sudden expansion [5; 6], depending on the oscillation frequency and amplitude. In a similar geometry but in the presence of swirl and premixed combustion, vortices were observed only for forcing above a critical amplitude, with this critical amplitude increasing sharply as the Strouhal number, defined as:

$$St = fd/U \tag{2.8}$$

decreased [65]. These vortices may then cause significant alterations to the flame shape and location, which in turn causes a significant change to the overall heat release in the combustor. Despite the practical relevance of this configuration, and despite the rapidly growing number of Reynolds-Averaged Navier-Stokes (RANS) simulations and Large-Eddy Simulations (LES) of this type of flow [3; 43; 99; 123], with or without swirl, it seems that little effort has been placed in understanding better the fluid mechanical effects when the flow is oscillating in a compound bluff body - sudden expansion configuration. This configuration will be investigated further in Chapter 4.

2.5 Pollutants emissions

2.5.1 Pollutants formation

One of the most undesirable sides of combustion is the formation of pollutants. The main species of concern found in combustors exhaust are unburned hydrocarbons, carbon monoxide, soot and oxides of nitrogen [45].

Both hydrocarbon (HC) and carbon monoxide (CO) are pollutants that result from rich or incomplete combustion. Although hydrocarbons are not toxic, their production should be avoided as they contribute to the production of smog. However carbon monoxide is toxic and contribute to heart and respiratory conditions. While they are largely removed by catalytic converters in spark-ignited engines and in lean premixed combustors, the formation of HC and CO is not limited in aeroengine gas turbines due to the need to prevent autoignition. In such turbines there is also often a rich pilot region that keeps the combustion stable. At low power conditions, there are incomplete reactions for HC and CO due to the low temperatures [45].

Soot is a collection of Polycyclic Aromatic Hydrocarbons (PAH) or benzene-like rings emmited from very rich combustion. Combining with other pollutants and moisture in the atmosphere, they create Particulate Matter (PM). PM are known to increase mortality rates and are a very challenging problem in the operation of diesel engines [45].

Nitric Oxides (NO_x) are toxic in low concentrations and contribute to the

formation of photochemical smog via a mechanism involving hydrocarbons and sunlight to form hydrocarbon nitrates and ozone. The amount of smog is generally limited by the availability of NO_x. Its prediction and the limitation of its exhaust is then of a primary concern for developers as the exhaust thresholds are becoming more and more strict [45]. To be able to predict their emissions, all physical phenomena influencing their formation have to be taken into account. They are generally divided into three categories: The thermal NO_x mechanism, which was discovered by Zel'dovich and operates through the direct oxidation of atmospheric nitrogen. It is responsible for the largest proportion of NO_x emissions in most combustion systems. It is important at temperatures above 1500 K, which are easily reached with most fuels used in combustion. It depends exponentially on temperature which makes it very sensitive to turbulent and acoustic fluctuations [99]. The fuel NO_x, which is created from the nitrogen bound to the hydrocarbon fuel. Finally, the prompt mechanism is responsible for relatively low emissions of NO_x in most combustion systems but can be important when the fuel-air mixture is somewhat rich. This mechanism operates through the formation of hydrocarbon radicals (HCN). Prompt NO_x has an exponential dependence on equivalence ratio [99].

2.5.2 Reduction of emissions

Regarding HC and CO production, they are generally removed by catalytic converters placed in the tailpipe of the spark-ignited engines.

In order to reduce NO_x emissions, modern gas turbines for power energy generation are now often operating under lean-burn conditions [15; 55]: by avoiding chemical reaction at stoichiometric condition, the flame temperature is reduced. As a consequence, thermal NO_x is reduced. Moreover, excess of air results generally in complete combustion of fuel, reducing hydrocarbon and carbon monoxide (CO) emissions. However, some authors have reported an increase in CO formation [42] in this kind of combustors. The pratical lean premixed combustors are made complicated to realize due to low reaction rates in lean flames and their suceptibility to extinction. They also tend to develop combustion instabilities [15; 42; 55]. On top of producing structural damages, an unstable combustion

is claimed to increase pollutants emissions of the gas turbines [15]. All these problems have so far made premixing impractical for aero gas turbine, leaving the problem of NO_x emissions in non-premixed flames still alive.

The strategies adopted in the design of Rolls-Royce aero gas turbines to decrease NO_x emissions are based on the lean burn technology. The new lean burn technology is based on the principle that with a higher Air-to-Fuel Ratio (AFR), the flame temperature will decrease and so will the NOx emissions. As a consequence, the aerodynamic combustor design has to change to increase the AFR ratio near the flame front, but this change also has large implications on the stability and performance of the combustor. The following description of the rich and lean burn technologies is based on discussions with Rolls-Royce engineers during a short placement in Derby, UK.

In a conventional combustor, a rich diffusion flame is generated in a primary recirculation zone. This rich zone is located at the front of the combustion chamber and provides a high level of resistance to flame out. Therefore it is used to keep the combustor alight at low power conditions. Throughout large ports located along the length of the combustor, air is introduced in a transition zone that dilutes the mixture and enables most of the smoke produced in the rich zone to be consumed. Overall the combustor is running very lean. However, as the mixture passes from rich to lean mixture, there are regions of the combustor where the mixing is at stoichiometric conditions and hence NOx emissions are high.

To lower NOx emissions significantly, a new combustor has been designed to operate in lean conditions also in the front part of the combustion chamber. In this configuration, all the air, apart from the cooling air, is admitted through the fuel injector to provide a lean burn AFR condition everywhere in the combustor, which is required for low NOx emissions. As a consequence, there is no longer large air ports along the combustor walls as in a rich combustor. The lean burn injector is also found to be much larger, as almost all the air needed for the combustion process will enter the combustor through the injector.

The drawbacks of lean burn configurations is that there are issues with the flame stability at low power conditions. In particular, there is a high risk of blow out. To overcome this problem, a staged combustion is used, where different

zones are created for a specific range of engine operation. At low power, fuel is supplied only through a small pilot injector while at higher power conditions more fuel is introduced through large main fuel injectors.

Rocha et al. [93] investigated the influence of an acoustic field on the combustion of a natural gas turbulent jet flames using the Delft burner, which is a non-premixed piloted jet flame. They found that flames undergoing acoustic oscillations show significant changes in their structures. These flames have shorter length and show premixing characteristics. These premixed characteristics are due to the acoustic field which increases the reactants mixing convective process due to the presence of oscillations. There is also a better distribution of temperature and a decrease of temperature peaks in the flame region. As a consequence, species formation alteration was found not only in the distribution of NO_x but also in the distribution of O_2, CO_2 and CO. Schmitt et al. [99] also note that pressure oscillation can lead to a large change in NO production compared to stable combustion that they attribute to the equivalence ratio fluctuations observed in the instability mechanism. They conclude that a proper description of the acoustics in LES of swirl turbulent burner may be necessary in order to predict not only combustion instabilities but also pollutants emissions. Rocha et al. [93] conclude that pulsating combustion can be a way to control pollutants emissions even though it was not possible to say if their acoustic actuation eventually increased or decreased the amount of emitted NO_x. They see combustion controlled by an acoustic field as a way to mix reactants in lean mixtures in order to decrease NO_x production without developing the problems associated with premixing such as ignition in the premixed chamber, flame anchoring and combustion instabilities.

2.6   Simulations of swirl flames

Numerical simulations of swirl flows have made impressive progress during the last decade with some recent LES calculations involving practical combustors [11; 52; 89]. This section briefly reviews some results obtained by numerical simulations.

2.6.1 Examples of simulations

Simulations of swirl flows have started with computations of axisymmetric, steady laminar and incompressible flows in the 70's [63]. Then computations have started resolving unsteady axisymmetric simulations making it possible to predict axisymmetric breakdown with periodic flow behavior [104]. The first turbulent swirl flow computations have been based on the $k - \epsilon$ model using RANS formulation [9]. However, since this time, it has been found that RANS approaches based on the $k - \epsilon$ model are too inaccurate for the simulation of strongly swirling flows due to the presence of evident large-scale unsteady motions in such flows and fundamental problems with the gradient diffusivity concept [9; 11; 52; 89].

Recently, LES of swirl stabilized combustors have been carried out. In the case of non-reactive simulations, we can quote the computations of a gas turbine injector [124] and of the Sydney swirl burner [52]. These computations show good predictions of the turbulent flow features such as the recirculation structures, the vortex breakdown, the precessing vortex core [52; 124] or Kelvin-Helmholtz instabilities [124]. In the reactive simulations of the Sydney swirl burner [52], LES predictions were found to be less satisfactory. In particular, temperatures predictions suffer from error propagation due to small deviations in the mixture fraction. Kim et al. [55] conducted the simulation of both non-reacting and reacting turbulent flows of a lean-premixed swirl stabilized annular combustor using LES turbulent model combined with a flamelet library approach to take into account the turbulent combustion. The vortex breakdown, shear layer and recirculation zones were reproduced well by the LES. In both the non-reacting and reacting flows, turbulent structures appear to oscillate periodically in the confined annular combustor and the strong periodic vortex ring is found to be a source of combustion oscillation. This comment agrees with other results carried out in Ref. [15]. In that study, LES of swirl flames acoustically perturbed were conducted. The main conclusion of the study was that combustion instabilities in gas turbine engines may also have an aerodynamic nature related to how swirling flows responded to acoustic perturbations. Other studies have been conducted where LES and acoustic analysis were used together to analyze swirled premixed combustor. Roux et al. [96] confirmed that hydrodynamic structures such as

PVC appearing in cold flow can disappear when combustion starts while acoustic modes are reinforced by combustion.

2.6.2 Prediction of emissions

In Ref. [99], Schmitt et al. take an interest in modelling NO_x production. They claim that the prediction of pollutants is strongly related to the modelling of oscillation levels inside the combustors and that the equivalence ratio fluctuations observed in the instability mechanism are the cause of the higher NO emissions. Another important mechanism pointed out is the vortex-driven combustion instabilities: the formation of a vortex of unburnt gases causes velocity fluctuations, and burns after a certain time delay, coupling velocity fluctuations and heat release fluctuations. The conclusion of the study was that a compressible formulation may be required to get the right fluid mechanics in enclosed flames with acoustics and undergoing oscillations, and may hence be necessary for this type of flow in order to predict NO emissions accurately.

Fairweather and Woolley [37] conducted a three dimensional Conditional Moment Closure (CMC) calculation coupled with a Reynolds-averaged Navier-Stokes (RANS) method to study a bluff body swirl-stabilized, turbulent non-premixed methane flame. Some discrepancies in the prediction of species were thought to arise from the combustion model, which cannot differentiate between diffusion and partially premixed flames. It was claimed that the model should contain elements of both premixed and non-premixed combustion to deliver better results [37]. However, Kim and Mastorakos [53] obtained good predictions of the lift-off height of the lifted flame even if their CMC model did not contain any representation of triple flame or edge flames, a typical structure in partially premixed combustion. Kim and Huh [56] computed a turbulent CH_4/H_2 flame over a bluff body using CMC coupled with PDF method and a modified $k - \epsilon$ model for turbulence, focusing on NO formation using different chemical mechanisms: the GRI Mech 2.11 and 3.0, and the Miller-Bowman. They found almost identical results for the major species and temperature. The conditional mean NO mass fractions by the GRI Mech 2.11 and Miller-Browman mechanism were close to each other and in agreement with the measurements. However, the GRI Mech

3.0 gave the NO mass fractions about twice as large as those from the other two mechanisms. Previous results seem to be consistent with these data [7; 95].

2.7 Context of the work and its objectives

As we saw previously, swirling flames can show various aspects of their aerodynamics such as precession or vortex formation caused by flow oscillations and various combustion aspects such as localized extinctions and lift-off. All the above affect flame stabilization in different ways and are explored through focused simulations in this thesis.

Chapter 4 investigates the stabilization problem from an aerodynamic point of view. The canonical configuration previously described in Section 2.2.1 and composed of a bluff body and a sudden expansion is investigated further, but this time different monochromatic pulsations are imposed at the flow inlet as described in Section 2.4.3. This study aims at delivering further insights on the aerodynamics of combustors experiencing self-exciting oscillations, in the continuity of the review presented in Section 2.4, but without the extra complexities of the combustion or the swirl itself. In particular, focus is given to the vortex shedding occuring when the flow is pulsated at high enough frequency.

Chapter 5 investigates a piloted non-premixed flame. The relatively simple configuration compared to bluff body or swirl flames allows to analyze further some key combustion aspects of combustors described in Section 2.1. In particular, the effects of the pilot flame on flame stabilization are investigated and further insights on the dynamics of localized extinctions and re-ignition are provided. The pollutants emissions, which were reviewed in Section 2.5.1, are also investigated and their analysis allows to evaluate the quality of the LES-CMC formulation compared to the other simulations and methods presented in Section 2.6.2.

These two previous chapters are thought to be preliminary studies that investigate independently several aspects of the aerodynamics (Chapter 4) and combustion process (Chapter 5). Chapter 6 focuses on the aerodynamic stabilization of a swirl flame. In particular, proper orthogonal decomposition of the LES datasets allows to gain further insight of the PVC-like structures develop-

ing in the burner, which is reviewed in Section 2.3, in both inert and reacting configurations. Further insights on the dynamics of these structures and their influence on the flame stabilization in the vicinity of the burner are presented. This study enriches the understanding of hydrodynamic instabilities presented in Section 2.4.2.

Finally, Chapter 7 investigates the combustion process occuring in the swirl flame in detail. In particular, a comprehensive analysis of the lift-off reproduced by the LES-CMC formulation is provided. The flame dynamics close to the burner and its stabilization process through the Central Recirculation Zone are also analyzed, along with pollutants emissions.

Chapter 3

Models and codes

3.1 Large Eddy Simulations

The different numerical investigations presented in the thesis have been conducted using Large-Eddy Simulation (LES). LES is based on the energy-cascade hypothesis: the turbulence is considered to be composed of eddies of different sizes with different characteristic velocities and timescales. The larger of these eddies are unstable and break up, transferring their energy to smaller scales and so on, until the eddies are small enough so that their kinetic energy can be dissipated by the molecular viscosity [91].

In LES, a low-pass spatial filtering operation is performed. Thus only the largest structures of the flow field are computed and the small scales have to be modelled. The filtered continuity and momentum equations are [90; 91]:

$$\frac{\partial \overline{\rho}}{\partial t} + \frac{\partial (\overline{\rho} \widetilde{u}_i)}{\partial x_i} = 0 \tag{3.1}$$

$$\frac{\partial (\overline{\rho} \widetilde{u}_j)}{\partial t} + \frac{\partial (\overline{\rho} \widetilde{u}_i \widetilde{u}_j)}{\partial x_i} = -\frac{\partial \overline{p}}{\partial x_j} + \frac{\partial \widetilde{\tau}_{ij}}{\partial x_i} - \frac{\partial (\overline{\rho} \tau^r_{ij})}{\partial x_i} \tag{3.2}$$

where $\overline{\rho}$ is the resolved density, $\widetilde{u}_i$ is the resolved velocity in the i direction, $\widetilde{\tau}_{ij}$ is the resolved stress tensor:

$$\widetilde{\tau}_{ij} = 2\overline{\mu} \left[\widetilde{S}_{ij} - \frac{1}{3} \delta_{ij} \frac{\partial \widetilde{u}_k}{\partial x_k} \right] \tag{3.3}$$

28

where $\widetilde{S}_{ij}$ is the filtered rate-of-strain tensor:

$$\widetilde{S}_{ij} = \frac{1}{2}\left(\frac{\partial \widetilde{u}_i}{\partial x_j} + \frac{\partial \widetilde{u}_j}{\partial x_i}\right) \tag{3.4}$$

and τ_{ij}^r is the residual stress tensor:

$$\tau_{ij}^r = \widetilde{u_i u_j} - \widetilde{u}_i \widetilde{u}_j \tag{3.5}$$

The term τ_{ij}^r appears in unclosed form and needs to be modelled. The dynamic Smagorinsky model, which can be viewed in two parts, is used here [39]. First, τ_{ij}^r is related to the filtered rate-of-strain tensor through a linear eddy viscosity model:

$$\tau_{ij}^r - \delta_{ij}/3\tau_{ii}^r = -2\nu_t \widetilde{S}_{ij} \tag{3.6}$$

where ν_t is the sub-grid scale viscosity. Next, ν_t is modelled as:

$$\nu_t = (C_S \Delta)^2 \widetilde{\mathcal{S}} \tag{3.7}$$

where C_S is the Smagorinsky parameter, Δ is the filter width and $\widetilde{\mathcal{S}}$ the characteristic magnitude of the filtered rate of strain:

$$\widetilde{\mathcal{S}} = \left(2\widetilde{S}_{ij}\widetilde{S}_{ij}\right)^{1/2} \tag{3.8}$$

C_S is calculated dynamically using a scale similarity approach [39] and Δ is equal to the size of the LES cell which is equal to the cubic root of its volume.

A transport equation for a conserved scalar (the mixture fraction ξ) is also solved:

$$\frac{\partial(\overline{\rho}\widetilde{\xi})}{\partial t} + \frac{\partial(\overline{\rho}\widetilde{\xi}\widetilde{u}_i)}{\partial x_i} = \frac{\partial}{\partial x_i}(\overline{\rho}D\frac{\partial \widetilde{\xi}}{\partial x_i}) - \frac{\partial(\overline{\rho}J_i^r)}{\partial x_i} \tag{3.9}$$

where $\widetilde{\xi}$ is the resolved mixture fraction and J_i^r represents the scalar transport due to sub-grid scale fluctuations:

$$J_i^r = \widetilde{u_i \xi} - \widetilde{u}_i \widetilde{\xi} \tag{3.10}$$

Fick's diffusion law with equal diffusivities for all species has been considered

and the diffusivity is $D = \nu/Sc$, where a constant Schmidt number $Sc = 0.7$ has been considered. The unclosed term J_i^r is modelled similarly to the residual stress tensor τ_{ij}^r in the momentum equation and assuming a constant turbulent Schmidt number $Sc_t = 0.7$ [16] i.e. by assuming that the sub-grid scale flux is proportional to the resolved gradient:

$$\widetilde{u_i \xi} - \widetilde{u}_i \widetilde{\xi} = -D_t \frac{\partial \widetilde{\xi}}{\partial x i} \tag{3.11}$$

In this PhD work, the sub-grid variance of the mixture fraction has been obtained by the following gradient type model:

$$\widetilde{\xi''^2} = C_v \Delta^2 \frac{\partial \tilde{\xi}}{\partial x_i} \frac{\partial \tilde{\xi}}{\partial x_i} \tag{3.12}$$

with C_v determined dynamically [25; 88]. For completeness, the filtered transport equation for $\widetilde{\xi''^2}$ is also given below (although it has not been used in this thesis):

$$\frac{\partial(\overline{\rho}\widetilde{\xi''^2})}{\partial t} + \frac{\partial(\overline{\rho}\widetilde{u}_i\widetilde{\xi''^2})}{\partial x_i} = \frac{\partial}{\partial x_i}(\overline{\rho}(D + D_t)\frac{\partial \widetilde{\xi''^2}}{\partial x_i}) - 2\overline{\rho}\widetilde{N} + 2\overline{\rho}(D + D_t)\frac{\partial \widetilde{\xi}}{\partial x_i}\frac{\partial \widetilde{\xi}}{\partial x_i} \tag{3.13}$$

where $\widetilde{N}$ is the scalar dissipation rate, which will be detailed in Section 3.2.2.

The simulations have been performed using the code PRECISE [49], which is a low Mach number, finite-volume code that uses structured grids. The pressure-correction equation is solved using the SIMPLE algorithm [85]. Convective transport is discretised using a second-order central scheme, while time derivatives are discretized with a second-order backward difference scheme and integration in time is done using the explicit Adams-Bashforth method. PRECISE is fully parallelised using domain decomposition. PRECISE has previously been used to simulate forced ignition of a non-premixed bluff body methane flame [118] with very good results.

3.2 Combustion modelling

3.2.1 Mixture fraction

In the thesis, we focus on non-premixed combustion, where fuel and oxidiser enter separately the combustion chamber. The rate of mixing between fuel and oxidiser can be described by a conserved scalar, the mixture fraction [10]. It takes the value of unity in the fuel stream and zero in the oxidiser stream. The mixture fraction may be physically interpreted as the mass fraction of material that originated in the fuel stream. The introduction of the mixture fraction leads to the conserved scalar methods that forms the basis of the models used in non-premixed turbulent combustion. In the conserved scalar method, the species mass fractions and temperature (or enthalpy) are considered to be functions of the mixture fraction only. The aim of the different mixture fraction based models is to calculate these functions.

3.2.2 3D-CMC

The CMC combustion model developed independenly by Bilger and Klimenko [60] has been used throughout this PhD work to model combustion. The CMC solver used for 0D (see Section 3.2.3) and multi-dimensional CMC computations has been developed in the Hopkinson Laboratory, Department of Engineering, University of Cambridge. It has been used in two-dimensional studies of a lifted [53] and an opposed flame [54], but also in auto-ignition problems [72; 125], as well as in diesel engine simulations [26].

The CMC model has recently been incorporated to the code PRECISE and details of the implementation can be found in Refs. [117; 118]. The CMC equations in a LES context are derived by filtering the transport equations for the reactive scalar Y_α [80] and can be written as:

$$\frac{\partial Q_\alpha}{\partial t} + \widetilde{u_i|\eta}\frac{\partial Q_\alpha}{\partial x_i} = \widetilde{N|\eta}\frac{\partial^2 Q_\alpha}{\partial \eta^2}$$
$$+ \widetilde{\omega_\alpha|\eta} + e_f \tag{3.14}$$

where $Q_\alpha = \widetilde{Y_\alpha|\eta}$ is the conditionally filtered reactive scalar, $\widetilde{u_i|\eta}$ is the condition-

ally filtered velocity, $\widetilde{N|\eta}$ is the conditional filtered scalar dissipation rate, $\widetilde{\omega_\alpha|\eta}$ is the conditionally filtered reaction rate, while the term:

$$e_f = -\frac{1}{\bar{\rho}\widetilde{P}(\eta)}\frac{\partial}{\partial x_i}\left[\bar{\rho}\widetilde{P}(\eta)\left(\widetilde{u_iY_\alpha|\eta} - \widetilde{u_i|\eta}Q_a\right)\right] \tag{3.15}$$

is the sub-grid conditional flux. This and the convection term account for the conditional transport in physical space. All the species are assumed to have equal diffusivities and the Lewis number is assumed to be unity. The terms $\widetilde{\omega_\alpha|\eta}$, $\widetilde{u_i|\eta}$, $\widetilde{N|\eta}$ and e_f are unclosed and require modelling.

First order closure is used for the chemical reaction rate; the CMC for non-premixed flames is based on the concept that the fluctuations of the reacting scalars are correlated with the fluctuations of the mixture fraction [61]. This leads to the notion of first order closure for the chemical source term in terms of conditional averages; since the fluctuations of the conditional reacting scalars are small, they may be neglected and the conditional chemical source term may be calculated based on the conditional averages of the scalars:

$$\widetilde{\omega_\alpha|\eta} = \omega_\alpha(Q_1, Q_2, ..., Q_n) \tag{3.16}$$

where n is the number of reacting scalars. First order closure will be used throughout this thesis.

The simple assumption that the conditional velocity is equal to the unconditional velocity is made here:

$$\widetilde{u_i|\eta} = \widetilde{u}_i. \tag{3.17}$$

The conditionally filtered scalar dissipation rate $\widetilde{N|\eta}$ is modelled by the Amplitude Mapping Closure (AMC) model, which is fully described in Refs. [22]. According to this model, the conditional scalar dissipation rate has a given shape in mixture fraction space, which is scaled according to the local value of the unconditional scalar dissipation rate:

$$\widetilde{N|\eta} = N_0 G(\eta)$$

where

$$G(\eta) = exp\left(-2[erf^{-1}(2\eta - 1)]^2\right)$$

and

$$N_0 = \frac{\widetilde{N}}{\int_0^1 G(\eta)\tilde{P}(\eta)d\eta} \tag{3.18}$$

where $\widetilde{N}$ is the filtered scalar dissipation rate, found by summing the resolved and the (modelled) sub-grid contributions:

$$\widetilde{N} = \widetilde{N}_{res} + \widetilde{N}_{sgs} \tag{3.19}$$

The resolved scalar dissipation rate is defined as:

$$\widetilde{N}_{res} = D\left(\frac{\partial\widetilde{\xi}}{\partial x_i}\right)^2 \tag{3.20}$$

and the sub-grid is estimated by:

$$\widetilde{N}_{sgs} = \frac{1}{2}C_N\widetilde{\xi''^2}/\tau_t \tag{3.21}$$

and assuming that the mixing timescale is proportional to a characteristic velocity timescale for the sub-grid $\tau_t = \Delta^2/\nu_t$. The absence of experimental data for the scalar dissipation rate in the experiments modelled throughout this PhD work does not allow to adjust properly the constant C_N. As a consequence, the value $C_N = 42$, which had been previously adjusted to match the experimental results of conditionally averaged $\langle N|\eta\rangle$ for Sandia flame D [38], has been used. No other parameter has been tuned. Finally, a gradient model is used for the sub-grid scale conditional flux:

$$\widetilde{u_iY_\alpha|\eta} - \widetilde{u_i|\eta}Q_a = -D_t\frac{\partial Q_a}{\partial x_i} \tag{3.22}$$

3.2.3 0D-CMC

In order to understand the structure of the steady flame and validate the accuracy of the chemical mechanisms, distributions against mixture fraction of temperature, T, and species mass fractions, Y_α, have been computed using the CMC

equations in the zero-dimensional formulation. In the 0D-CMC calculations, only the micromixing and chemical reaction terms are considered:

$$\frac{\partial Q_\alpha}{\partial t} = N|\eta \frac{\partial^2 Q_\alpha}{\partial \eta^2} + \omega_\alpha|\eta \qquad (3.23)$$

where $Q_\alpha = Y_\alpha|\eta$ is the conditional reactive scalar, $N|\eta$ is the conditional scalar dissipation rate and $\omega_\alpha|\eta$ is the conditional reaction rate. The 0D-CMC equations (Eq. 3.23) do not contain any spatial transport. All the species are assumed to have equal diffusivities and the Lewis number is assumed to be unity. The terms $\omega_\alpha|\eta$ and $N|\eta$ are unclosed and require modelling. First order closure is also provided for the chemical reaction rate. The conditional scalar dissipation rate $N|\eta$ is modelled by the Amplitude Mapping Closure (AMC) model, which has been described in Section 3.2.2. According to this model, the conditional scalar dissipation rate has a given shape in mixture fraction space, which is scaled by its peak value, N_0, across η-space. N_0 is here pre-selected and kept at the prescribed value while the CMC equations are solved. In order to solve Eq. 3.23, the η-space is discretised into several nodes clustered around the stoichiometric mixture fraction ξ_{st}. At $\eta = 0$ the air stream conditions are imposed and at $\eta = 1$ the fuel stream conditions.

For different values of N_0, the unsteady CMC equations (Eq. 3.23) are then computed until eventually converging to a steady solution. As N_0 increases, the limit where heat is diffused quicker than it is produced is reached and the flame extinguishes. In this thesis, 0D-CMC has also been used as a sub-grid combustion model to perform preliminary simulations. The method is similar to a steady flamelet model with unity Lewis number.

3.2.4 Coupling LES-CMC

Fig. 3.1 summarizes the coupling between the CFD and CMC solvers. This sequence takes place at each timestep of the simulation. The CFD code computes the resolved velocity, the resolved mixture fraction, its sub-grid variance and the filtered scalar dissipation rate. It is assumed that the Filtered probability Density Function (FDF) $\widetilde{P}(\eta)$ has a β-function shape, which is calculated based on the

resolved $\widetilde{\xi}$ and the modelled sub-grid variance $\widetilde{\xi''^2}$ of the mixture fraction (Eq. 3.12). $\widetilde{P}(\eta)$ is therefore computed for each LES cell.

At the end of the LES timestep, the information for $\widetilde{u_i|\eta}$ and $\widetilde{N|\eta}$ needed in each CMC node are mass-weighted and PDF-averaged over all LES cells associated with that CMC node. The integrated conditionally filtered velocity $\widetilde{u_i|\eta}^*$ is thus obtained through the formula:

$$\widetilde{u_i|\eta}^* = \frac{\int_{CMC\ cell} \widetilde{P}(\eta)\ \widetilde{\rho|\eta}\ \widetilde{u_i|\eta}\ dV}{\int_{CMC\ cell} \widetilde{P}(\eta)\ \widetilde{\rho|\eta}\ dV} \tag{3.24}$$

assuming that the velocity is constant in η-space (Eq. 3.17).

A filtered probability density function $\tilde{P}^*(\eta)$ is computed for each CMC cell by applying the β-PDF assumption at the CMC resolution. An integrated resolved mixture fraction is used:

$$\widetilde{\xi}^* = \frac{\int_{CMC\ cell} \bar{\rho}\widetilde{\xi}dV}{\int_{CMC\ cell} \bar{\rho}dV} \tag{3.25}$$

and an integrated sub-grid scale variance. In this thesis, we use the following formula which has been derived in Ref. [117]:

$$\widetilde{\xi''^2}^{**} = \widetilde{\xi''^2}^* + \widetilde{\xi}^{2*} - \widetilde{\xi}^{*2} \tag{3.26}$$

where

$$\widetilde{\xi''^2}^* = \frac{\int_{CMC\ cell} \bar{\rho}\widetilde{\xi''^2}dV}{\int_{CMC\ cell} \bar{\rho}dV} \tag{3.27}$$

The first term of Eq. 3.26 is based on the same volume averaged procedure as for the resolved mixture fraction (Eq. 3.25). The two last terms that appear in the derivation of Eq. 3.26 account for the variations of the resolved mixture fraction inside every CMC cell. The different options available for these integrations are discussed in Ref. [117].

The integrated conditionally filtered scalar dissipation rate $\widetilde{N|\eta}^*$ is computed by applying the AMC model (Eqs. 3.18) directly to the CMC cells. This is done by replacing N_0 by:

$$N_0^* = \frac{\widetilde{N}^*}{\int_0^1 G(\eta)\tilde{P}^*(\eta)d\eta} \tag{3.28}$$

where $\widetilde{N}^*$ is the integrated filtered scalar dissipation rate:

$$\widetilde{N}^* = \frac{\int_{CMC\ cell} \bar{\rho}\widetilde{N}dV}{\int_{CMC\ cell} \bar{\rho}dV} \tag{3.29}$$

The system of CMC equations can then be solved resulting in the conditionally filtered species mass fractions Q_α and the conditionally filtered temperature Q_T, based on which the conditional density is calculated.

In both LES/0D-CMC and LES/3D-CMC, the filtered value of a variable f can be obtained by integration over η-space:

$$\widetilde{f} = \int_0^1 \widetilde{f|\eta}\widetilde{P}(\eta)d\eta \tag{3.30}$$

Note again that $\widetilde{P}(\eta)$ is available at every LES cell, while $\widetilde{f|\eta}$ is available at each CMC cell, which may encompass many LES cells, the number depending on each problems studied. Each LES cell uses therefore the conditional temperature and density from its associated CMC node to find the new unconditional values of density and temperature after integrating by the presumed sub-grid FDF of the mixture fraction at the LES resolution (Eq. 3.30). The coupling between the CMC model and the LES code is thus achieved through density and temperature.

3.3 Proper Orthogonal Decomposition

3.3.1 Principle

LES is a very powerful tool in reproducing temporal variation of 3D flows and flames. However, most of the analyses of numerical results are still based on averaged information i.e. radial profiles of the mean quantities and their Root Mean Squares. In this thesis, we focus on the dynamics of the flow and the flame. In order to take advantages of the full potential of the LES, the Proper Orthogonal Decomposition (POD) Method has been applied using the Method of Snapshots [105]. The idea behind POD is to find an orthonormal vector basis for which the projection of the turbulent flow/flame fields (i.e. snapshots) on it maximizes the fluctuation energy for any subset of the basis. Having found
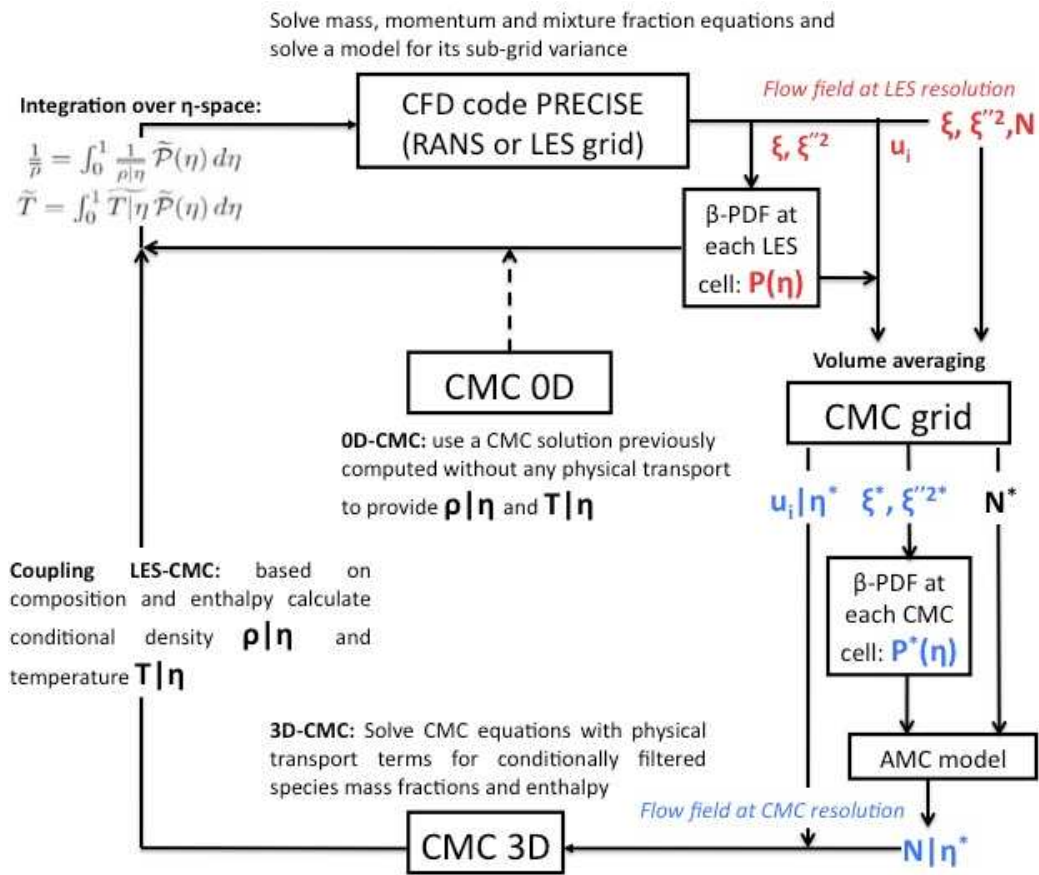
Figure 3.1: Schematic showing the coupling of the CFD and the CMC solvers according to the type of computation: 0D-CMC or 3D-CMC.

such a basis, the first modes contain the most energetic unsteady structures of the flow and hence some understanding of the flow dynamics can be obtained by analyzing only a few modes.

3.3.2 Method

POD has been applied to different 3D numerical datasets of both inert and reactive simulations throughout this thesis. The numerical data from the LES mesh are first interpolated on a coarser grid to decrease the computational load. The set of interpolated snapshots is then loaded into a self-written MATLAB programme. The POD routines are able to compute the spatial POD modes, project the snapshots on each POD mode to calculate the associated temporal coefficient, and to reconstructe the snapshots based on any combination of modes. The variables used to calculate the POD basis always include the three components of the velocity fluctuations, but other variables have been added depending on the case, such as the mixture fraction fluctuations, the pressure fluctuations for inert simulations, while in the reactive case the temperature fluctuations have also been used. The variables from each snapshot are stored into a single matrix column, each row corresponding to the values of a variable at a single cell. Hence each matrix column corresponds to a single snapshot (i.e. the instantaneous fluctuation fields) and these snapshots are organized chronologically inside the matrix. Unlike previous studies where POD was applied separately to the different variables of the flame (Ref. [32] or Ref. [33] for extended POD), here POD has been applied simultaneously to the different variables such as the velocity, the mixture fraction, the pressure or the temperature. This method is expected to bring to light the correlations among the flow dynamics, the mixing dynamics and the flame dynamics. In order to give the same weight to each variable used to perform the POD modes computation, the fluctuating component of each quantity has been divided by its standard deviation. However, in practice it has been found that the same modes are identified with or without scaling the variables by their standard deviations. The only differences between the two methods is a slight discrepancy in the distribution of the modes energy. In the case of a POD computation with N snapshots on a computational domain of m points, the

matrix obtained is:

$$U = [u_1...u_n] = \begin{pmatrix} \frac{U_1^1 - \bar{U}_1}{\sigma(U_1)} & \frac{U_1^2 - \bar{U}_1}{\sigma(U_1)} & \cdots & \frac{U_1^N - \bar{U}_1}{\sigma(U_1)} \\ \vdots & \vdots & \vdots & \vdots \\ \frac{U_m^1 - \bar{U}_m}{\sigma(U_m)} & \frac{U_m^2 - \bar{U}_m}{\sigma(U_m)} & \cdots & \frac{U_m^N - \bar{U}_m}{\sigma(U_m)} \\ \vdots & \vdots & \vdots & \vdots \end{pmatrix} \tag{3.31}$$

The matrix $C = U^T U$ of dimension $N \times N$ is then computed. C is a real and symmetric matrix, and therefore it is diagonalizable in an orthonormal basis. It has N positive eigenvalues $\{\lambda_i\}_{i \subset [1;N]}$ and N orthogonal eigenvectors $\{a_i\}_{i \subset [1;N]}$ such as $Ca_i = \lambda_i a_i$. In order to solve this eigenvalue problem, the MATLAB routine eig has been used. The solutions are then arranged according to their eigenvalues as $\lambda_1 \geq \lambda_2 \geq ... \geq \lambda_N > 0$ and the POD modes can be written as linear combination of the snapshots:

$$\Phi_i = \frac{\sum_{n=1}^{N} a_{in} u_n}{\|\sum_{n=1}^{N} a_{in} u_n\|}, i = 1...N \tag{3.32}$$

If $\Psi = [\Phi_1 \Phi_2 ... \Phi_N]$ is the POD basis, then the fluctuating part of a snapshot can then be reconstructed as:

$$U_j = \sum_{i=1}^{N} a_{ij} \Phi_i = \Psi a_j, j = 1...N \tag{3.33}$$

In practice, reconstructing a snapshot using only the first few modes allows to filter the data by removing the least energetic modes, regarded as noise, and conserve only the most energetic structures of the flow. The reconstruction can also be based on some specific modes of the flow, without including the most energetic ones, if for instance we want to focus on a specific structure such as the Precessing Vortex Core.

Chapter 4

Large-eddy simulations of forced bluff body flows

4.1 Introduction

4.1.1 Motivation

The isothermal air flow behind an enclosed axisymmetric bluff body, with the incoming flow being forced at a single frequency and with large amplitude, has been explored with Large-Eddy Simulations (see Chapter 3, Section 3.1). The configuration studied is shown schematically in Fig. 4.1. It consists of an air flow in a pipe of diameter D, the near wake behind an axisymmetric bluff body (a disk of diameter d) located at the end of the pipe, and a circular enclosure of diameter D_o ($d < D < D_o$). The flow coming out of the annular passage between the disk and the inner wall of the pipe has time-averaged velocity of U_b, but is forced to pulsate at given frequencies and amplitudes. We focus on high Reynolds number flows only. The aim of this chapter is to study this flow numerically by Large-Eddy Simulation, while velocity measurements of the experimental set-up have been previously obtained at Cambridge University Engineering Department (CUED).

The main motivation is that this flow has strong similarities to flows found in model and realistic combustors. Therefore, the flows behind a bluff body and over a backward-facing step, when the incoming flow rate is pulsating at large
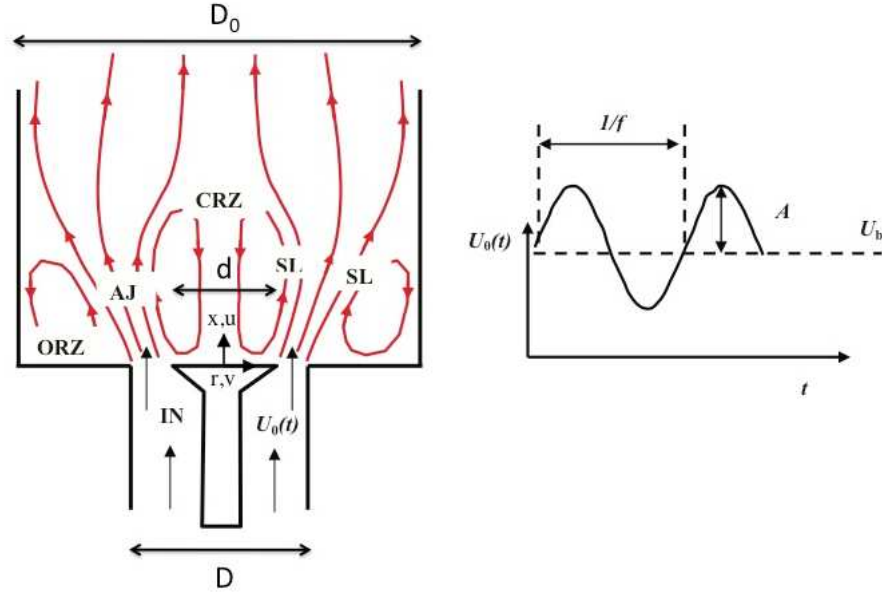
Figure 4.1: Schematic of the flow studied and the initial condition.

amplitudes relative to the mean flow, can be considered as canonical problems for self-excited combustors (see the literature review in Chapter 2). The density variations associated with flames of course change the velocity field, but isothermal studies are useful first steps in understanding the fluid mechanics in burners. Combustors usually have the additional complexity of swirl, but even in the absence of swirl the interaction between the inner and outer recirculation zones and the pulsating flow introduces significant complexities. There are many aspects that have not been studied in detail yet, as it was demonstrated from the discussion in the literature review (Chapter 2).

The experimental rig (Fig. 4.2) has been developed previously at Cambridge [5] and has been used as a burner to study the response of turbulent premixed flames under acoustic forcing, with the level of forcing commensurate to the one used in the present inert flow measurements. CFD with a Reynolds-stress model has also been performed [3] with emphasis on the flame response, while variants of this burner include its use for non-premixed flames [1] and for sprays [71]. Premixed flames forced at two frequencies (the fundamental and its harmonic) have also been explored [6].

41
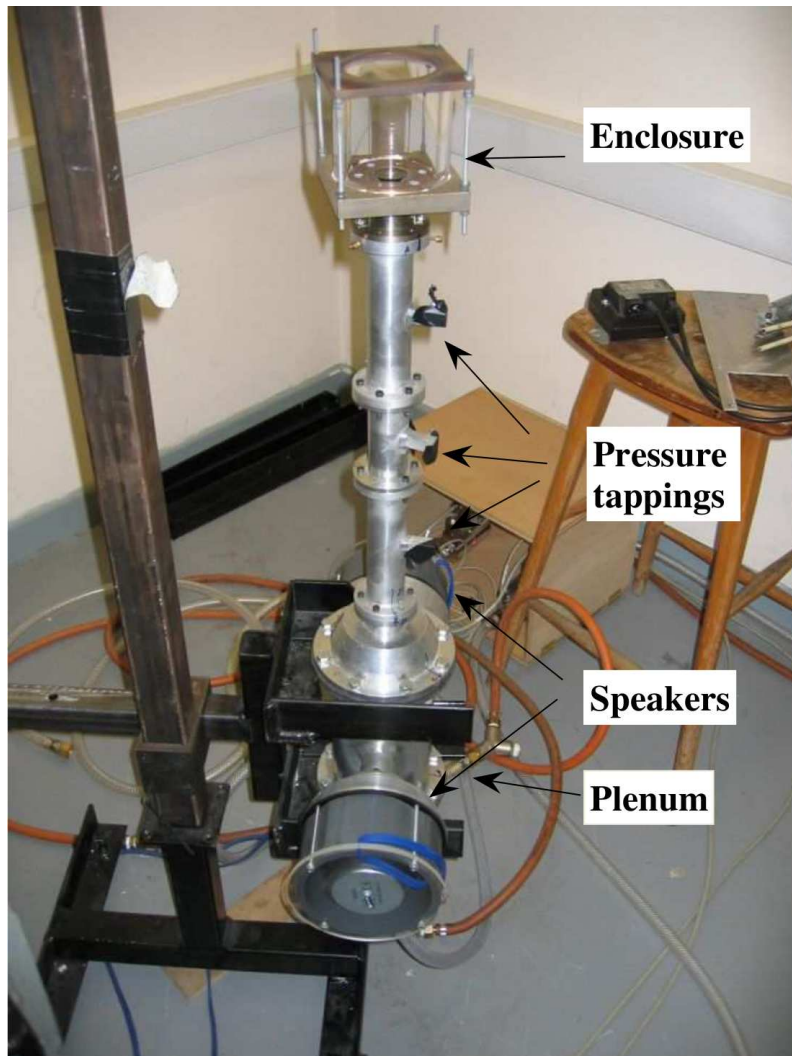
Figure 4.2: Photograph of the burner assembly. From Ref. [4].

4.1.2 Objectives

It is evident from the literature review in Chapter 2 that the configuration schematically shown in Fig. 4.1 is composed of simpler "sub-flows" that have been widely studied, but the flow has not been examined in its entirety, and especially when the incoming flow rate is oscillating. Measurements from this arrangement can also serve as validation data for LES of combustors. These show a great promise in capturing self-excited oscillations, but detailed validation of the fluid mechanics of pulsating flows is a prerequisite step to increase the reliability of the simulations.

The main objectives of this chapter are: (i) to examine the vortex formation process and the mean and fluctuating velocity field in pulsating enclosed bluff body wakes using large-eddy simulation; and (ii) to understand better the flow structure in this arrangement and hence be in a position to understand reacting flow results better.

4.2 Methods

4.2.1 Flow conditions

The flow arrangement is identical to that developed by R. Balachandran (Ref. [5]) for studying flames, but used for inert (air) flow at ambient temperature and pressure. The PhD thesis of R. Balachandran also contains useful details [4]. As shown in Fig. 4.1, one may distinguish various parts of the flow: the annular jet (AJ), which forms two shear layers (SL) with the central (CRZ) and outer recirculation zones (ORZ). Figure 4.3 shows the bluff body used and the enclosure (sudden expansion). The region upstream of the sudden expansion is designed to facilitate external acoustic forcing and can be operated in the absence or presence of strong acoustic oscillations.

The rig consists of two concentric circular ducts of length 300 mm. The inner diameter (ID) of the outer duct was $D = 35$ mm, which also housed pressure taps for acoustic pressure measurements. The inner and outer diameter of the inner pipe were 6 mm and 8 mm respectively; this pipe acts as the holder of the bluff body. The bluff body was conical (45° half-angle) with diameter $d = 25$ mm,
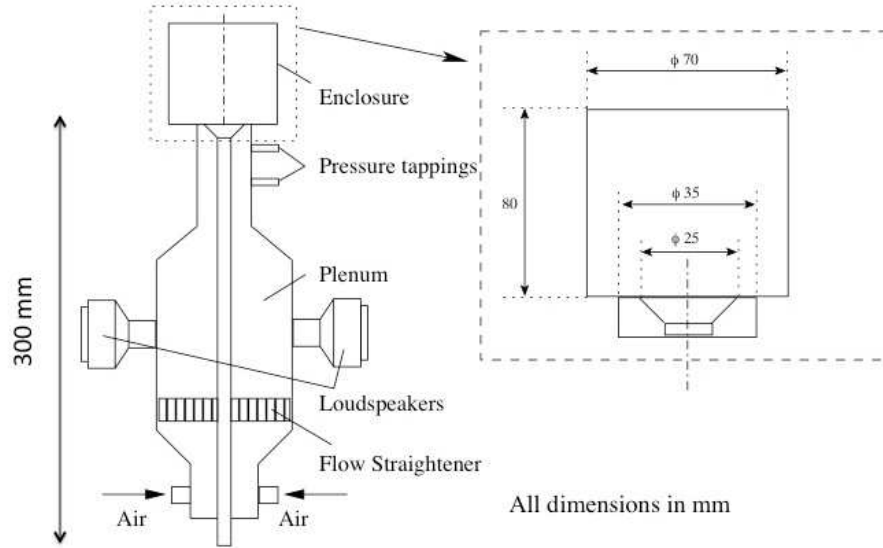
Figure 4.3: The bluff body and the sudden expansion. All lengths in mm.

giving a blockage ratio of 50%. The enclosure was a 80 mm long fused silica quartz cylinder of inner diameter $D_o = 70$ mm which provided optical access for the velocity measurements and also avoided air entrainment from the surroundings. In order to reduce the interference from the acoustics of the downstream geometry on upstream forcing, the length of the enclosure was chosen to be small so that its resonant frequency was much higher than the frequency of forcing. The range of operation of the forcing frequency in the apparatus was between 20 to 400 Hz while the fundamental frequency of the downstream duct is around 1000 Hz, hence the resonant effects of the downstream geometry are minimized. For details on the acoustic performance of the plenum, see Section 3 of Ref. [4].

The time-averaged volume flow rate divided by the annular passage area $(\pi(D^2 - d^2)/4)$ gives the time-averaged bulk velocity U_b and was equal to 10 m/s for all experiments. This gives a Reynolds number $Re = dU_b/\nu$ equal to 16,000. Experimentally, the flow upstream of the duct (in a plenum about 300 mm long and 200 mm diameter) is pulsed by loudspeakers fed by a signal generator of varying frequency and voltage, hence producing a pure tone. Due to the interaction of this tone with the acoustic characteristics of the plenum, a strong

Table 4.1: Flow conditions studied. $U_0 = U_b[1 + A\sin(2\pi ft)]$, $St = fd/U_b$.

Case	U_b(m/s)	f (Hz)	St	A
U	10	0	0	0
A	10	40	0.1	0.89
B	10	160	0.4	0.60
C	10	320	0.8	0.75

velocity oscillation is achieved at the exit of the pipe that is almost monochromatic, and the amplitude of this oscillation varies with the forcing frequency. An approximately sinusoidal fluctuation is therefore superimposed, so that the velocity at the annular passage follows:

$$U_0 = U_b[1 + A\sin(2\pi ft)] \qquad (4.1)$$

with A the ratio of oscillation amplitude to mean flow velocity U_b. In the LES, a velocity oscillation following the same equation has been imposed at the air pipe inlet (numerical inlet at $x = 25$ mm) in order to mimic the loudspeakers action.

The flow conditions studied are summarized in Table 4.1. Three frequencies f were tested: 40 Hz, 160 Hz and 320 Hz, giving rise to Strouhal number (based on the bluff body diameter d and U_b) 0.1, 0.4, and 0.8 respectively. The amplitudes for every one of these frequencies are shown in Table 4.1 and they are in the range 0.6-0.9. It is evident that these amplitudes are much higher than those studied in the literature of forcing separation regions for control purposes, where amplitudes in the range of only a few percent are commonly used [29; 40].

As discussed in the Literature Review in Chapter 2, we may expect a weak helical-type vortex shedding at a Strouhal number of about 0.135, which implies a frequency of $f_n = 54$ Hz. For the vortices associated with the Kelvin-Helmholtz instability of the separated shear layer, we must consider the local momentum thicknesses of the two shear layers (between the annular jet and the central and outer recirculation zones respectively), but it is difficult to estimate these in the present problem. A Strouhal number based on the bluff body diameter and the (steady) incoming velocity for a sphere in unconfined flow, $St_{KH} = f_{KH}d/U_b$, has been measured as a function of Reynolds number [58], and for $Re = 16000$ (which is the value used in the present experiments), we get $St_{KH} = 3$ from which we

evaluate $f_{KH} = 1200$ Hz. Although the present flow is confined and the bluff body is a disk, we may wish to consider this estimate as a guide to the expected frequency of the shear layer Kelvin-Helmholtz instability, at least of the shear layer towards the CRZ. Considering now the sudden expansion, we discussed in the Literature Review the possibility of central jet precession and of a frequency peak associated with the re-attachment length fluctuations. The slow precession would be estimated to happen at a frequency of about $0.01 U_b/D$, extrapolating the results of Ref. [79] to the present flow, which gives a f_p=2.9 Hz. Ref. [24] reported $f_r D/U_b \approx 0.3$ for the re-attachment length fluctuations, which gives a frequency of $f_r = 86$ Hz. It is evident that the present forcing frequencies are not expected to resonate with these natural vortex shedding or instability processes.

A flow without any periodic oscillations at the inlet has also been examined previously by both experiment [1] and LES [118]. Here it has been recomputed in order to perform spectral analysis and to provide a reference case to the forced simulations.

4.2.2 Mesh and modelling

The flows have been simulated numerically with Large-Eddy Simulation (LES) using the code PRECISE, which is described in Chapter 3, Section 3.1.

The mesh extends 25 mm upstream of the bluff body, to allow some flow development, and 50 mm downstream of the cylindrical enclosure. It consists of 1.8M cells. The unforced flow has also been recomputed with the same mesh and it was found in a earlier work [118] that a finer grid did not improve the results, which suggests that the present grid is sufficient.

The numerical inlet had an area A_{in} (slightly smaller than $\pi D^2/4$ due to the diameter of the rod holding the bluff body in place). The mean velocity there, U_{in}, has been chosen in order to get a mean velocity of U_b=10 m/s at the annular opening between the bluff body and the sudden expansion following the conservation of mass equation:

$$U_{in}A_{in} = U_b\pi(D^2 - d^2)/4 \tag{4.2}$$

The amplitude A (Eq. 4.1) fits exactly the amplitudes obtained in the exper-

iments (Table 4.1). The velocity at the inlet is forced at a single frequency, uniform across the duct and contains white noise in order to trigger instabilities and turbulence downstream [50]. Therefore, in the simulations, the velocity U_0 at the annular passage given by Eq. 4.1 already contains some turbulence due to the boundary layers at the duct walls from the inlet to the annular opening and refers to an area-averaged, phase-averaged velocity.

For the 40 and 160 Hz, a timestep of 1.0×10^{-5} s has been used, while for the 320 Hz case, the timestep was 5.0×10^{-6} s. These values ensure the CFL number is less than 0.3 everywhere in the domain. No-slip velocity conditions have been enforced on solid walls, while zero gradient boundary condition has been enforced at the outlet.

The LES for the 40 Hz, 160 Hz and 320 Hz cases have been performed for 14 cycles, 34 cycles and 32 cycles respectively. Phase averaging has been performed by averaging data from each of these cycles. We expect therefore a relatively large statistical uncertainty especially for the phase-averaged fluctuations. Spectra have been calculated with Matlab routines using Welch windowing on the whole data record.

4.2.3   Data processing and comparison with experiments

Experimental measurements are available at five downstream positions, x=5, 15, 25, 35 and 50 mm, with radial traverses taken in 1 mm increments from the centerline to as close to the wall as possible.

The coordinate system used is shown in Fig. 4.1. The instantaneous velocity $u_i(x, r, t)$ can be decomposed in three parts:

$$u_i(x, y, z, t) = \overline{u}_i(x, y, z) + \hat{u}_i(x, y, z, \phi) + u_i'(x, y, z, t) \tag{4.3}$$

with $\overline{u}_i$ the time-averaged velocity, $\hat{u}_i$ the periodic component of imposed period T at phase angle ϕ $(0 < \phi < 2\pi)$, called velocity modulation, and u_i' the fluctuating or turbulent velocity. This fluctuation is therefore the fluctuation about the phase-averaged velocity:

$$\langle u \rangle(\phi) = \overline{u}_i(x, y, z) + \hat{u}_i(x, y, z, \phi) \tag{4.4}$$

In the Results section and dropping the explicit dependence on the spatial coordinates for simplicity, the phase-averaged mean ($\langle u \rangle(\phi)$) and phase-averaged velocity variance ($\langle u'^2 \rangle(\phi)$) are presented. In addition, some phase-averaged quantities are presented at a few selected locations as a function of phase. Finally, spectra of the instantaneous axial velocity (i.e. including both the cyclic and turbulent parts) are also shown to determine any peaks and their evolution.

4.3 Results and Discussion

4.3.1 The unforced flow

For the unforced flow (Case U of Table 4.1), direct comparison with the experimental data in terms of axial and radial mean and Root Mean Square (RMS) velocities has been presented elsewhere [118]. During the present work, the unforced simulation was restarted in order to record some time-series of the three velocity components and perform spectral analysis. The new results from that simulation are presented here to facilitate the discussion on the forced flow. Very good agreement with the experimental data of Ref. [1] has been obtained for both mean and RMS axial and radial velocities. The mean axial velocity has a peak value of approximately $1.2 U_b$ in the annular jet and a minimum value of approximately $-0.5 U_b$ inside the recirculation zone at $x/d = 0.62$. After the exit of the bluff body, mixing makes the velocity profiles more uniform. The zero-velocity zone is predicted to be approximately $0.8d$ wide and $X_s = 1.2d$ long, which is consistent with experimental studies of other flows behind bluff bodies [116]. The level of fluctuations of the axial velocity is also predicted accurately. They reach their highest value at the shear layers (at the location of maximum radial gradient of the mean axial velocity) and they are about 15% of U_b inside the recirculation zone.

To show more clearly the overall flow structure, typical snapshots of the instantaneous axial velocity and the azimuthal component of the vorticity:

$$\omega_\theta = \partial v / \partial x - \partial u / \partial r \tag{4.5}$$
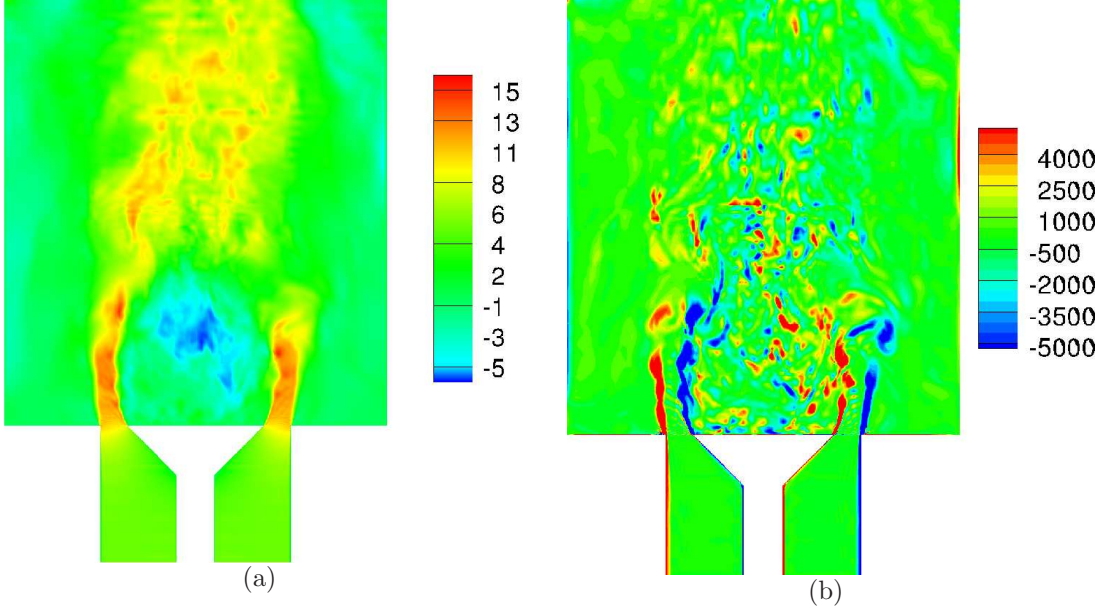
Figure 4.4: Snapshots of (a) axial velocity (in m/s) and (b) azimuthal vorticity ($\omega_\theta = \partial v/\partial x - \partial u/\partial r$; in 1/s) on a plane going through the axis from LES. Unforced flow (Case U).

are shown in Fig. 4.4. The high velocity annular jets and the negative velocity in the CRZ and the ORZ are evident. The vorticity graph shows small Kelvin-Helmholtz instabilities at the shear layers surrounding the annular jet up to about $x/d = 0.5$ and the disintegration of these vortices downstream. These vortices are smaller than the vortices associated with the forced flow and do not appear in a regular pattern in space nor with a given frequency in time, in contrast to the vortices shed in the forced flow, discussed later. The overall rotation of the flow inside the CRZ is also evident by the prevailing sign of the vorticity. To facilitate the discussion that follows in Section 4.3.2, Fig. 4.5 shows the time-averaged axial velocity from LES, with a few points marked. For ease of reference when comparing the mean and RMS velocities in the forced flow with the unforced flow, the normalised time-averaged axial velocity ($\overline{u}/U_b$) and its RMS (u_{rms}/U_b) value pairs of the unforced flow at these six locations are as follows: A: -0.336, 0.126; B: 1.165, 0.086; C: -0.01, 0.039; D: 0.707, 0.112; E: 0.478, 0.203; and F: -0.159, 0.090.

Finally, the spectra at a few axial and radial locations from experiment and
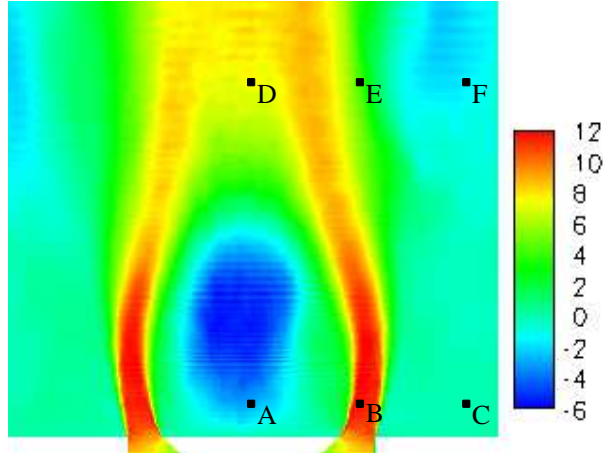
Figure 4.5: Contour of the time-averaged axial velocity (in m/s) from the LES. Points A-F are at locations (x, r)=(5,0), (5,15), (5,30), (50,0), (50,15), (50,30) respectively, in mm; r is distance from the axis and x the axial distance from the bluff body. Unforced flow (Case U).

LES are shown in Fig. 4.6. It is clear that the frequency content increases as we go downstream and it is higher at the shear layers than in the annular jet or the CRZ at low x/d, while the frequency content seems to be equally wide for all r/d at long distances from the bluff body. No clear peaks are discernible in either the LES or the experiment. The LES shows a broad peak at about 1200 Hz at the outer shear layers and at small axial distances from the bluff body (not shown here). This peak could be associated with the Kelvin-Helmholtz instability visualised in Fig. 4.4. A small region with a slope of $-5/3$ is evident from both experiment and LES, which suggests that the flow is fully turbulent except perhaps inside the annular jet and at very short distances from the bluff body, where the turbulence levels and frequency content are weak.

The comparison between LES and experiment in the unforced flow shows that the simulations capture the major features of the flow adequately.

4.3.2 Phase-averaged velocities and turbulent intensities

The mean ($\langle u \rangle (\phi)$) and RMS ($\langle u'^2 \rangle^{1/2}(\phi)$) of phase-averaged axial velocity from the experiment and LES are discussed here for the forced flows (Cases A-C of
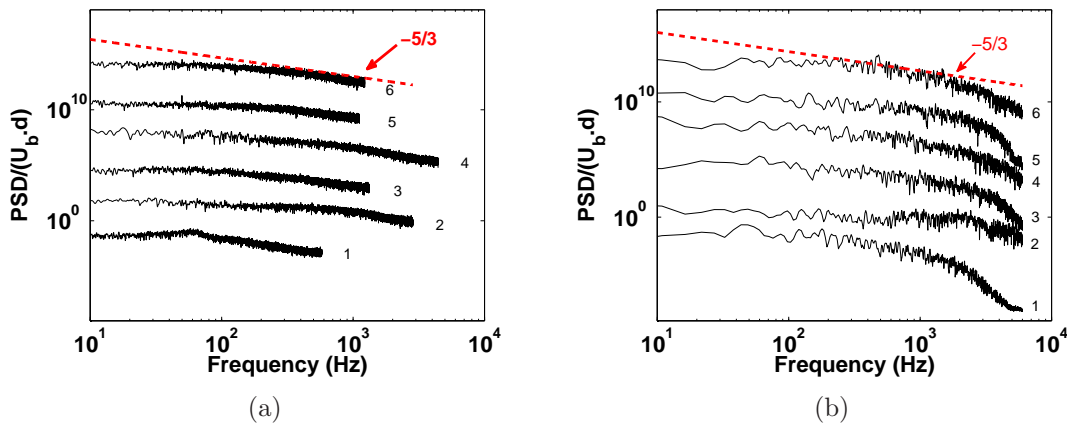
Figure 4.6: Frequency spectra of the axial velocity from (a) experiment and (b) LES. Unforced flow (Case U). Locations 1-6 correspond respectively to an (axial, radial) coordinate in mm of: (5,0), (5,15), (15,0), (15,15), (25,0), and (25,15). Each spectrum has been shifted upwards by a factor of 10^3. Points 1 and 2 are, respectively, the locations A and B marked on Fig. 4.5.

Table 4.1). The velocity profiles at the annular exit (i.e. at $x = 0$) as calculated from the LES are given in Fig. 4.7. Profiles of the phase-averaged mean and RMS velocity as a function of phase angle ϕ are shown in Figs. 4.8, 4.9, and 4.10 for 40, 160, and 320 Hz respectively for the locations marked on Fig. 4.5. Comparisons will be made between experiment and LES, between the velocities at the different locations, and between the forced and the unforced flow.

At the inlet, Fig. 4.7, the LES shows that the phase-averaged axial velocity distribution across the annular opening is similar for all forcing frequencies and at all phase angles, i.e. it follows the time-varying bulk velocity, although the boundary layers at the walls fluctuate by a smaller amount than the centre of the flow at the 160 and 320 Hz forcing. No flow reversal occurs, although at the trough of the forcing cycle the velocity is very low. The experimental data do not extend to this location due to the inability of locating the LDV probe so close to the pipe exit, however the mean and r.m.s. velocities of the unforced flow are close to experimental values obtained by a separate hot wire system [4]. The velocity fluctuations peak at the sides of the annular jet and reach high values: at the particular phase corresponding to the highest velocity through the cycle,

when $\langle u \rangle / U_b \approx 2$ in the centre of the annular opening, the maximum phase-averaged RMS across the opening is about 25-30% of U_b, which is very similar to the corresponding value from the unforced flow. This is so for all forcing frequencies tested. This suggests that the turbulence inside the pipe scales with the time-varying bulk velocity.

For forcing at 40 Hz, $\langle u \rangle$ seems to be very well captured by LES for all phase angles and for all positions shown (Fig. 4.8). The accuracy of the calculation is similar to that of the unforced flow observed by Ref. [118]. The strong pulsation is evident at the annular jet (see the curve for Point B, $(x, r) = (5, 15)$), but the pulsation seems to be weaker at other positions (this can be visualized by considering the magnitude of the cyclic fluctuation as a percentage of the time-averaged velocity, $\hat{u}(\phi)/\overline{u}$). If we compare the curves for Point B ($(x, r) = (5, 15)$) with the curves for Point E ($(x, r) = (50, 15)$), locations associated with the annular jet, it is evident that the peak velocity arrives at the downstream location about 1.1 rad later than at the upstream location, implying a time delay of about 4.8 ms or a "phase speed" of about 10.3 m/s, which is very close to the value of the bulk velocity U_b. If we now consider the curves for Points A and D, locations along the centreline, we can observe again good agreement between experiment and LES and a small relative magnitude of modulation. At $(x, r) = (5, 0)$ (i.e. inside the CRZ), at two phase angles through the cycle, the velocity may switch from negative to positive in the experiment (see Fig. 4.8, at about $\phi = 0.8$ and $\phi = 3.8$ rad). The same behaviour is seen in the LES, although the exact phase angle at which the zero-crossings occur are slightly shifted compared to the experiment. It is evident that inside the CRZ, a frequency doubling has occurred, with the phase-averaged mean velocity showing two oscillations in a forcing period. Downstream of the forward stagnation point (Point D), a frequency doubling is not immediately evident (although harmonics are revealed in the spectra, as discussed later). The outer recirculation zone far from the bluff body (Point F) shows a pulsation approximately in-phase with the forcing (i.e. the flow in the annular jet), while at Point C there is a phase shift. At Point F, which is inside the ORZ, the phase-averaged mean axial velocity switches from positive to negative, indicating a large fluctuation in the re-attachment length through the forcing cycle. Although the incoming phase-averaged velocity has a
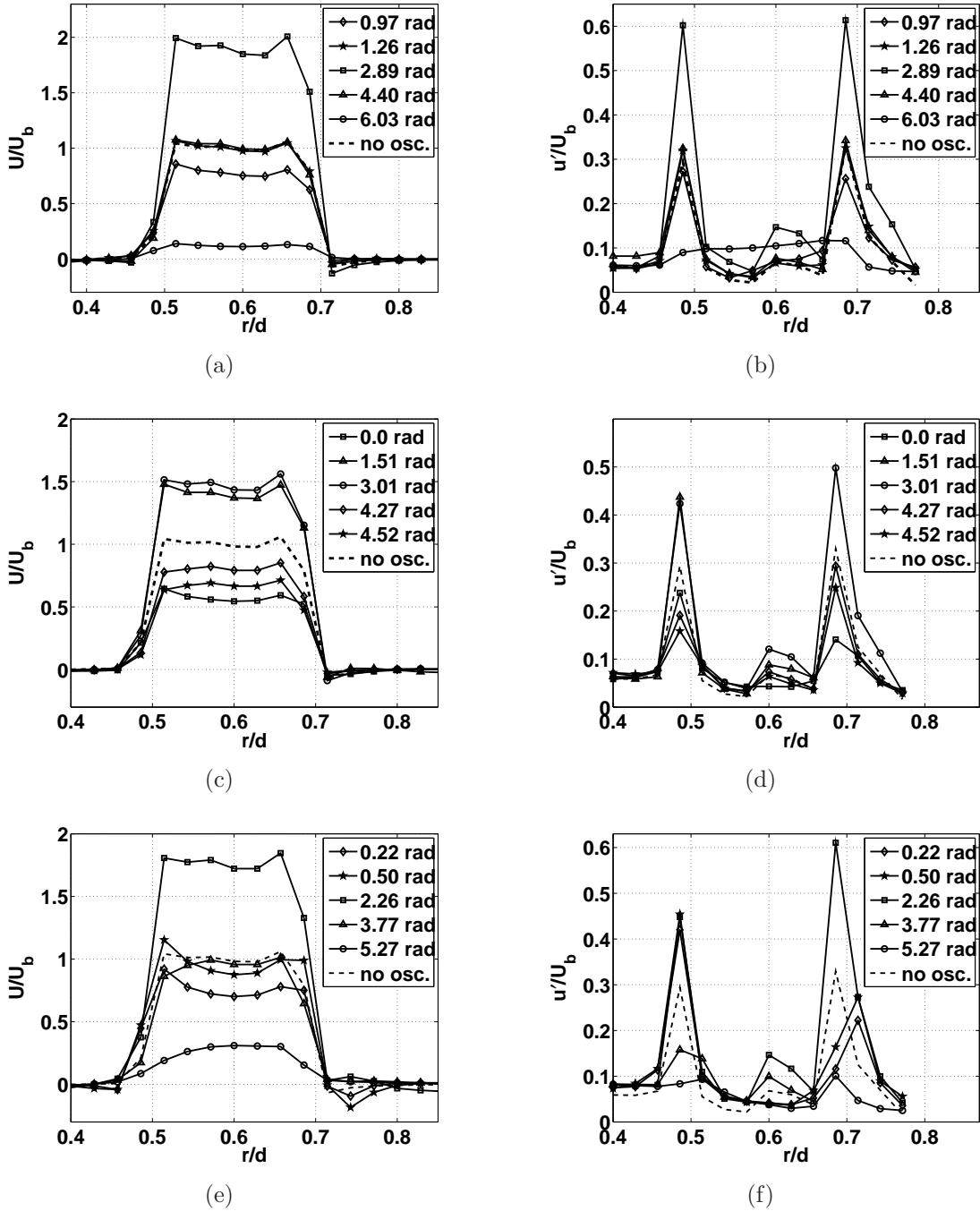
Figure 4.7: Phase-averaged mean (a,c,e) and RMS (b,d,f) axial velocity from the LES at the annular exit ($x = 0$). (a,b): Case A; (c,d): Case B; (e,f): Case C.

virtually pure sine wave periodic behaviour, the wave shape at other locations is far from this. A comparison with the time-averaged velocities from the forced flow with the time-averaged velocities of the unforced flow shows that these are only slightly different close to the bluff body, but they are significantly different at the downstream locations.

The phase-averaged axial RMS velocities $\langle u'^2 \rangle^{1/2}(\phi)$ at the same positions are shown in Figs. 4.8(c) and 4.8(d) as a function of phase angle. The following observations can be made. (i) Overall good agreement between experiment and LES is found for most locations. The largest discrepancy is for location F, i.e. inside the ORZ, and for location A, i.e. inside the CRZ and close to the bluff body. The relatively large scatter in the LES data is due to the small number of cycles used. (ii) Close to the bluff body (x=5 mm; Points A-C), the normalised intensity $\langle u'^2 \rangle^{1/2}/U_b$ lies between 0.1 and 0.2 and varies little with phase. Far from the bluff body (x=50 mm; Points D-F), the turbulence intensities reach very large values ($\langle u'^2 \rangle^{1/2}/U_b \approx 0.5$) and fluctuate significantly with phase angle. These large values may be associated with large fluctuations of the re-attachment length. (iii) The intensities reach their peaks at a phase angle that depends on location and are not everywhere in phase with $\langle u \rangle$: the peak values far downstream are reached when the local mean velocity changes quickest with phase (i.e. when $|\partial \langle u \rangle / \partial \phi|$ is high), while in the annular jet the turbulence is weakest and becomes a minimum when the mean velocity reaches its peak. Finally, (iv) a close comparison with the data of the unforced flow reveals that the phase-averaged fluctuations are larger than the turbulence intensities in the unforced flow, with the difference increasing as we go downstream.

For forcing at 160 Hz (Case B), Fig. 4.9, similar conclusions are drawn. In most locations the $\langle u \rangle(\phi)$ profiles behave as a pure oscillation, although some distortion is evident. The time-averaged value is close to the average from the unforced case. The phase-averaged velocity fluctuations are high inside the CRZ and ORZ and follow, approximately, the phase of the mean velocity. As for the 40 Hz case, the turbulent fluctuations are higher than the unforced flow at the same position, but they are smaller than for the 40 Hz case. Relatively good agreement between the LES and experiment is found.

We now consider Case C, i.e. forcing at 320 Hz (Fig. 4.10) and let us first
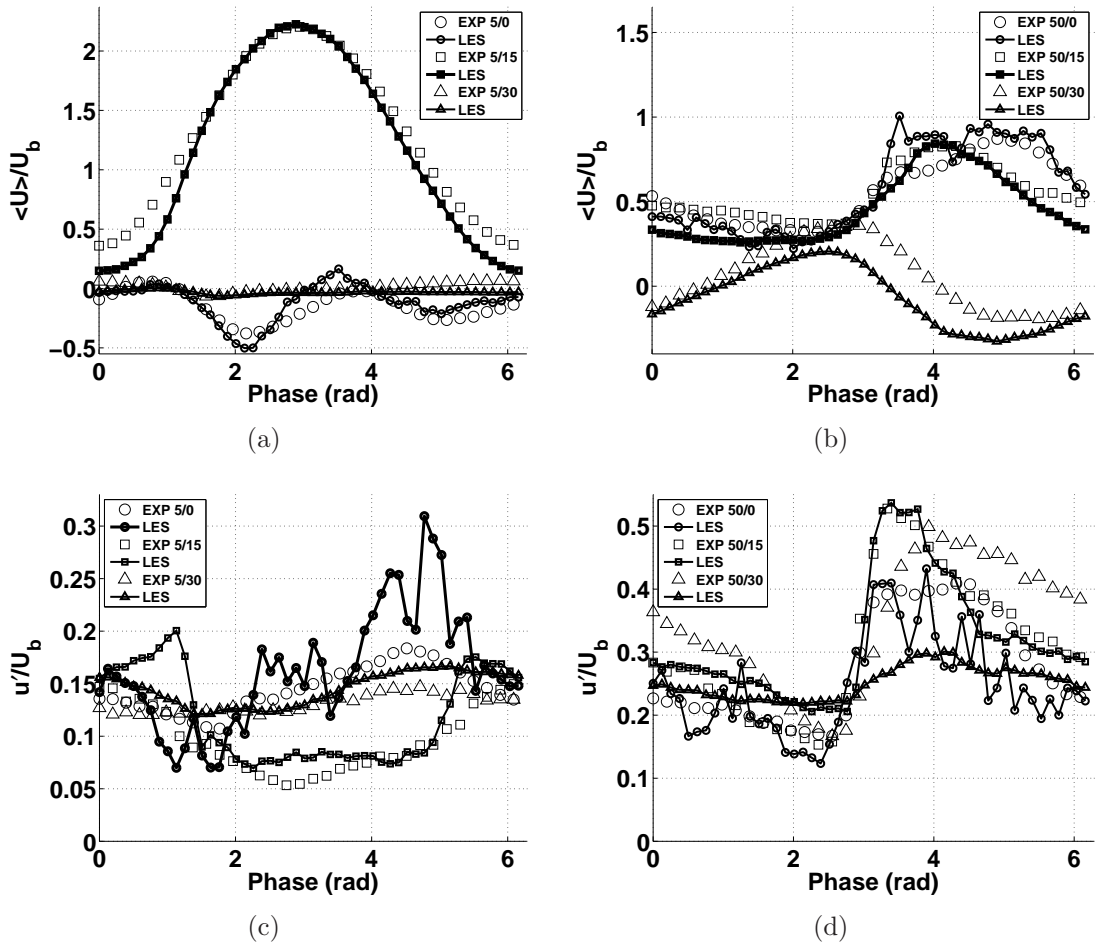
Figure 4.8: Phase-averaged mean (a,b) and RMS (c,d) axial velocities from experiment and LES. Forced flow, 40 Hz (Case A). The locations are given in terms of (x, r) in mm and correspond to points A-C (a,c) and D-F (b,d).
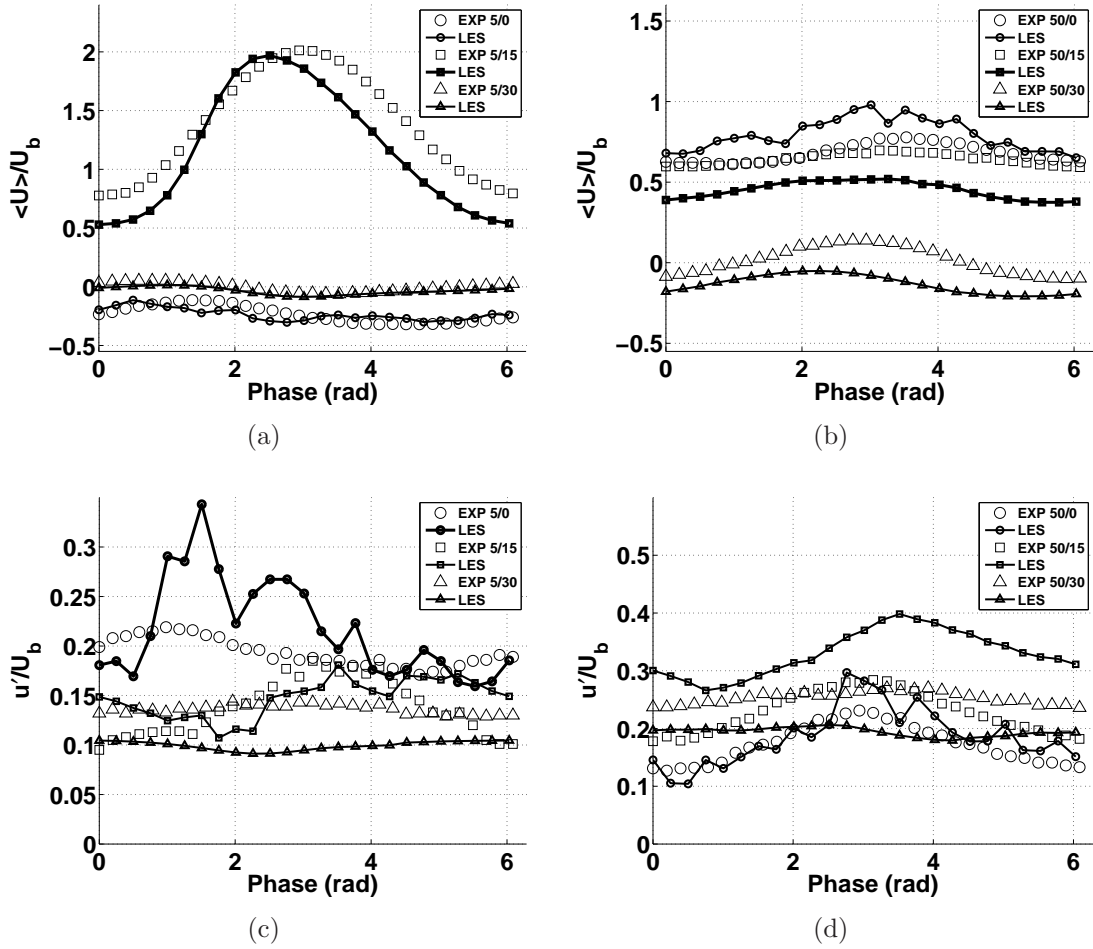
Figure 4.9: Phase-averaged mean (a,b) and RMS (c,d) axial velocities from experiment and LES. Forced flow, 160 Hz (Case B). The locations are given in terms of (x, r) in mm and correspond to points A-C (a,c) and D-F (b,d).

focus on the phase-averaged mean velocities. For all locations shown, there is very good agreement between the experimental data and LES. As in the cases with forcing at lower frequencies, the annular jet pulsates significantly throughout the cycle due to the large value of forcing amplitude A used in this flow. However, in all other locations, the cyclic modulation is much smaller than for forcing at $f = 40$ Hz (Fig. 4.8) and also smaller than for forcing at $f = 160$ Hz (Fig. 4.9). The wave shape now resembles a pure sine wave and frequency doubling is not evident. A comparison with the time-averaged velocities from this forced flow with the time-averaged velocities of the unforced flow shows that these are close everywhere. The turbulence intensities, presented in Figs. 4.10(c) and 4.10(d), also show very good agreement between experiment and LES, except at $(x, r) = (5, 0)$, where the LES predicts higher fluctuations than the experiment. The variation of the turbulence during the forcing cycle is much weaker than for lower forcing frequencies for all positions and is approximately in phase with the mean velocity variation. As in the other forcing cases, the turbulent fluctuations are higher than in the unforced flow, but they are smaller than for forcing at 40 and 160 Hz.

A common feature for all forcing frequencies is that the cyclic fluctuation as a percentage of the time-averaged velocity is lower inside the flow than at the inlet, and that, at the same location, the random turbulent fluctuations are higher than in the unforced flow. A comparison of $\langle u \rangle / U_b$ and $\langle u'^2 \rangle^{1/2} / U_b$ between the various cases shows that, in general, the mean velocity at downstream locations is altered with forcing, that the velocity modulation $\hat{u} / U_b$ is largest at low forcing frequencies, and that $\langle u'^2 \rangle^{1/2} / U_b$ decreases with increasing forcing frequency. The bulk of the flow at high frequencies behaves as a high-pass filter, i.e. it becomes unresponsive. The results are consistent with the view that the injected energy in the mean flow eventually becomes turbulent kinetic energy and that this transfer is most efficient for the 40 Hz case. The LES seems to be able to predict the phase-averaged mean and RMS velocities reasonably well for all tested forcing frequencies.

Snapshots sequences of the axial velocity at forcing frequency of 40 Hz (Fig. 4.11) and 160 Hz (Fig. 4.12) confirm the previous observation. In these figures, the black lines represent the zero-velocity isolines. The CRZ and ORZ are seen
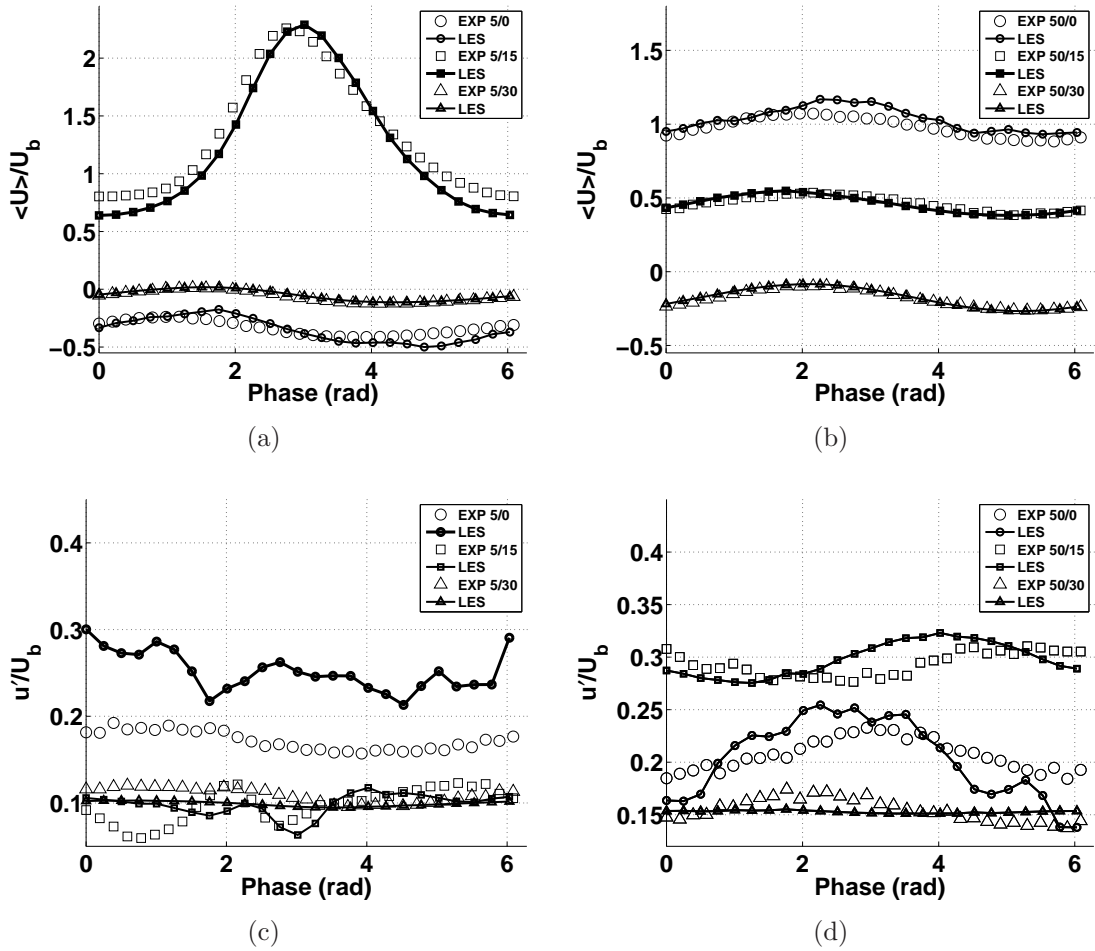
Figure 4.10: Phase-averaged mean (a,b) and RMS (c,d) axial velocities from experiment and LES. Forced flow, 320 Hz (Case C). The locations are given in terms of (x, r) in mm and correspond to points A-C (a,c) and D-F (b,d).

to pulsate strongly with the incoming flow at 40 Hz (Fig. 4.11), while the whole flow, in particular the RZs, appears much more frozen at high frequency (160 Hz case for the animation represented in Fig. 4.12).

4.3.3   Spectra and vortex formation

Spectra of axial velocity from the experiment and the LES are shown in Figs. 4.13, 4.14, and 4.15 for Cases A-C respectively and for a few positions. A comparison between the various positions and flow conditions reveals the following characteristics. (i) A strong peak at the forcing frequency is evident everywhere. (ii) The broadband turbulence spectrum is similar to the spectrum of the unforced flow. (iii) Harmonics of the fundamental forcing frequency appear consistently, but their relative strength varies with position and forcing frequency. (iv) Under some forcing conditions and at some locations, we observe the presence of a sub-harmonic peak. Finally, (v) the LES and experimental spectra have quite similar features in terms of presence and relative magnitude of harmonics and the sub-harmonic. These observations are discussed in more detail below.

At $f = 40$ Hz, close to the inlet (position 2, $(x, r) = (5, 15)$; this is also marked Point B on Fig. 4.5), we do not see any harmonics, which provides evidence of the purity of the forcing. This is so in both the experiment and the LES. The forcing peak and the harmonics are evident everywhere else. As we go downstream, the strength of the harmonic increases, while at position 1 (inside the CRZ; this was also marked Point A on Fig. 4.5), the experiment shows a first harmonic stronger than the fundamental, something roughly borne out by the LES as well. The presence of a strong harmonic inside the CRZ was also observed in the phase-averaged velocities (Fig. 4.8) and is consistent with their non-sinusoidal behaviour.

At $f = 160$ Hz (Fig. 4.14), similar observations, in general, can be made, although now the harmonics are evident even close to the inlet and, inside the CRZ (spectra 1,3,5), the first harmonic is not stronger than the fundamental as was the case for 40 Hz forcing. An important qualitative difference observed in this case in both experiment and LES is the presence of a sub-harmonic broad peak (at about 80 Hz), in the CRZ which becomes evident in the downstream
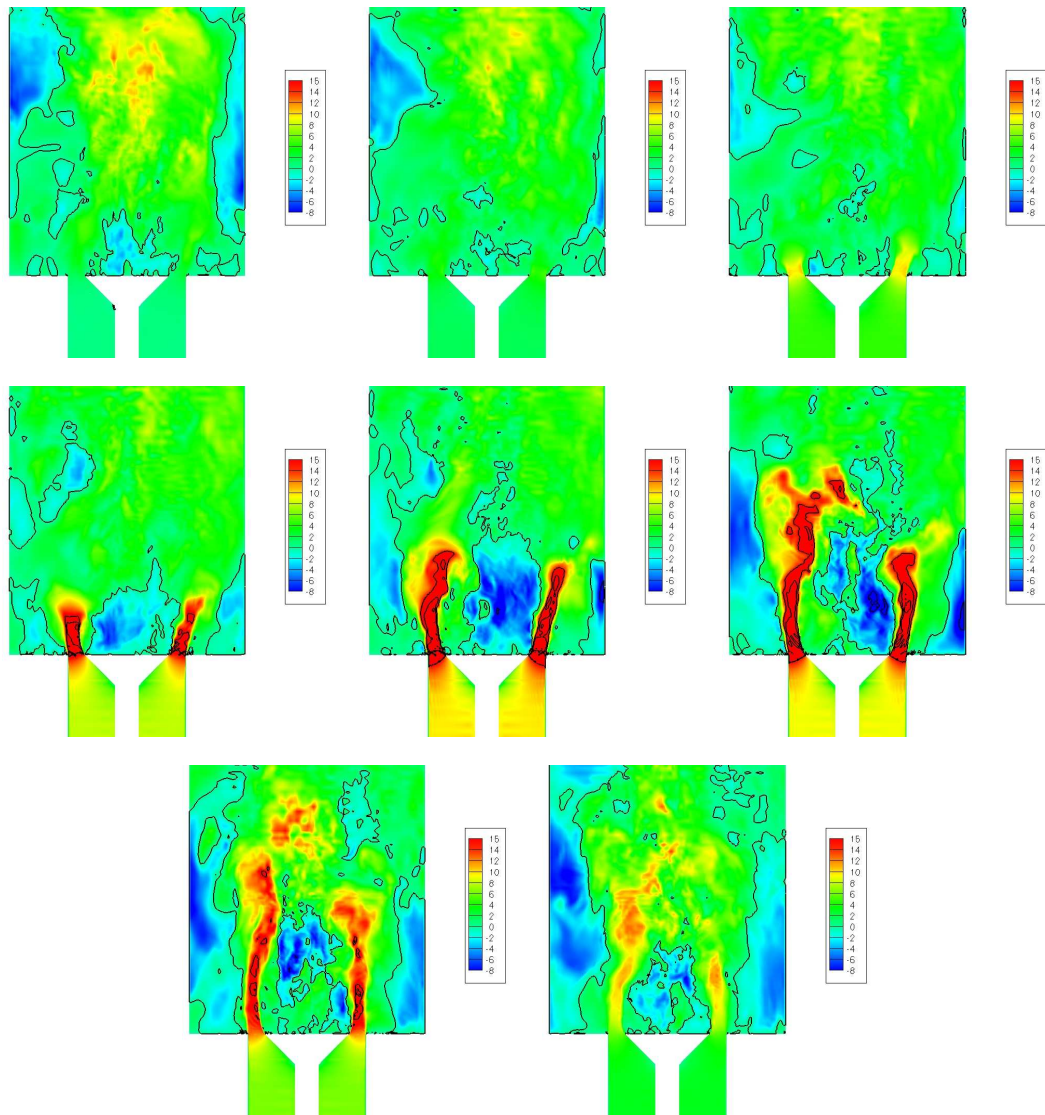
Figure 4.11: Sequence of instantaneous axial velocity snapshots at different consecutive instants and over one period for the 40 Hz forced case.
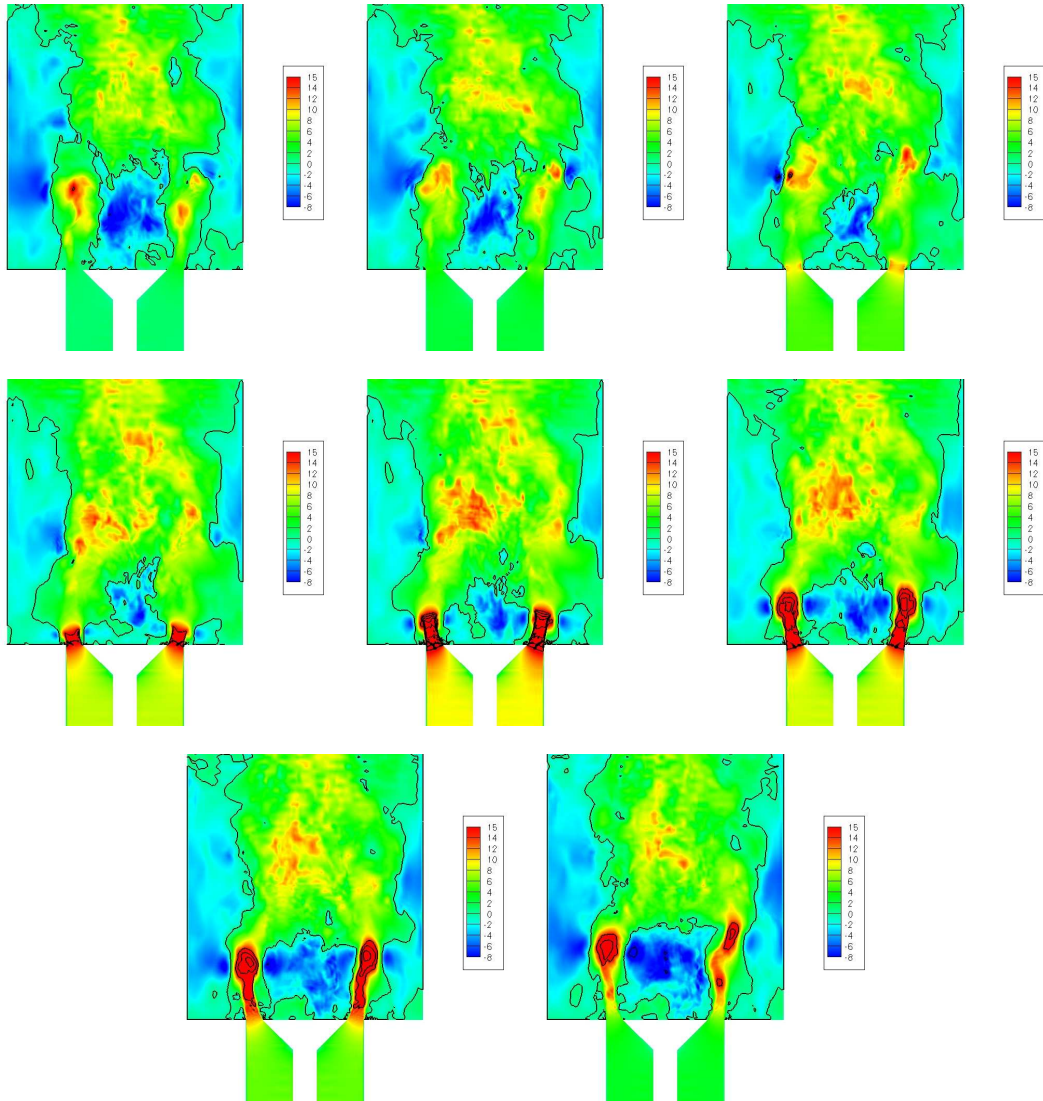
Figure 4.12: Sequence of instantaneous axial velocity snapshots at different consecutive instants and over one period for the 160 Hz forced case.
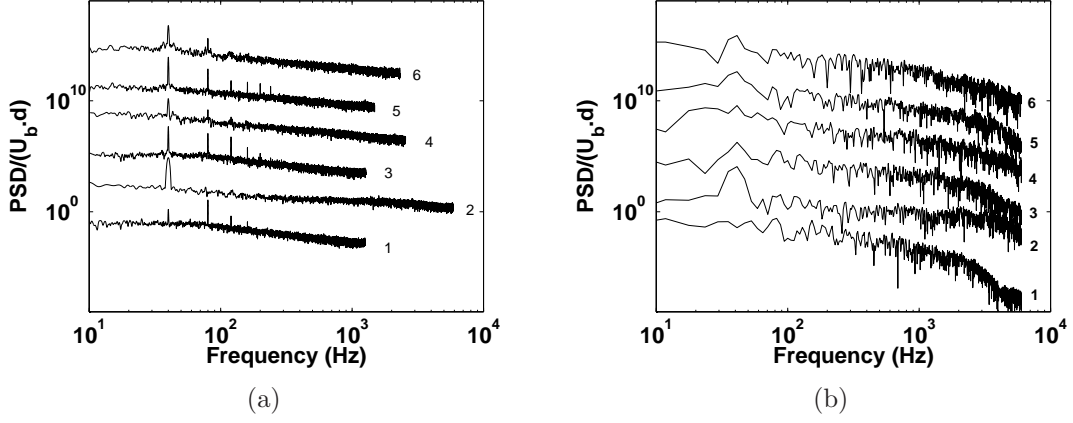
Figure 4.13: Frequency spectra of the axial velocity from (a) experiment and (b) LES. Forced flow, 40 Hz (Case A). Locations as in Fig. 4.6.

locations (positions 3-6; $x = 15$ and 25 mm).

Finally, with forcing at 320 Hz (Fig. 4.15), the fundamental peak at the downstream locations has a broader base than at the lower forcing frequencies, the sub-harmonic is absent, and the fundamental is always stronger than the harmonics. In general, the LES captures well the experimentally-observed trends in the spectra, except at the location inside the CRZ and close to the bluff body (position 1), where the forcing peak is less pronounced in the LES than in the experiment.

Presence of harmonics is typical of nonlinear phenomena. Monochromatic acoustic waves propagating in nonlinear medium give birth to harmonics of the fundamental as the waves propagate further into the medium [35]. However it has to be emphasized that in our case the presence of harmonics inside the simulated flow for each forcing frequency is not due to any acoustic phenomena as PRECISE is an incompressible code. As a consequence, the harmonics found in the experimental flow may also originate in aerodynamic phenomena and not only in the acoustic of the flow. Similarly to the theory of acoustic, a Burger's equation can be derived in the case of hydrodynamic waves. In the case of a one dimensional incompressible and inviscid flow, the Navier-Stokes equation simplifies into the
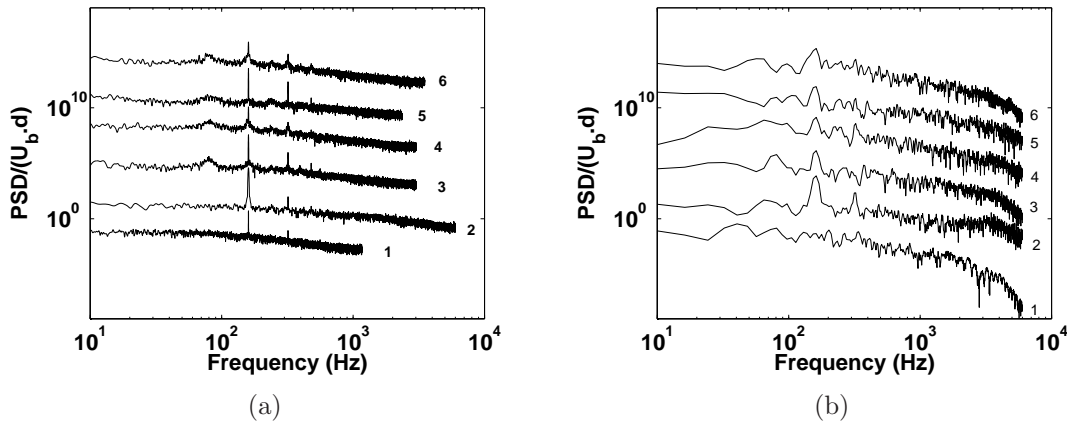
Figure 4.14: Frequency spectra of the axial velocity from (a) experiment and (b) LES. Forced flow, 160 Hz (Case B). Locations as in Fig. 4.6.

Riemann equation as follows:

$$\frac{\partial (U)}{\partial t} + U \frac{\partial (U)}{\partial x} = 0 \tag{4.6}$$

The general solution of Eq. 4.6 is $U = f(x - Ut)$ and describes the evolution of hydrodynamic waves travelling at the fluctuating velocity U. In the case of streamlines located inside the jet, $U \approx U_0$, which corroborates the value of the "phase speed" found in Section 4.3.2.

In order to understand better the flow structure as a function of forcing frequency, LES snapshots were used. Figure 4.16 shows visualisations of the vortices developed due to the oscillating flow. This is achieved by plotting the quantity Q, defined as:

$$Q = (\omega^2 - 2\widetilde{S}_{ij}\widetilde{S}_{ij})/4 \tag{4.7}$$

with ω the vorticity magnitude and $\widetilde{S}_{ij}$ the strain rate calculated from the gradients of the resolved velocity. Positive Q has been used extensively to mark vortical regions in turbulent flows [47; 48]. The figures show iso-surfaces of $Q = 15 \times 10^6$ 1/s^2 ($\approx 94\ U_b^2/d^2$) as a function of phase angle from snapshots from the LES. It is evident that the 40 Hz case does not show strong vortex formation at any point in the cycle. Vortex tubes seem to be randomly oriented. The dominant presence of the iso-surface of Q in the CRZ denotes the higher vorticity mag-
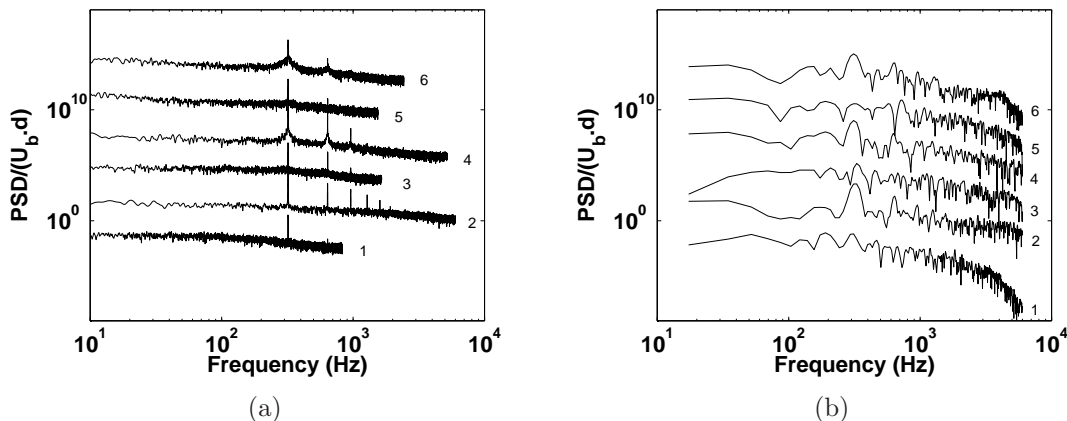
Figure 4.15: Frequency spectra of the axial velocity from (a) experiment and (b) LES. Forced flow, 320 Hz (Case C). Locations as in Fig. 4.6.

nitude there, as also evident in the unforced case (Fig. 4.4b). At the points of the cycle where the incoming velocity is low, the magnitude of Q drops and hence we see low Q for some phase angles in Fig. 4.16a. In contrast to the above behaviour, the cases with forcing at 160 Hz (Fig. 4.16b) and 320 Hz (Fig. 4.16c) show vortex rings being shed from either corner of the annular opening (i.e. at the bluff body corner and at the sudden expansion corner). The shedding seems to occur when the phase-averaged velocity begins to increase. The outer vortex ring is convected downstream, becomes highly wrinkled and eventually breaks up towards the end of the cycle at an axial distance about one bluff body diameter. The inner vortex ring is again convected downstream, but it breaks up quickly inside the CRZ, feeding this region with vorticity and hence velocity fluctuations. The same features are found in Case C (320 Hz; Fig. 4.16c), with the important additional characteristic that a second set of vortex rings is shed before the first one is convected out of the domain due to the shorter wavelength of the velocity modulation.

The presence of vortices shed from the separation points at some forcing frequencies is consistent with flow visualization studies [6; 65] and with data concerning flame response [5; 6]. A more detailed comparison with the data of Ref. [65] with forced premixed flames, shows that while Ref. [65] observed vortex rings for a Strouhal number of 0.1 (our 40 Hz case; Table 4.1) for an amplitude
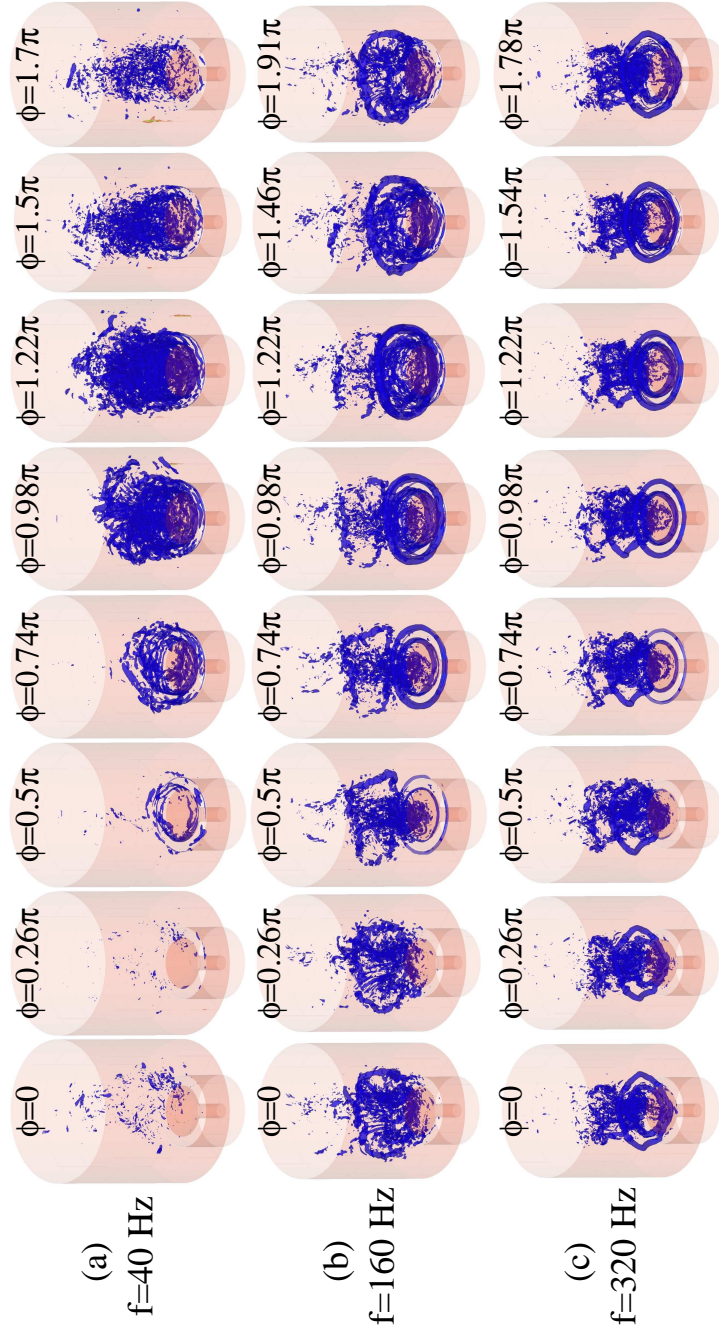
Figure 4.16: Iso-surfaces of $Q = 15 \times 10^6$ $1/s^2$ from sequential snapshots from the LES, showing the evolution of the shed vortices for (a) Cases A, (b) Case B, and (c) Case C. For the definition of Q, see text.

$A > 0.42$, in the present isothermal flow the Strouhal number of 0.1 and $A = 0.89$ does not show vortex rings. This may suggest that the density difference between the cold incoming gases in the shear layers and the hot gases inside the CRZ and ORZ in flames facilitates the formation of vortices. The absence of a well-defined vortex ring at $f = 40$ Hz is also consistent with experiments of forced jets [18], where vortices were formed only above certain frequencies.

The existence of harmonics in the spectra at most conditions except very early in the flow inlet is consistent with observations in forced jets by Ref. [126], where a single spectral peak in a low-turbulence jet close to the nozzle gave rise to multiple harmonics and eventually to a fully-turbulent spectrum with downstream distance. Case B (160 Hz) has the special feature of the presence of the sub-harmonic in the spectra (Fig. 4.14). This may be equivalent to vortex pairing in shear layers or jet columns [126] as the inner vortex ring contracts and disintegrates while it is being squeezed inside the CRZ (Fig. 4.16).

Finally, the presence of well-defined, regularly-spaced vortices can be used to explain the difference in turbulence intensities for the various forcing frequencies. Both experiment and LES show that $\langle u'^2 \rangle^{1/2}/U_b$, in general, decreases with increasing forcing frequency f. As f increases, more vortices are formed, and their spacing (i.e. the wavelength of the flow oscillation) decreases, which suggests that there exists a larger number of vortices in the flow with increasing f. The presence of vorticity associated with these vortices will enhance kinetic energy dissipation, which will therefore decrease the turbulent velocity fluctuations.

4.4 Proper Orthogonal Decomposition analysis of the 160Hz forced flow

In order to understand further the structures of the forced bluff body flows, Proper Orthogonal Decomposition has been applied to the 160 Hz forced case. Here POD has been based on the three components of the velocity and the pressure. The first ten modes are reproduced with the spectral analysis of their temporal coefficients. The analysis provides key insights on the recirculation zones pulsation, vortex shedding and spectra of such a flow.

4.4.1 Mode 1

Mode 1 is represented in Fig. 4.17. Application of the $Q-$criterion (Figs. 4.17(a) and 4.17(b)) shows clearly a row of several large outer annular vortex rings distributed along the chamber of combustion. At least one inner vortex ring shed from the bluff body edges is also present. As we go further downstream inside the combustion chamber, the vortices envelopes are more and more wrinkled and the flow is filled with more and more vorticity. Towards the end of the combustion chamber, the vortices have broken up into small vortical structures. In Fig. 4.17(d), the axial velocity fluctuations of mode 1 have been plotted. The jet is characterized by a blue color i.e. negative fluctuations of the axial velocity while the central recirculation zone has positive fluctuations associated with it. This is expected as the jet entering in the chamber is slowed down by the slower fluid around it while the fluid in the central recirculation zone tends to be accelerated by the fast jet fluid. Fig. 4.17(c) shows the pressure fluctuations map of mode 1 and confirms the presence of outer and inner vortex rings in mode 1. The spectrum of the temporal coefficient associated with mode 1 is represented in Fig. 4.35. It shows a single and very clear peak at 160 Hz. It is the only mode to exhibit a single frequency peak. In fact, Proper Orthogonal Decomposition enforces spatial orthogonality between the POD modes, hence leading to decorrelated structures associated with each mode. However, the Fourier analysis of the temporal coefficients of POD modes shows that, in general, multiple frequencies are associated with the evolution of each POD mode (Figs. 4.35 and 4.36). Here, mode 1 is clearly associated with the forced frequency at 160 Hz. Mode 1 can thus be regarded as a mode associated with the cyclic fluctuations of the flow i.e. the fluctuations directly associated with the inlet pulsation at 160 Hz. This explains why this mode alone contains a very large amount of the total fluctuating energy as reported in Fig. 4.34 and Table 4.2.

The reconstruction of the flow based on the mean flow and mode 1 are visualized in Fig. 4.18 through the $Q-$criterion. It shows the successive appearance and disappearance of the different vortex rings inside the combustion chamber. There is no convection of the rings with a reconstruction based on a single mode. The reconstruction of the axial velocity is also shown in Fig. 4.19. The black lines

Table 4.2: Relative energy of POD modes.

Mode	%
Mode 1	86.9443
Mode 2	4.1937
Mode 3	1.5706
Mode 4	1.1035
Mode 5	0.6378
Mode 6	0.3357
Mode 7	0.2930
Mode 8	0.1748
Mode 9	0.1402
Mode 10	0.1321

represent the isoline defined as $u = 0$. The pulsation of the central recirculation zone is clearly visible and follows the pulsation of the inlet jet at 160 Hz, although with a time delay. In Fig. 4.20, the reconstructed axial velocity fields have been superimposed over one period. The black lines represent the zero-velocity isolines for each snapshot. It is noticeable that the boundary of the CRZ oscillates like a standing wave.

4.4.2   Modes 1 and 2

Mode 2 (Fig. 4.21) is similar to mode 1: large annular vortices are also visible in the upstream flow, although at different positions (Figs. 4.21(a) and 4.21(b)). They tend to occupy the space between the vortices of mode 1, as a result of the spacial orthogonality resulting from POD. Two inner vortices are clearly visible through the $Q-$criterion in Fig. 4.21(b) and the pressure fluctuations map in Fig. 4.21(c). The downstream part of the chamber is also filled with vorticity due to the breakdown of the large vortex rings. As for mode 1, there is a clear peak at 160 Hz in the spectra of the temporal coefficent associated with mode 2 and represented in Fig. 4.35. However, a small harmonic at 320 Hz is also visible. Despite their similarities, mode 1 and mode 2 do not form a perfect pair of modes. In addition to exhibiting discrepancies in their spectra, mode 1 and mode 2 contain different amount of fluctuations energy: mode 1 accounts for 87 % of the total energy while mode 2 contains only 4.2 % of the energy (see Fig 4.34
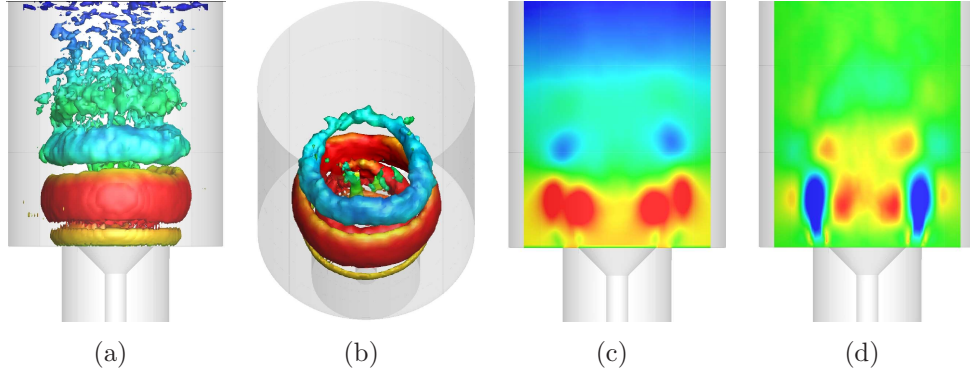
Figure 4.17: Mode 1. (a,b) Isosurfaces of the $Q-$criterion coloured by the pressure fluctuations. Contours of the fluctuations of (c) the pressure and (d) the axial velocity. The blue colour shows the negative fluctuations, the red colour shows the positive fluctuations, while the green colour shows the zero-fluctuation area. Forced case at 160 Hz.

and Table 4.2).

If now we perform a reconstruction of the snapshots over one period based on the two first modes, plot the $Q-$criterion at different time (Fig. 4.22) and then animate the figures, a clear vortex shedding at 160 Hz becomes evident and the vortex rings are seen being convected downstream before breaking up and feeding the downstream part of the combustion chamber with vorticity.

The reconstruction of the axial velocity based on the two first modes is shown in Fig. 4.23. The figure gives an insight on the pulsation of the jet and the recirculation zones. A high velocity bubble can be seen travelling along the jet while the outer recirculation zone and the central recirculation zone can clearly be seen pulsating with the incoming flow, again with a time delay. This observation confirms that mode 1 and mode 2 behave partially like a pair of modes accounting for the cyclic part of the flow fluctuations i.e. the part of the flow that follows the sinusoidal pulsations at 160 Hz of the inlet velocity. They describe the shedding and convection of the double vortex rings inside the combustor at the forced 160 Hz frequency.

69
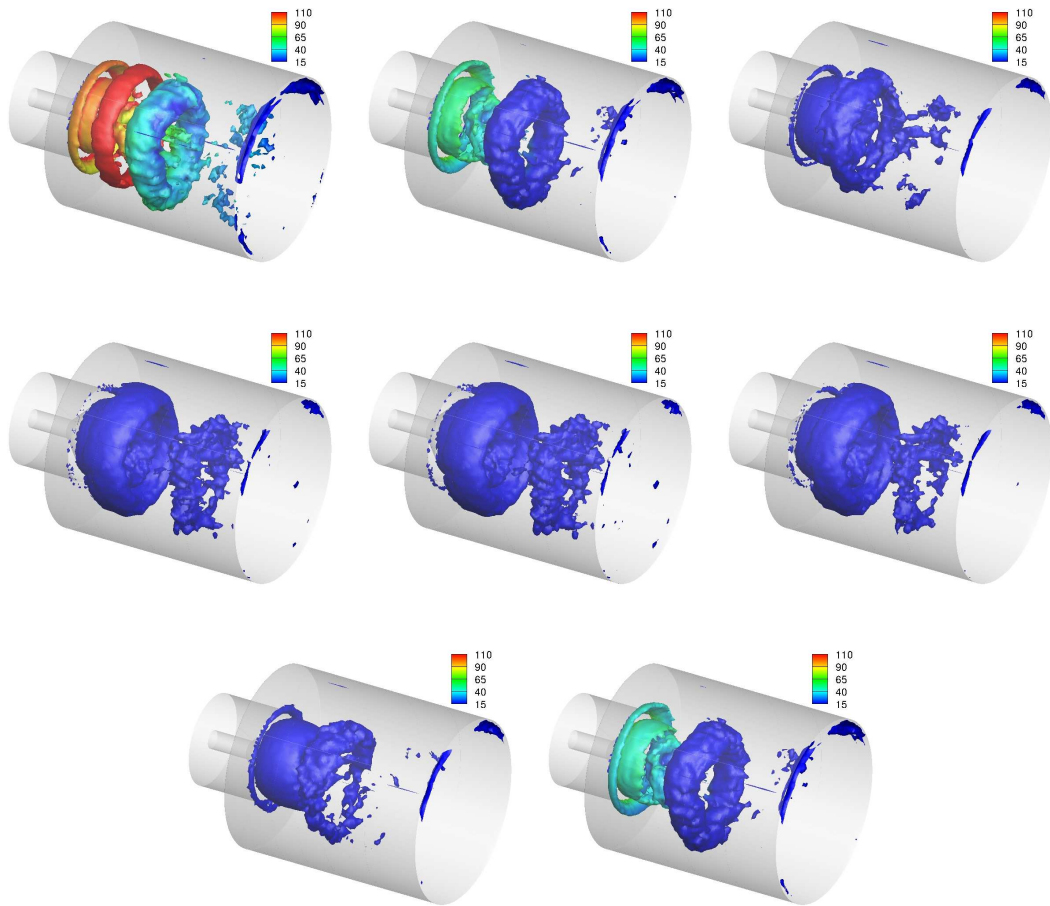
Figure 4.18: Sequence of the $Q-$criterion of the reconstructed instantaneous flow coloured by the reconstructed pressure at different consecutive instants and over one period using mode 1. Forced case at 160 Hz.
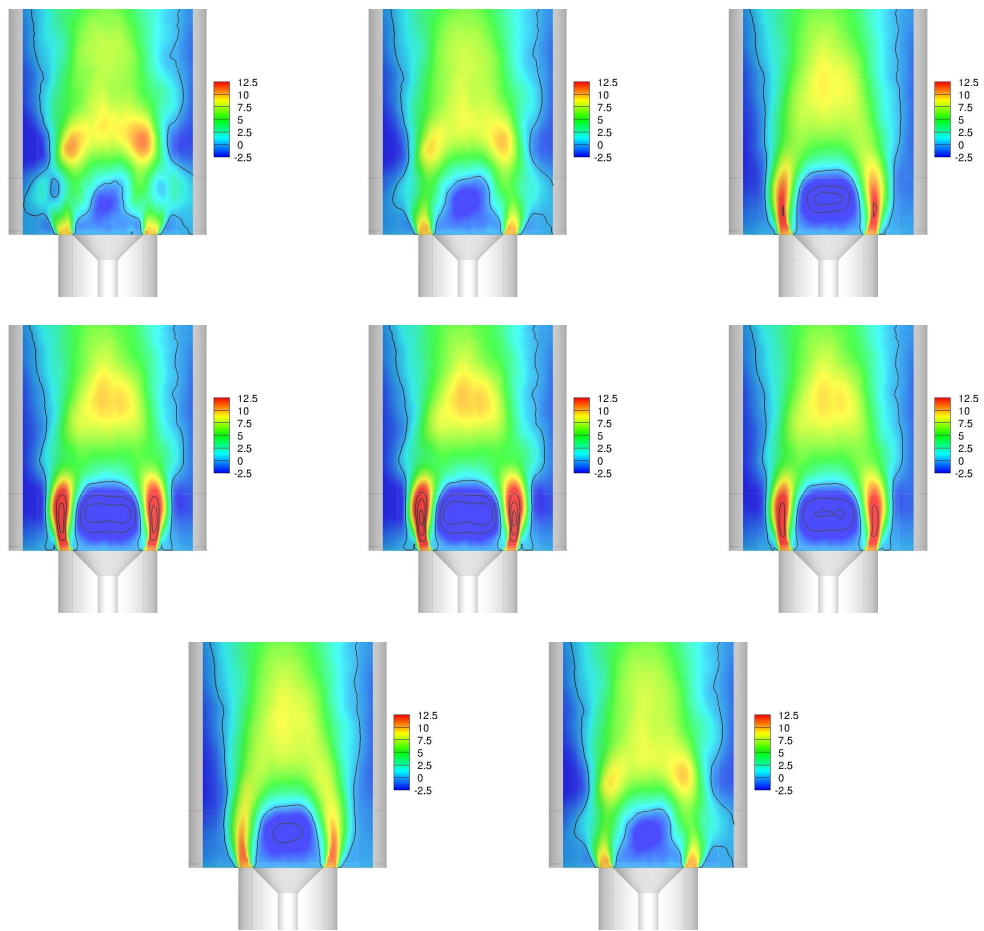
Figure 4.19: Sequence of the axial velocity of the reconstructed instantaneous flow at different consecutive instants and over one period using mode 1. Forced case at 160 Hz.
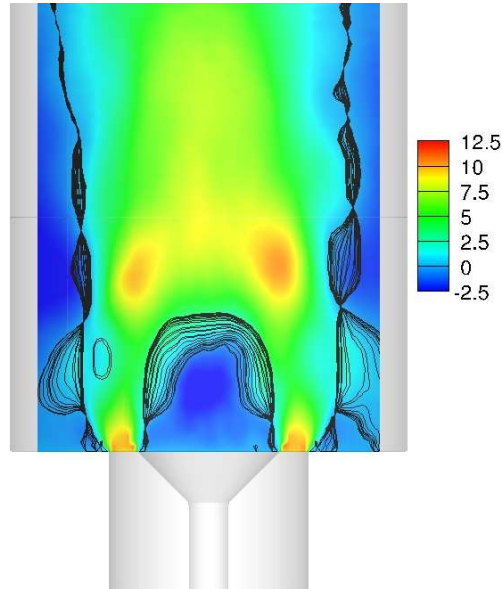
Figure 4.20: Axial velocity fields superimposed over one period. The black lines represent the instantaneous zero axial velocity isoline. Forced case at 160 Hz.

| (a) | (b) | (c) | (d) |
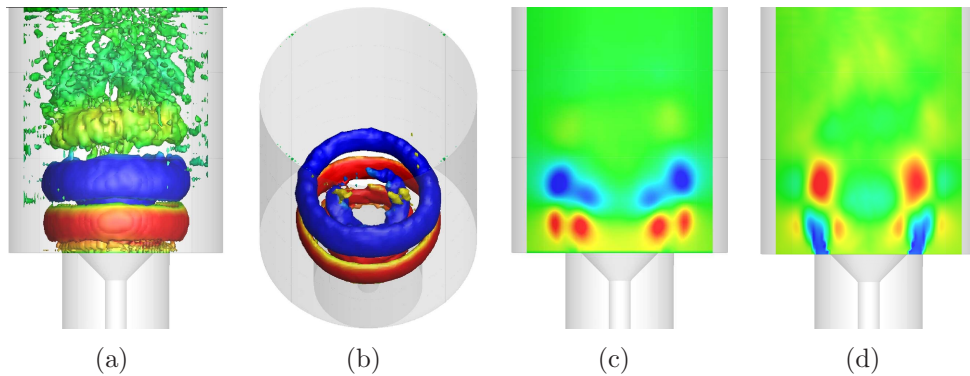
Figure 4.21: Mode 2. (a,b) Isosurfaces of the $Q-$criterion coloured by the pressure fluctuations. Contours of the fluctuations of (c) the pressure and (d) the axial velocity. Colours as in Fig. 4.17. Forced case at 160 Hz.
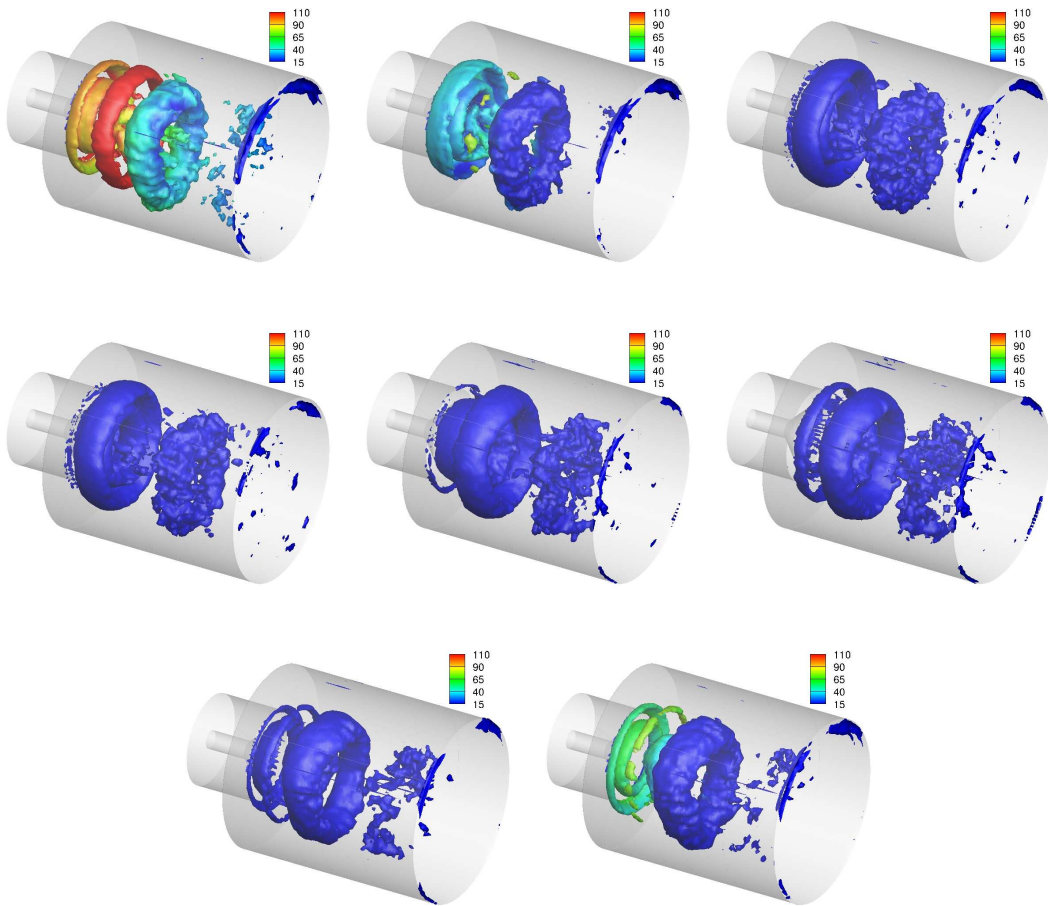
Figure 4.22: Sequence of the $Q-$criterion of the reconstructed instantaneous flow coloured by the reconstructed pressure at different consecutive instants and over one period using modes 1 and 2. Forced case at 160 Hz.
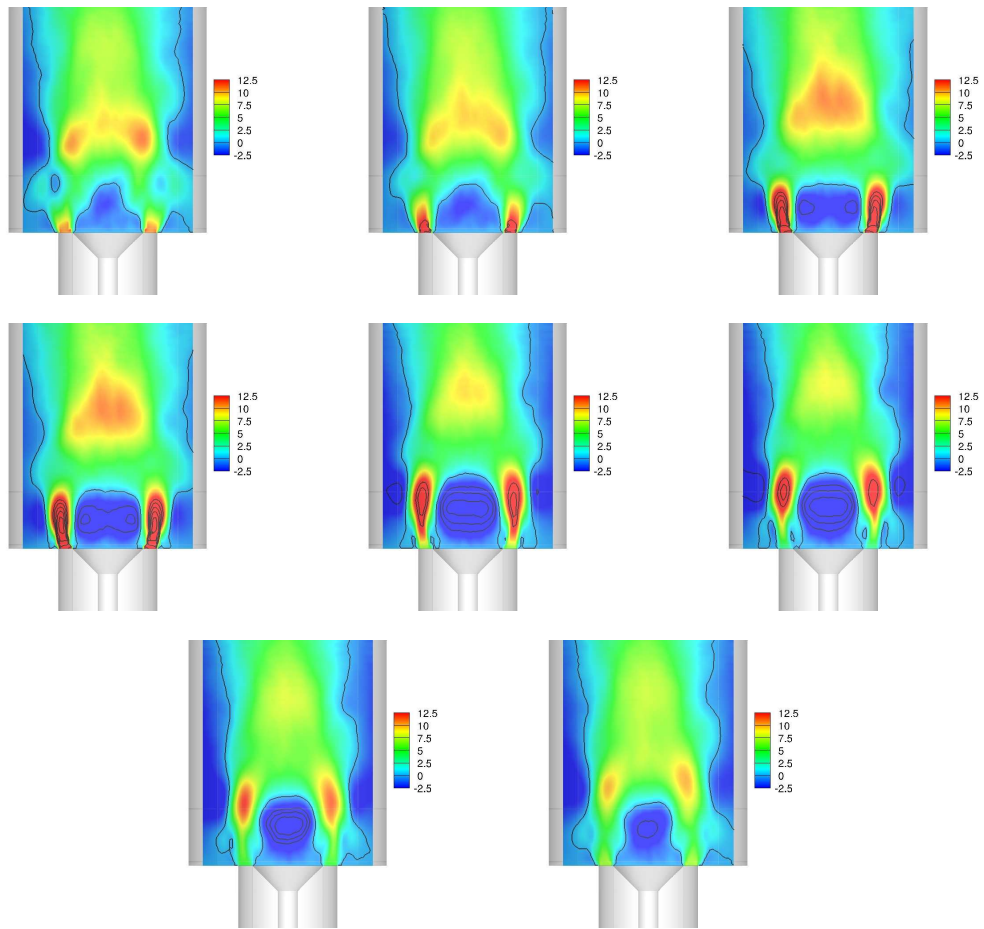
Figure 4.23: Sequence of the axial velocity of the reconstructed instantaneous flow at different consecutive instants and over one period using modes 1 and 2. Forced case at 160 Hz.

(a)	(b)	(c)	(d)
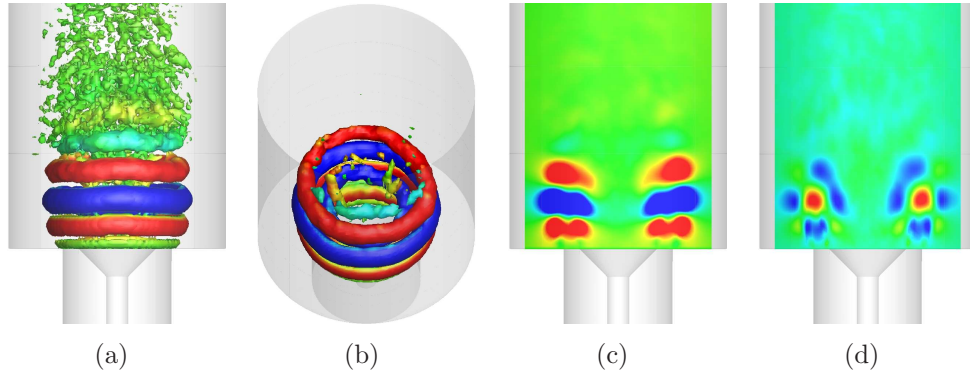
Figure 4.24: Mode 3. (a,b) Isosurfaces of the $Q-$criterion coloured by the pressure fluctuations. Contours of the fluctuations of (c) the pressure and (d) the axial velocity. Colours as in Fig. 4.17. Forced case at 160 Hz.

4.4.3   Modes 3 and 4

Mode 3 (Fig. 4.24) and mode 4 (Fig. 4.25) seem identical. Their $Q-$criterion isosurfaces show a row of inner and outer vortices upstream while the chamber is filled with vorticity further downstream. This is similar to modes 1 and 2. The main difference in modes 3 and 4 is the number of rings present in the chamber. It has roughly doubled compared to modes 1 and 2. The vortices in mode 4 occupy the space left empty between two annular vortices of mode 3. If we now look at the spectra associated with modes 3 and 4 (Fig. 4.35), we see a clear peak at 320 Hz in both modes, which coresponds to the first harmonic of the forced frequency. Mode 3 also exhibits a smaller peak at 480 Hz (second harmonic) while mode 4 contains a small peak at the fundamental (160 Hz) and another component corresponding to the second harmonic (480 Hz) that has roughly half the amplitude of the first harmonic. Mode 3 and mode 4 contain similar level of energy, with mode 3 accounting for 1.6 % of the total energy and mode 4 for 1.1 % (see Fig. 4.34 and Table 4.2).

If now we reconstruct the flow based only on modes 3 and 4, a clear vortex shedding at 320 Hz is evident from both the bluff body and sudden expansion, the rings being convected downstream before breaking up (see $Q-$criterion representation in Fig. 4.26). The reconstructed axial velocity field (Fig. 4.27) shows the convection of pockets of high velocity ejected from the air pipe exit at a fre-
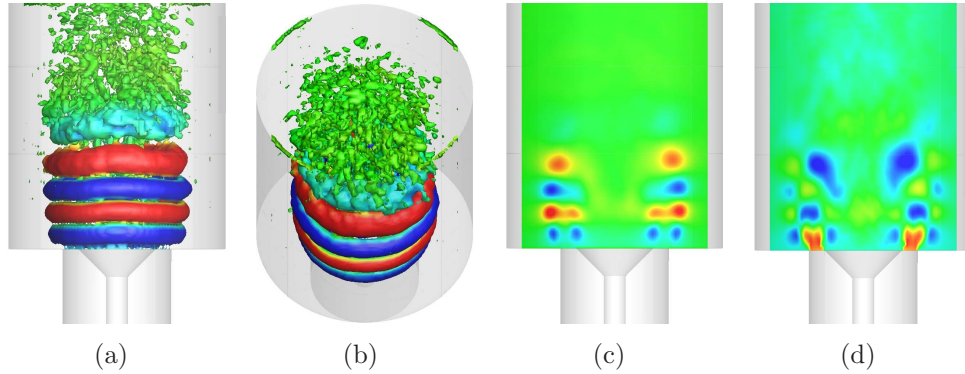
Figure 4.25: Mode 4. (a,b) Isosurfaces of the $Q-$criterion coloured by the pressure fluctuations. Contours of the fluctuations of (c) the pressure and (d) the axial velocity. Colours as in Fig. 4.17. Forced case at 160 Hz.

quency of 320 Hz. This observation and the previous ones show that modes 3 and 4 can be seen, at least partially, as a pair of modes accounting for the shedding and convection of double vortex rings inside the combustion chamber at the first harmonic (320 Hz) of the forced frequency (160 Hz). In consequence, this set of modes (modes 3 and 4) can roughly be understood as a harmonic of the first two modes (modes 1 and 2).

4.4.4   Modes 6 and 7

Mode 5 is different from the other modes previously described and therefore is commented later in the text. However, modes 6 and 7 seem again to form a pair of modes (at least partially) that account for a vortex shedding and their convection, similarly to what has been found for modes (1,2) and modes (2,3). The $Q-$criterion applied to modes 6 and 7 (respectively in Figs. 4.28 and 4.29) show again a row of several annular vortices, and their number has roughly doubled compared to modes 3 and 4. As for modes 3 and 4, mode 6 and mode 7 contain similar level of energy, with mode 6 accounting for 0.34 % of the total energy and mode 7 for 0.29 % (see Fig. 4.34 and Table 4.2). However, in this case, there is nothing like a single clear peak in these modes spectra but rather four clear peaks at 320 Hz, 480 Hz, 640 Hz and 800 Hz, corresponding to the four first harmonics of the flow. In both modes 6 and 7, the higher peak is found at 640
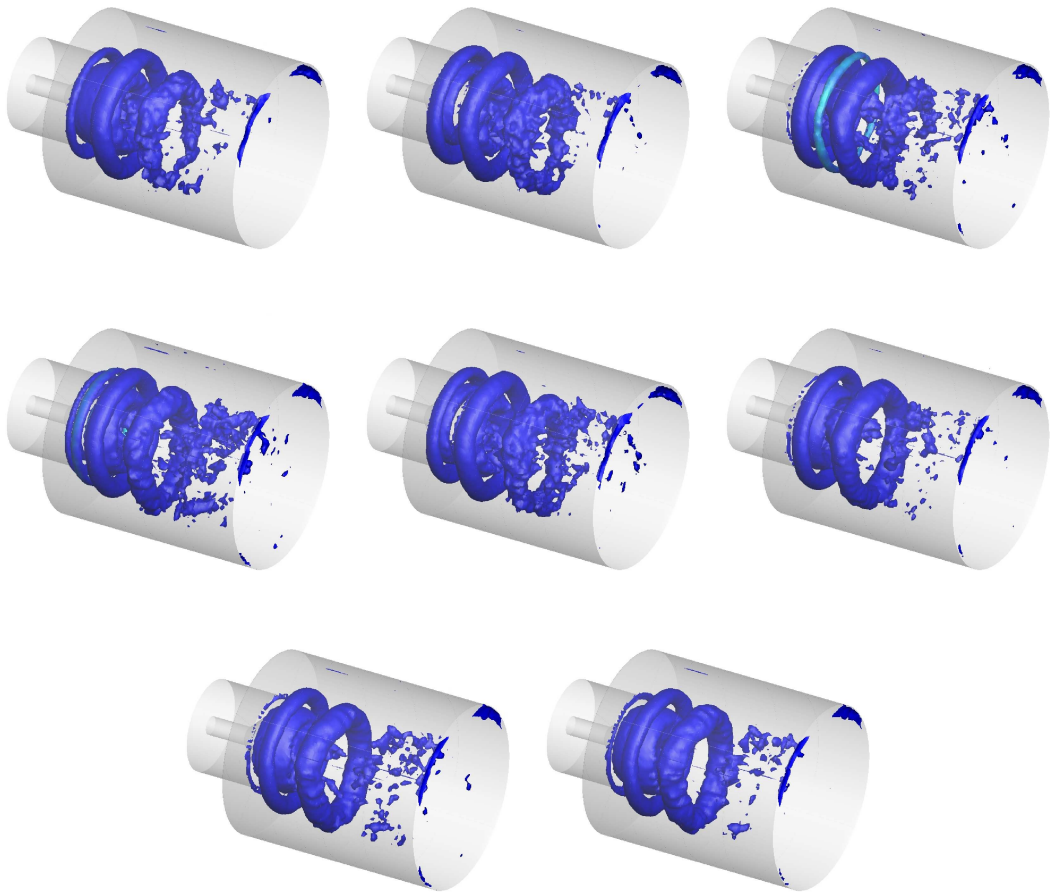
Figure 4.26: $Q-$criterion of the reconstructed instantaneous flow over one period using modes 3 and 4. Forced case at 160 Hz.
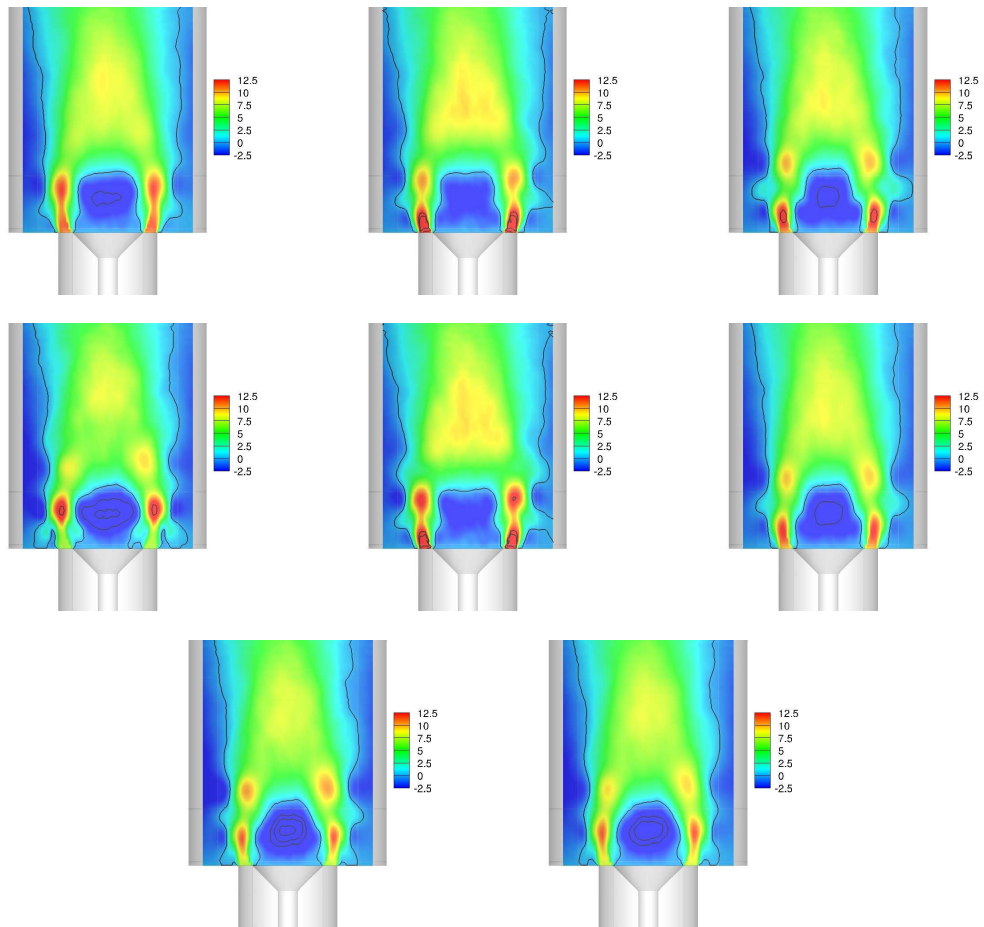
Figure 4.27: Axial velocity of the reconstructed instantaneous flow over one period using modes 3 and 4. Forced case at 160 Hz.

(a)   (b)   (c)   (d)
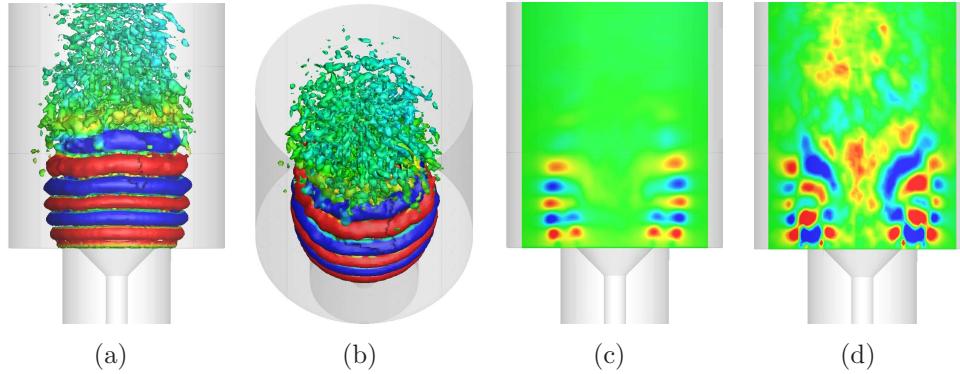
Figure 4.28: Mode 6. (a,b) Isosurfaces of the $Q-$criterion coloured by the pressure fluctuations. Contours of the fluctuations of (c) the pressure and (d) the axial velocity. Forced case at 160 Hz.

Hz. The snapshots reconstruction based on modes 6 and 7 only (Fig. 4.30 for the $Q-$criterion and Fig. 4.31 for the axial velocity) shows the vortex rings being shed then convected away at higher frequency than modes 1 and 2 (160 Hz) and modes 3 and 4 (480 Hz). Consequently, modes (6,7) could be understood as a spatial harmonic of modes (1,2) but there is not a single frequency that can be associated with them. Modes (6,7) are rather associated with an ensemble of four spectral harmonics of the fundamental (320 Hz, 480 Hz and 640 Hz).

4.4.5 Mode 5

Mode 5 is represented in Fig. 4.32. Unlike the previous modes, it doesn't have a frequency peak well above the others, but rather two peaks at the fundamental frequency (160 Hz) and the second harmonic (480 Hz) (see Fig. 4.36). It contains an intermediate level of energy between modes (3,4) and modes (6,7) with 0.6378 % of the total fluctuating energy. It is interesting to note that there is a strong correlation between the number of vortex rings present in each mode and their spectra. Roughly, a doubling of the number of vortex rings (equally spaced in the combustion chamber) corresponds to a doubling of the frequency. In this context, mode 5 appears to be an odd mode, as it exhibits characteristics from both the fundamental frequency and higher frequency modes. On one hand, for locations close to the combustor center, the $Q-$criterion applied to mode 5 (Fig.

(a)	(b)	(c)
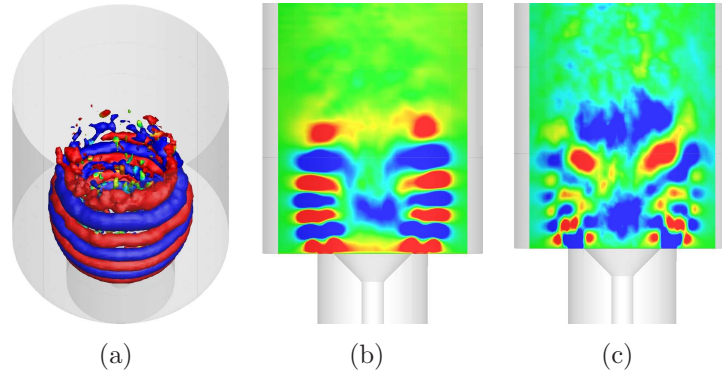
Figure 4.29: Mode 7. (a,b) Isosurfaces of the $Q-$criterion coloured by the pressure fluctuations. Contours of the fluctuations of (c) the pressure and (d) the axial velocity. Forced case at 160 Hz.

4.32) shows large vortex rings separated by a large vacuum as previously observed in modes 1 and 2. These modes exhibit their strongest frequency peaks at 160 Hz. Therefore these rings are thought to be associated with the frequency peak at 160 Hz observed in the spectra of mode 5 (Fig. 4.36). On the other hand, close to the chamber entrance, a row of close thin vortex rings is observed, as observed for higher harmonic modes (see modes 3, 4, 6 and 7). The vortex rings close to the inlet pipe are hence thought to be associated with the frequency peak at 480 Hz observed in mode 5 spectra (Fig. 4.32).

4.4.6   Mode 8

Other modes do not exhibit any vortex rings and they are more complicated to analyse. There are not reported here, with the exception of mode 8. Mode 8 is interesting through the analysis of its spectra that shows non harmonic frequencies. There are three visible peaks at 44 Hz, 88 Hz and 118 Hz. Therefore this mode could account for the sub-harmonic previously reported in the axial velocity spectra of the 160 Hz case (see Fig. 4.14). Different representations of mode 8 are plotted in Fig. 4.33. It can be noted that mode 8 contains very little energy, representing only 0.17 % of the total energy (see Fig 4.34 and Table 4.2).
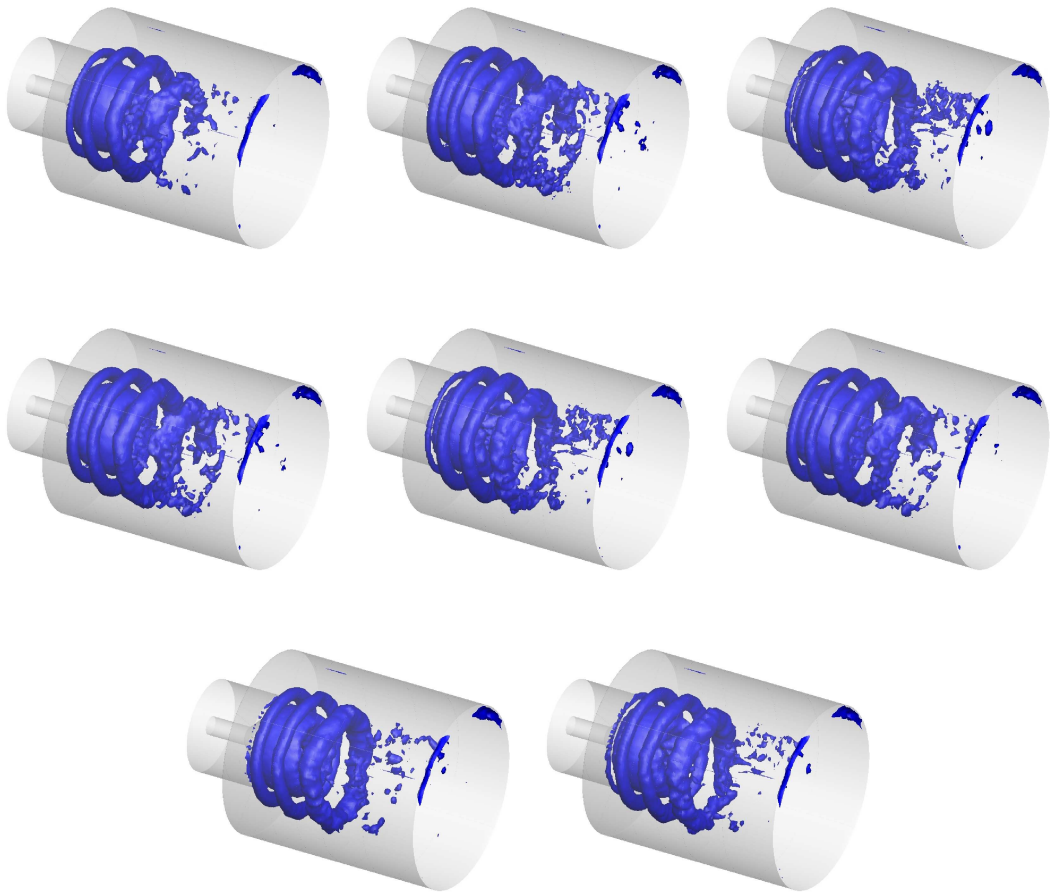
Figure 4.30: $Q-$criterion of the reconstructed instantaneous flow over one period using modes 6 and 7. Forced case at 160 Hz.
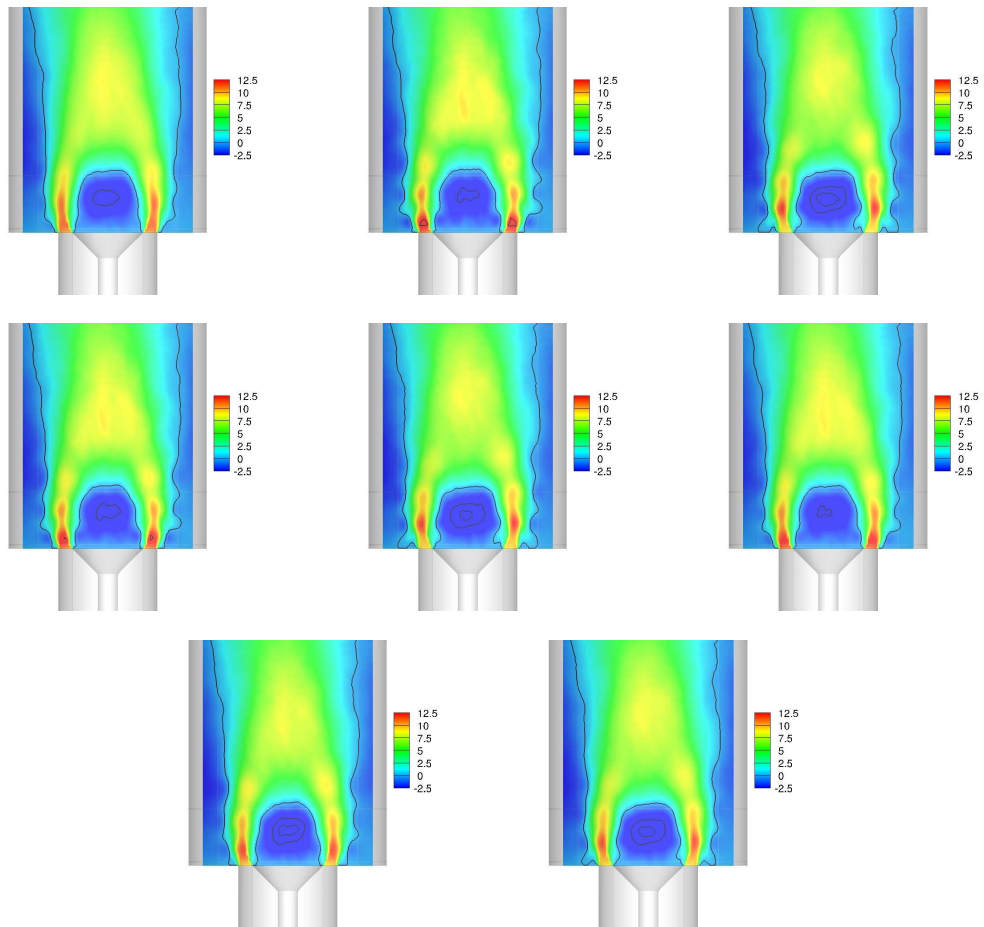
Figure 4.31: Axial velocity of the reconstructed instantaneous flow over one period using modes 6 and 7. Forced case at 160 Hz.

(a)   (b)   (c)   (d)
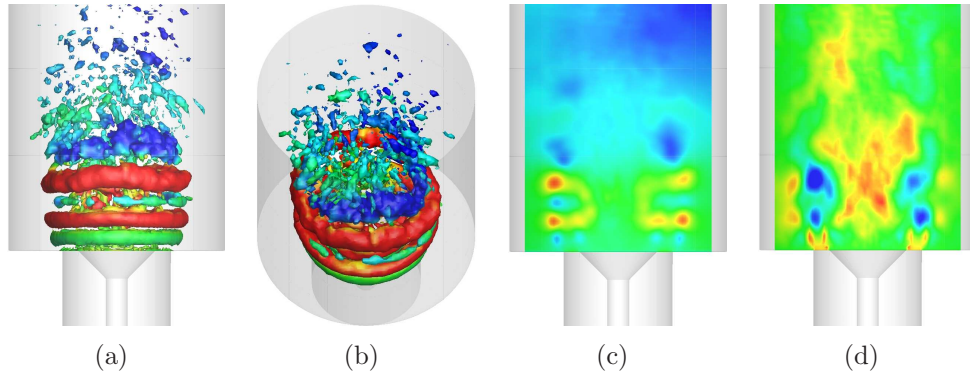
Figure 4.32: Mode 5. (a,b) Isosurfaces of the $Q-$criterion coloured by the pressure fluctuations. Contours of the fluctuations of (c) the pressure and (d) the axial velocity. Forced case at 160 Hz.

(a)   (b)   (c)

(d)   (e)
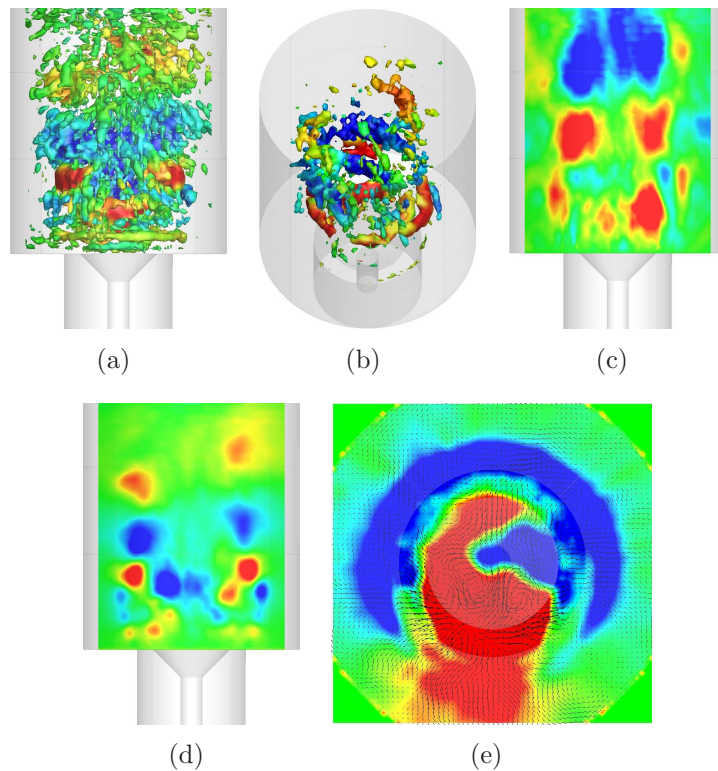
Figure 4.33: Mode 8. (a,b) Isosurfaces of the $Q-$criterion coloured by the pressure fluctuations. Contours of the fluctuations of (c) the axial velocity and (d,e) the pressure, with Fig. (e) showing a transverse plane. Forced case at 160 Hz.
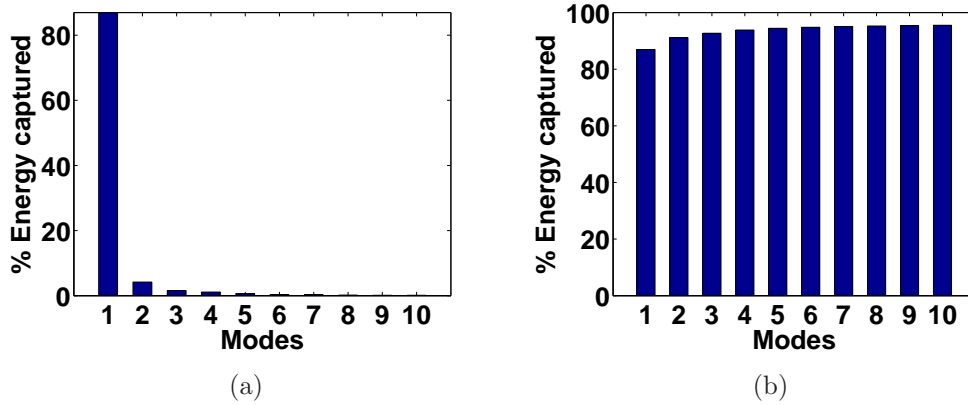
Figure 4.34: Energy distribution of the POD modes. (a) Energy relative per mode. (b) Cummulative energy. Forced case at 160 Hz.

4.4.7 Conclusions from the POD analysis of the 160 Hz case

POD analysis of the forced flow at 160 Hz develops further insight on the hydrodynamic structures associated with pulsating flows. It seems to indicate that the harmonics of the forced frequency revealed in the velocity spectra could be attributed to some weaker vortex sheddings of thinner vortical rings occuring at harmonic frequencies of the pulsating frequency. These weak vortex sheddings are superimposed to the large vortex shedding at the forced frequency (160 Hz). Because of their relative weakness (modes 3 and 4 account together for 2.7 % of the total fluctuating energy as opposed to the 91.2 % of modes 1 and 2), these harmonic vortex sheddings have not been detectable by directly applying the $Q-$criterion to the LES dataset, even though several threshold values have been tried. In that sense, POD can be considered as an attractive method to analyse and reveal the physics underlying our LES datasets. But this analysis reveals also the limitations of the POD analysis for pulsating flows. In fact, POD, while enforcing the spatial orthogonality of the modes, describes the temporal evolution of the modes based on multiple frequencies. Therefore, the method is not able to separate the different harmonics of the flow into different modes, which would have led to an easier understanding of these kind of flows.

(a) Mode 1

(b) Mode 2

(c) Mode 3
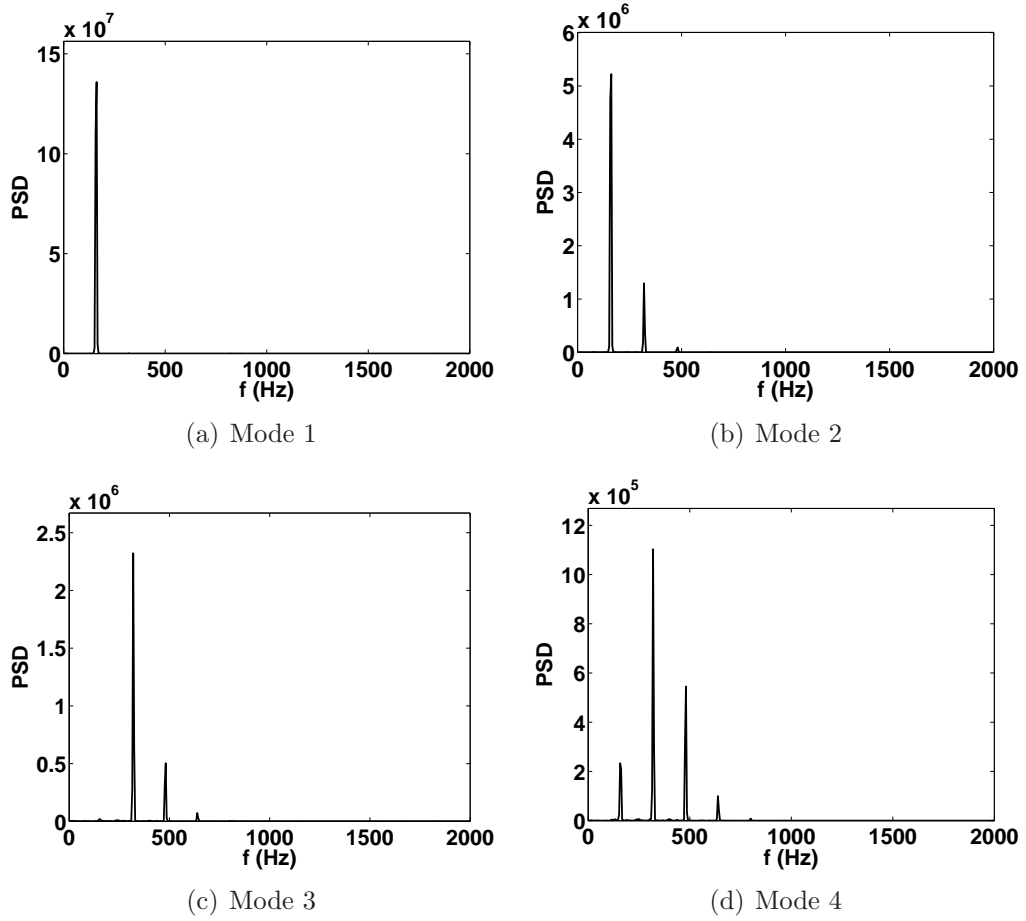
(d) Mode 4

Figure 4.35: Fourier analysis of the temporal coefficents of POD modes 1 to 4. Forced case at 160 Hz.

(a) Mode 5

(b) Mode 6

(c) Mode 7
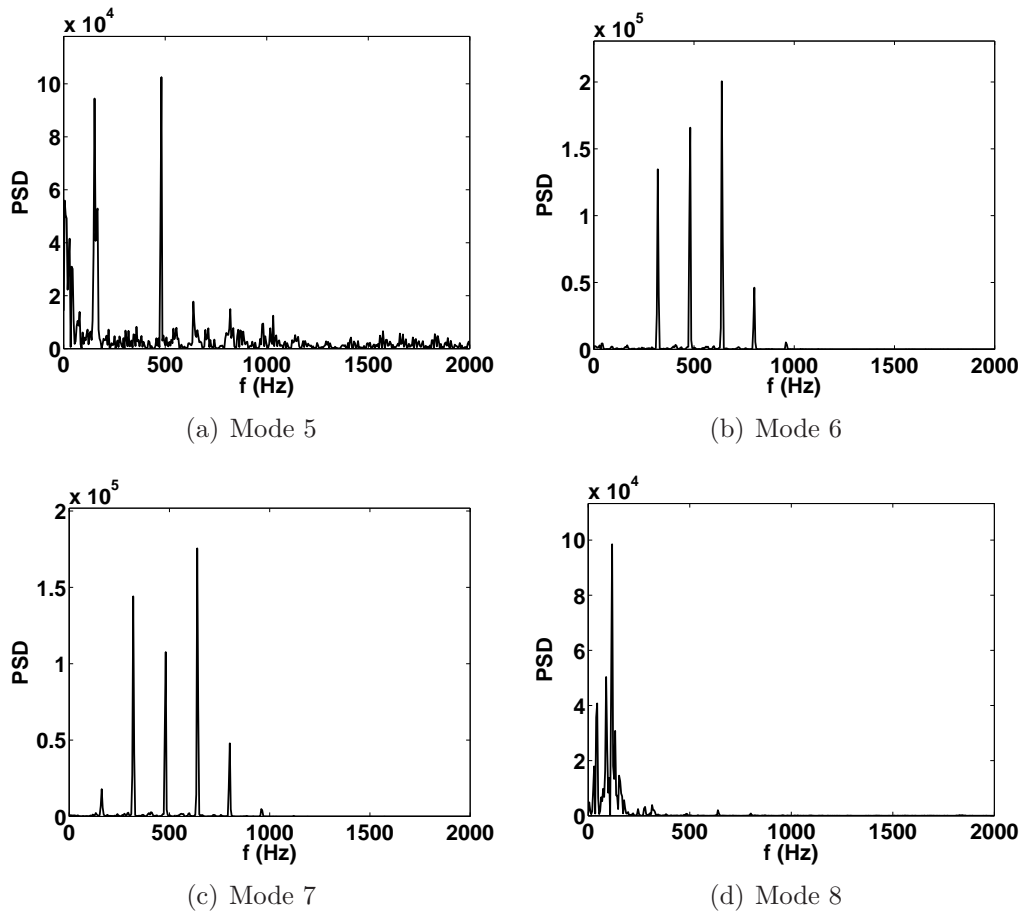
(d) Mode 8

Figure 4.36: Fourier analysis of the temporal coefficents of POD modes 5 to 8. Forced case at 160 Hz.

4.5 Summary of main findings

The isothermal air flow behind an axisymmetric conical disk, enclosed in a circular pipe of larger diameter that undergoes a sudden expansion, and with the incoming flow being forced at a single frequency and with large amplitude, has been explored with Large-Eddy Simulations. This flow may be thought of as a model problem for combustors undergoing self-excited oscillations and the results can help validate LES for complex turbulent flows involving recirculation zones and periodicity. At low forcing frequencies, the recirculation zone pulsated with the incoming flow, at a phase lag that depended on spatial location. No clear vortex shedding was observed. At high forcing frequencies, vortices were shed from the bluff body and the recirculation zone, as a whole, pulsated less. The velocity spectra showed peaks at various harmonics, whose relative magnitudes varied with location. These harmonics may be due to extra vortex sheddings occuring at harmonic frequencies of the forced frequency, as revealed by the POD analysis. A sub-harmonic peak was also observed inside the recirculation zone possibly due to merging of the shed vortices. The phase-averaged turbulent fluctuations showed large temporal and spatial variations and were higher than the turbulent fluctuations of the unforced flow at the same position. The Large-eddy simulations reproduced accurately the experimental findings in terms of phase-averaged mean and r.m.s. velocities, vortex formation, and spectral peaks.

Chapter 5

Conditional Moment Closure/Large Eddy Simulation of the Delft-III natural gas non-premixed jet flame

5.1 Introduction

5.1.1 Motivation

In this chapter, Large Eddy Simulation (LES), coupled with the Conditional Moment Closure (CMC) sub-grid model and the GRI3 detailed chemical mechanism, are used to explore the structure of the Delft III piloted turbulent non-premixed flame. The relatively simple configuration compared to bluff body or swirl flames allows to analyze key combustion aspects of combustors described in Section 2.1. In fact, a very detailed dataset [27; 70; 81; 86; 110; 111] is available for the "Delft III", which shows significant finite-rate chemistry effects, including local extinctions and re-ignitions. In addition, the pollutants emitted (CO and NO) have been measured, and hence this flame offers a very challenging test case for capturing practically-important combustion phenomena. The Delft Flame III is also a target in the TNF workshop series ($http://www.sandia.gov/TNF$).

The use of a quite refined multi-dimensional CMC grid and the detailed chemistry, together with the capability of LES to follow local fluctuations of the scalar dissipation, is expected to capture localised extinctions and re-ignitions, as well as pollutants emissions. LES also offers advantages due to its ability to capture turbulent mixing better than Reynolds-Averaged Navier-Stokes (RANS) models, but often the combustion process occurs at the sub-grid scale and therefore models are necessary. As a consequence, extensive validation of LES for flames is necessary to increase the reliability of the available models.

5.1.2 Background works

Several attempts have been conducted to model this flame using RANS formulations and various combustion models, including the transported PDF method with reduced and detailed chemistry [75; 76; 82; 86]. Nooren et al. [82] and Merci et al. [76] have shown that transported PDF results are strongly dependent on the micro-mixing model used, especially in the case of the temperature PDFs, while Merci et al. [76] reported that it was not possible to predict accurately both the RMS of the mixture fraction and the amount of local extinction. The CO mass fraction prediction was considered unsatisfactory whatever mixing model is used. Nooren et al. [82], Merci et al. [76] and Roekaerts et al. [94], in their different studies, have also emphasized the importance of an accurate modelling of the pilot flames.

5.1.3 Objectives

Here, the Conditional Moment Closure (CMC) is used as the combustion sub-model in LES. The LES is expected to capture better than RANS the mixing in the flame, and to also track (some of) the scalar dissipation fluctuations that are thought to be responsible for extinction. CMC is used in its multi-dimensional form (i.e. no cross-stream averaging is used), which allows the possibility to capture the local response of the combustion to the imposed scalar dissipation transients, but also to allow the effects of the pilot to be included. CMC has previously been used in a LES context to simulate among others the Sandia flame D [80] with a relatively coarse grid, and with quite refined grids it has been

used for spark ignition problems [118] and the Sandia flame F [38].

The objectives of the present chapter are: (i) to demonstrate the validity of the LES-CMC approach, with full detailed chemistry, for a well-characterised non-premixed flame showing significant finite-rate effects; (ii) to provide some further insights on the transient events occuring during local extinctions and re-ignitions.

5.2 Method

5.2.1 Model and codes

A first order LES-CMC formulation has been used for this simulation (see Chapter 3). The absence of experimental data for the scalar dissipation rate in the Delft flame does not allow to adjust properly the constant C_N of Eq. 3.21. Here we use the value $C_N = 42$ previously adjusted to match the experimental results of $\langle N|\eta \rangle$ for Sandia flame D [38]. No other parameter has been tuned.

The detailed chemistry mechanism GRI-Mech 3.0 has been used for these simulations. This mechanism contains 53 species and 325 reactions [106]. The refined CMC grid and the use of detailed chemistry makes this a very expensive calculation.

5.2.2 Flow considered, boundary conditions and numerical methods

Figure 5.1 shows the flow studied. The Delft III flame is composed of a central fuel jet, with a velocity at the burner exit of 21.9 m/s ($Re = 9700$), surrounded by two concentric coflows of air. The primary air flow velocity is 4.4 m/s ($Re = 8800$) and the secondary air flow velocity is 0.3 m/s at the burner exit. The jet has a diameter of $D_j = 6$ mm. The inner diameter of the primary air annulus is 15 mm and its outer diameter is 45 mm. The outer diameter of the secondary air flow is set to 400 mm for the simulation. In the experiment, the secondary air flow was produced by positioning the burner in a wind tunnel, its exact configuration depending on the place where the experiments were conducted (Netherlands or California). The fuel jet is separated from the primary air stream by a rim of
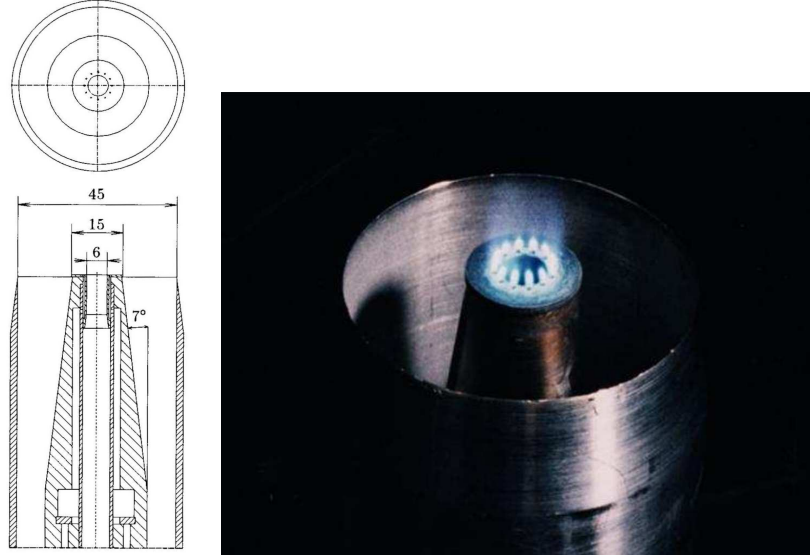
Figure 5.1: Delft piloted jet burner. From Ref. [81].

outer diameter 15 mm. The pilot flames are located on this rim. They consist of 12 holes of 0.5 mm diameter located on a circle of 7 mm diameter. These pilot flames are modelled as an axisymmetric annular ring of 0.5 mm thickness around the fuel jet. In the experiment, the pilot fuel is different from the jet fuel, but in order to be in a position to work with a single mixture fraction, the pilot flames were modelled as a fully-burnt stoichiometric mixture of the jet fuel and air, with the same mass flow rate as in the experiment. The fuel was natural gas. The GRI 3.0 chemistry mechanism does not cover all the species in the experiment. For example, Butane (C_4H_{10}), Pentane (C_5H_{12}) and Hexane (C_6H_{14}) are not present in this chemistry mechanism. As a result, the missing species have been re-distributed into other species in order to conserve the total calorific value of the fuel calculated by means of the individual calorific values. We end up with an approximation of its composition based on the species available in the GRI-Mech 3.0 mechanism, as reported in Table 5.2. The natural gas used by the CMC code and the natural gas in the experiment both give a stoichiometric mixture fraction of $\xi_{st} = 0.07147$. Table 5.1 summarizes the inlet conditions used for the Delft flame III modelling.

Before starting any multi-dimensional computations, a series of the so-called

Table 5.1: Numerical setup used by the LES code to model the Delft flame III. These values are the experimental ones except the ones flagged with the symbol (*), which have been obtained through the modelling process.

Stream	Vel. (m/s)	Diam. (mm)	R_e	ξ	T (K)
Fuel	21.9	$0-6$	9700	1	295
Pilot	13.98(*)	$6(*) - 7(*)$		$\xi_{st}(*)$	1997.5(*)
Rim		$7(*) - 15$			
Primary air flow	4.4	$15 - 45$	8800	0	295
Secondary air flow	0.3	$45 - 400(*)$		0	295

Table 5.2: Fuel composition used by the CMC code to model the Delft flame natural gas

Constituents Formula	Mass fraction %
CH_4	70.013
C_2H_2	0.0695
C_2H_4	0.289
C_2H_6	4.873
C_3H_8	1.1155
N_2	21.54
CO_2	2.10
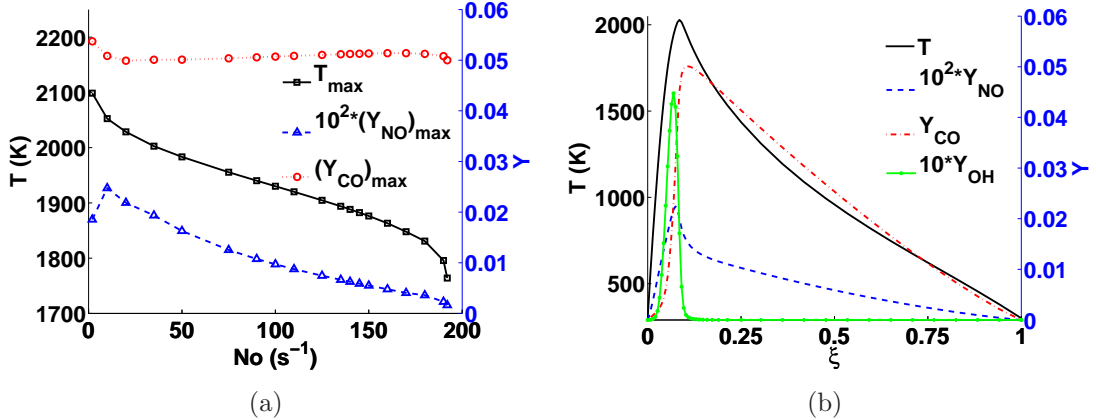
Figure 5.2: (a) Maximum values of some reactive scalars of the steady flame against the scalar dissipation rate N_0, using the detailed chemistry GRI-Mech 3.0 (53 species, 325 reactions). The extinction strain rate is found to be equal to 193 1/s. (b) Conditional profiles of some reactive scalars from the 0D-CMC computation with $N_0 = 20$ 1/s. This solution is used as the prescribed distribution in the LES/0D-CMC computation and is injected at the pilot location in the LES/3D-CMC.

"0D-CMC" calculations of the Delft flame III were performed with the above fuel composition and the detailed GRI-Mech 3.0 chemistry mechanism. 0D-CMC refers to solving Eq. 3.23 i.e. Eq. 3.14 without spatial transport terms and for different values of prescribed $\widetilde{N|\eta}$ parametrised by the peak value, N_0. As a result, a set of solutions were obtained that can be understood as steady flamelet calculations with unity Lewis number. Figure 5.2(a) shows the maximum values of different reactive scalars (the temperature, Y_{NO} & Y_{CO}) for different values of N_0. The curve of temperature gives access to two global properties of the flame, i.e. (i) its operating temperature range, with the flame existing from $T_l = 1794$ K up to $T_u = 2099$ K and (ii) the extinction scalar dissipation rate, which is found to be:

$$N_{0ext} = 193 \ 1/s. \tag{5.1}$$

The latter is a fundamental parameter in the study of localized extinction that is developed in Section 5.3.3. The figure also reveals the well-known strong dependency between the temperature and NO production as the two curves have overall similar trends, while Y_{CO} is found to be relatively independent of the
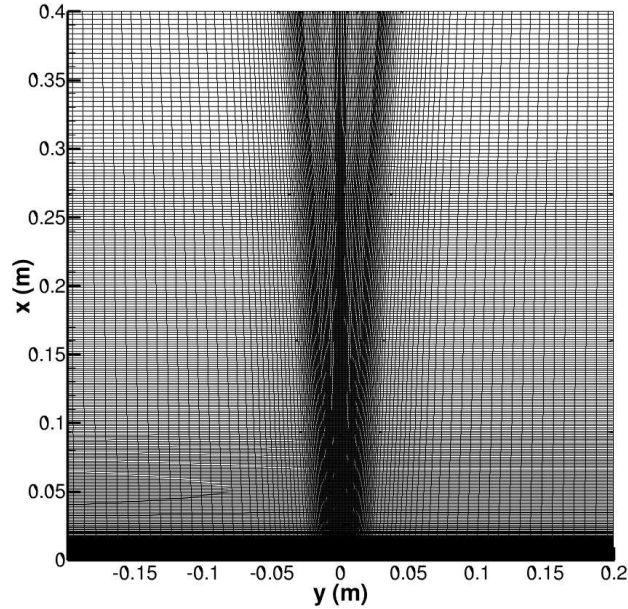
Figure 5.3: Longitudinal cutting plane (z=0) of the LES grid (1.3M cells).

scalar dissipation rate in the domain of existence of the flame.

The LES grid used for the multi-dimensional computation has a cubic shape and extends $66D_j$ in the axial and $33D_j$ in the radial direction, which is larger than the range in which experimental data is available ($41D_j \times 6D_j$). This is done in order to allow the flow to develop. The grid created for the simulation is an O-grid mesh (Fig. 5.3) using a minimum spacing of 0.18 mm across the pilot with a smooth expansion downstream and radially so that a total of approximately 1.3M cells ($75 \times 60 \times 268$) are used. The CMC equations are solved on a structured grid of $16 \times 16 \times 32 = 8192$ cells, with 32 cells being used in the axial direction and some refinement being made around the mixing layer of the jet and the primary coflow. Fig. 5.4(a) shows a part of the LES grid (black line) with its associated CMC grid superimposed (red line). Each CMC cell has its center located at an intersection of the red lines.

The LES boundary conditions at the burner exit are the experimentally-obtained velocities at the jet and the coflows, which are injected with a top-hat profile and without any added fluctuations. The mixture fraction is set to 1.0 in the jet, 0.0 in the co-flow and to the value of 0.071, close to the stoichiometric
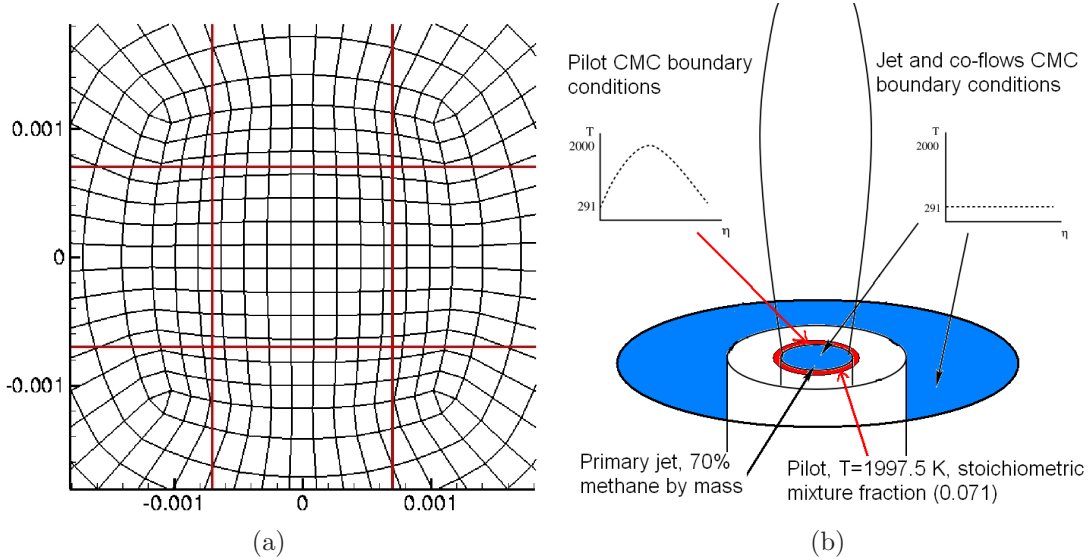
Figure 5.4: (a) Enlargement of the LES grid (black) and CMC grid (red) in the transverse direction. A CMC cell contains several LES cells, the ratio depending on the location inside the domain. Each CMC cell has its center located at an intersection of the red lines. (b) Sketch of the CMC boundary conditions: inert everywhere except for the pilot where a fully burning flamelet is imposed.

mixture fraction value, in the pilot. The fuel jet and air coflows temperatures are all set to the experimental value of 295 K. For the pilot, the "0D-CMC" solution (see above) obtained for $N_0 = 20$ 1/s was used. The distribution of some reacting scalars in mixture fraction space from this 0D-CMC solution is plotted in Fig. 5.2(b) and will be commented below. Using this solution, the stoichiometric temperature and density of the modelled pilot is determined and the modelled pilot stream velocity is obtained by dividing the experimental pilot mass flow rate by this stoichiometric 0D-CMC density and the annular area of the pilot. The inlet conditions at the modelled annular pilot for the simulations are as follows: velocity 13.98 m/s; mass flow rate 2.3×10^{-5} kg/s; temperature 1997.5 K; density 0.1611 kg/m^3 (Table 5.1).

The boundary conditions for CMC are described in Fig. 5.4(b) and are the following: inert (i.e. unburnt) distributions of Q_α are injected in the jet and the coflows, while the burning "flamelet" obtained with the prescribed $N_0 = 20$ 1/s is injected in the pilot. Therefore we expect that the physical transport terms

in Eq. 3.14 will be responsible for "igniting" the rest of the flow (i.e. the Q_α's becoming those corresponding to burning distributions in mixture fraction space), which is equivalent to how the flame is ignited in the experiment. Zero gradients in physical space of all conditional averages are imposed at the sides and the downstream edge of the domain.

A RANS computation with the 0D-CMC solution was performed first, followed by a LES simulation using this prescribed "flamelet" everywhere in the flow. We refer to these different simulations as RANS/0D-CMC and LES/0D-CMC. The value of $N_0 = 20$ 1/s used for these simulations is about 10% of the extinction value of 193 1/s. Figure 5.2(b) shows the conditional profiles of temperature and mass fractions of NO, CO and OH for this "flamelet". The profile shape of the conditonal Y_{OH} profile is noticeable and demonstrates that the reaction zone occupies only a small range in the mixture fraction space.

The full LES with the CMC equations (Eq. 3.14) is denoted as LES/3D-CMC and constitutes the main result of the present chapter. Each figure presented in the next section is for LES/3D-CMC computation unless specified otherwise. The time-step used was 1.0×10^{-5} s, which ensures that a maximum CFL number is around 0.65 during a whole stable simulation. This time-step is also expected to be small enough to capture at least some of the interesting transient events observed experimentally in the flame such as local extinctions and re-ignitions. The simulations were carried out on 52 dual-core processors at 3.0 GHz with 2 GB of RAM per core, producing 1.0 ms of simulated time in approximately 147 min. The CMC code took most of the CPU time.

5.3 Results and Discussion

5.3.1 Instantaneous distributions

An instantaneous distribution of the axial velocity is shown in Fig. 5.5(a). The different streams (jet, pilot, co-flows) are evident. Between the fuel jet and the primary co-flow, the rim creates a small recirculation zone, which provides another mechanism to stabilise the flame, in addition to the pilot flame. In Fig. 5.5(b), the vorticity snapshot reveals that two shear layers develop: an inner one between

the fuel jet and primary air and an outer one between the primary and secondary air flows. Close to the burner, Kelvin-Helmholtz instabilities arise along these shear layers, visualized by the fragmented vorticity contours. Fig. 5.5(c) uses the Q-criterion method [48] to visualise vortical structures:

$$Q = (\omega^2 - 2\widetilde{S}_{ij}\widetilde{S}_{ij})/4 \tag{5.2}$$

with ω the vorticity magnitude and $\widetilde{S}_{ij}$ the strain rate, both calculated from the gradients of the resolved velocity. The Q iso-surfaces have been colored according to the resolved temperature. In the center, the turbulent fuel jet is clearly visible. Vortices are formed by the Kelvin-Helmoltz instabilities at the outer shear layer as described above. These structures are then convected before eventually breaking-up around 150 mm downstream, increasing the turbulence intensity there. These instabilities are pronounced along the inner shear layer due to the large difference of velocities between the fuel jet and the primary co-flow and are therefore expected to be the main source of turbulence in the fuel jet.

A snapshot of the mixing field is shown in Fig. 5.6(a). The non-premixed fuel jet is evident again, flowing out from the burner with a mixture fraction equal to 1 before mixing with the surrounding co-flows. The pilot flame can be located on this snaphsot by the position of the stoichiometric iso-line (the black line) on the inlet plane, as the modelled pilot is fed with a stoichiometric mixture of the Delft flame fuel. The other snaphots in Figs. 5.6 and 5.7 include the instantaneous contours of the temperature, Y_{NO}, Y_{CO} and Y_{CO_2} at the same instant, and allow an overall visualization of the flame. In addition, the instantaneous contour of Y_{OH} is represented in Fig. 5.6(c) and will be commented in Section 5.3.3.

5.3.2 Velocity and mixture fraction fields

The calculated mean and RMS of the axial velocity (Fig. 5.8 & 5.9 respectively) and the mixture fraction (Fig. 5.10 & 5.11 respectively) show a good agreement with the experimental data. A close observation of the three simulations reveals that two LES results (LES/0D-CMC and LES/3D-CMC) show some discrepancies, which implies that the local variations of Q_α's, as offered by the 3D-CMC
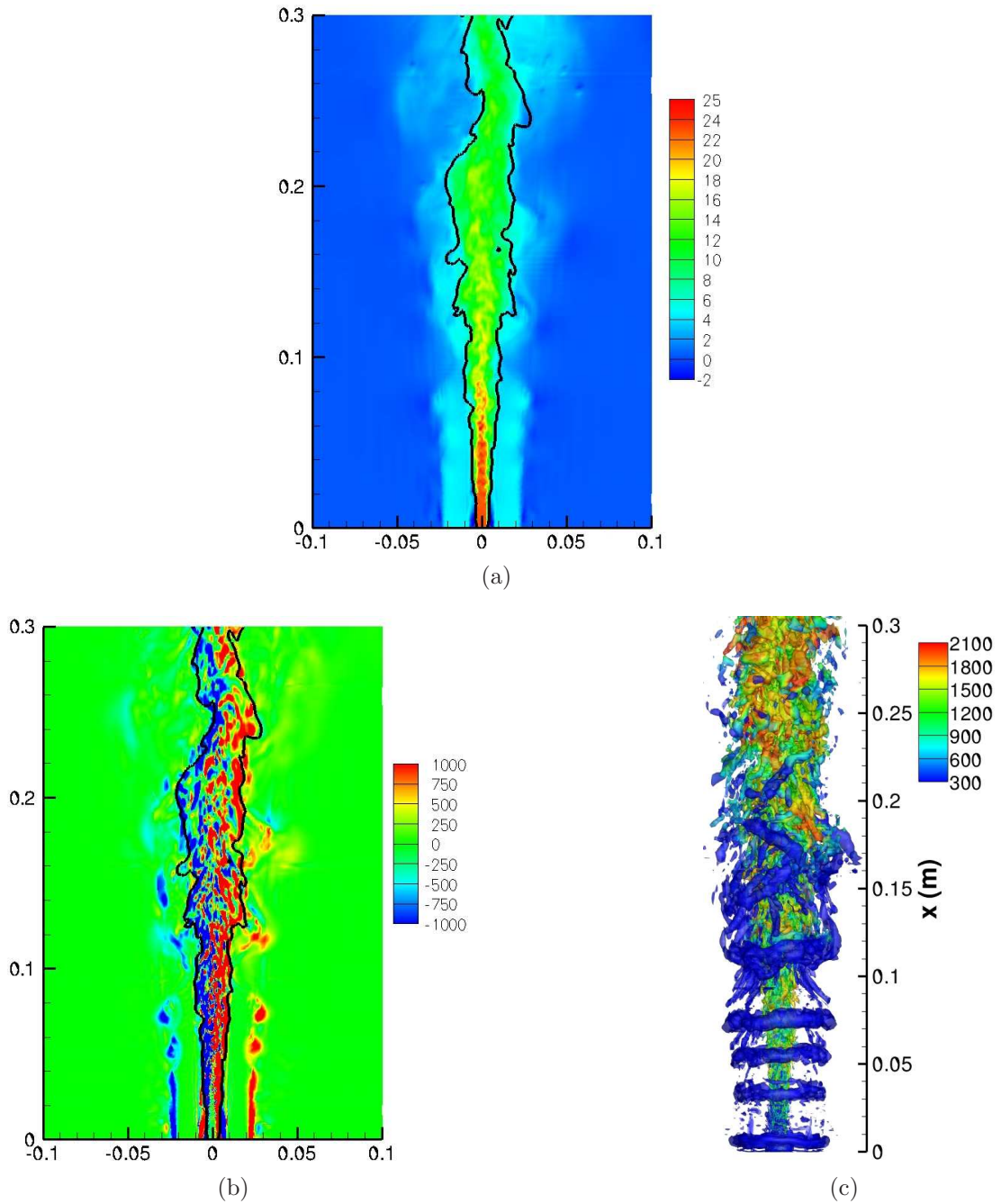
Figure 5.5: Typical instantaneous contours of (a) axial velocity (in m/s) and (b) $z-$vorticity (in 1/s) at the same instant. The stoichiometric iso-surface is shown with the black line. Axes in m. (c): Instantaneous iso-surface of $Q = 50 \times 10^3 s^{-2}$ colored with the temperature (in K).

(a) Mixture fraction

(b) Temperature (K)

(c) Y_{OH}
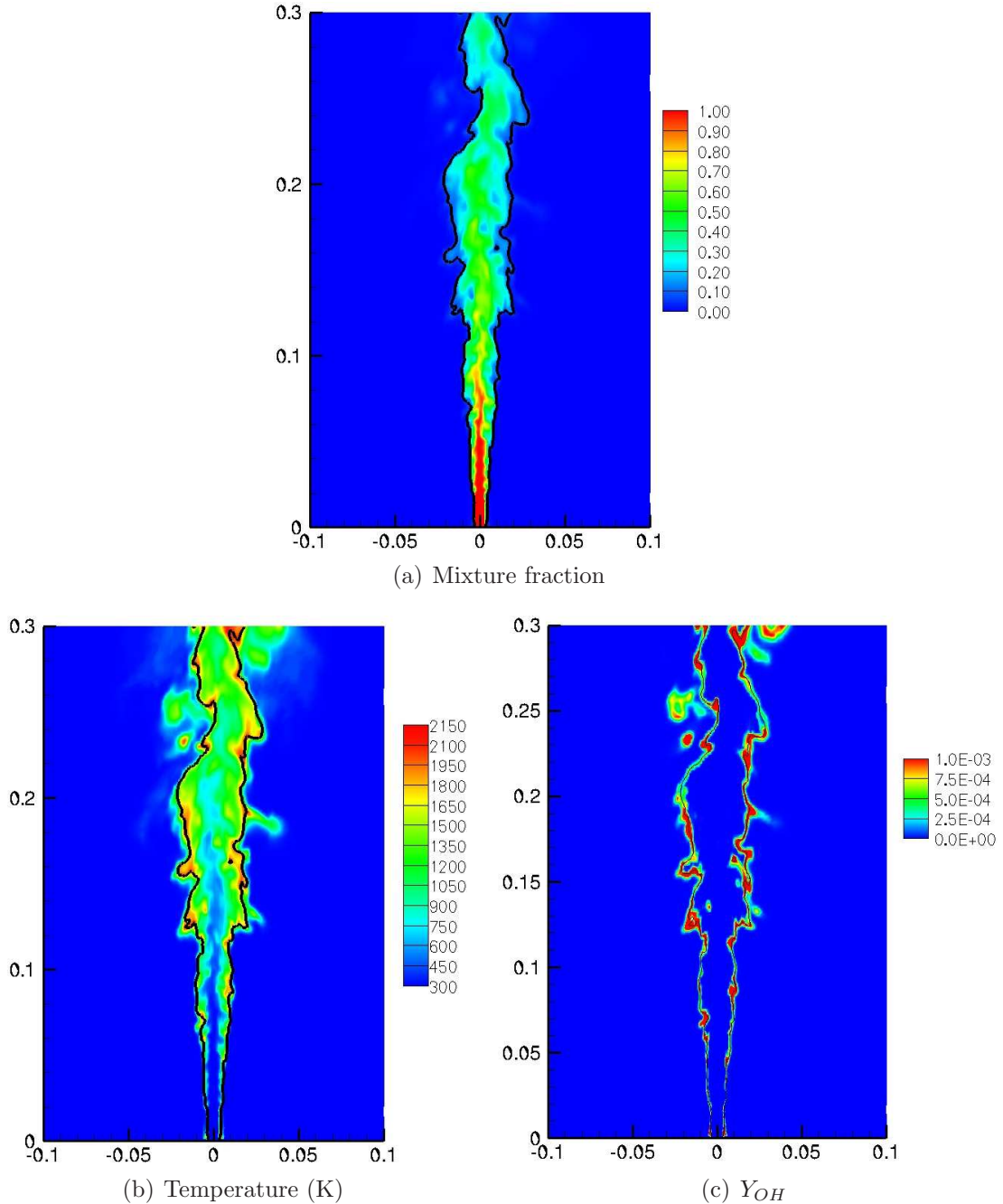
Figure 5.6: Typical instantaneous contours of the mixture fraction, temperature and mass fractions of OH at the same instant. The stoichiometric iso-surface is shown with the black line.

(a) Y_{NO}

(b) Y_{CO}

(c) Y_{CO_2}
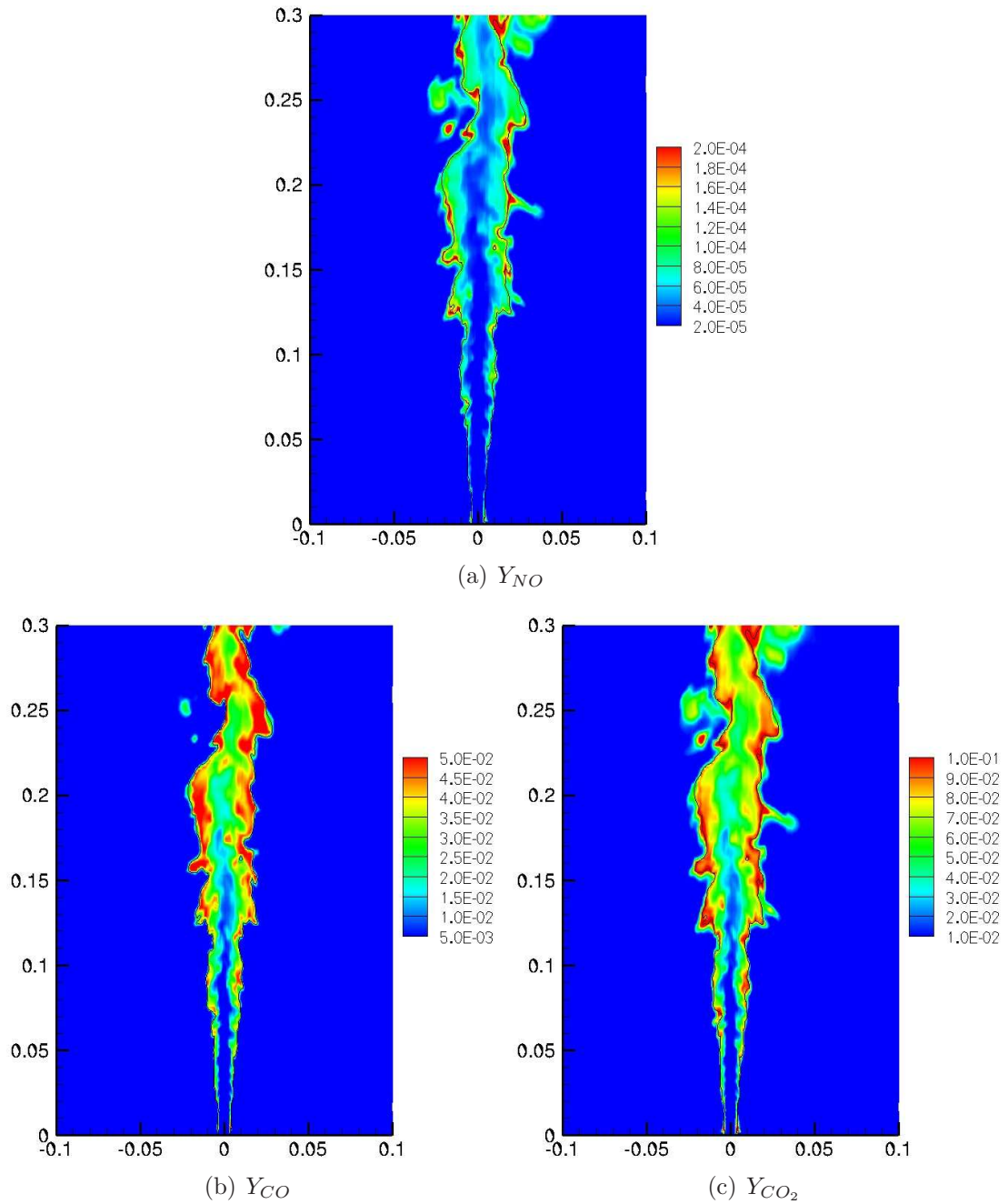
Figure 5.7: Typical instantaneous contours of the mass fractions of the indicated species at the same instant. The stoichiometric iso-surface is shown with the black line.

solution, result in a big enough change to the conditional density over the "steady flamelet" solution to affect the velocity and mixture fraction fields. The mixing field (Fig. 5.10) predicted by the LES/3D-CMC is closer to the experimental data than the other simulations, but this is obtained to the detriment of the axial velocity field. A good example of this behaviour is found at $x = 16.7D_j$ around the centreline where the 3D-CMC formulation results in the largest changes compared to the 0D formulations in both the velocity and mixing fields (Figs. 5.8 & 5.10). The recirculation zone previously observed in Fig. 5.5(a) is also evident in Fig. 5.8 at $x/D_j = 0.5$ ($x = 3$ mm) and for $r/D_j \approx 1$. The absence of inlet velocity fluctuations in the LES results in an underprediction of the turbulence intensity in the early part of the jet, as shown in Fig. 5.9 by the RMS of the axial velocity at $x = 0.5D_j$. However, further downstream well-developed turbulence is found everywhere across the jet, showing that the shear layers instabilities have fed the flow with turbulence: from about 8 jet diameters and up to 33 jet diameters (48 mm<x< 200 mm), the velocity fluctuations are in good agreement with the data (Fig. 5.9). For $x/D_j > 33$ the RMS of the mixture fraction and, to a lesser extent, the velocity fluctuations are overpredicted: at this location in the domain and further downstream, the LES mesh becomes coarser due to the mesh expansion, as visualized in Fig. 5.3.

5.3.3   Reaction zone and localised extinctions

In Fig. 5.12, the instantaneous flame front is visualised by the contour of OH mass fraction. The reaction zone is thinner in this flame compared to other piloted flames like the Sandia flame F [38]. This is attributed to the absence of premixing in the fuel jet in Delft III compared to the Sandia F that leads to a low stoichiometric mixture fraction ($\xi_{st} \approx 0.0715$) and to a narrower range of reaction in mixture fraction space, as shown by the conditional profile of OH mass fraction in Fig. 5.2(b). The reaction zone in Figs. 5.12 & 5.6(c) and the ξ_{st} isoline in Fig. 5.5(a) show that the OH zone is not strongly convoluted close to the burner. This is attributed to the low ξ_{st} that places the reaction zone in the fuel-lean side of the inner shear layer where the shear stresses are relatively low. Further downstream ($x/D_j = 20$), the turbulence has developed in the fuel jet
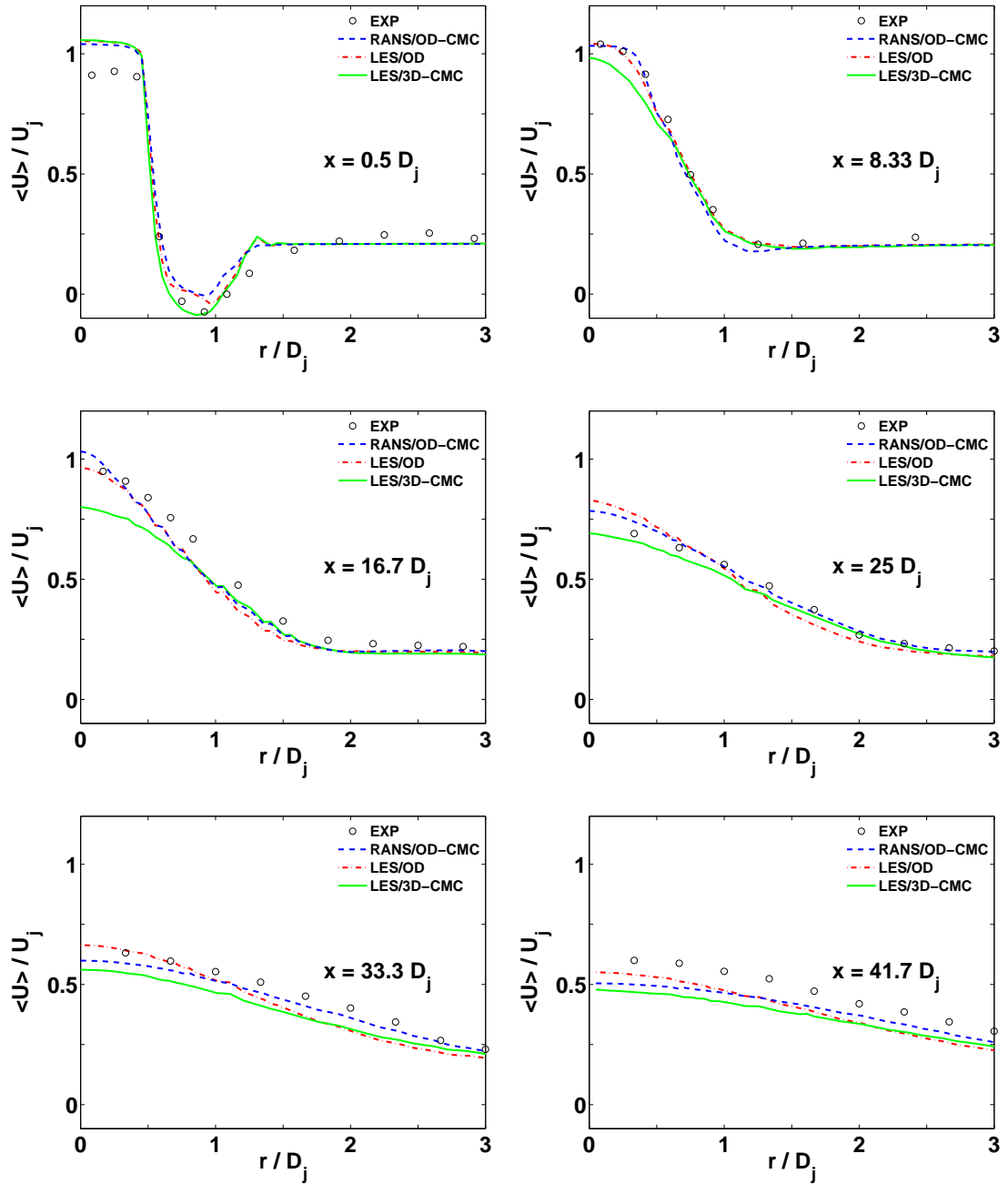
Figure 5.8: Radial profiles of the mean axial velocity at the indicated axial position. Experimental data from Ref. [27].
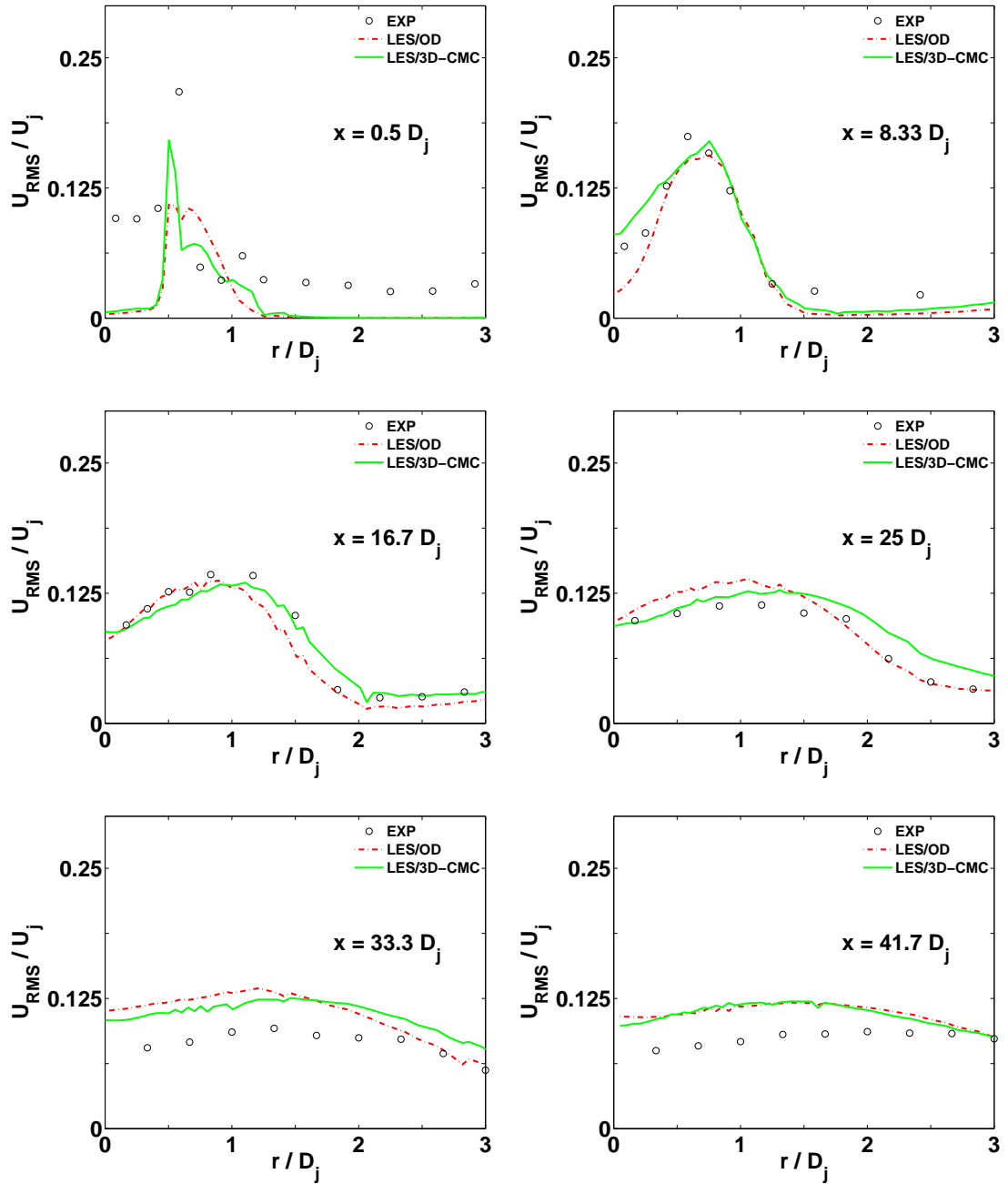
Figure 5.9: Radial profiles of the RMS of the axial velocity at the indicated axial position. Experimental data from Ref. [27].
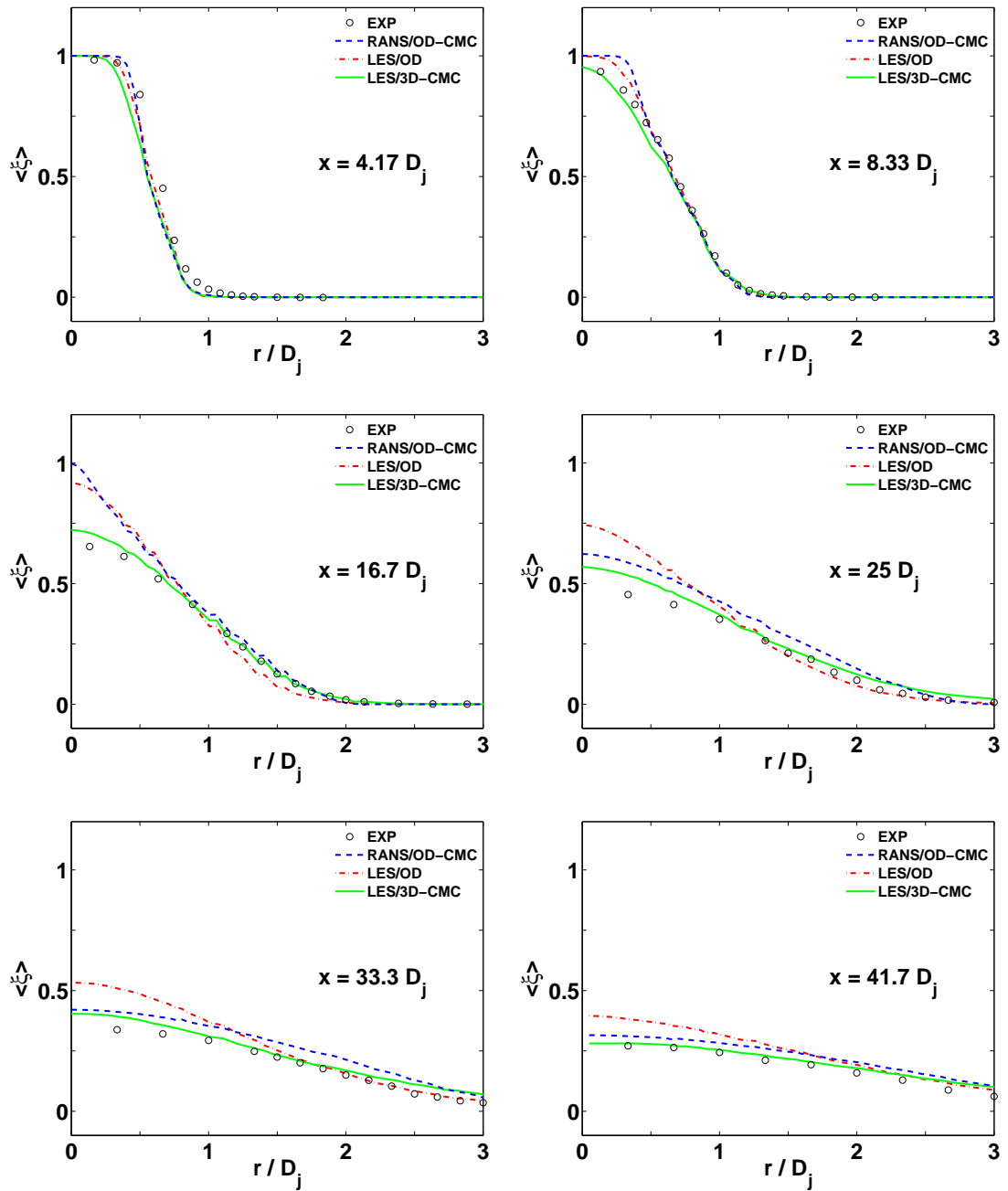
Figure 5.10: Radial profiles of the mean of the mixture fraction at the indicated axial position. Experimental data from Ref. [27].
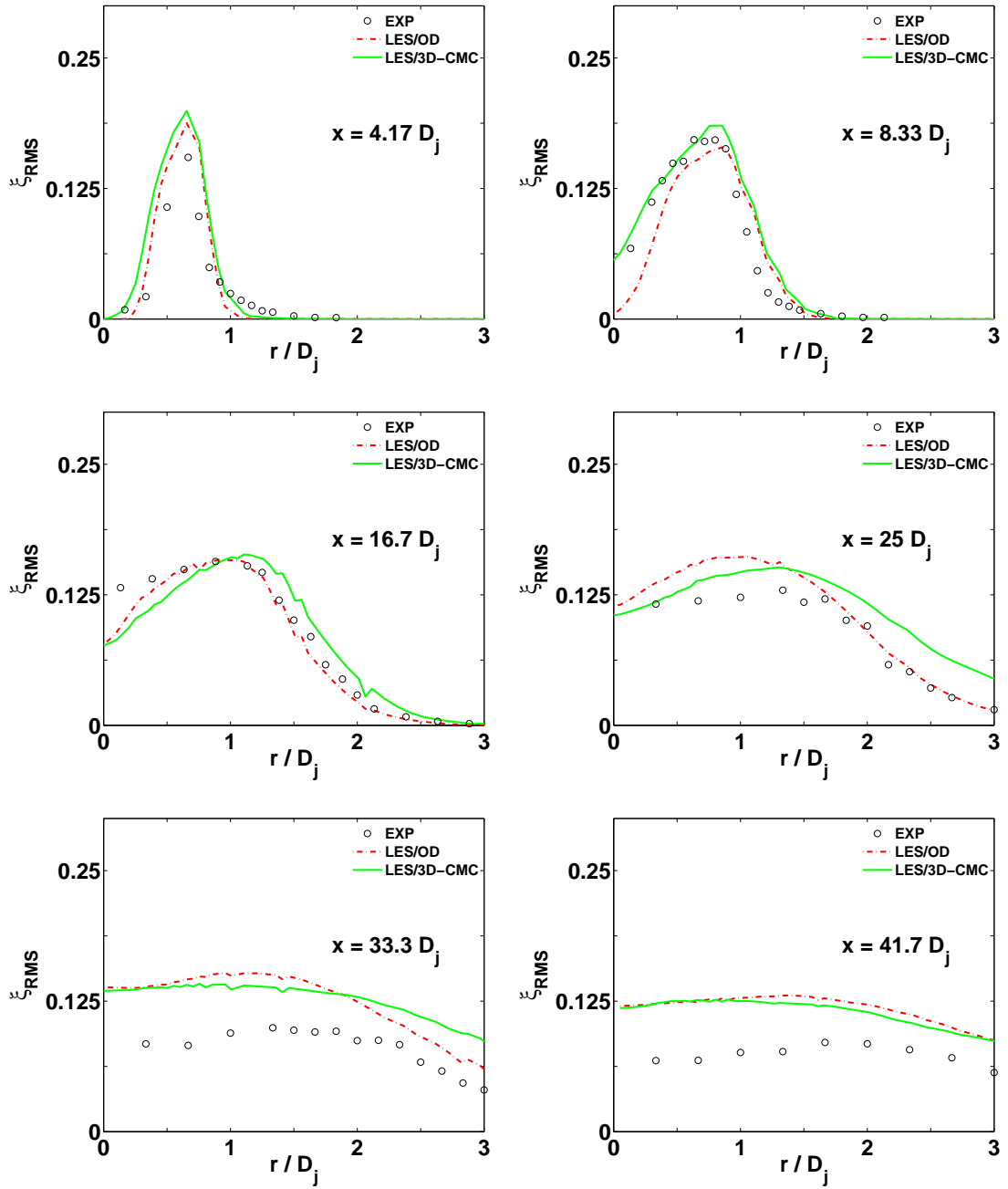
Figure 5.11: Radial profiles of the RMS of the mixture fraction at the indicated axial position. Experimental data from Ref. [27].
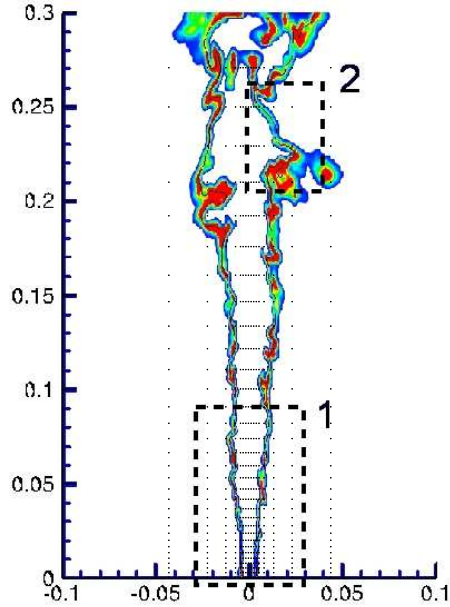
Figure 5.12: Typical instantaneous OH mass fraction contour, with the CMC grid superimposed. Regions 1 and 2 are discussed in the text.

and the OH zone is distorted significantly. The ξ_{st} iso-surface has also expanded to the radial location of the Kelvin-Helmoltz vortices visualized in Fig. 5.5(c) at around 150 mm downstream, which results in a strong convolution of the OH zone further than about $x/D_j = 25$. All these observations are qualitatively consistent with the experiments as shown by the experimental OH contour visualization in Fig. 5.13.

In Fig. 5.14, three snapshots separated by 1 ms are shown at around $x/D_j = 39$ (marked '2' in Fig. 5.12) while in Fig. 5.15 the three snaphots are located at around $x/D_j = 3$ (marked '1' in Fig. 5.12) and are separated by 0.5 ms. Both these sequences show strong variations of the reaction zone, visualized using OH mass contour. As a result, these two behaviours can appear quite similar at first glance while the mechanisms behind them and their physical interpretations are completely different. The drop in the OH mass fraction that appears in the snapshots marked '2' (Fig. 5.14) is observable from both the LES/0D-CMC and the LES/3D-CMC computations. In this case, obviously $\widetilde{Y_{OH}|\eta}$ does not reach zero (since a burning distribution is prescribed), even if a sudden fall in OH mass
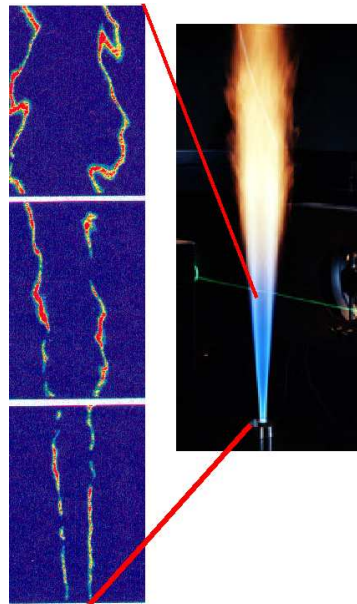
Figure 5.13: Typical instantaneous OH images, covering the regions $x = 15$ to 93 mm, 100 to 178 mm and 185 to 263 mm. Each image from the different regions has been taken at different time.The OH images (left) are from Ref. [27]. This figure has been kindly provided by Prof. D. Roekaerts.

fraction is observed. The mechanism behind this is not linked to an extinction phenomenon. It is due to the integration over η-space of the conditional OH mass fraction weighted by the β-PDF, following Eq. 3.30. In this case, the decrease of OH mass fraction can be understood by analysing the results in Fig. 5.16. As detailed in Section 3.2.4 of Chapter 3, the Filtered probability Density Function (FDF) is approximated using a β function. Some β-PDF are plotted at two locations inside each domain of Fig. 5.12, the left part of the figure corresponding to the domain marked '1' in Fig. 5.12, the right to the domain marked '2'. The different curves for each location correspond respectively to the same instants as the snapshots in Figs. 5.14 and 5.15. These graphs reveal that the β-PDF function varies against time and position, according to the value of the local mixture fraction ξ and its sub-grid variance $\widetilde{\xi''^2}$ (see Section 3.2.4). Keeping in mind that the conditional OH mass fraction profile $\widetilde{Y_{OH}|\eta}$ has a shape close to a δ-function centred on the stoichiometric mixture fraction (Fig. 5.2(b)), the mechanism behind the OH mass fraction contour variations observed in Fig. 5.14 (domain marked '2') becomes straighforward: when the β-PDF around the stoichiometric value (shown by a vertical red line) becomes close to zero, the value of $\widetilde{Y_{OH}}$ computed through Eq. 3.30 tends to drop drastically, leading to the observable shrinking of the OH contour at this place of the flame.

On the other hand, the series of snapshots marked '1' (Fig. 5.15) shows the evolution of a real "flame hole" or localized extinctions close to the burner. In this case, $\widetilde{Y_{OH}|\eta}$ drops to zero inside the hole. This type of behaviour is observable only with the LES/3D-CMC computation as it takes into account the temporal and spatial evolution of finite-rate effects. The prediction of these localised extinctions close to the burner are qualitatively consistent with the experimental observations from Fig. 5.13.

The analysis of the conditional data from the CMC solver is the only way to check that there are localized extinction and so to make a clear distinction between the two kinds of behaviour described above. Figure 5.17 shows the conditional profiles of the temperature and the OH mass fraction at three axial positions. At each of these axial position, the conditional profile predicted by the CMC code has been plotted for all CMC cells at the indicated x and for every timestep over a period of 78 ms. In order to find a representative conditional
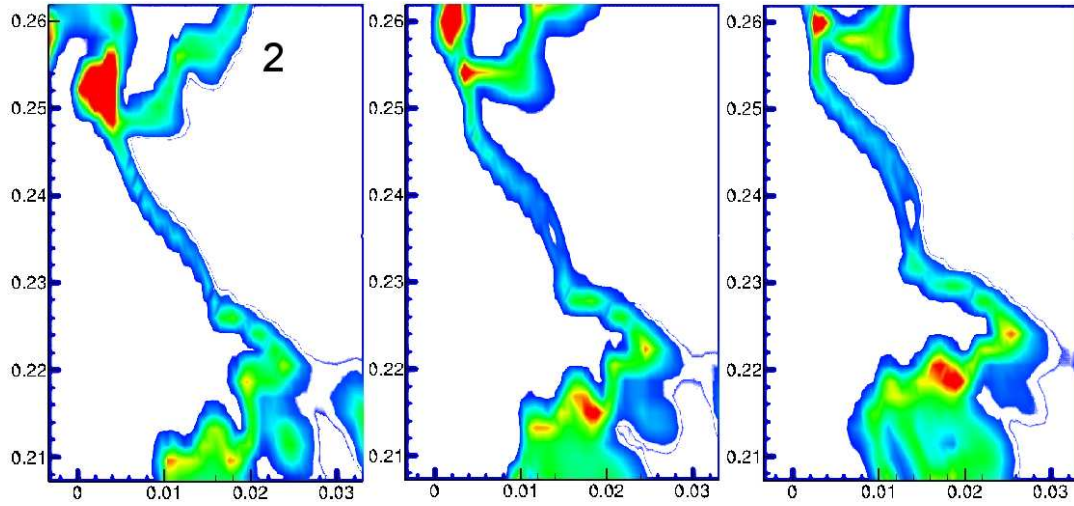
Figure 5.14: Sequential images of OH with 1 ms spacing in region 2 shown in Fig. 5.12.
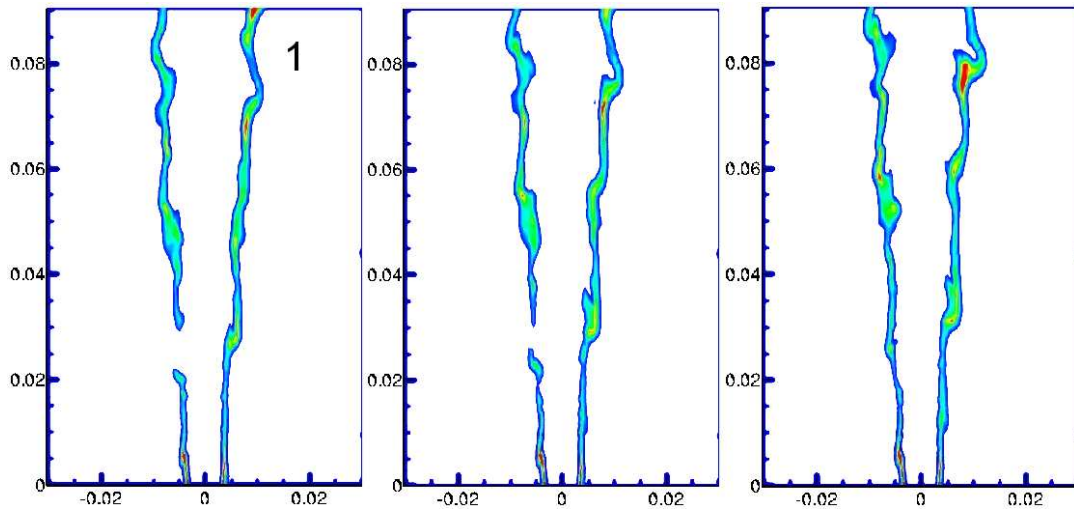
Figure 5.15: Re-ignition sequence with 0.5 ms spacing in region 1 as shown in Fig. 5.12.
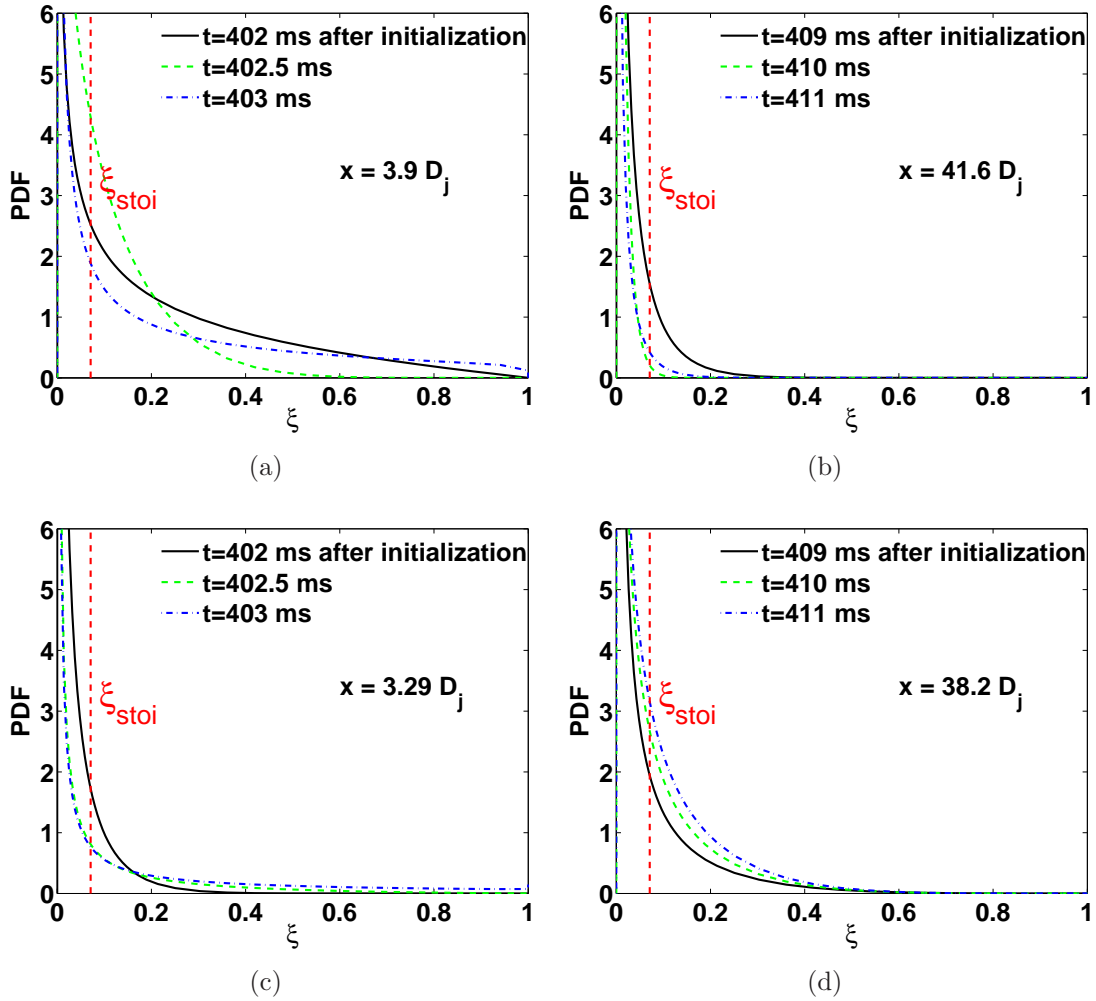
Figure 5.16: Integrated FDFs assuming a β function shape for 4 different CMC cells centred at $x = 19.7$ mm and $x = 23.4$ mm (c & a corresponding to Fig. 5.12, domain marked '1') and at $x = 229.1$ mm and $x = 249.9$ mm (d & b corresponding to domain marked '2'), at the same instants as the snapshots in Fig. 5.15 (c & a) and Fig. 5.14 (d & b).

average for a particular axial location h, the different CMC solutions over time at that axial position were also PDF-weighted averaged using the following process:

$$\widetilde{\phi|\eta}^{\,*}(h) = \frac{\int_{t_1}^{t_2} \int_{x=h} \widetilde{\phi|\eta} \, \widetilde{P}(\eta) \, \bar{\rho} \, dV dt}{\int_{t_1}^{t_2} \int_{x=h} \widetilde{P}(\eta) \, \bar{\rho} \, dV dt} \tag{5.3}$$

where the integration is over all the CMC nodes corresponding to that axial position and over time, with $t_1 < t < t_2$. The graphs allow to visualize that the LES/3D-CMC formulation predicts a strong fluctuation of the conditional profiles against the position, both axial and radial, as well as against time. The former contradicts a previously used hypothesis according to which conditional moments are independent of the radial position in shear layers [59] and that the pilot will not affect the radial dependence of conditional moments significantly [80]. Figure 5.17 reveals that the LES/3D-CMC formulation predicts a succession of extinction and re-ignition events close to the burner around $3 - 5D_j$ and the occasional extinctions and re-ignitions further downstream up to $10D_j$.

Figure 5.18(a) gives a 3D visualization of these extinctions by plotting the stoichiometric mixture fraction iso-surface coloured according to the OH mass fraction. Areas with Y_{OH} reaching zero are surrounded by a black line. It is evident that: (i) the OH at stoichiometry drops to zero in some locations; (ii) the OH at stoichiometry is not constant, but fluctuates in space and time. Some of these variations are due to the integration process over the η-space (Eq. 3.30) through the fluctuations of the β-PDF as described above (in this case due only to the mixture fraction variance fluctuations as ξ remains equal to ξ_{st}). Most of the variations of OH mass fraction observed in Fig. 5.18(a) are only captured by the LES/3D-CMC code through the temporally and spatially-varying $\widetilde{Y_\alpha|\xi}$ that respond to spatial and temporal variations of $\widetilde{N|\eta}$.

To clarify this point further, Fig. 5.19 shows time-series of the peak conditional scalar dissipation rate (i.e. at $\eta = 0.5$; the value at $\eta = \xi_{st}$ is a constant proportion of N_0 due to the use of the AMC model, see Fig. 5.20), $\widetilde{T|\xi_{st}}$, $\widetilde{Y_{OH}|\xi_{st}}$, $\widetilde{Y_{NO}|\xi_{st}}$ and $\widetilde{Y_{CO}|\xi_{st}}$, at various locations downstream and at radial locations corresponding to the middle of the annular pilot ($r = 0.58D_j$, left) and around the pilot ($r = 0.82D_j$, right). At $x = 3.29D_j$ and for radial positions be-

tween $r = 0.58D_j$ and $r = 0.82D_j$, which are locations where extinctions occur, the scalar dissipation rate has a very large temporal variation and occasionally crosses the value corresponding to the extinction of the "0D-CMC" solution. Figure 5.20 shows the conditionally filtered scalar dissipation rates at $x = 3.29D_j$ and $r = 0.82D_j$ at different times. The shape of the curves are identical due to the use of the AMC model. As in the time series, the maximum value of the conditionally filtered scalar dissipation rate is seen to reach its extinction value from time to time. Further downstream, the scalar dissipation relaxes and is well below the extinction value. An examination of the conditional stoichiometric temperature shows excursions down to about $800K$ that coincide with zero OH. This is the footprint of a localized extinction. It is interesting to note that Fig. 5.19 shows that at $x = 3.29D_j$ and for a radial position $r = 0.58D_j$ (left) localised extinctions occur even if the scalar dissipation rate is slightly *below* the nominal value for extinction of the steady flamelet (found to be equal to 193 1/s in Fig. 5.2(a)). This is due to the fact that the transport terms in the CMC equation are responsible for convecting at the locations of high scalar dissipation the Q_α distributions associated with the incoming, "frozen" shapes from the entry, which the pilot cannot always ignite successfully. In other words, the localised extinction at the neighbourhood of the pilot can sometimes be understood as a lack of "ignition" by the pilot due to the high scalar dissipation rate. It must be emphasized that the presence of localised extinctions at these different locations is qualitatively consistent with the experimental data. In particular, animations of the resolved OH contour are consistent with experimental visualizations of OH contour [27; 111] reproduced in Fig. 5.13. The way LES-CMC captures localized extinctions here is also consistent with similar findings in Ref. [38] for Sandia flame F using a reduced chemistry scheme.

Further downstream, the LES-CMC produces a smaller degree of extinction than the experiment. In Fig. 5.21, conditional profiles of temperature and CO mass fractions are plotted from various instants at a specific axial position and compare to experimental scatterplots. The different CMC solutions over time at that axial position are also PDF-weighted averaged for comparison with the experimental average. These instantaneous conditional profiles predicted by the LES/3D-CMC formulation, although fluctuating, correspond always to burning

distributions. The conditional PDF-weighted average temperature and CO mass fraction show that the model tends to predict more accurately the lean part than the rich part in η-space. A slight overprediction of the temperature and mass fraction peaks is visible, which is due to the absence of extinctions in the simulation at this location, while the experimental scatterplots show that they still occur occasionally at the location. However, it is obvious that the model has predicted realistic conditional profiles and that the agreement with experiments is quite good in general.

5.3.4 Temperature prediction and pollutants emissions

In Fig. 5.18, the instantaneous iso-surfaces of $\xi = \xi_{st}$ colored according to the local resolved (a) OH mass fraction, (b) temperature, (c) NO mass fraction & (d) CO mass fraction are plotted at the same instant. Figures 5.18 (b), (c) & (d) show the flame from the same prespective, which allows to compare the pictures to one another, while the image of OH mass fraction has been rotated to allow the best visualization of the localized extinction occuring at that instant. Comparison between Fig. 5.18 (b) and (c) allows to highlight the strong correlation between Y_{NO} and the temperature for any axial position above around 125 mm (21 D_j). In fact, on the upper part of the flame, temperatures are above 1500 K on average triggering the formation of NO_x through the thermal mechanism. Along the stoichiometric mixture fraction on the upper part of the flame, Y_{NO} is found to fluctuate strongly with values from less than 1.0×10^{-4} to more than 2.0×10^{-4}. On the other hand, Y_{NO} shows only small fluctuations along the stoichiometric iso-surface on the lower part of the flame, with the exception of regions were localized extinctions occur, typically close to the burner. The emission of NO remains low in the lower part of the flame. One explanation comes from the high sensitivity of the NO reaction rate on the temperature in the Zel'dovich mechanism while the temperature remains overall below $1500K$ in this region. Another explanation of this low NO production is the presence of localized extinctions in this part of the flame, which affects strongly the pollutant emissions as developed in the next paragraph.

The conditional averages for NO and CO are seen to fluctuate as the scalar

dissipation rate fluctuates (Fig. 5.19). The $\widetilde{Y_{NO}|\xi_{st}}$ at the pilot (Fig. 5.19 left, blue dotted curve) is high because of the injection of the "burning flamelet" at this location. As the pilot stream mixes with the surroundings, NO is reduced and, at the instants of the localised extinction, NO is reduced significantly. It increases as we go downstream and the flame becomes fully alight. The conditional CO is in reasonable agreement with experiment (Fig. 5.21(b)) and so is the temperature (Fig. 5.21(a)). The Favre-mean and RMS temperature (Figs. 5.22 & 5.23 respectively) and CO mass fractions (Figs. 5.24 & 5.25 respectively) compare well with the experiments. A slight underprediction of both reactive scalars close to the burner ($x = 4.17D_j$ and $x = 8.33D_j$) could be due to an over-prediction of extinctions in this part of the flame. Finally, the mass fraction of NO is, however, increasingly overpredicted as we go downstream (Fig. 5.26 and Fig. 5.27). This may be attributed to the neglect of radiation, which may be responsible for the slight over-prediction of the temperature, but also to the chemical scheme used. Significant over-predictions of NO using GRI3 have been previously observed in both turbulent [20] and laminar flames [7].

5.4 Summary of main findings

A LES - first order CMC formulation has been applied to the Delft III natural gas non-premixed jet flame. Localised extinctions, which lead to the succession of burning and extinguished stoichiometric fluid along the flame front, have been successfully captured. These transient events occur mainly close to the nozzle, consistent with experimental observations. The simulations reproduce well the experimental data in terms of time-averaged statistics for velocity, mixture fraction, CO and temperature, with the exception of NO which is overpredicted.
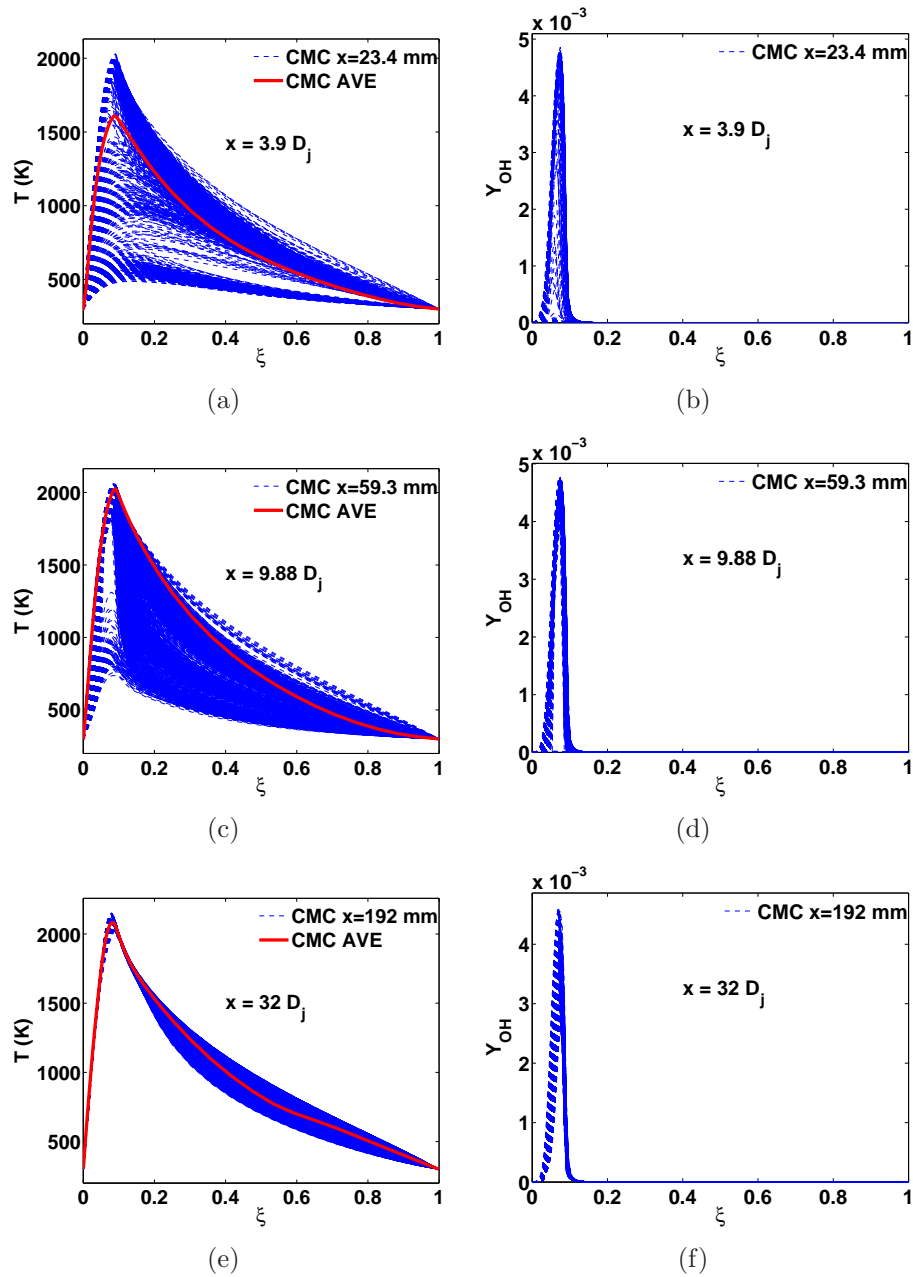
Figure 5.17: Typical instantaneous conditional ("CMC") and PDF-weighted conditional average ("CMC AVE") profiles of the temperature and OH mass fraction at the indicated axial positions. The PDF average is done over all the CMC nodes corresponding to a given axial position and over time.
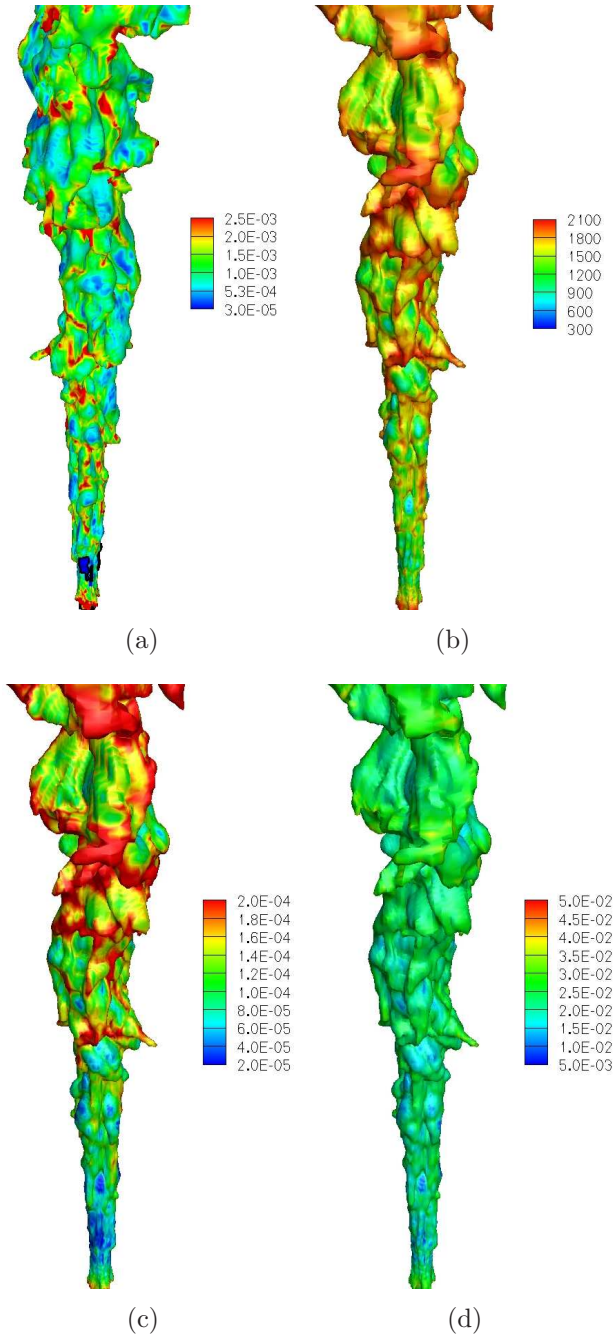
Figure 5.18: Typical instantaneous iso-surface of $\xi = \xi_{st}$ colored according to the local resolved (a) OH mass fraction, (b) temperature, (c) NO mass fraction & (d) CO mass fraction at the same instant. Length of images: 300 mm. All the pictures are seen from the same perspective except (a) which has been rotated to highlight the localized extinction.
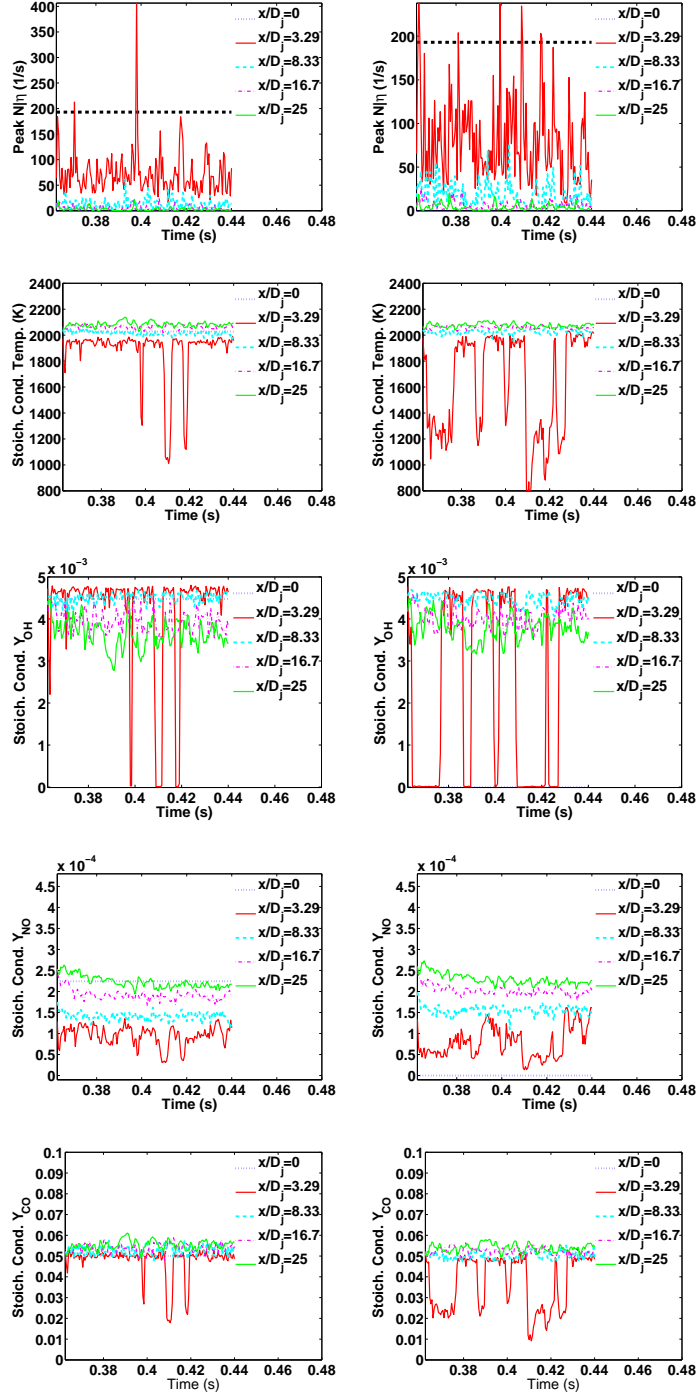
Figure 5.19: Time series of $\widetilde{N|0.5}$, $\widetilde{T|\xi_{st}}$, $\widetilde{Y_{OH}|\xi_{st}}$, $\widetilde{Y_{NO}|\xi_{st}}$ and $\widetilde{Y_{CO}|\xi_{st}}$ at $r = 0.58D_j$ (left, corresponding to the radial position of the pilot) and at $r = 0.82D_j$ (right) and the indicated x. Time zero refers to the initialization of the LES. The black dotted lines on the two top graphs refer to the extinction value of the scalar dissipation rate (193 1/s).
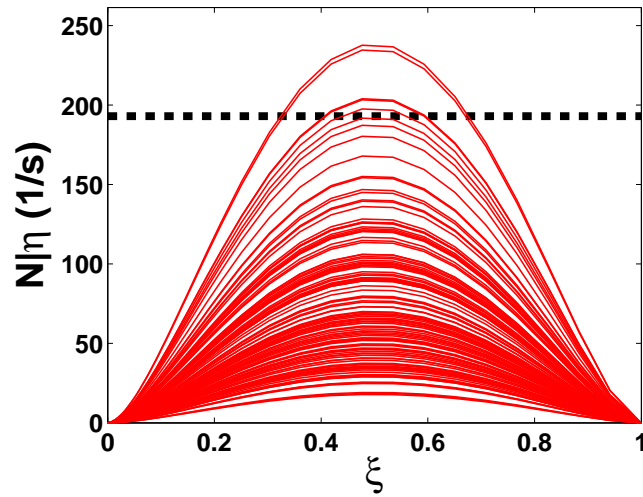
Figure 5.20: $\widetilde{N|\eta}$ at $x = 3.29D_j$ and $r = 0.82D_j$. The black dotted line refers to the extinction value of N_0 (193 1/s).
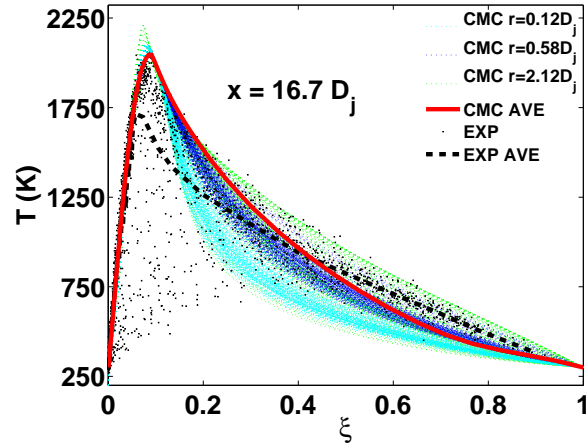
(a)
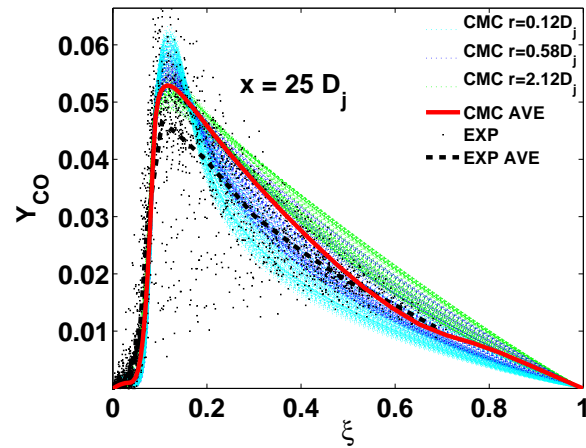
(b)

Figure 5.21: Typical instantaneous conditional ("CMC") and PDF-weighted conditional average ("CMC AVE") profiles of (a) the temperature and (b) CO mass fraction at respectively $x = 100$ mm and $x = 150$ mm and at the indicated radial positions. The PDF average is done over all the CMC nodes corresponding to a given axial position and over time. Scatterplots and conditional averages from experimental data [27] are superimposed for comparison.
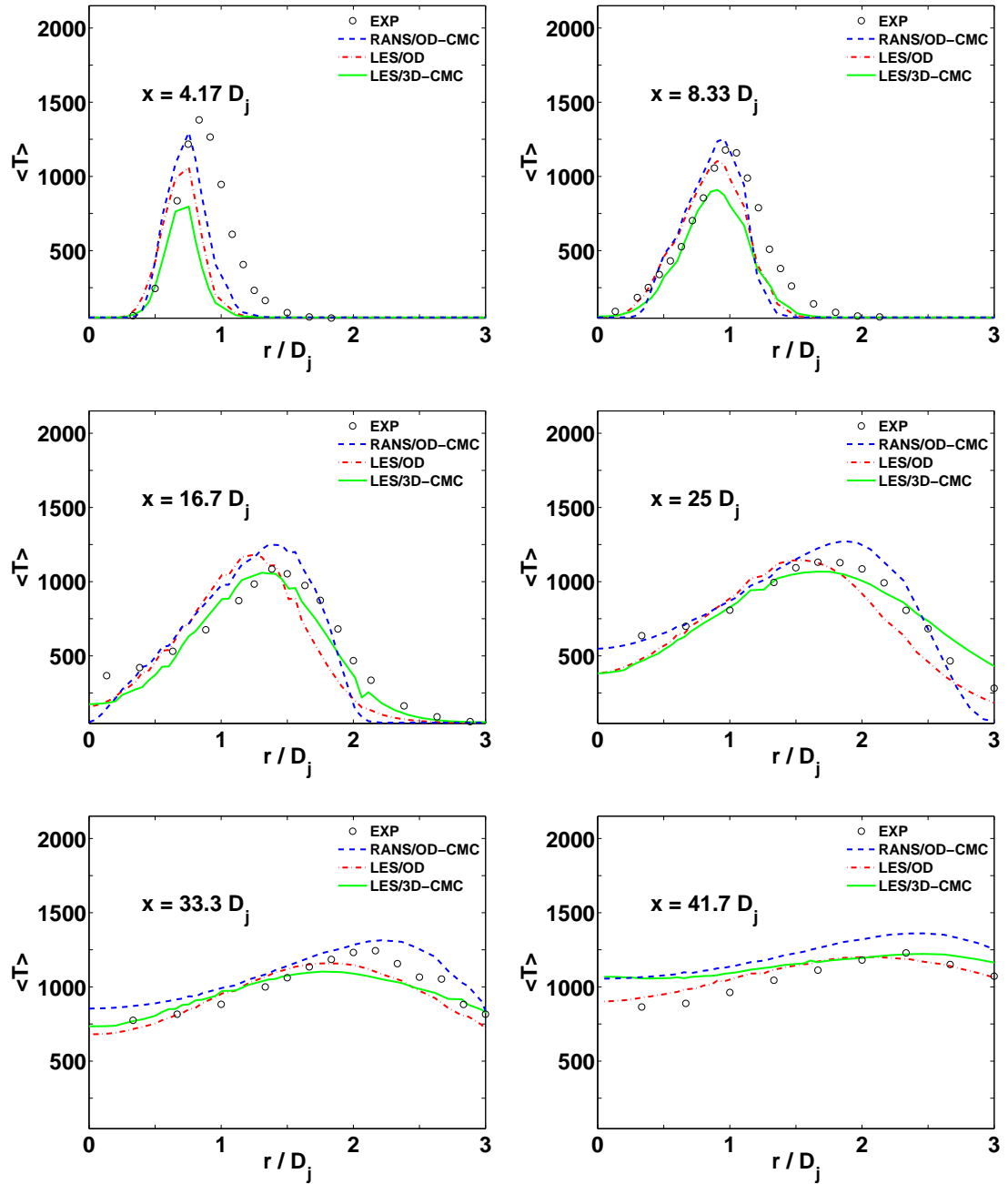
Figure 5.22: Radial profiles of the mean temperature at the indicated axial position. Experimental data from Ref. [27].
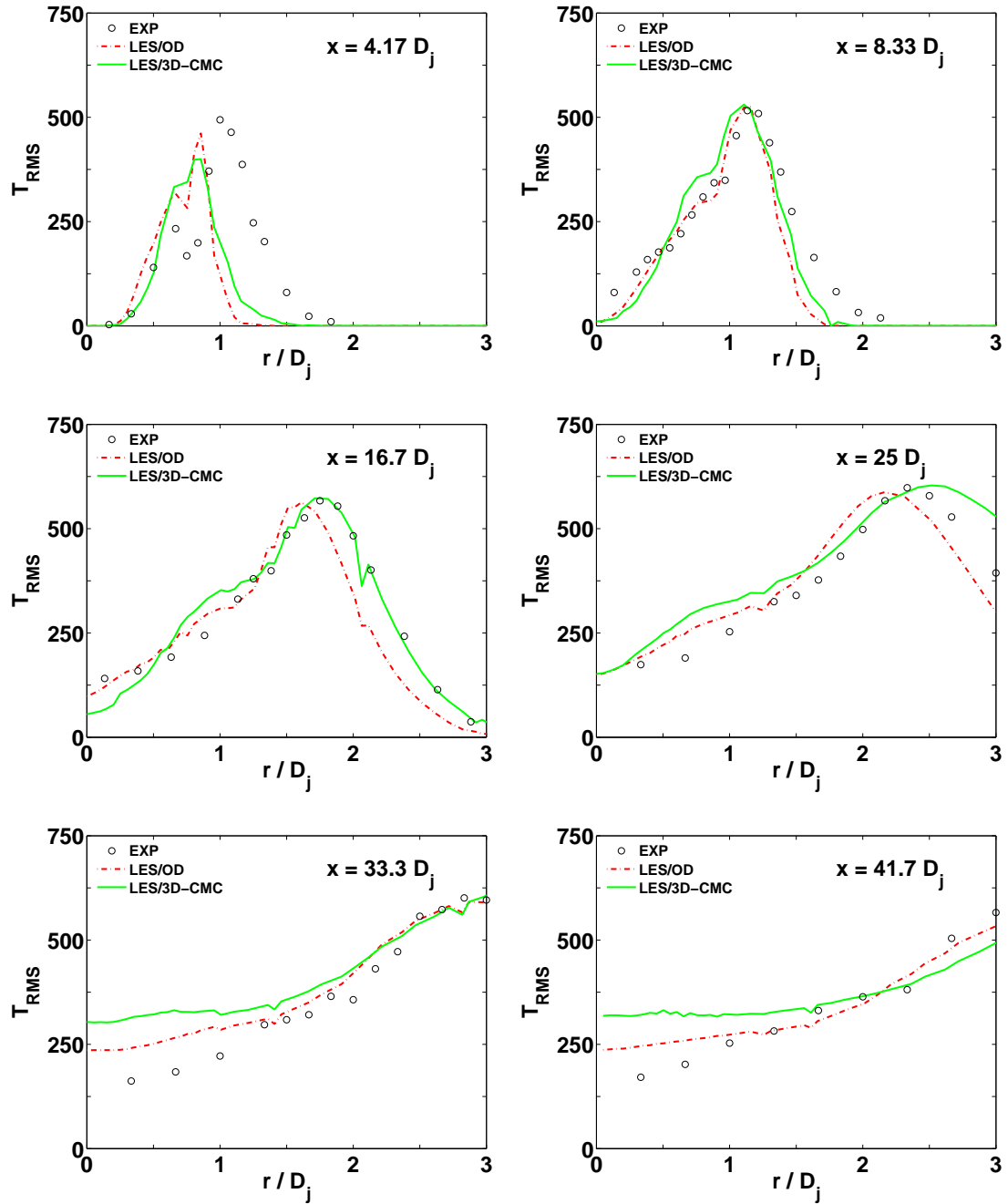
Figure 5.23: Radial profiles of the RMS of the temperature at the indicated axial position. Experimental data from Ref. [27].
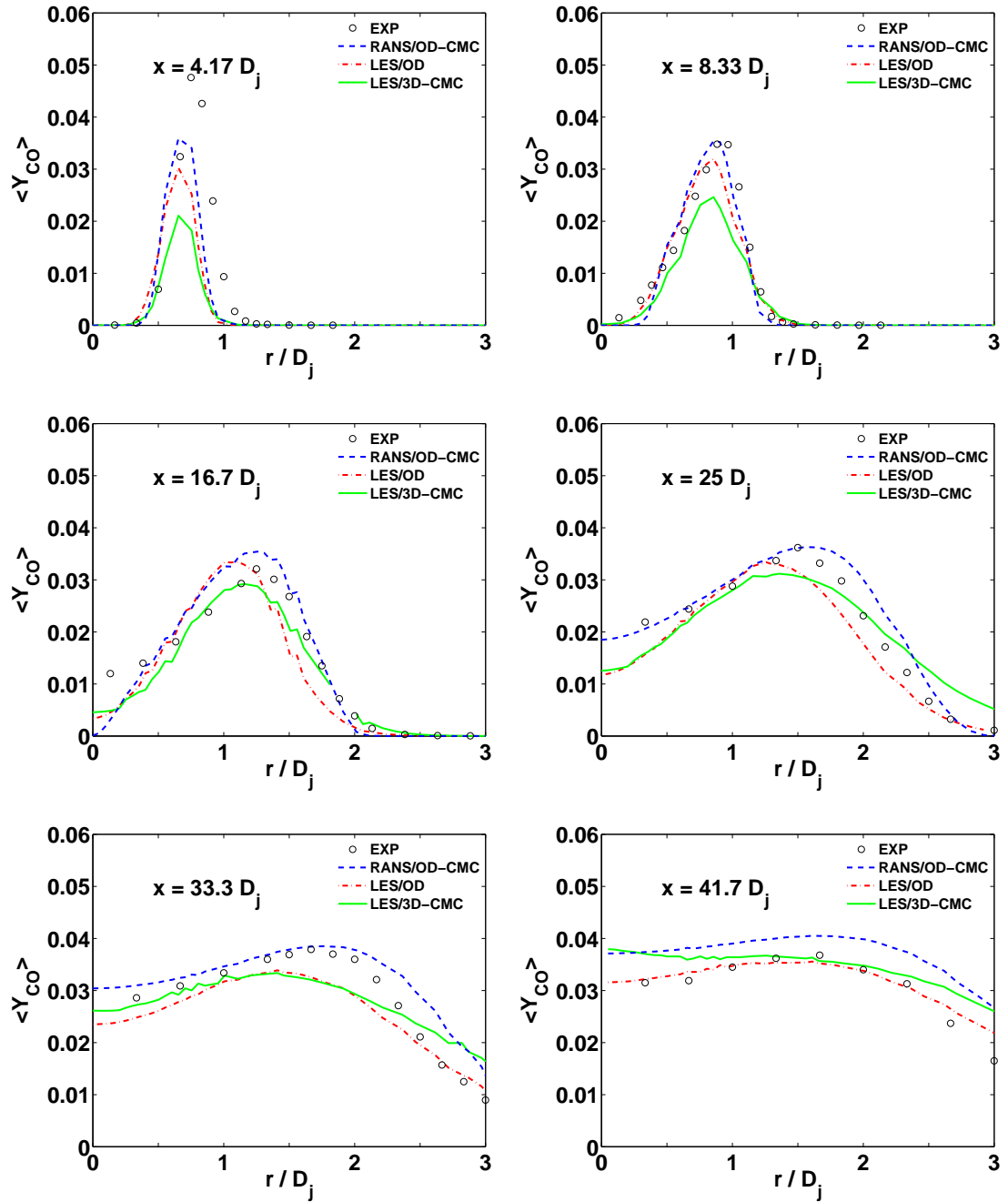
Figure 5.24: Radial profiles of the mean Y_{CO} at the indicated axial position. Experimental data from Ref. [27].
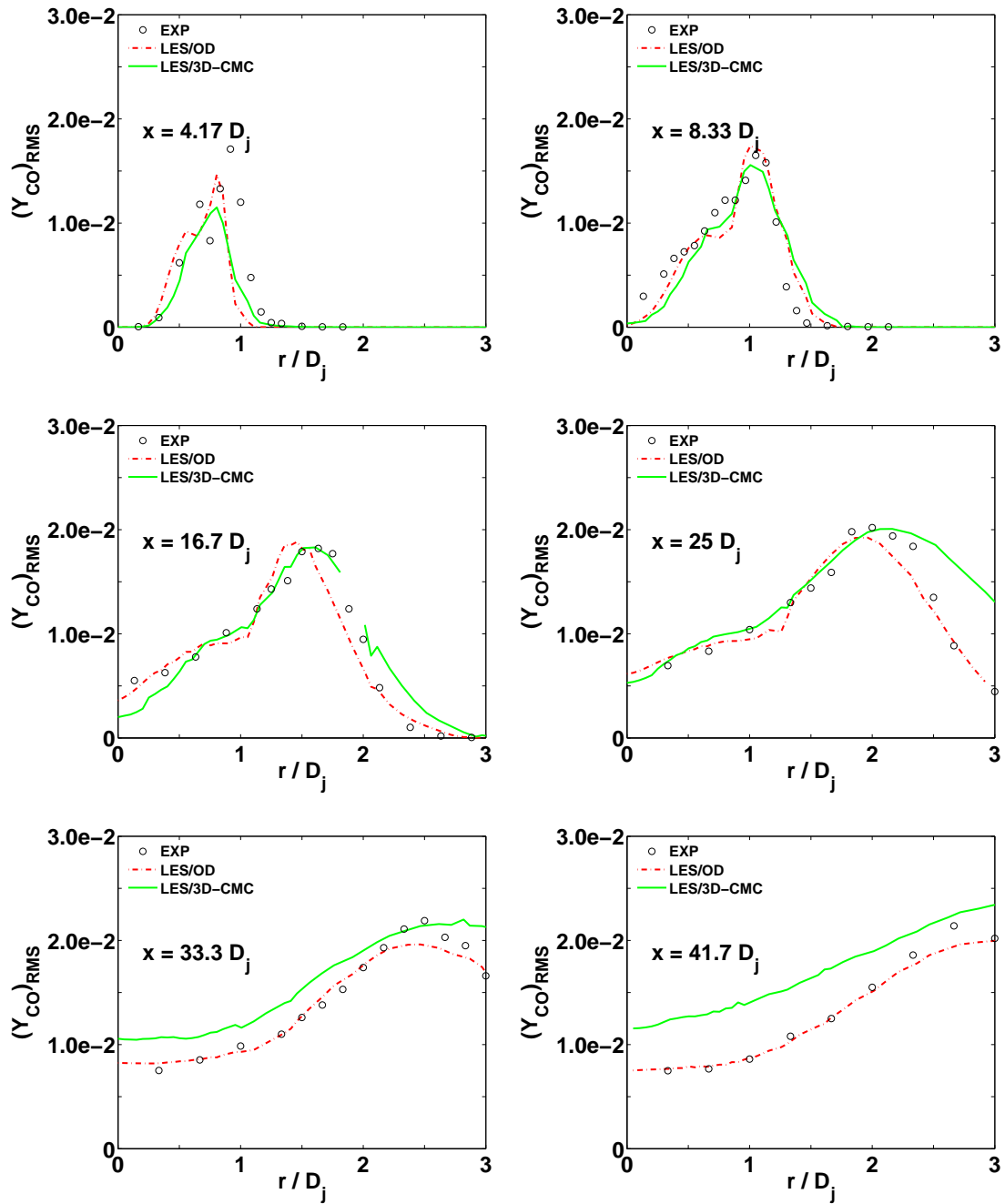
Figure 5.25: Radial profiles of the RMS of Y_{CO} at the indicated axial position. Experimental data from Ref. [27].
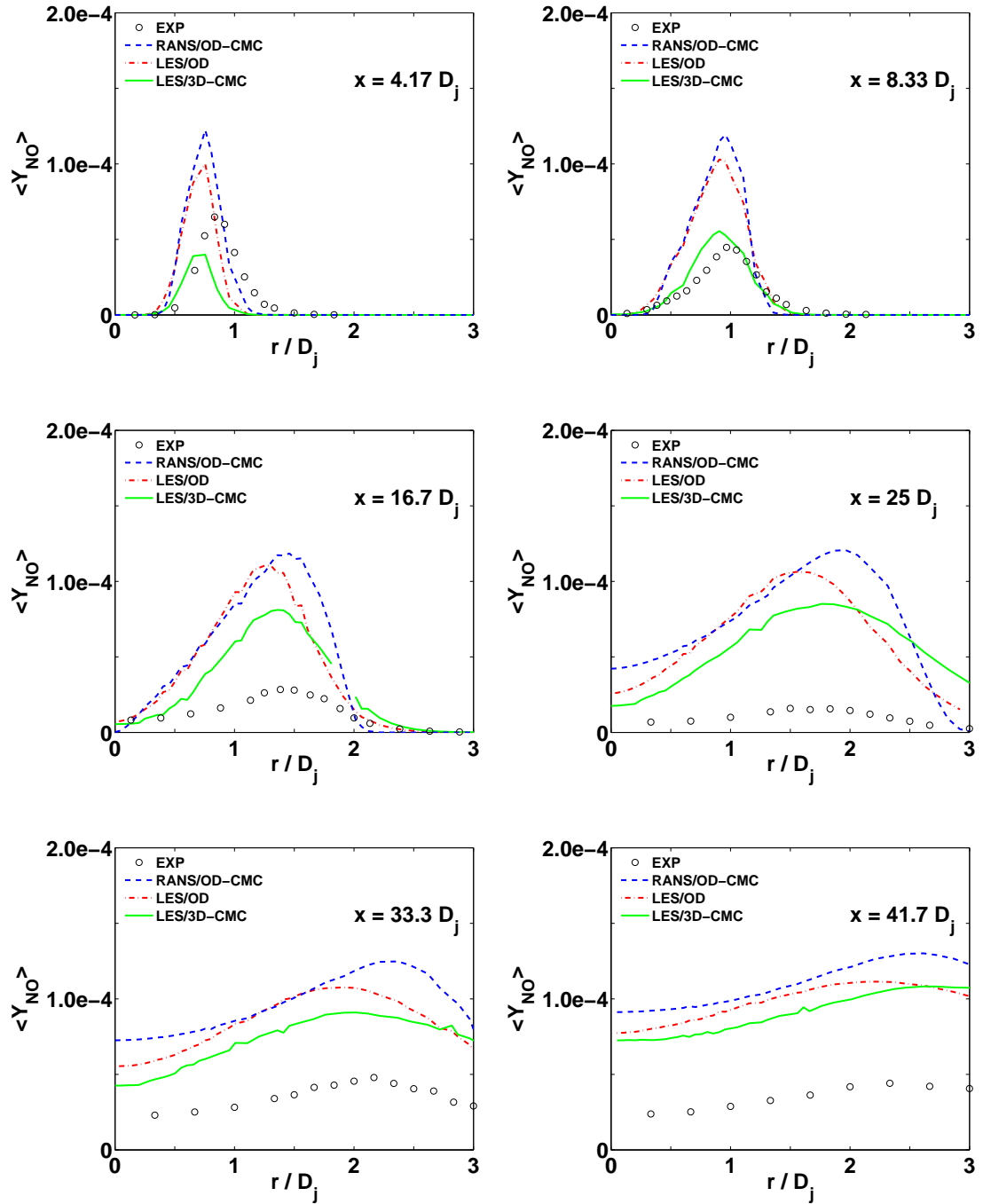
Figure 5.26: Radial profiles of the mean Y_{NO} at the indicated axial position. Experimental data from Ref. [27].
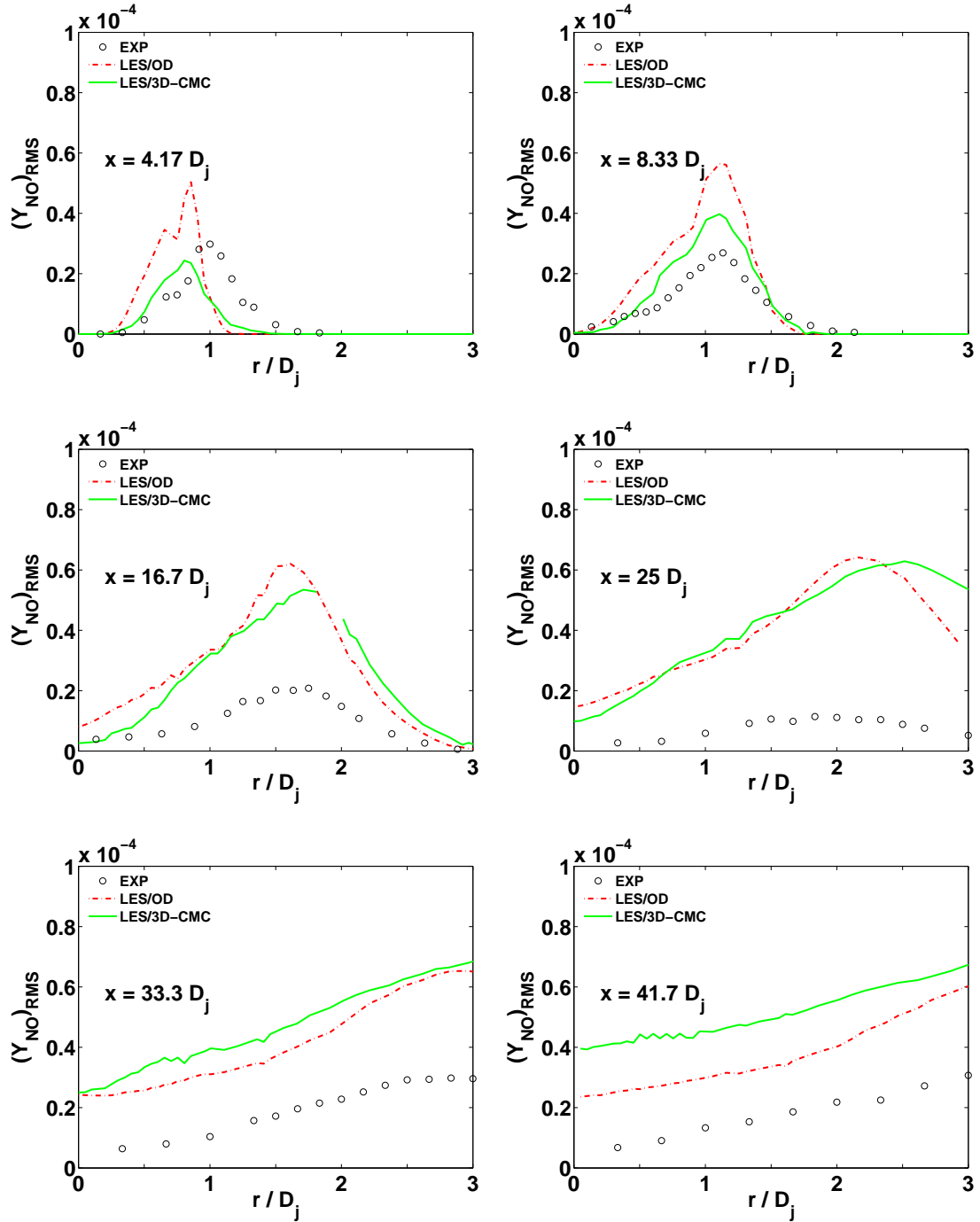
Figure 5.27: Radial profiles of the RMS of Y_{NO} at the indicated axial position. Experimental data from Ref. [27].

Chapter 6

Investigation of the aerodynamics of a non-premixed swirl flame using LES

6.1 Introduction

6.1.1 Motivation

The confined turbulent swirling non-premixed TECFLAM S09c flame has been investigated using Large Eddy Simulation and a pre-calculated mixture-fraction-based flamelet model in a preliminary step to simulate this flame. The analysis of this swirl flame is of great interest as it mimics the main features that are observed in industrial burners and offers an opportunity for a better understanding of their dynamics. The challenge of simulating this swirl flame comes from the very complex aerodynamics created by the imposed swirl. The swirl leads to the formation of a Central Recirculation Zone (CRZ) via the Vortex Breakdown (VB) mechanism [69]. One structure expected in a swirl flow and related to the VB process is the Precessing Vortex Core [112], described in Section 2.3.3 of Chapter 2. The PVC is expected to interact with the flame and hence induce heat release fluctuations. Reproducing accurately this large structure or any similar structure induced by the VB is required to predict accurately the flame dynamics and the pollutants emission.

6.1.2 Background works

The non-premixed TECFLAM configuration has been extensively studied experimentally and is a target of the international workshop on Turbulent Non-premixed Flames (TNF). Radial profiles of the mixing field, flow field and species concentrations are available [12; 13; 14; 51; 66]. Several numerical studies have been attempted to model this flame. In Ref. [74], a RANS formulation based on a Reynolds-stress turbulence model, a presumed $\beta-$PDF combustion model and assuming chemical equilibrium was performed. The general behaviour of the flow field could not be predicted accurately. A LES of the unconfined non-premixed TECFLAM [17] has also previously been performed using a flamelet model coupled to a β-subgrid PDF. The pattern of the recirculation zones were found to diverge considerably from the experimental data. This was related to the failure of the fuel jet to spread radially in the near burner regions, due to the inability of the simulation to reproduce negative axial velocity in the airstream at the burner exit. Therefore, the conclusion was that the injector has to be included in the computational domain, at least partially.

6.1.3 Objectives

In this study, LES is used to solve the flow and mixing fields and has been coupled with a prescribed first order CMC solution, as a preliminary attempt to model this complex non-premixed flame. This formulation is relatively fast compared to the LES coupled with the full CMC equations resolved in a 3D grid at each LES iteration. Statistical analysis such as spectral analysis, correlations, and Proper Orthogonal Decomposition can then be performed with a very good statistical convergence. As a result, a comprehensive analysis of swirl flow structures (PVC...) has been developed in this chapter, while the next chapter focuses on the combustion process of such a swirl flame (localized extinctions, lift-off, pollutants emissions) based on the full 3D-CMC equations. Therefore, the objectives of this chapter are: (i) to model the main features of the TECFLAM S09c swirl flame; (ii) to investigate in depth the combustor aerodynamics using various techniques, in particular the Proper Orthogonal Decomposition (POD), and to compare with an inert flow simulation; (iii) to provide an initial solution for a second type of

LES using three-dimensional CMC, in a future attempt to capture the extinction observed in this flame experimentally.

6.2 Method

6.2.1 Flow computed

Fig. 6.1 shows the flow studied. The TECFLAM S09c flame is composed of a fuel jet, with an average injection velocity at the burner exit of 21 m/s, surrounded by a swirling air jet. The fuel annulus has an inner diameter of 20 mm and an outer diameter of 26 mm. The air stream bulk velocity at the burner exit is 23 m/s. Its inner diameter is 30 mm and its outer diameter is 60 mm. Movable blocks inside the burner create the swirl in the air stream. The swirl number is calculated based on geometrical consideration and the value of $S = 0.9$ has been reported for this experiment. The air and fuel streams are separated by a rim of inner diameter 26 mm and outer diameter 30 mm. The length used for non-dimensionalisation in this study is the diameter of the bluff body: D=30 mm. The diameter of the simulated domain is equal to the diameter of the combustion chamber used in the experiments, which is 500 mm. The computational domain extends vertically from 50 mm below the burner exit to 350 mm above it, while the real total length of the combustion chamber is 1 m.

6.2.2 Mesh

The mesh is shown in Fig. 6.2. It reproduces part of the burner. Typically the numerical inlet has been located at 50 mm upstream of the burner exit. As stated in Section 6.1.2, it has been reported that the absence of the burner in the simulated domain leads to a wrong prediction of the recirculation shape. By including part of the air pipe in the computational domain, the flow can develop itself before entering the combustion chamber. In particular, flow features such as the PVC start developing inside the burner [83] and this study aims at reproducing it. The grid used for these computations is an O-grid mesh, very refined around the burner air and fuel exits, and with a smooth expansion

Table 6.1: Fuel composition used by the CMC code to model the TECFLAM natural gas

Constituents Formula	Mass fraction %
CH_4	96.8284
C_2H_6	0.9184
N_2	1.7144
CO_2	0.5388

downstream and radially so that a total of approximately 7.9M cells are used $(303 \times 162 \times 160)$.

6.2.3 Large Eddy Simulation and combustion modelling

A LES/0D-CMC formulation (see Section 3.2.3 of Chapter 3 for details of the numerical formulation) has been used to model the flame. The time-step used for all the simulations is 5.0×10^{-6} s and the simulations were carried out on 23 quad-core CPUs at 2.53 GHz with 24 GB of RAM available per CPU, producing 1.0 ms of simulated time in approximately 93 min. The reduced chemistry mechanism ARM2 derived from the detailed GRI-Mech 3.0 mechanism [106] has been used. This mechanism contains 19 species and 15 reactions. The fuel used in the experiments was natural gas. The ARM2 chemistry does not cover all the species in the experiment (such as Propane (C_3H_8) and Butane (C_4H_{10})). The missing species have been re-distributed into other species in order to conserve the total calorific value of the fuel calculated by means of the individual calorific values. One ends up with an approximation of its composition based on the species available, as reported in percentage by mass in Table 6.1. The natural gas approximation used by the CMC code gives a stoichiometric mixture fraction of $\xi_{st\ CMC} = 0.056$ while the natural gas in the experiment was reported to give $\xi_{st\ exp} = 0.055$ [51]. No-slip velocity conditions have been enforced on solid walls, while zero gradient boundary condition has been enforced at the outlet.

6.2.4 Boundary conditions

The mixture fraction is set to 1 in the fuel stream and 0 in the air stream. Both stream temperatures are set to the experimental value of 300 K. Imposing the right velocities at the boundaries is challenging as no experimental data is available inside the burner. As no swirl is imposed on the fuel stream annulus, the numerical Boundary Conditions (BCs) for the fuel stream are only located 7 mm upstream from the fuel exit and a top-hat profile with the same mean velocity as the experimental one is injected without any added fluctuations. The velocity BCs in the air annulus are much more complicated to choose as the numerical inlet is located deep inside the burner and as no experimental data of the velocity (in particular the tangential component) is available for that location. The only information provided is the value of the mean axial velocity at the burner exit and the geometrical swirl number at the swirl generator exit, located upstream the simulated part of the burner. In order to find the most appropriate BCs, an extensive parametric study has been conducted. Firstly the tangential velocity component at the numerical air inlet was chosen in order to reproduce the experimental swirl number $S = 0.9$. Then several simulations with different tangential velocities at the numerical air inlet were computed and their results were assessed against the experimental data 1 mm downstream from the burner exit. The best match was then selected and is reproduced in Fig. 6.3. The comprehensive flow analysis presented in the next section is based on this simulation.

6.3 Results and Discussion

6.3.1 Analysis of the steady flame

Prior to run any LES simulation, a series of 0D-CMC calculations (see Section 3.2.3 of Chapter 3) have been performed with the above fuel composition (Table 6.1). The aim of the 0D-CMC computations is to evaluate the quality of the reduced chemistry mechanism used by the CMC equations and to investigate the structure of the steady flame. Fig. 6.4(a) shows the maximum temperature of the flame for different values of N_0 for both the GRI3.0 and ARM2 mechanisms. The results from the 19 species reduced ARM2 mechanism and the 53 species

detailed GRI3.0 mechanism agree very well: the maximum temperature of the flame is $T_{max} = 2124$ K with ARM2 and $T_{max} = 2130$ K with GRI3.0, i.e. a difference of only 6 K; the extinction scalar dissipation rate is $N_{0ext} = 176$ 1/s for ARM2 and $N_{0ext} = 185$ 1/s for GRI3.0, i.e. a discrepancy of ~ 5 %. Figure 6.4(b) shows the burning distribution obtained with the prescribed $N_0 = 20$ 1/s.

6.3.2   Mean and instantaneous flow fields

Figures. 6.5 and 6.6 show some time-averaged statistics from the reacting case. The averaging has been done over 195 ms of simulated time. Figure 6.5(a) shows the time-averaged axial velocity contour. The black line represents the time-averaged zero-velocity isoline. The incoming air stream, the Central Recirculation Zones (CRZs), and the Outer Recirculation Zone (ORZ) of the combustion chamber are evident. We can notice the presence of two CRZs along the centre-line. Similar behaviours have been reported in Ref. [69]. The fuel jet is visible on the burner bluff body. The flow exiting from the fuel annulus quickly encounters the recirculated flow, which pushes back the rich mixture towards the air stream, leading to a quick and efficient mixing. The white line shows the stoichiometric mixture fraction isosurface and it is evident that the time-averaged stoichiometric mixture fraction extends into the air annulus, inside the burner, while only air has been injected in this pipe at the numerical inlet ($\xi = 0$). This leads to the conclusion that a certain amount of fuel is present at the top extremity of the air pipe. The time-averaged mixture fraction field in Fig. 6.5(b) confirms this observation. Looking now at the time-averaged temperature (Fig. 6.5(d)), we note that the flame contour is shaped of the narrow RCZs (visualized by the black lines). This results in a narrow flame with a very limited expansion along the combustion chamber. Figure 6.5(c) also reports the time-averaged density, while Figs. 6.6(a) and 6.6(b) represent respectively the time-averaged radial velocity and the time-averaged tangential velocity.

Figures 6.7 (a,c,e) and (b,d,f) represent respectively the flow around the burner from instantaneous snapshots of the axial velocity and out-of-plane vorticity at different instants. Figure 6.9 provides a zoom of Fig. 6.7 (e) around the burner. From this picture, it is clear that a recirculation occurs inside the burner

along the inner wall of the air annulus and that this recirculation is responsible for sucking some of the fuel injected at the top of the burner inside the air annulus (the white line represents again the stoichiometric mixture fraction).

The $z-$vorticity snapshots (Figs. 6.7 (b,d,f)) reveal that two main shear layers develop in the air swirling jet: one between the air flow and the CRZ and one between the air flow and the outer flow. Along the shear layers, the large difference of velocities between the air jet and the rest of the flow leads to the formation of Kelvin-Helmholtz instabilities, visualized by fragmented vorticity contours. Further downstream, these instabilities have fed the flow with further turbulence, leading to the strong convolution of the stoichiometric iso-surface (white line). The vorticity map shows that significant amount of vorticity is found in the shear layers, but also in a small region along the inner pipe immediately before the burner exit.

An animation of the reactive mixing field (Fig. 6.8) shows that a periodic increase and decrease of the mixture fraction occurs on the upper part of the air annulus, along the inner wall, from $\xi = 0$ to values as high as $\xi = 0.6 - 0.7$. The fuel stream exiting from the top of the burner bluff body is seen as being periodically sucked into the air annulus. The stoichiometric mixture fraction isosurface at this location is therefore pushed down deep inside the air pipe. The observation of an axial velocity contour animation (Figs. 6.7 (a,c,e)) leads to the conclusion that both the fuel and air streams close to the burner follow this oscillating motion. This phenomenon has to be related to the formation of recirculations along the inner wall of the air annulus, as observed in Fig. 6.9. An animation of the $Z-$vorticity (Figs. 6.7 (b,d,f)) shows that the point of separation of the inner shear layer oscillates along the inner wall, the separation of the air stream occurring up to 25 mm below the burner exit. The whole phenomenon can thus be understood as a cycle of separations and recirculations occuring along the inner wall of the air pipe. These separation-recirculation cycles are responsible for sucking some amount of the fuel injected at the top of the bluff body into the air annulus.

6.3.3   Mean radial profiles

The following time-averaged quantities of the reactive flow simulated by the LES/0D-CMC formulation have been computed over 195 ms. Prior to start the averaging, the flow had already been computed over 160 ms of simulated time in order to let it develop and obtain a stabilization of its velocity spectra. Figure 6.10 shows the time-averaged radial profiles of the axial velocity at a few axial positions. The closest available experimental data to the burner exit correspond to an axial position of $x = 0.033D$ ($x = 1$ mm). This graph and the time-averaged radial profiles of the tangential velocity at the same position (Fig. 6.11) shows that the numerical inlets for the air and fuel streams have been carefully applied in term of magnitude. The RMS of these quantities (Fig. 6.12 for the RMS of the axial velocity and Fig. 6.13 for the tangential ones) show that the flow is already turbulent 1 mm above the burner exit despite the absence of any numerical fluctuations (except white noise) in the velocity profile injected in the air annulus. However the RMS values remain overall underpredicted at this distance of the burner. Further downstream, the RMS data show that the flow has become very turbulent with velocity fluctuations reaching 60% of the injected axial velocity magnitude in some locations. The computed fluctuations are moving closer and closer to the experimental data as the downstream distances increase. These very high values of the RMS quantities found close to the burner exit are remarkable and will be explained later in this chapter. The axial velocity profile (Fig. 6.10) is found to be well predicted in the main jet at all axial positions, while there is an underprediction of the strength of the CRZ above $x = 0.667D$ by a factor of 2. This underprediction of the CRZ leads to a slight overprediction of the jet velocity for positions above $x = 2.33D$. The radial profiles of the tangential velocity (Fig. 6.11) are very well predicted by the LES for $x < 5.33D$ ($x = 160$ mm). The trends of the mixture fraction radial profiles (Fig. 6.14) are also well captured by the LES despite an overall slight underestimation of the mixing, leading to an overestimation of ξ in the main jet, while ξ is therefore lightly underestimated in the area between the jet and the outer walls. The radial profiles of ξ-RMS (Fig. 6.15) show an overall underestimation of the fluctuations, while once again the trends are well captured by the formulation. Overall the time-averaged ra-

dial profiles compare well with the experiments and the numerical dataset can therefore be used for further analysis.

6.3.4 Inert simulation

As stated in the Literature Review (Chapter 2), it has been reported that the combustion process tends to damp the Precessing Vortex Core present in an inert combustor flow, especially in non-premixed configurations, while some residual instabilities can still be detected. In order to understand further the separation-recirculation cycles inside the burner previously described, the inert flow of this TECFLAM non-premixed configuration has been simulated. There is no experimental data to compare our LES prediction. Nevertheless, the simulation is very important for the understanding of the complex aerodynamics of the burner and combustion chamber of swirl combustors, the associated hydrodynamic structures and how the combustion process modifies the fluid dynamics and the hydrodynamic structures in swirl flames.

Figure 6.16 shows the inert flow throughout the instantaneous axial velocity (a), pressure (b) and mixture fraction (c) fields. The fluid dynamics appears to be rather different from the reactive one. The CRZ has a much more complicated shape than in the reacting flow. It appears much weaker than in the reacting case, although it is found to extend much further in both radial and axial directions. As a result of the CRZ radial expansion increase, the air stream is found to open up much more than in the reacting case. The area of the CRZ with strong reverse flow ($u > 5$ m/s) is limited to the space located directly around the burner exit and, unlike CRZ of the reactive flow, does not reach the centre of the combustion chamber. The consequence is that the rich mixture zone of the flow remains confined around the burner exit at axial positions below $x = 70$ mm, while it can reach positions as far as 200 mm in the reactive flow. Along the centreline, a column of low pressure developing from inside the burner is clearly visible. This low-pressure column is not visible in the reacting case. If now we focus on the fluid dynamics inside the burner, we notice that the same kind of cycle of separations and recirculations occurs along the inner wall of the air pipe as reported in the reacting case. Once again, this results in a certain amount

of fuel being sucked at the top of the air pipe. This can be seen in Fig. 6.16 throughout the stoichiometric fraction isoline, which is also found to enter inside the air pipe.

6.3.5 Autocorrelation and spectra

To investigate further the temporal evolution of the flow, autocorrelations from both the inert and reactive flow simulations have been calculated at several positions in the domain (Figs. 6.17 and 6.18). At $x = 0.167D$ ($x = 5$ mm), both the autocorrelations from the inert (left side of the figures) and reactive LES (right side of the figures) confirm the presence of a periodic component close to the air annulus exit at two diametrically opposed locations corresponding to $r = 0.75D$. At the same axial position no oscillation is observed along the centreline ($r = 0D$) and at the burner edges ($r = 1.667D$). Further downstream some oscillations are still observed in the autocorrelations at $x = 0.833D$ ($x = 25$ mm) in both the inert and reactive flows. These oscillations are already largely damped at $x = 1.67D$ ($x = 50$ mm) and are no longer visible further downstream in the inert flow. However, the oscillations are found further downstream in the reactive flow before disappearing around $x = 3.33D$ ($x = 100$ mm). The oscillations in the reactive flow can thus be found at higher axial positions than in the inert flow. This observation will be explained later. By comparing the oscillations from the inert and reactive flows, we conclude that the period found for the inert flow is longer than its reactive counterpart, while the oscillations amplitude is much lower in the reacting case.

In Fig. 6.19(c), the spectra of the axial velocity fluctuations confirm the presence of oscillations in the inert flow as a clear frequency peak at 392.5 Hz can be identified at the air annulus exit ($x = 5$ mm, $r = 22.5$ mm). A small harmonic at 785 Hz is also visible. In Fig. 6.19(d), the spectra of the reactive flow axial velocity at the air annulus exit shows a fundamental at 640 Hz and several harmonics can also be observed (961 Hz and 1281 Hz) among other small frequency peaks. A sub-harmonic at 320 Hz is also present in the spectrum. The difference of fundamental frequencies between the inert flow and the reactive flow is expected as the recirculation of hot gases in the burner exit vicinity strongly

affects the fluid mechanics in this region. The inert and reactive fundamental frequencies are already observable deep inside the air pipe 25 mm upstream from the burner exit in Figs. 6.19(a) and 6.19(b) respectively. The sub-harmonic at 320 Hz is also present at this location in the reacting case. This leads to the conclusion that any structures associated with these frequencies develop themselves deep inside the burner. Figures 6.19(c) and 6.19(d) also show that the fundamental frequency amplitude is damped by a factor of 10 when combustion occurs. Some spectra in log-log format from both the inert and reacting cases have also been plotted in Fig. 6.20 for reference. From their observation, it is obvious that the turbulence has developed itself in the downstream part of the flow, despite the absence of fluctuations injected at the flow inlets ($x = -50$ mm for the air stream, $x = -7$ mm for the fuel stream).

6.3.6   Swirl-induced separation inside the burner

Iso-surfaces of low pressure from the inert simulation are reproduced in Fig. 6.21(a). The isosurface $P - P_0 = -450$ Pa has been plotted in blue and it shows two low-pressure columns located almost diametrically opposite. Animations show that these structures rotate around the bluff body at a period corresponding to the frequency peak observed in the inert spectra (392.5 Hz). As a result, they impose their dynamics to the flow inside and close to the burner and are responsible for the appearance of recirculations in the air annulus as well as the oscillation of the flow around the burner. The structures are hence expected to be responsible for the recirculation observed inside the burner as well as the flow oscillation observed around the burner exit. They are linked to the occurences of flow separation along the air annulus inner wall due to the centrifugal forces created by the swirl (as observed in the vorticity contour of the reactive flow plotted in Fig. 6.7). These structures must also generate the high level of turbulence detected as early as 1 mm above the air pipe exit as commented previously (Fig. 6.12) for the reacting case. The separation-recirculation cycle created by these structures is thought to be similar to the flashback phenomenon observed experimentally in the premixed configuration of the TECFLAM burner [44]. Along the centreline of the flow, the low-pressure column observed in Fig.

6.21(b) (isosurface $P - P_0 = -250$ Pa in blue) represents the vortex core induced by the swirl in the inert flow.

As the inert and reactive flows experience similar behaviour in and around the burner, it is expected that similar structures are present in the reactive flow and that they are also responsible for the occurence of the separation inside the air pipe. However, in practice, such structures have not been observed with conventional visualization methods ($Q-$criterion applied to the instantaneous velocity components) in the reactive flow. This is consistent with our previous observation stating that the fundamental frequency amplitude is damped by a factor of 10 in the reactive flow. Previous studies have also reported that the combustion tends to remove a large part of the hydrodynamic structures (such as the PVC), especially in non-premixed configuration, while some remaining instabilities may still be present in the reactive flow [112]. In order to try to visualize these structures in the reactive flow and perform further analysis, Proper Orthogonal Decomposition (POD) of both the inert and reactive flows have been performed.

6.3.7 Proper Orthogonal Decomposition

POD has been used to visualize, identify and then analyze the structures associated with the different frequencies observed in the flow spectra. The method has been applied to both the inert and reactive fields, with the aim of understanding better how the combustion process affects the flow dynamics. We start with a POD analysis of 2D LES planar cuts before applying the method to 3D LES datasets. Details of how the POD has been performed are given in Section 3.3 of Chapter 3. For both the 2D and 3D POD analysis more than 400 snapshots sampled at 4000 Hz have been used from both the inert and reactive flow fields. As a result, the data used for each POD span a time interval of more than 100 ms.

6.3.7.1 2D POD

POD has been applied simultaneously to the velocity, pressure and mixture fraction fields of the inert LES datasets for different 2D planar cuts. However, the modes found at different axial positions close to the burner are similar and only

the results from the plane at $x = 5$ mm are reported here. For the reacting case, the pressure variable has been replaced by the temperature. The energy distributions of the modes from both the inert and reacting cases are reproduced in the first row of Fig. 6.22. The second row represents the time coefficients associated with the two first modes (left side for the inert case, right side for the reacting case). The 15 first modes are reproduced in Figs. 6.23, 6.24, 6.25 and 6.26 for the inert flow, and in Figs. 6.27, 6.28, 6.29 and 6.30 for the reactive flow. In each figure, the first row represents the axial velocity fluctuations field, the second row the projected velocity fluctuations vector map, the third row the pressure fluctuations field (respectively the temperature fluctuations field for the reacting case) and the forth row the mixture fraction fluctuations field. The red colour refers to positive fluctuations of the quantity, the blue colour refers to negative fluctuations, and the green colour refers to a no-fluctuation area. In the last row, the Fourier analysis of the temporal coefficient associated with the mode has been plotted. Each column of each figure corresponds to a single mode. The temporal coefficients are obtained by projection of the fluctuating velocity (a snapshot) on the POD basis. Using the notation of Section 3.3 with j the discrete time counter, one obtains:

$$a_j = \Psi^T U_j, j = 1...N \tag{6.1}$$

Inert case   We focus here on Figs. 6.23, 6.24, 6.25 and 6.26 that correspond to the 2D POD analysis of the inert flow. Modes 1 and 2 contain almost the same amount of energy, respectively 17.9 % and 17.8 % (Fig. 6.22(a)) and represent clearly the most energetic structures of the flow accounting for 35.7 % of the total fluctuation energy. Two structures corresponding to negative fluctuations of the axial velocity (in dark blue in the figure) are visible, surrounded by two structures of positive velocity fluctuations (in red) due to mass conservation. The same kind of structures are visible using the pressure field. The vector maps reveal that each of these structures experiences a rotating motion around themselves, leading to the conclusion that there are vortices. Each two diametrically opposed vortices rotate in the same direction around themselves, which is opposite to the direction of the rotation around themselves of the two other diametrically opposed vortices.

6. Investigation of the aerodynamics of a non-premixed swirl flame

The temporal modes $a_1(t)$ and $a_2(t)$ associated with the spatial modes 1 and 2 are plotted in Fig. 6.22(c). Both feature the same periodic, sinus-like variations at a frequency of $f_{a_1,a_2} = 397.1$ Hz (see spectra in Fig 6.23 (q)). The phase angle between the two modes is found to be $\phi_{a_2-a_1} = \frac{\pi}{2}$. As a result, when the contribution of mode 1 is at its maximum, the contribution of mode 2 reaches zero. These observations show that mode 1 and mode 2 form a pair of mode, which is associated with the rotation of 4 vortices around the inner wall of the air pipe. The structures associated with the axial velocity and pressure fluctuations are induced by the rotation of the low-pressure columns observed in Fig. 6.21(a). Modes 1 and 2 also exhibit structures throughout the mixture fraction fluctuations field. Their interpretation, as well as further analysis of these modes, will be given in Section 6.3.7.2 with the POD analysis of the 3D LES datasets.

Mode 3 contains 5.45 % of the fluctuating energy. No clear structure is visible but this mode may account for an axial displacement of the CRZ.

Modes 4 and 5 are very interesting. They both contain roughly the same amout of energy (4.01 % and 4.00 % respectively) and represent also a pair of modes. Their spectra are identical and show a clear peak at 794.2 Hz, which is the exact first harmonic of the frequency peak found in modes 1 and 2. This leads to the interpretation that the pair of modes 4 and 5 actually represents a harmonic of the pair of modes 1 and 2. The number of vortices in modes 4 and 5 has doubled in the upper part of the figure, compared to modes 1 and 2, while no clear vortices are visible in the lower part of the figure.

Mode 6 shows two large counter-rotating vortices with a frequency peak at 222.8 Hz and another smaller peak at 377.7 Hz. It contains 3.62 % of the fluctuating energy.

There is no clear interpretation for mode 7. Modes 8 and 9 are very similar to modes 4 and 5. They contain respectively 2.48 % and 2.45 % of the total energy. Their spectra also show a frequency peak at 794.2 Hz and they represent the same structures as in modes 4 and 5, with the exception that this time the vortices are located on the lower part of the figure. Modes 8 and 9 can then also be interpreted as accounting for a part of the first harmonic of modes 1 and 2.

Mode 10 is similar to mode 6. It represents two large counter-rotating vortices with a frequency peak at 213.1 Hz and another smaller peak at 106.5 Hz. Mode

11 is also similar to mode 6 and mode 10, with a clear frequency peak at 232.4 Hz. This leads to the interpretation that modes 6, 10 and 11 are modes that have not statistically converged and that roughly account for the rotation of two large vertical vortices in the combustion chamber at a frequency around $215 - 230$ Hz.

Modes 12 and 13 do not show any clear features. However modes 14 and 15 form a clear pair of modes accounting for the rotation of around 10 vortices around the burner. They contain respectively 1.19 % and 1.15 % of the total energy. They clearly show two peaks at 1007 Hz and 1191 Hz. As a result, this pair of modes must account for some non-linear interaction between a second harmonic characterizing the rotation of the four vortices around the burner, represented by modes 1 and 2 ($1191 = 3 \times 397.1$ Hz), and another frequency characterizing another phenomenon in the flow.

In conclusion, the 2D POD analysis of the inert flow from a plane located at $x = 5$ mm above the burner exit shows that 8 modes among the 15 modes reproduced here account (at least partially) for the dynamics of some rotating vortices at the burner exit. They corresponds to 50.98 % of the total fluctuating energy at this distance from the burner. 35.7 % of the energy is contained in the two fundamental modes (modes 1 and 2), while the 15.28 % of remaining energy are spread among the two first harmonics of the frequency associated with the vortices rotation inside the burner.

Reactive case We focus now on Figs. 6.27, 6.28, 6.29 and 6.30, corresponding to the 2D POD analysis of the reactive flow. The POD analysis from the reacting LES gives results that are consistent with its inert counterpart, although the energy distribution is rather different (see Fig. 6.22(b)). The energy distribution has a stairs-like shape, and several modes appear to behave like pairs of modes (as several pairs of consecutive modes seem to contains similar amount of energy). The energy decrease is also much slower than in the inert case, where the first pair of modes (modes 1 and 2) clearly contained much of the flow fluctuating energy.

As in the inert case, modes 1 and 2 contain almost the same amount of energy, although they appear here to be much weaker with (only) 6.68 % and 6.63 % respectively of the total fluctuating energy (Fig. 6.22(b)). They represent

the most energetic structures of the flow and account for 13.3 % of the total fluctuating energy. The structures corresponding to these modes are similar to their inert counterpart: they consist of four counter-rotating vortices (two by two) that rotate also as a whole around the burner. The pressure and velocity fields reveal that the combustion process has rather transformed the shape of the vortices, which now appear to be much more elongated. The frequency associated with the temporal coefficients has also been modified by the combustion process. The vortices are now rotating at 668.3 Hz (see Fig. 6.27 (q)) around the inner wall of the air annulus. The temporal modes $a_1(t)$ and $a_2(t)$ associated with the spatial modes 1 and 2 are plotted in Fig. 6.22(d). As in the inert case, both feature the same periodic, sinus-like variations.

Modes 3 and 4 are also a pair of modes, featuring six vortices (see for example the pressure field) rotating around the burner. They account for 5.96 % and 5.90 % respectively of the total energy (11.86 % overall). Their spectra show two peaks, the strongest at 926 Hz and a smaller one at 964.2 Hz.

Mode 5 seems to be associated with a coupling between the fluctuation of the pressure and mixture fraction fields in the center of the flow. Its corresponding spectrum shows a peak at 28.64 Hz and a small one at 343.7 Hz.

Modes 6 and 7 are again a pair of modes that accounts for the rotation of two thin, elongated vortices around the burner exit. Their spectra show a very clear peak at 343.7 Hz.

Modes 8 and 9 are a pair of modes representing 8 vortices rotating inside the burner at a frequency of 1270 Hz, while modes 10 and 11 are a pair of modes representing 10 vortices rotating inside the burner at a frequency of 1632 Hz. The other modes do not allow a very clear interpretation and are not commented here.

In conclusion, the 2D POD analysis of the reactive flow from a plane located at $x = 5$ mm above the burner exit shows that at least 10 modes among the 15 modes reproduced here account for the dynamics of the rotating vortices at the burner exit. They corresponds to 41.19 % of the total fluctuating energy at this distance from the burner.

6.3.7.2 3D POD

3D POD analysis has been performed for both the inert and reactive flows. This study, coupled with the autocorrelations, spectral analysis and 2D POD analysis allows to understand further the dynamics of the vortices developing inside the burner and how the combustion process affects this dynamics.

Inert case Fig. 6.31(a) shows that the first three 3D POD modes of the inert flow contain much more energy than the rest of the modes and account for 28 % of the total fluctuation energy. Modes 1 and 2 contain 9.8 % each i.e. 19.6 % overall of the total fluctuating energy. The first three modes of the velocity and mixture fraction from the inert simulation are represented in Fig. 6.32 and Fig. 6.33.

Figures 6.32 (a, b, c) and (d, e, f) show respectively mode 1 and mode 2. Both modes consist of two pairs of vortices as confirmed by the $Q-$criterion visualisation in Figs. 6.32 (b, e). The $Q-$criterion states that a vortical structure is identified by positive values of $Q = (\omega^2 - 2\widetilde{S}_{ij}\widetilde{S}_{ij})/4$, with the vorticity magnitude and the strain rate calculated from the gradients of the velocity fluctuations associated with the POD mode. These vortices develop along the inner wall of the air annulus before expanding inside the combustion chamber at the burner exit. Figs. 6.32 (a, d) show that each pair of vortices is composed of two diametrically opposed vortices and that each pair is counter-rotating around their own axis. In addition, one pair is associated with an axial velocity increase and the other one with a decrease. Modes 1 and 2 are therefore similar. They are only shifted by a rotation approximately equal to $\pi/8$ around the x-axis. In fact, the vortices roots in mode 2 are located at positions that correspond to the space left free of vortices in mode 1, i.e. the space in the plane of the air pipe exit located between each vortex of mode 1. This is due to the spacial orthogonality of the modes resulting from the Proper Orthogonal Decomposition. Mode 1 and mode 2 form therefore a pair of modes that characterizes the rotation of these four vortex cores as a whole around the inner wall of the burner air pipe. These structures are thought to be similar to a Precessing Vortex Core (PVC) [112]. In the presence of the bluff body of the TECFLAM configuration, the precession is

transformed into a more rotation-like motion of a double helical vortex core.

Fourier analysis (Fig. 6.34(a)) of the temporal coefficients of modes 1 and 2 shows a clear peak at 397.1 Hz ($S_t = fD/U_{bulk} = 0.518$) while their phase angle is found to be $a_2a_1 = \pi/2$ (not shown here). By comparing these results with the ones from the 2D POD analysis, it is clear that modes 1 and modes 2 computed from the 2D and 3D POD analysis of the inert flow are identical. The frequency reported in Fig. 6.19(c) from the spectral analysis of the axial velocity at the burner exit is likely to be associated with the rotation of these vortices. They impose their dynamics to the flow inside the inlet pipe and in the burner near-field and are responsible for the oscillating behaviour of the flow there. These Rotating Vortex Cores (RVC) are created by the flow separations occuring along the inner wall of the air pipe. These separations are themselves due to the centrifugal forces created by the swirl, as described previously in Section 6.3.6. These RVC inside the burner are responsible for the presence of recirculations in the air annulus. On top of that, these structures contribute to the high level of turbulence observed in the radial profiles 1 mm above the air pipe exit (Fig. 6.12). The separation-recirculation cycle coupled to these Rotating Vortex Cores is thought to be similar to the flashback phenomenon observed experimentally in the premixed configuration of the TECFLAM [44].

As described in Section 6.3.6, the presence of the rotating recirculations inside the burner results in some of the fuel injected at the top of the bluff body being sucked into the air pipe. This phenomenon has been captured by the POD and is visible in Figs. 6.32 (c, f) through the plotting of isosurfaces of negative and positive mixture fraction fluctuations. Here modes 1 and 2 are represented by two pairs of 2 diametrically opposed structures along the inner walls, each pair of structures representing respectively a mixture fraction increase or decrease in the air annulus. Each of these structures is located between two Rotating Vortex Cores. In addition, modes 1 and 2 are characterized by small pockets of high mixture fraction fluctuations at radial positions corresponding to the fuel injection inlet. These pockets are diametrically aligned with the larger structures and represent mixture fraction fluctuations that are opposite to the fluctuations of the larger structures in the air pipe. Therefore modes 1 and 2 analyzed through the fluctuations of the mixture fraction represent the periodic increase and decrease

of the mixture fraction inside the air pipe induced by the Rotating Vortex Cores. The suction of the fuel towards the air pipe results in a decrease of the mixture fraction at a location just above the fuel annulus exit and next to the vortex-induced recirculation. The spacial shift between the vortical structures of mode 1 and mode 2 (Figs. 6.32 (a, b) and (d, e) respectively) and the mixing structures (Figs. 6.32 (c) and (f) respectively) is due to the time-delay occuring between the passage of a vortex and the displacement of the fuel mass resulting from it.

The interaction between the rotating vortices in the burner and the near-burner mixing field is also represented in Figs. 6.35. In this set of figures, the reconstruction at different instants of the inert flow based on modes 1 and 2 is visualized through the $Q-$criterion (blue color). The red surfaces represent the area where the mixture fraction has a value above 0.35. From this montage, it is evident that the pair of vortices rotates around the burner. An area of fuel-rich mixture is found to follow each vortex, as the fuel is sucked inside the air annulus following the passage of a vortex core and its associated recirculation zone.

Mode 3 accounts for 8.46 % of the total energy. Fig. 6.33 represents the $Q-$criterion applied to mode 3 velocity fluctuations. Its corresponding 2D vector map at $x = 100$ mm has also been plotted. Mode 3 is characterized by two long column-like counter-rotating vortices located parallel to the centreline of the combustion chamber. The pressure isosurface of the instantaneous flow field (Fig. 6.21(b)) shows that one of these vortices (on the left in Fig. 6.33) creates a low-pressure column inside the flow and is associated with the CRZ created by the Vortex Breakdown. The second vortex is found to be much weaker. There is no frequency peak from the spectral analysis of the temporal coefficient $a_3(t)$ in Fig. 6.34(a). In fact, $a_3(t) = 0$ at anytime and the peak observed at 9.685 Hz is an artefact corresponding to the time interval on which the inert 3D POD was computed: $Dt_I = 0.10325$ ms). Modes 4 to 6 are more difficult to interpret, as they do not contain a single type of structure or a single frequency peak and are therefore not reported here.

Reactive case   Analysis of Fig. 6.31(b) shows that the distribution of the energy for the reacting case is rather different from the inert case. Mode 1 accounts for 8.12 % of the fluctuating energy and is by far the most energetic mode. It

is represented in Fig. 6.36(a) by one negative and one positive isosurface of the axial velocity fluctuations. It does not belong to a pair of modes and, unlike most of the other modes, does not represent a vortex. It rather accounts for the axial displacement of the CRZ and hence for a longitudinal motion of the flame. Fourier analysis of its associated temporal coefficient in Fig. 6.34(b) shows two small peaks at 28.64 Hz and 57.28 Hz, the sharpest peak at 9.547 Hz corresponding again to the time interval on which the reactive 3D POD has been computed: $Dt_R = 0.10475$ ms.

Reactive modes 2 and 3 respectively account for 4.48 % and 4.32 % of the energy i.e. 8.8 % overall (Fig. 6.31(b)). They are represented in Fig. 6.37. They form again a pair of modes and are similar to the 3D POD modes 1 and 2 from the inert flow, except that they contain only two counter-rotating vortices (against four vortices counter-rotating two by two for modes 1 and 2 of the inert flow). Their interpretation is identical to the ones previously made for the inert case regarding both the $Q-$criterion (Figs. 6.32 (b, e)) and the mixture fraction isosurfaces (Figs. 6.32 (c, f)) representations. Figs. 6.37 (a, d) represent respectively the $Q-$criterion applied to modes 2 and 3 and coloured by the respective axial velocity fluctuations of each mode. Similarly, Figs. 6.37 (b, e) represent respectively the $Q-$criterion applied to modes 2 and 3 and coloured by the respective temperature fluctuations of each mode. These figures show that the temperature tends to decrease inside the two vortices associated with a decrease of the axial velocity and vice versa. The spectra of the temporal modes associated with the spatial modes 2 and 3 (Fig. 6.34(b)) show a clear peak at 343.7 Hz ($S_t = fD/U_{bulk} = 0.448$), associated with the rotation of the vortices around the burner. Based on the shape of the vortices associated with the 3D POD modes 2 and 3 of the reactive flow and their spectral analysis, we conclude that their 2D counterparts correspond to the pair of modes 6 and 7 of the 2D POD analysis.

Mode 4 (Fig. 6.36(b)) accounts for an axial displacement as mode 1. Modes 5 and 6 (Figs. 6.38) form again a pair of modes: they are similar to each other and contribute to 5.84 % (2.94 %+2.90 %) of the energy (Fig. 6.31(b)). They represent four counter-rotating vortices. Fourier analysis (Fig. 6.34(b)) shows several peaks present in both modes at 572.8 Hz, 620.5 Hz, 668.3 Hz and 696.9 Hz,

i.e. around the double frequency of the modes 2 and 3 ($S_t = 2fD/U_{bulk} = 0.896$). This leads to the conclusion that the pair of modes 5 and 6 may be understood as a harmonic of the pair of modes 2 and 3. Therefore the effect of the Rotating Vortex Core in the reacting case would be represented by (at least) four modes (modes 2, 3, 5 & 6), which account overall for 14.64 % of the total fluctuation energy. Following that interpretation, modes 2, 3, 5 & 6 would describe the dynamics (fundamental and first harmonic) of a single helical vortex core.

Because the spectra of modes 5 and 6 do not show a perfect harmonic of the frequency associated with modes 2 and 3, another interpretation of these modes could be that modes 2 and 3 account for a single helical vortex core that rotates at 343.7 Hz, while modes 5 and 6 could account for a different double helical vortex core similar to the one captured by modes 1 and 2 of the inert flow (Fig. 6.32). The fact that the number of vortices doubles from modes 2-3 to modes 5-6 could explain why the spectra of modes 5-6 roughly double compared to modes 2-3, leading to the (possibly wrong) interpretation that modes 5-6 are a harmonic of modes 2-3.

6.3.7.3   Inert versus reactive rotating vortices

Figure 6.39(a) represents the $Q-$criterion from a snapshot of the inert flow reconstructed using its 6 first POD modes and coloured by the reconstructed pressure. Figure 6.39(b) shows a similar reconstruction for the reacting case but the isosurface has been coloured by the temperature. A first observation when comparing the two figures is that the strong vortex observed inside the CRZ of the inert flow (corresponding to the 3D POD mode 3 of the inert flow) is no longer present in the reacting case. This is consistent with previous studies that have also reported that the combustion tends to remove some flow structures, such as the PVC, especially in non-premixed configuration [112]. A second observation is that the rolling vortices developed in the burner air annulus extend much further in the reacting case than in the inert one. Figures 6.37, 6.38 & 6.39(b) show that the vortex heads reach locations as far as 160 mm above the burner exit when the flow is burning, compared to an axial expansion limited to a range of 30-40mm for the inert case (Figs. 6.32 & 6.39(a)). This observation explains why oscillations

are found in the autocorrelations further downstream in the reacting case than in the inert case, as commented in Section 6.3.5.

6.4   Summary of main findings

LES with a pre-calculated flamelet model has been applied to simulate a non-premixed swirl flame and its inert flow. The formulation is found to reproduce the experimentally-observed vortex breakdown and the results agree well with available experimental data for velocity and mixture fraction. Autocorrelation and spectral analysis reveal the presence of a periodic component inside the air inlet and around the central bluff body, for both the inert and reactive flows, while the fundamental frequency of this periodic motion increases by a factor of 1.6 in the reacting case. In order to investigate further the dynamics of the flow, Proper Orthogonal Decomposition has been applied. The method shows that large longitudinal vortices are formed along the air inlet inner wall, whose axes rotate around the burner. These vortices become highly curved inside the combustion chamber. They impose their dynamics to the flow in the combustion chamber and create a cycle of separations and recirculations inside the air annulus, which is thought to be similar to the flashback phenomenon observed in some premixed swirl flames. The POD analysis reveals that the dynamics of these Rotating Vortex Cores (RVC) is mainly represented by one pair of POD modes in the inert case. The combustion process is found to trigger several other pairs of modes, resulting in a more complex dynamics for the flow.
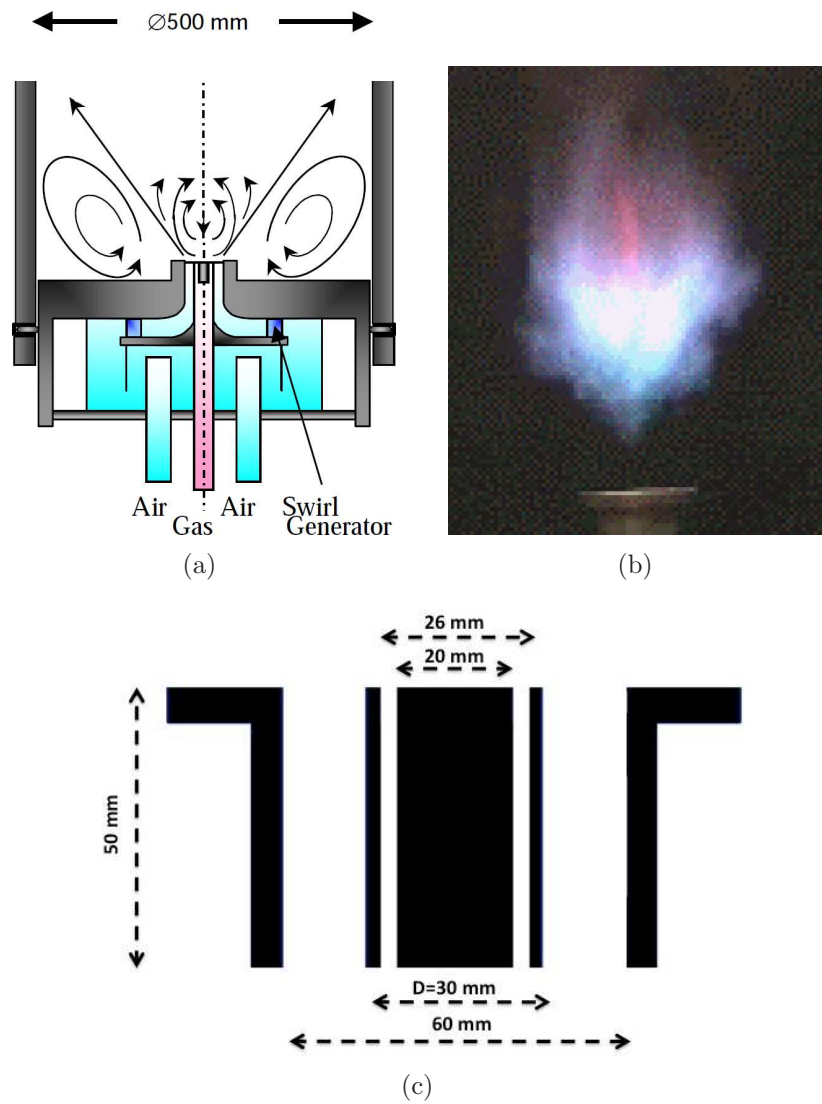
Figure 6.1: (a) Sketch of the TECFLAM burner. (b) Picture of the swirl flame and its burner. (c) Dimensions of the TECFLAM burner. From Ref. [51].
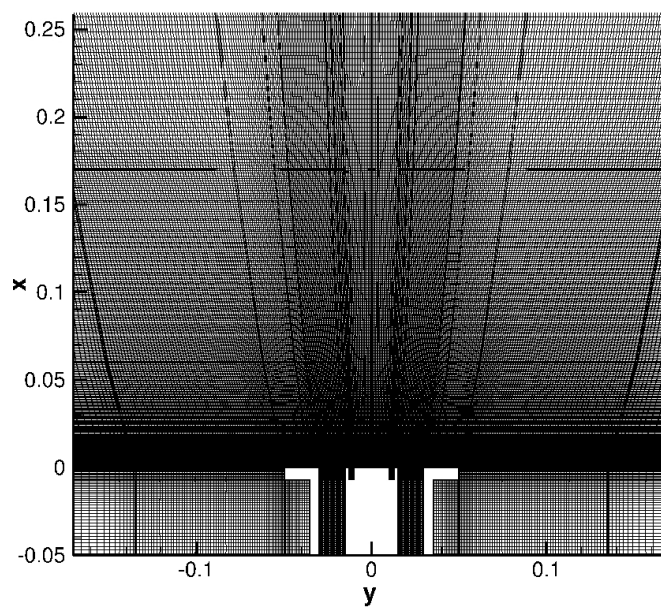
Figure 6.2: Mesh used for the LES computation of the TECFLAM.
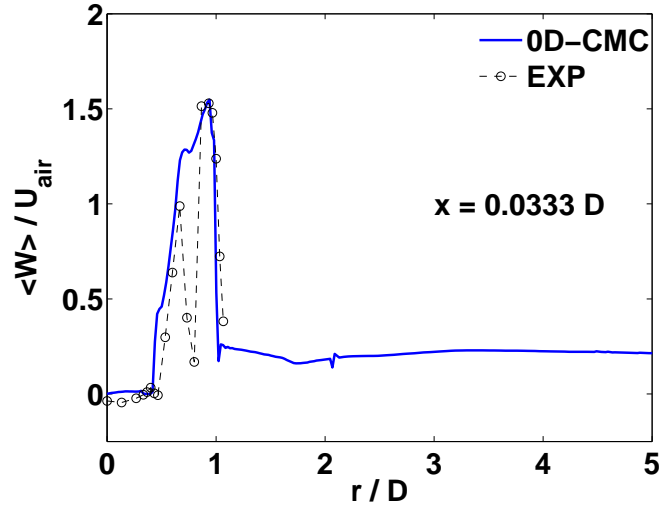
Figure 6.3: Radial profile of the mean tangential velocity 1 mm above the burner exit. Experimental data from Ref. [51].
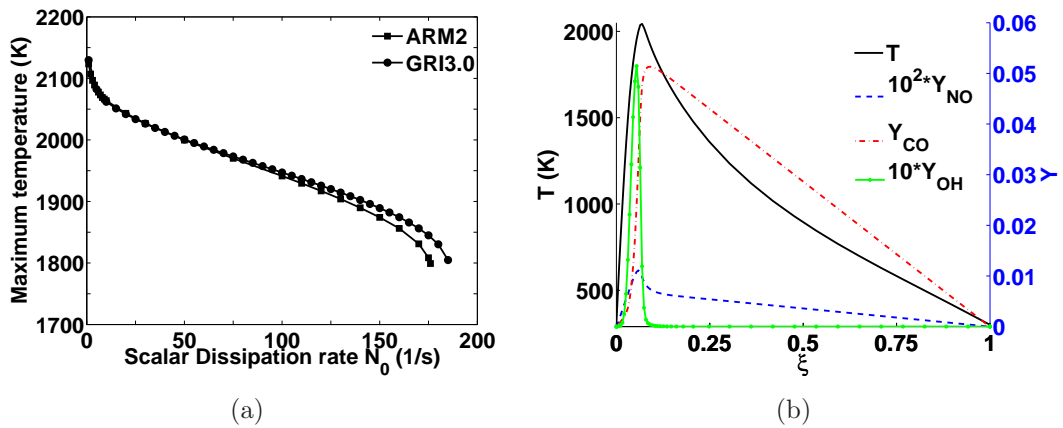
Figure 6.4: (a) T_{max} of the steady flame against the scalar dissipation rate N_0. (b) Distributions of some reactive scalars of the steady flame obtained for $N_0 = 20$ 1/s with the ARM2 reduced chemistry mechanism.

(a) Mean axial velocity

(b) Mean mixture fraction

(c) Mean density

(d) Mean temperature
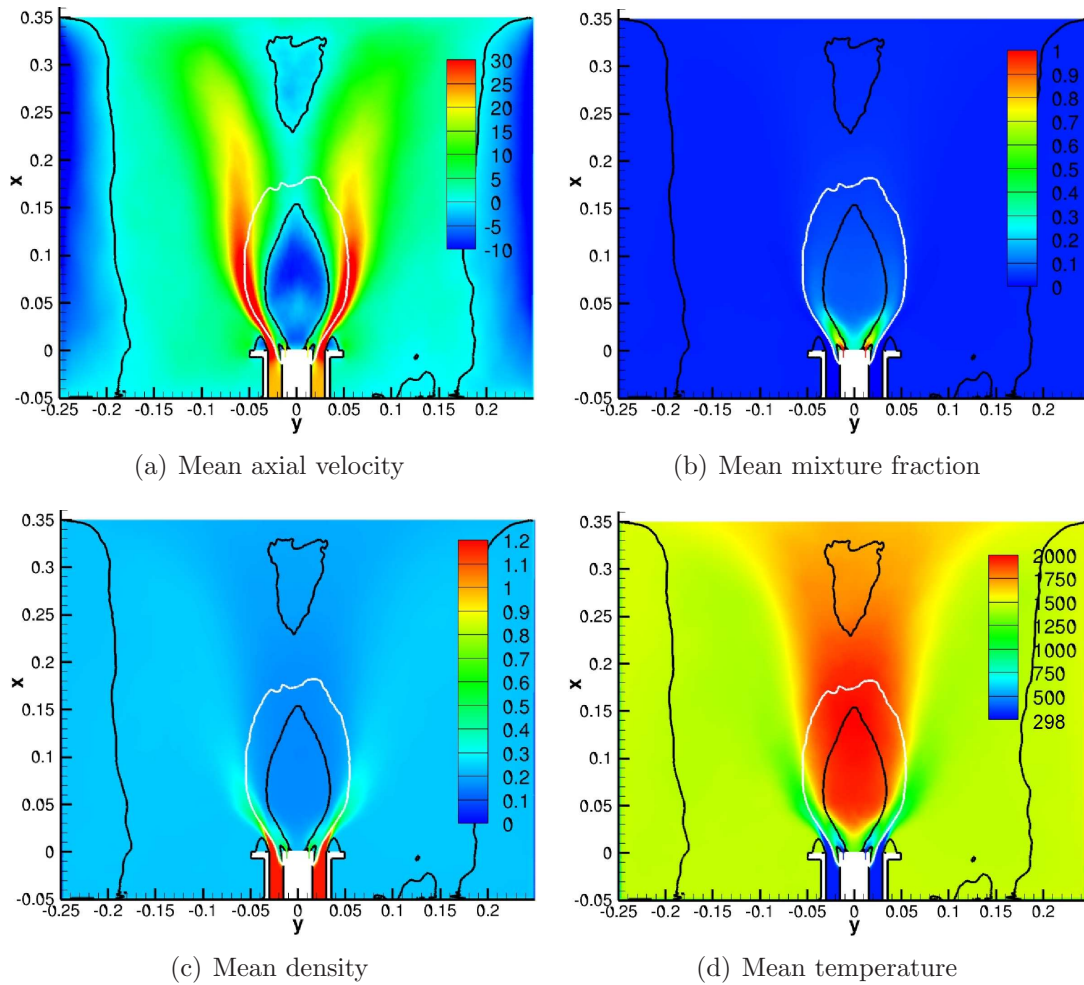
Figure 6.5: Distributions of time-averaged quantities in the reacting flow. White line: stoichiometric isoline; black line: zero-axial velocity isoline. Axes in m.
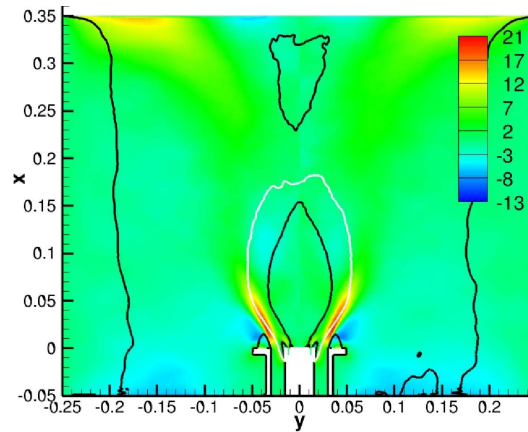
(a) Mean radial velocity
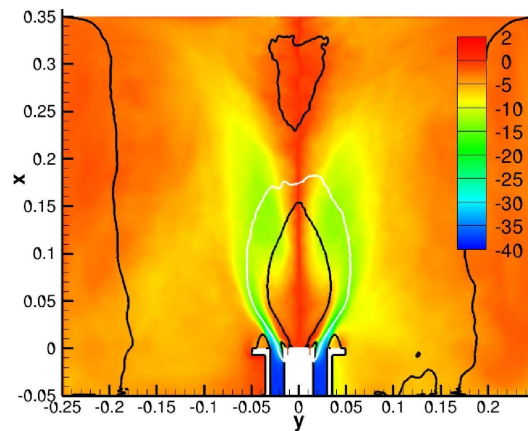
(b) Mean tangential velocity

Figure 6.6: (a) Mean radial and (b) tangential velocity for the reacting flow. White line: stoichiometric isoline; black line: zero-axial velocity isoline. Axes in m.

(a)

(b)

(c)

(d)

(e) Axial velocity (m/s)
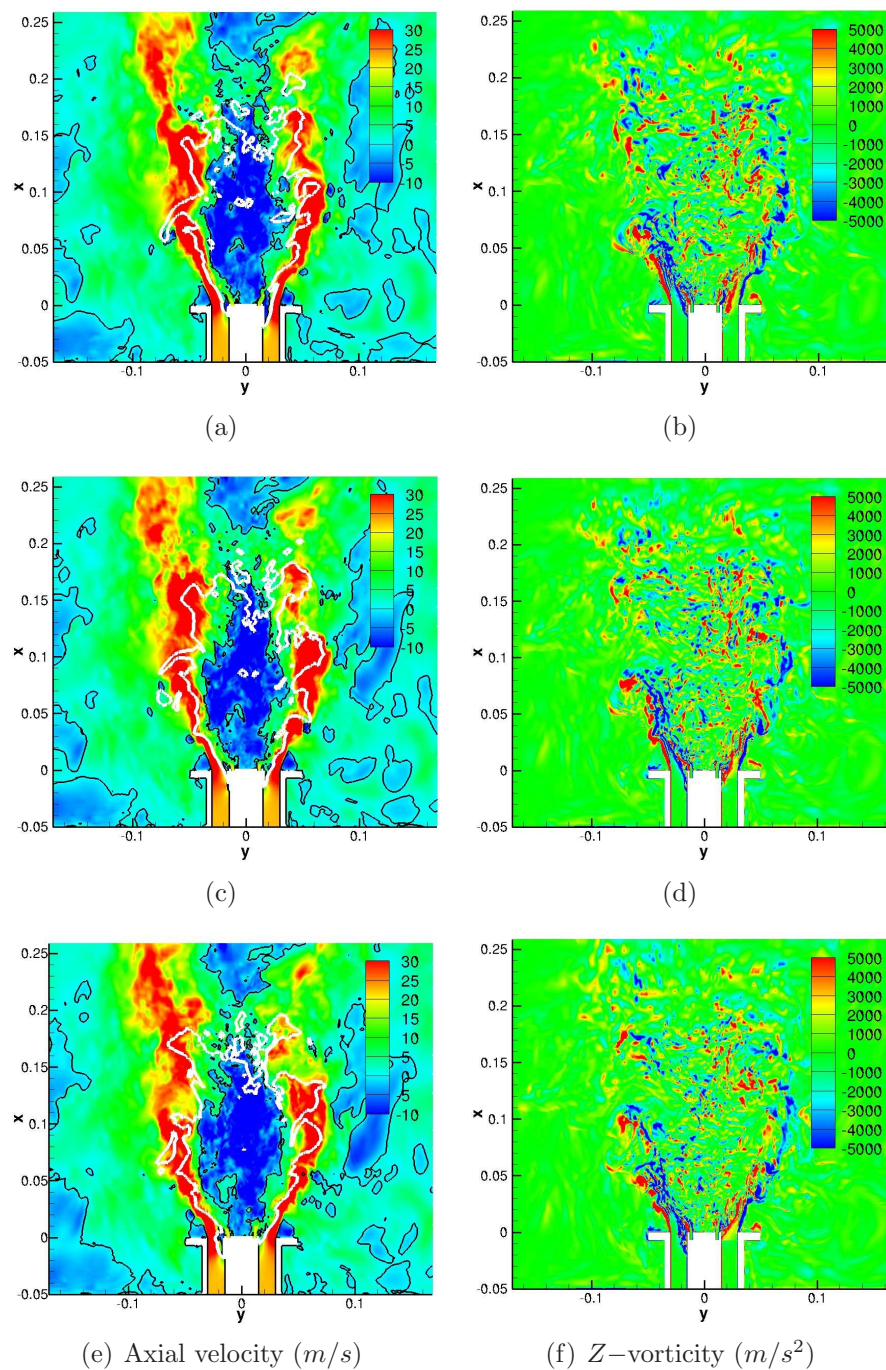
(f) $Z-$vorticity (m/s^2)

Figure 6.7: Snapshots at three consecutive instants of (a,c,e) the axial velocity and (b,d,f) the $z-$vorticity. White line: stoichiometric isoline; black line: zero-axial velocity isoline. Axes in m.
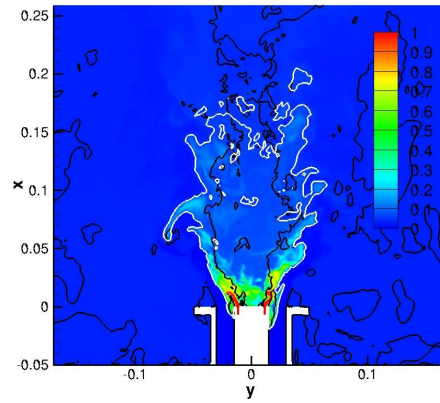
(a)
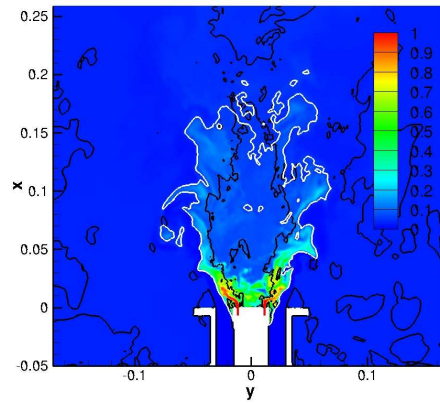
(b)
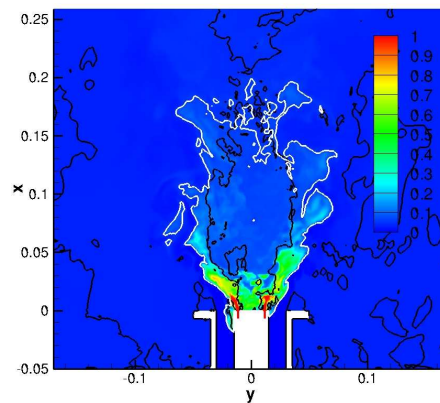
(c) Mixture fraction

Figure 6.8: Snapshots at three consecutive instants of the mixture fraction. White line: stoichiometric isoline; black line: zero-axial velocity isoline. Axes in m.
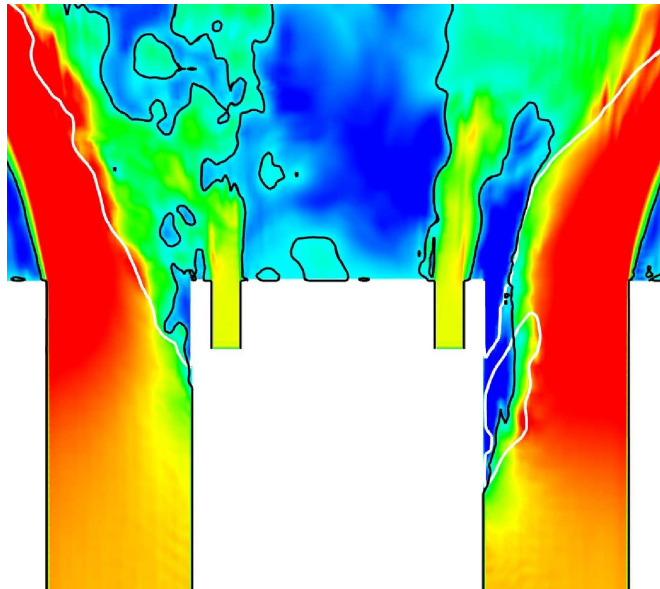
Figure 6.9: Zoom of the instantaneous axial velocity field inside the burner. White line: stoichiometric isoline; black line: zero-axial velocity isoline
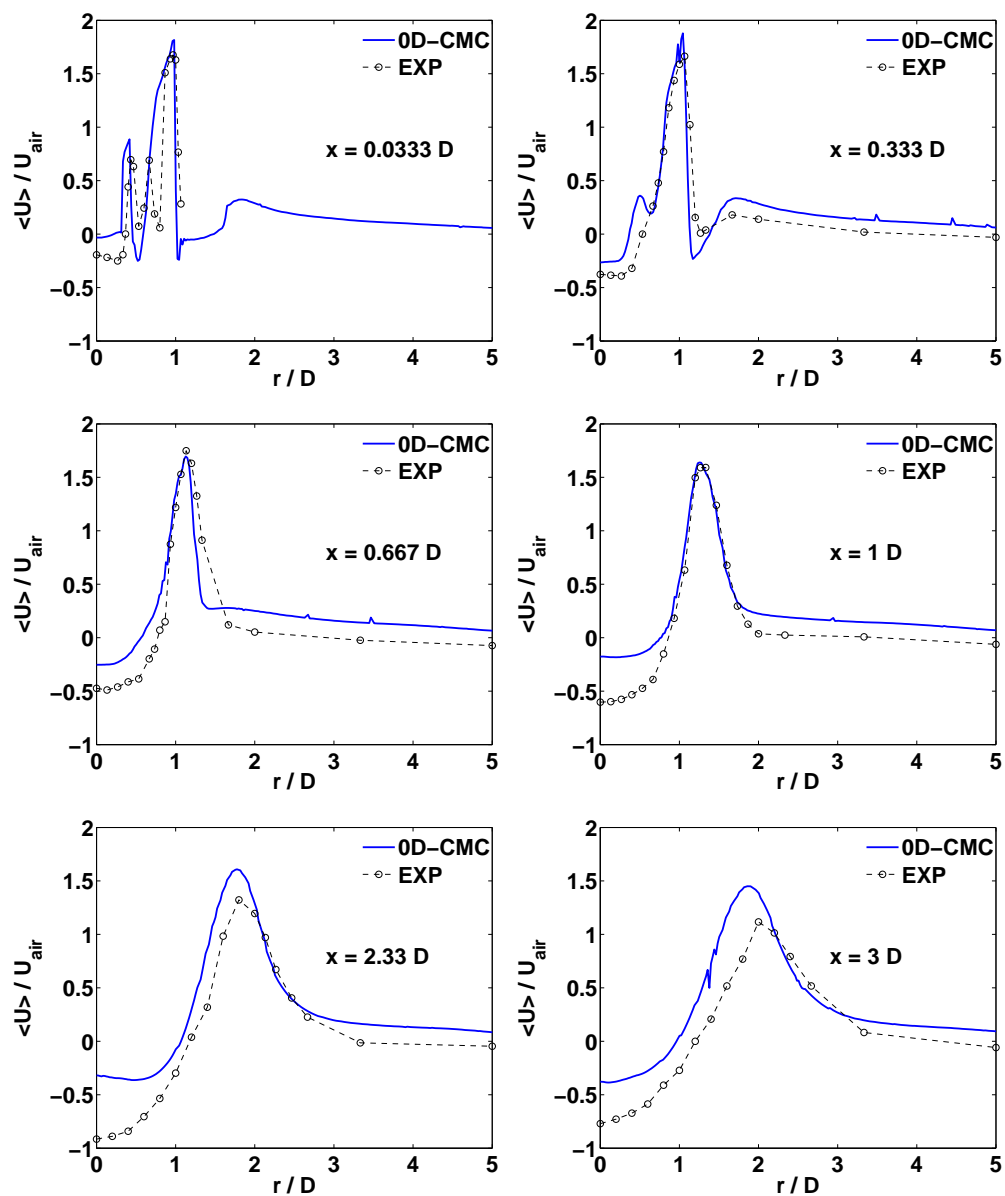
Figure 6.10: Radial profiles of the mean axial velocity at the indicated axial position. Experimental data from Ref. [51].
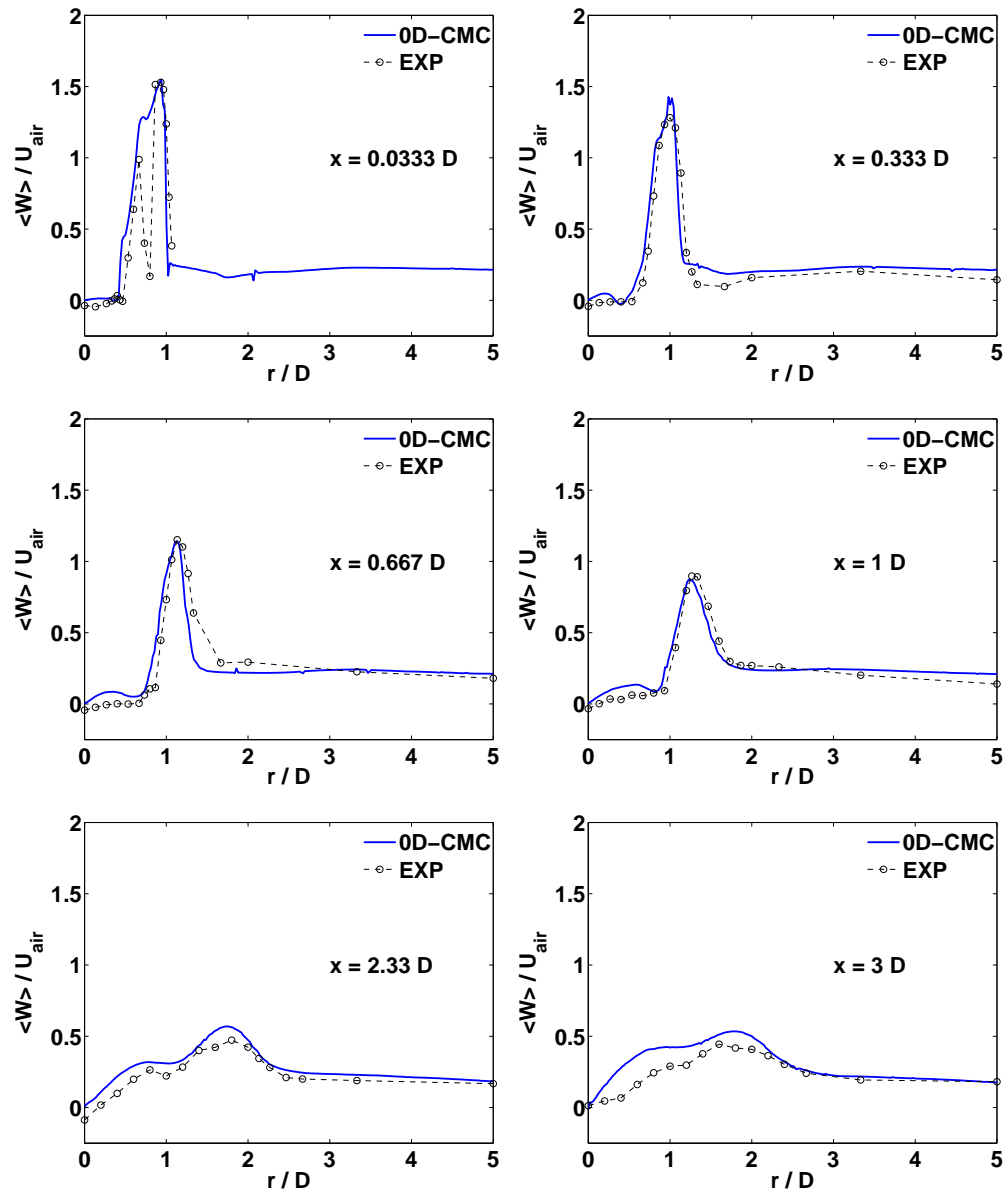
Figure 6.11: Radial profiles of the mean tangential velocity at the indicated axial position. Experimental data from Ref. [51].
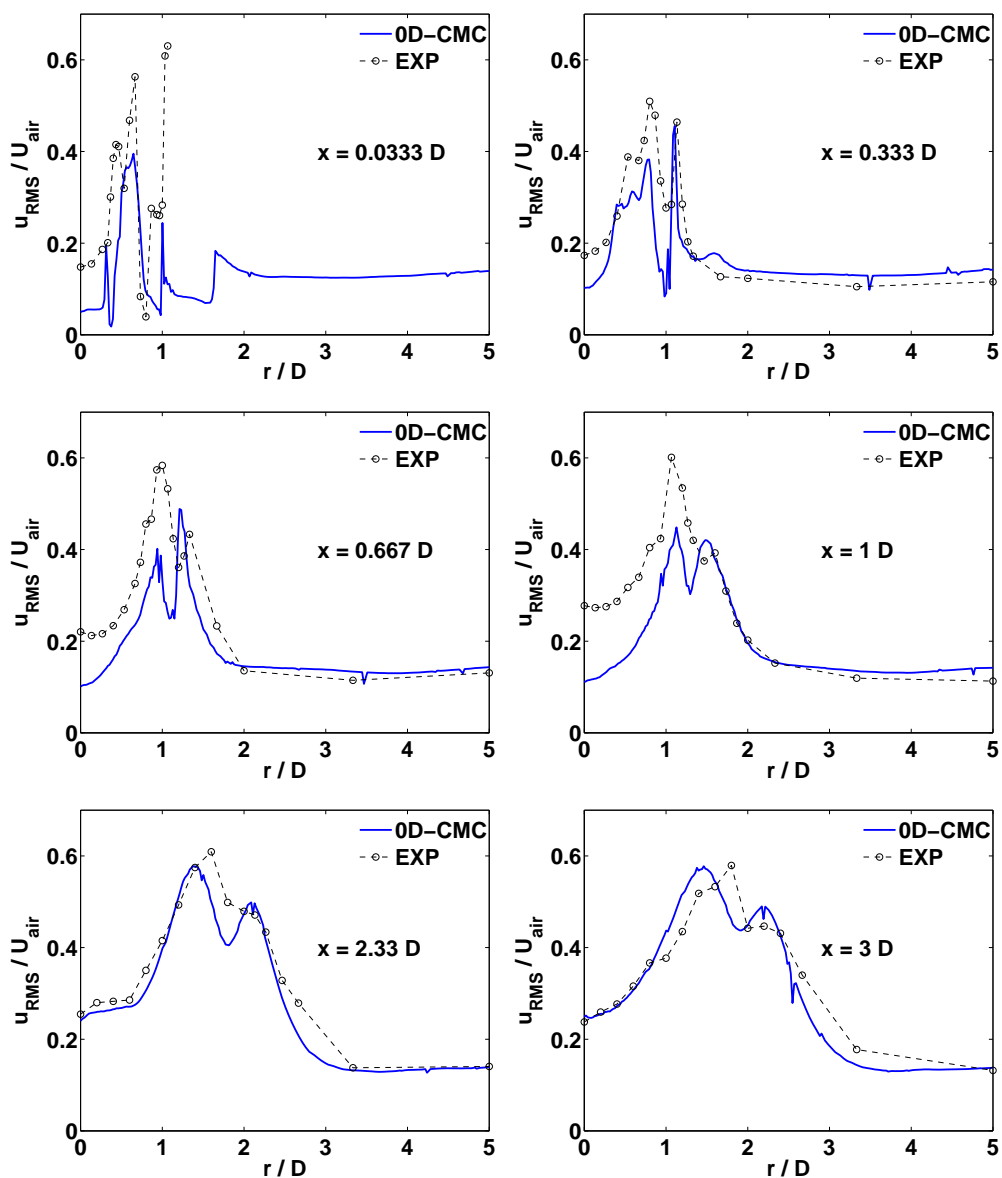
Figure 6.12: Radial profiles of the RMS of the axial velocity at the indicated axial position. Experimental data from Ref. [51].
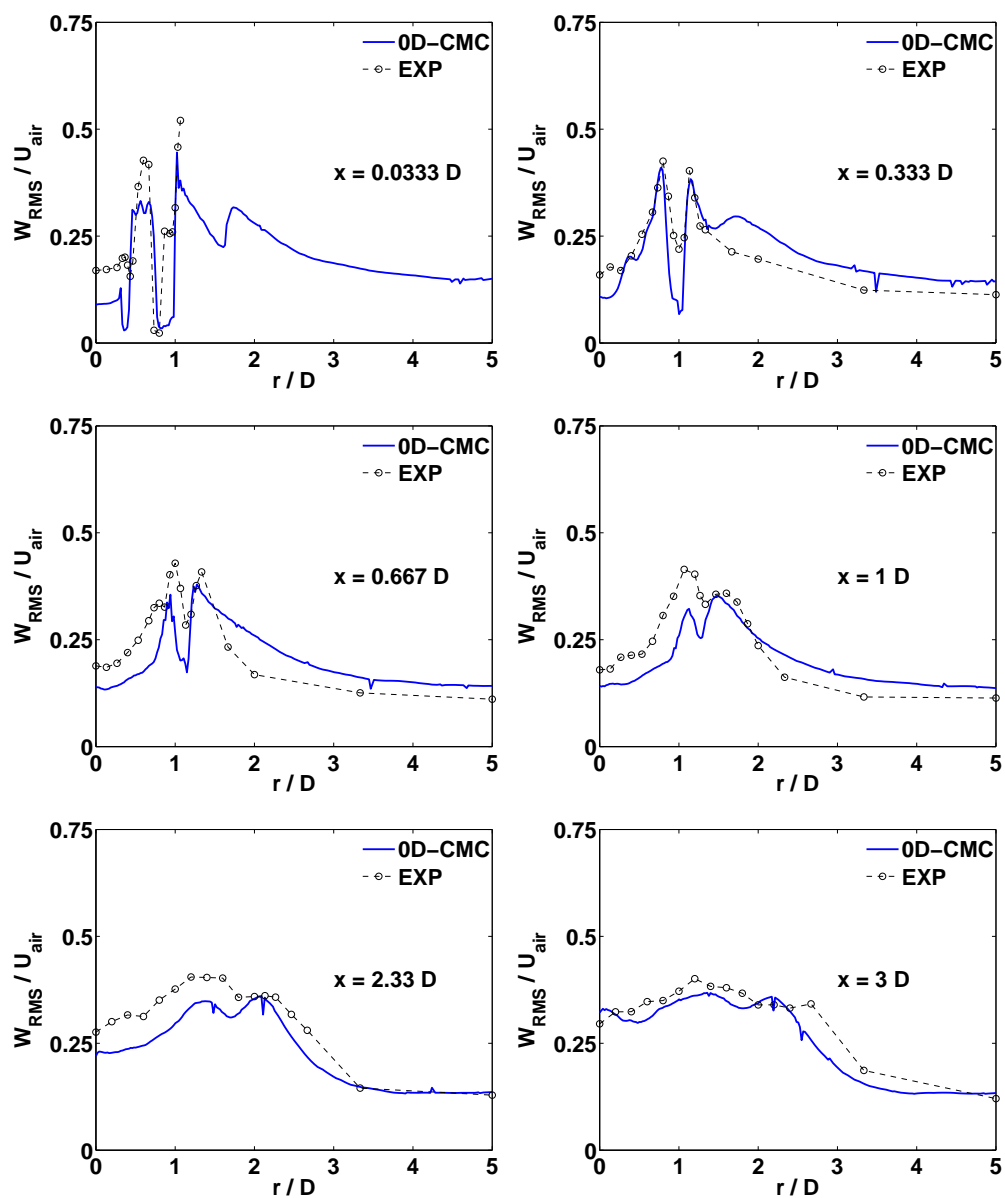
Figure 6.13: Radial profiles of the RMS of the tangential velocity at the indicated axial position. Experimental data from Ref. [51].
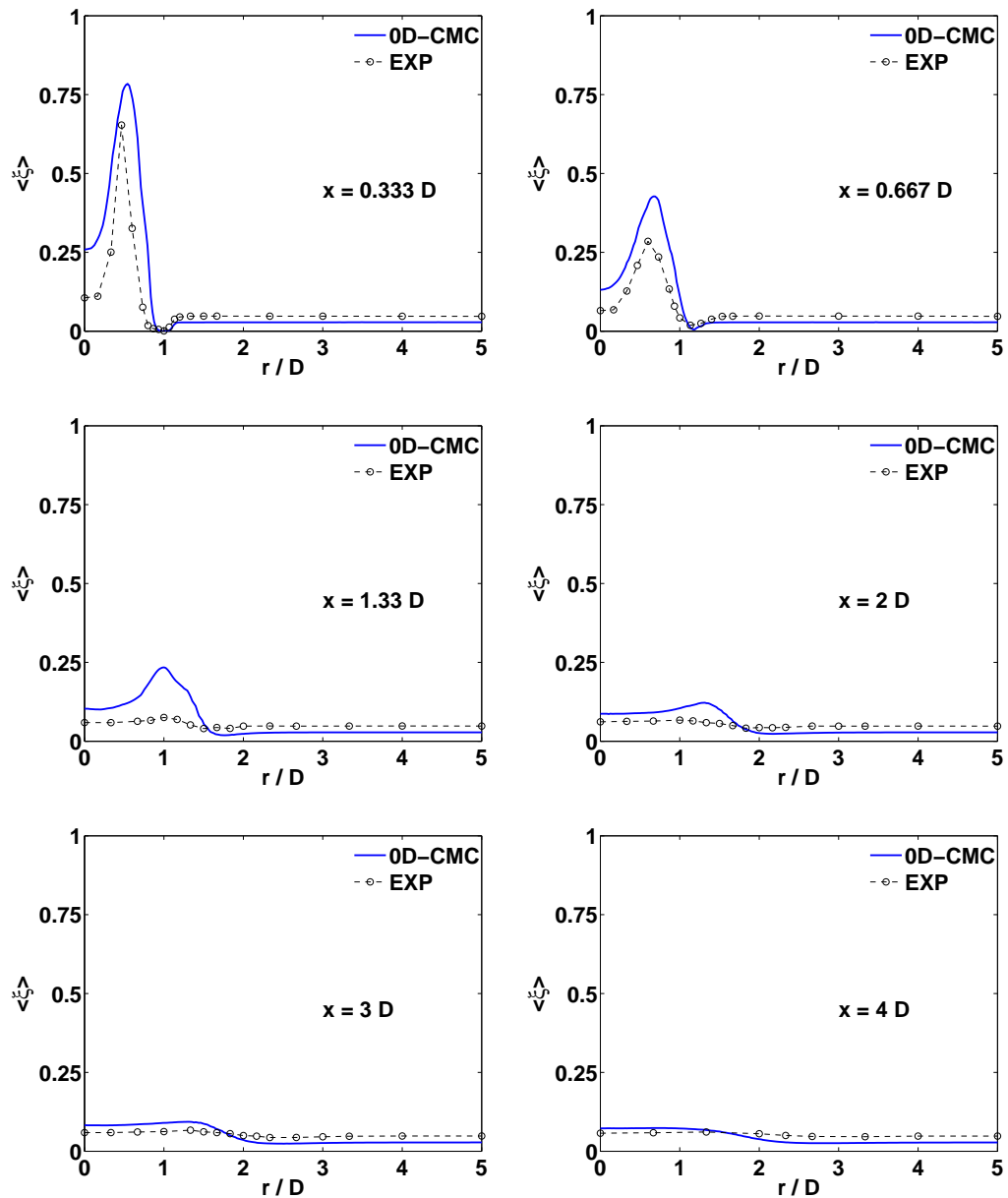
Figure 6.14: Radial profiles of the mean mixture fraction at the indicated axial position. Experimental data from Ref. [51].
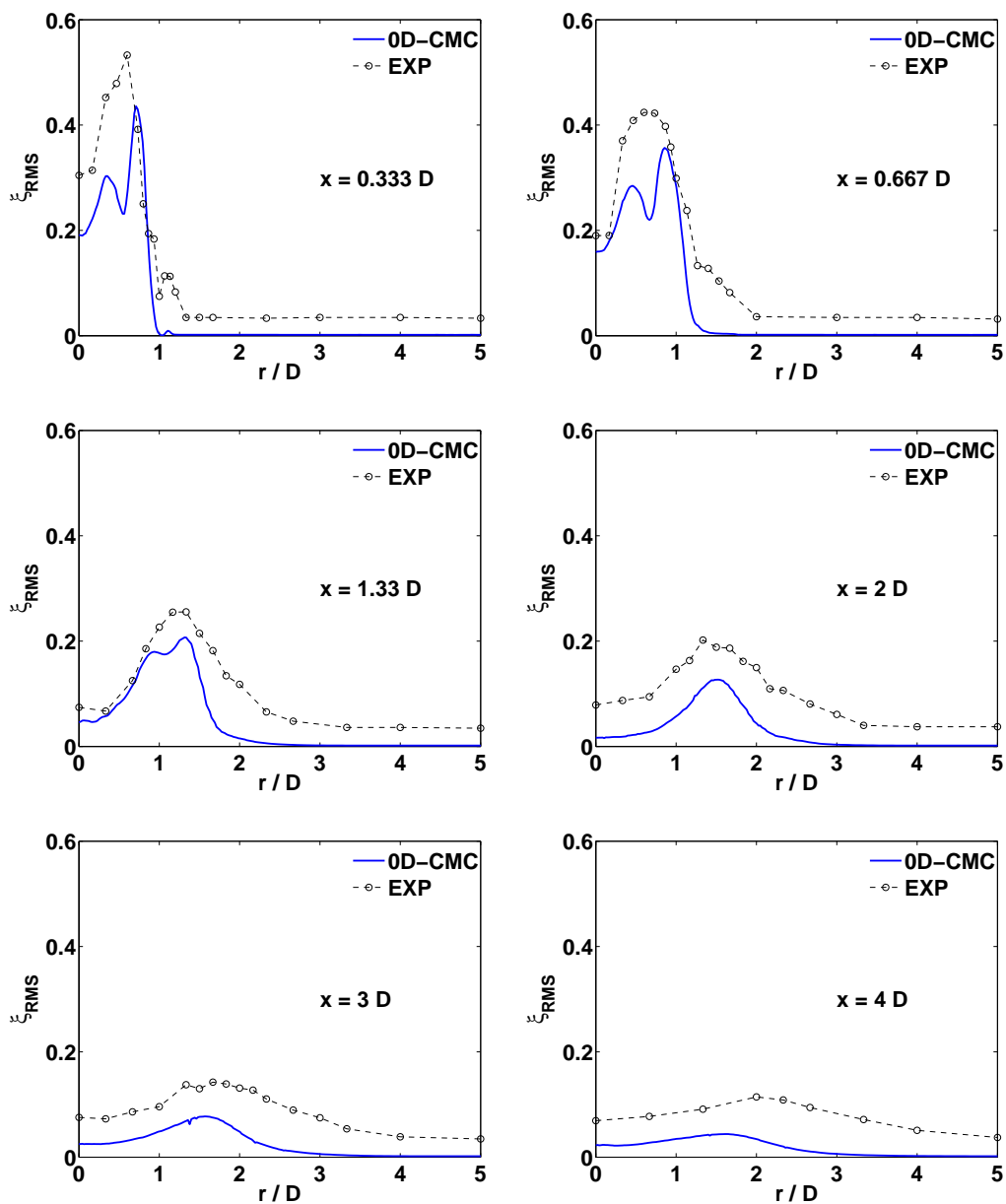
Figure 6.15: Radial profiles of the RMS of the mixture fraction at the indicated axial position. Experimental data from Ref. [51].

(a) Axial velocity

(b) Pressure
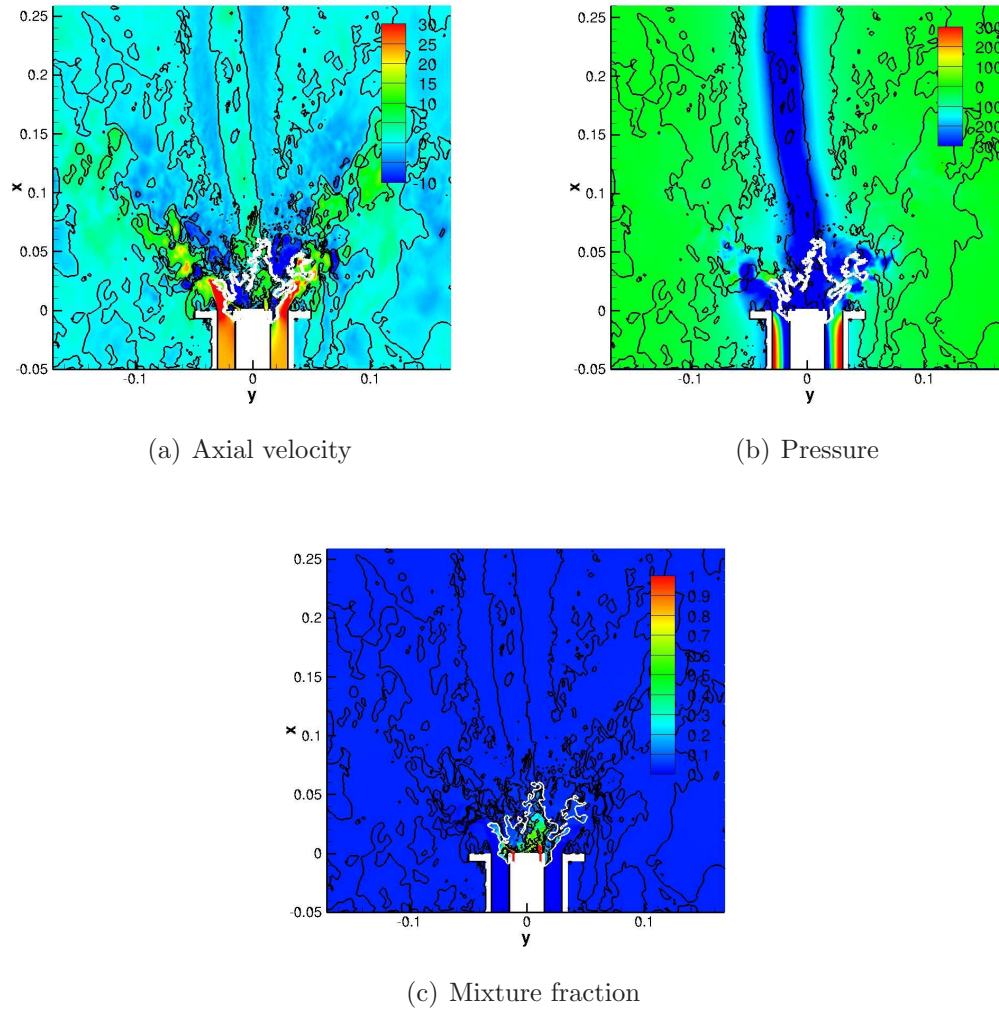
(c) Mixture fraction

Figure 6.16: Inert flow. Snapshots of the (a) axial velocity, (b) pressure, and (c) mixture fraction. White line: stoichiometric isoline; black line: zero-axial velocity isoline. Axes in m.
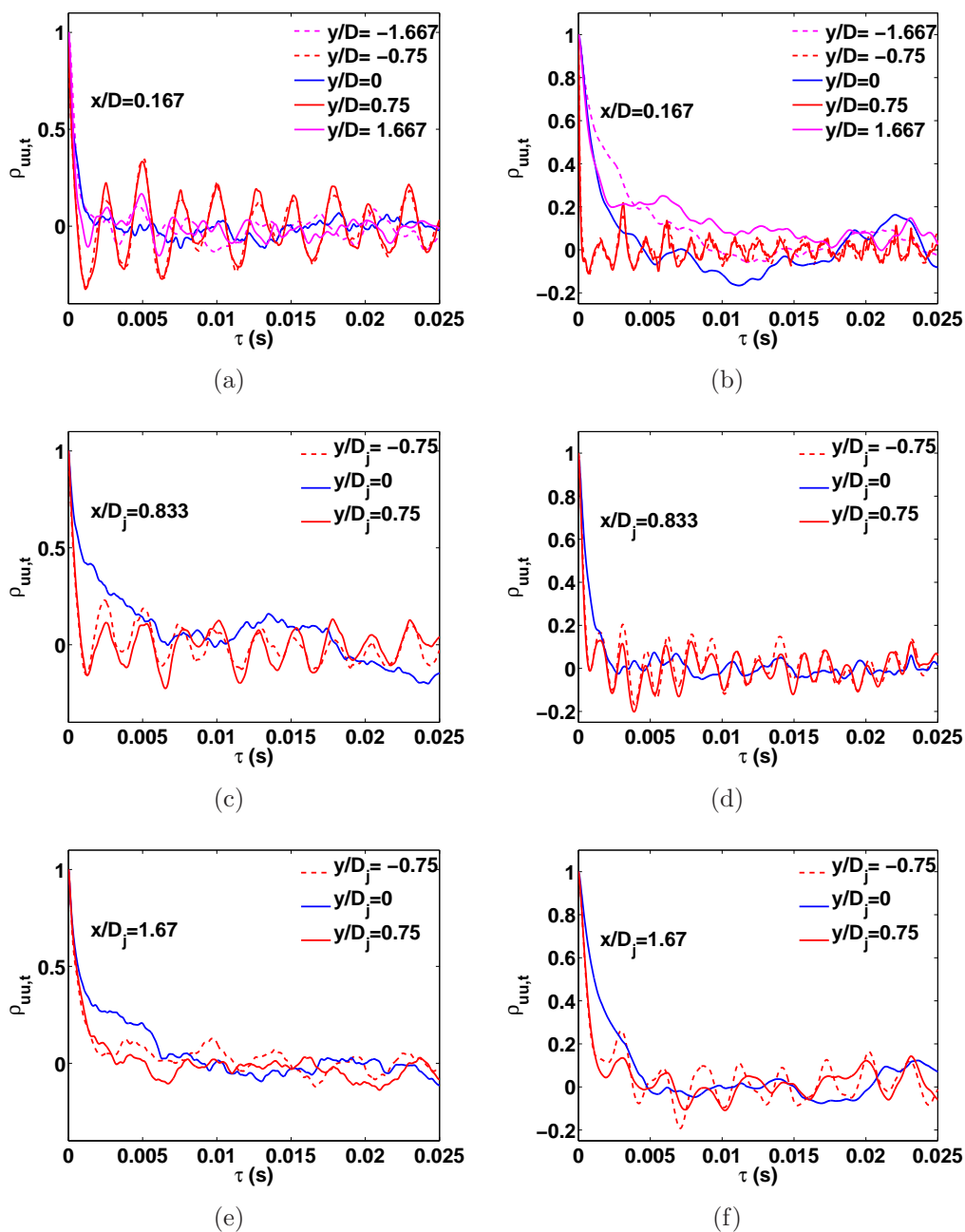
Figure 6.17: (a, b) Temporal autocorrelations at the indicated axial and radial positions. Left/Right: inert/reacting cases.
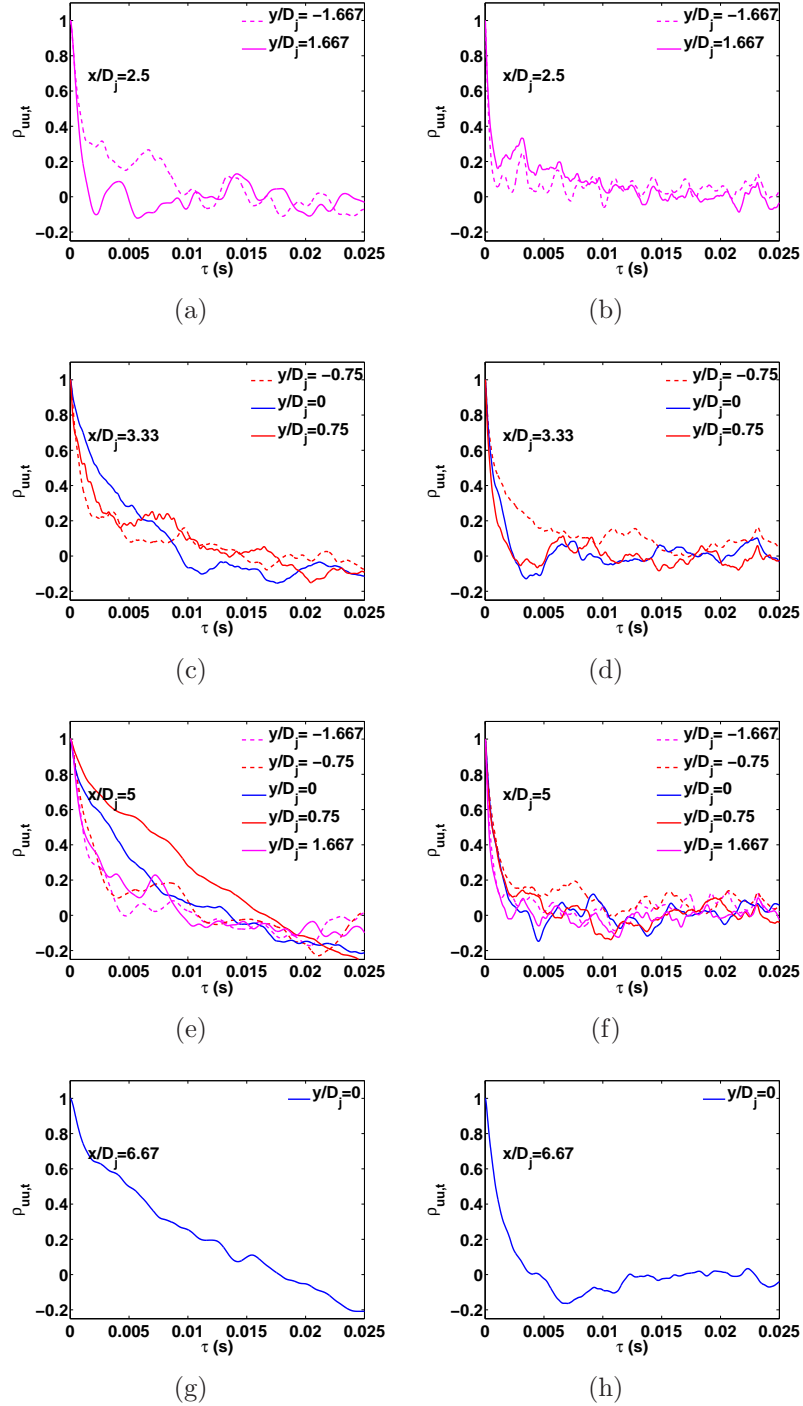
Figure 6.18: (a, b) Temporal autocorrelations at the indicated axial and radial positions. Left/Right: inert/reacting cases.
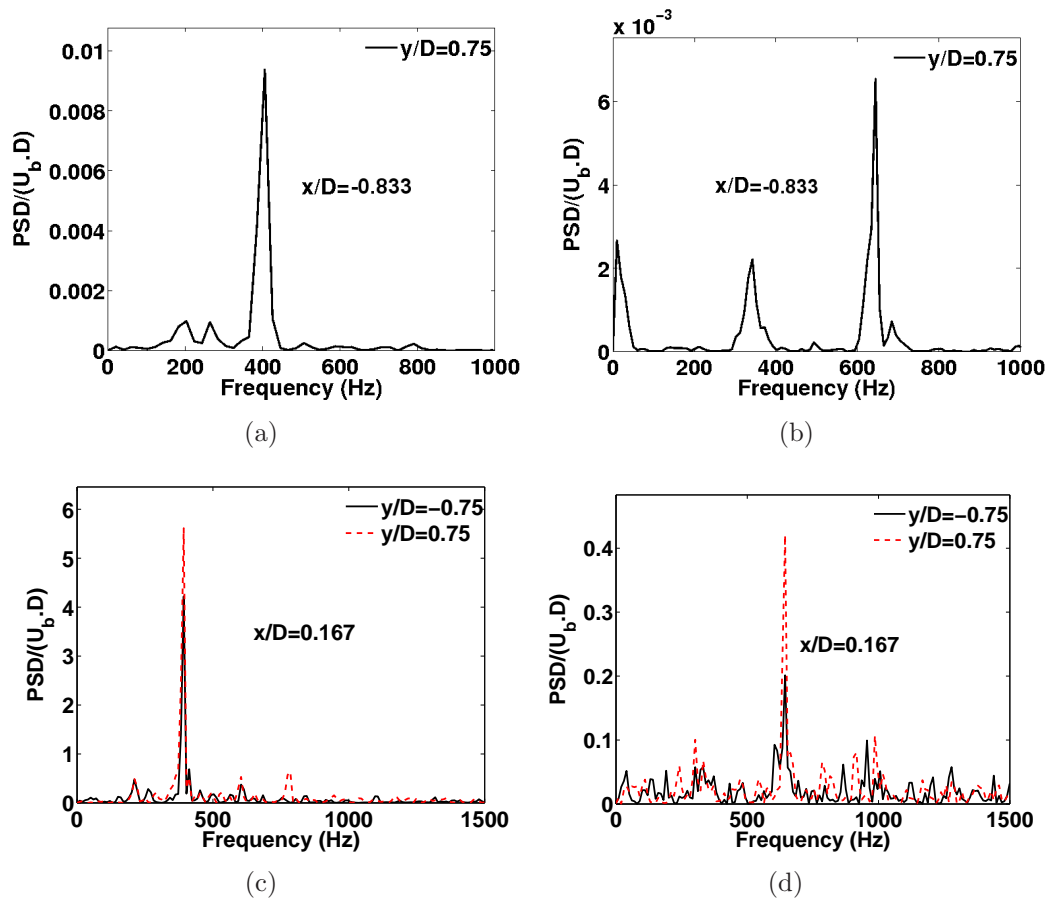
Figure 6.19: (a, b) Spectra of the axial velocity inside the air pipe at $x = -25$ mm & $r = 22.5$ mm ($r = 0.75$ D). (c, d) Spectra of the axial velocity at two positions above the air pipe exit with $x = 5$ mm & $r = 22.5$ mm ($r = 0.75$ D). Left/Right: inert/reacting cases.
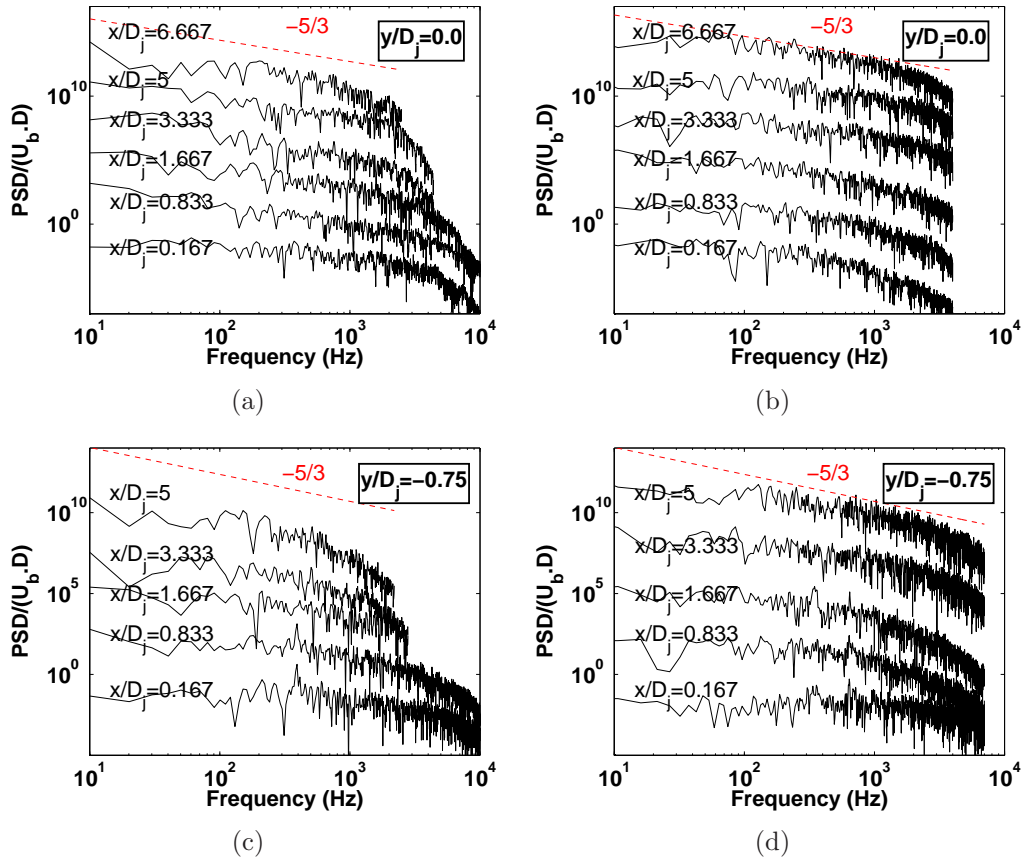
Figure 6.20: Log-log spectra of the axial velocity at the indicated positions. The top row corresponds to positions along the centreline and the bottom row corresponds to positions along the line $r = 0.75\ D_j$. Left/Right: inert/reacting cases.
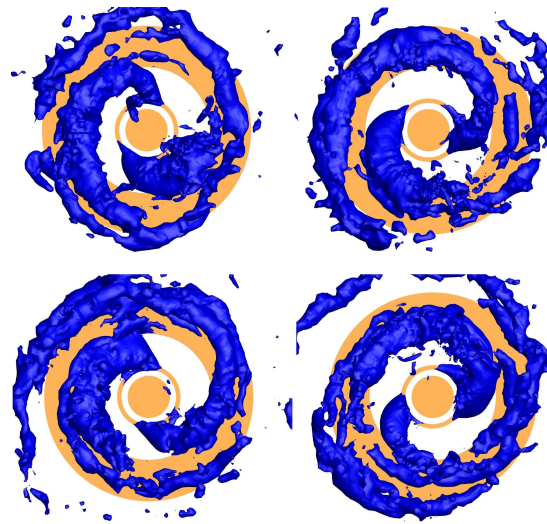
(a)
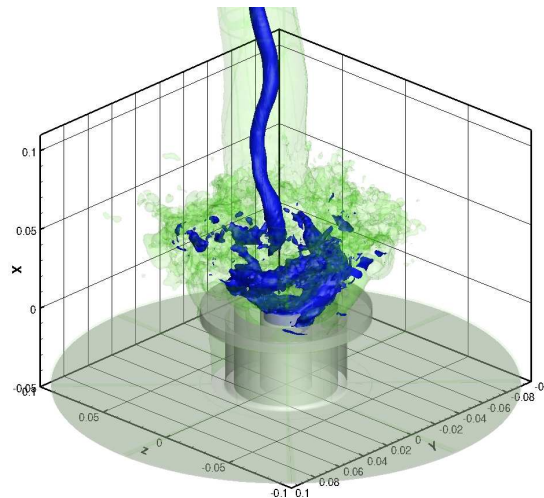
(b)

Figure 6.21: Inert flow. (a) Several instantaneous iso-surfaces of low pressure ($P - P_0 = -450\ Pa$) over one period of rotation. Visualization of the isothermal structures around the burner. (b) Instantaneous iso-surfaces of two different low pressure values (blue color: $P - P_0 = -250\ Pa$; green color: $P - P_0 = -150\ Pa$) to visualize the isothermal structures around the burner and inside the combustion chamber. Axes in m.

(a)

(b)

(c)

(d)
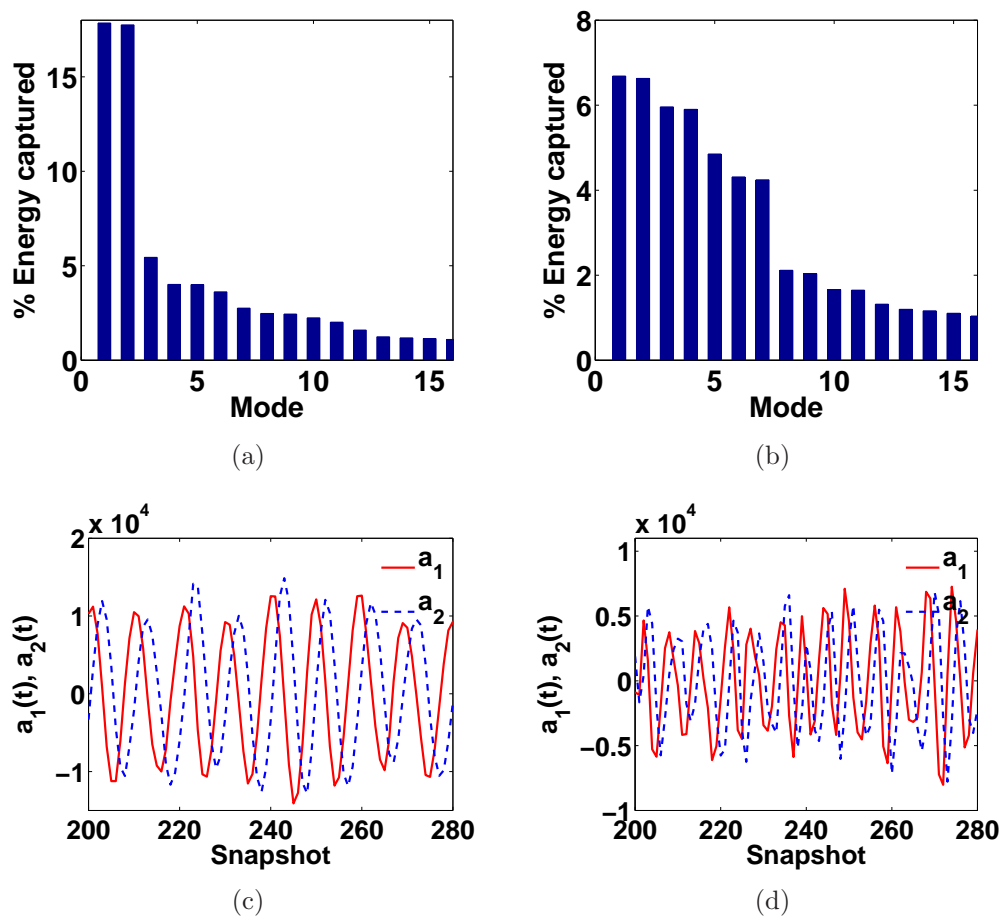
Figure 6.22: 2D POD analysis from the plane $x = 5$ mm. (a, b) Contribution to the fluctuation energy for each mode. (c, d). POD time coefficients (temporal modes) of the first two spatial modes. Left/right: inert/reacting case.

(a) Mode 1, V (b) Mode 2, V (c) Mode 3, V (d) Mode 4, V

(e) Mode 1, $\overline{V}$ (f) Mode 2, $\overline{V}$ (g) Mode 3, $\overline{V}$ (h) Mode 4, $\overline{V}$

(i) Mode 1, P   (j) Mode 2, P (k) Mode 3, P (l) Mode 4, P

(m) Mode 1, ξ (n) Mode 2, ξ (o) Mode 3, ξ (p) Mode 4, ξ

(q) Mode 1, spectrum   (r) Mode 2, spectrum   (s) Mode 3, spectrum   (t) Mode 4, spectrum
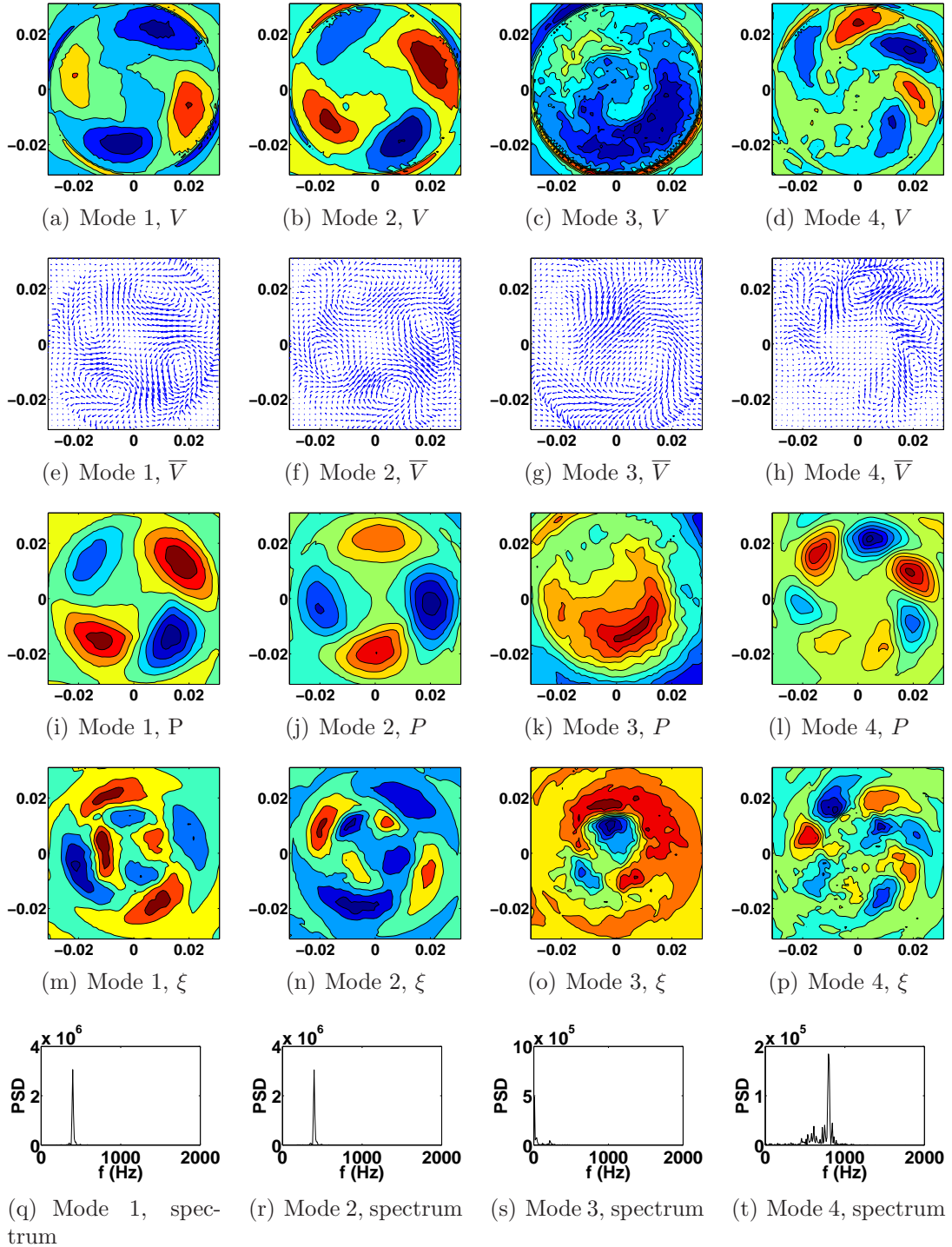
Figure 6.23: Inert flow. 2D POD modes 1-4 at $x = 5$ mm. The spectra refer to the Fourier analysis of the temporal coefficient associated with each mode.

(a) Mode 5, V (b) Mode 6, V (c) Mode 7, V (d) Mode 8, V

(e) Mode 5, $\overline{V}$ (f) Mode 6, $\overline{V}$ (g) Mode 7, $\overline{V}$ (h) Mode 8, $\overline{V}$

(i) Mode 5, P (j) Mode 6, P (k) Mode 7, P (l) Mode 8, P

(m) Mode 5, ξ (n) Mode 6, ξ (o) Mode 7, ξ (p) Mode 8, ξ

(q) Mode 5, spectrum   (r) Mode 6, spectrum   (s) Mode 7, spectrum   (t) Mode 8, spectrum
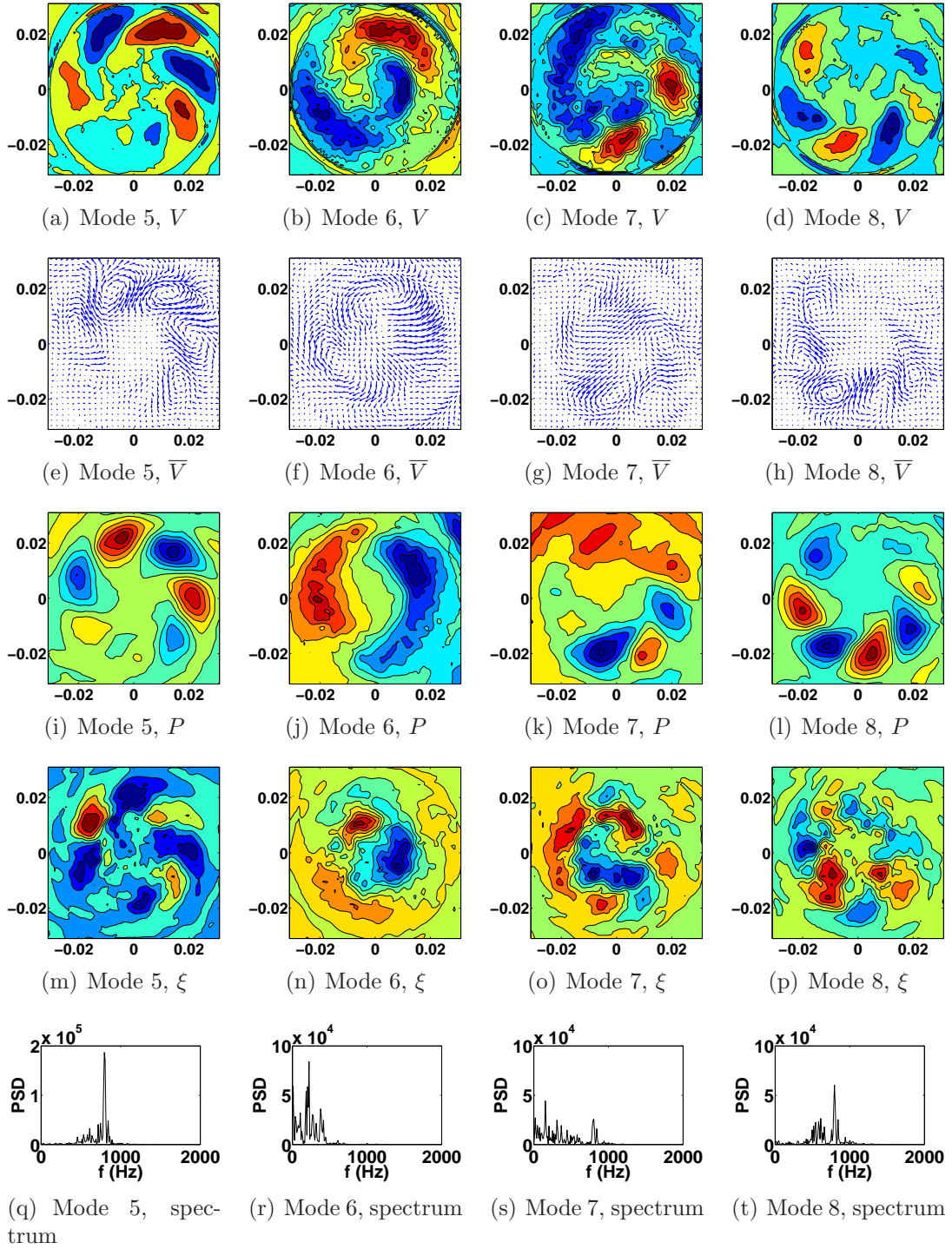
Figure 6.24: Inert flow. 2D POD modes 5-8 at $x = 5$ mm. The spectra refer to the Fourier analysis of the temporal coefficient associated with each mode.
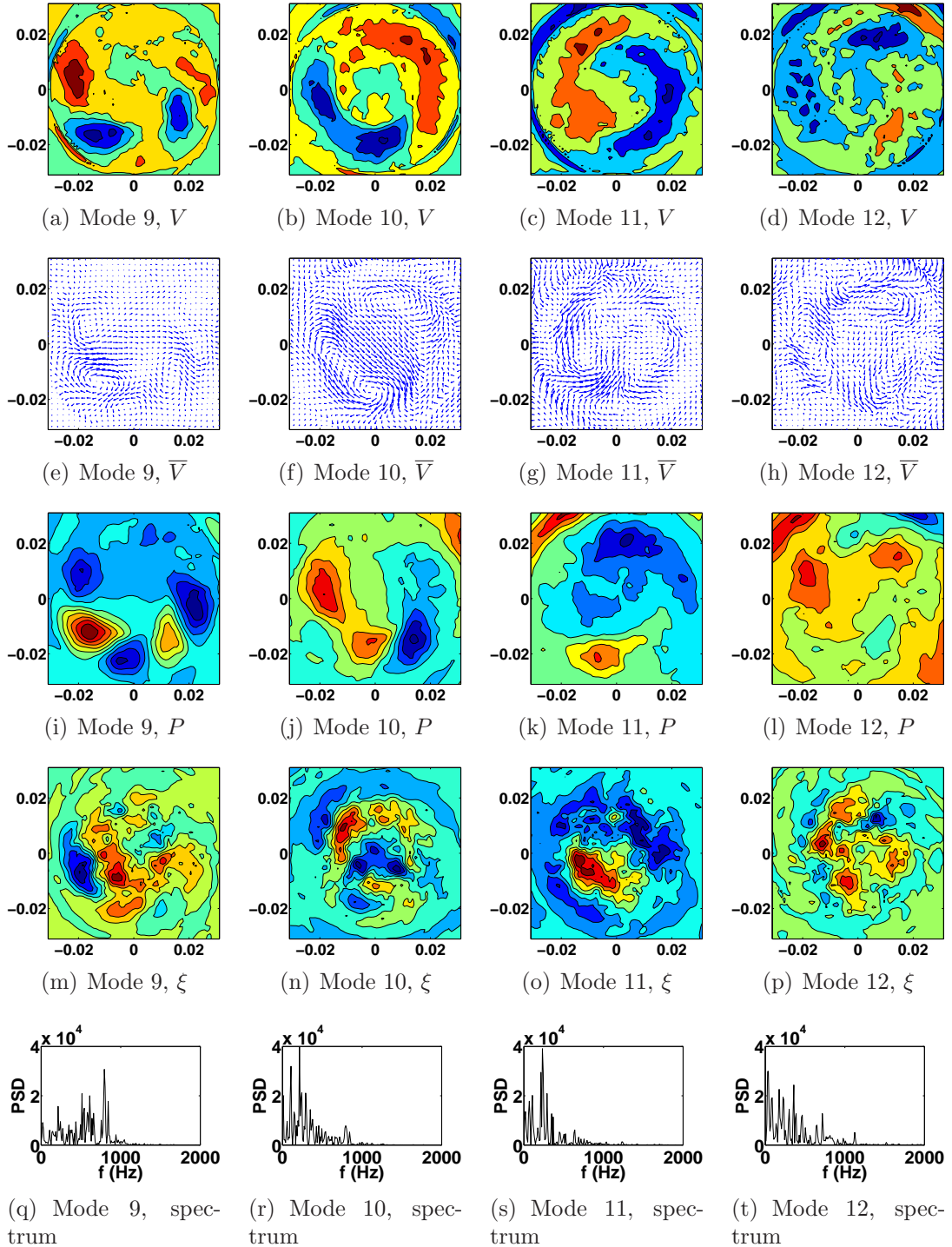
Figure 6.25: Inert flow. 2D POD modes 9-12 at $x = 5$ mm. The spectra refer to the Fourier analysis of the temporal coefficient associated with each mode.

(a) Mode 13, V (b) Mode 14, V (c) Mode 15, V

(d) Mode 13, $\overline{V}$ (e) Mode 14, $\overline{V}$ (f) Mode 15, $\overline{V}$

(g) Mode 13, P (h) Mode 14, P (i) Mode 15, P

(j) Mode 13, ξ (k) Mode 14, ξ (l) Mode 15, ξ

(m) Mode 13, spectrum   (n) Mode 14, spectrum   (o) Mode 15, spectrum
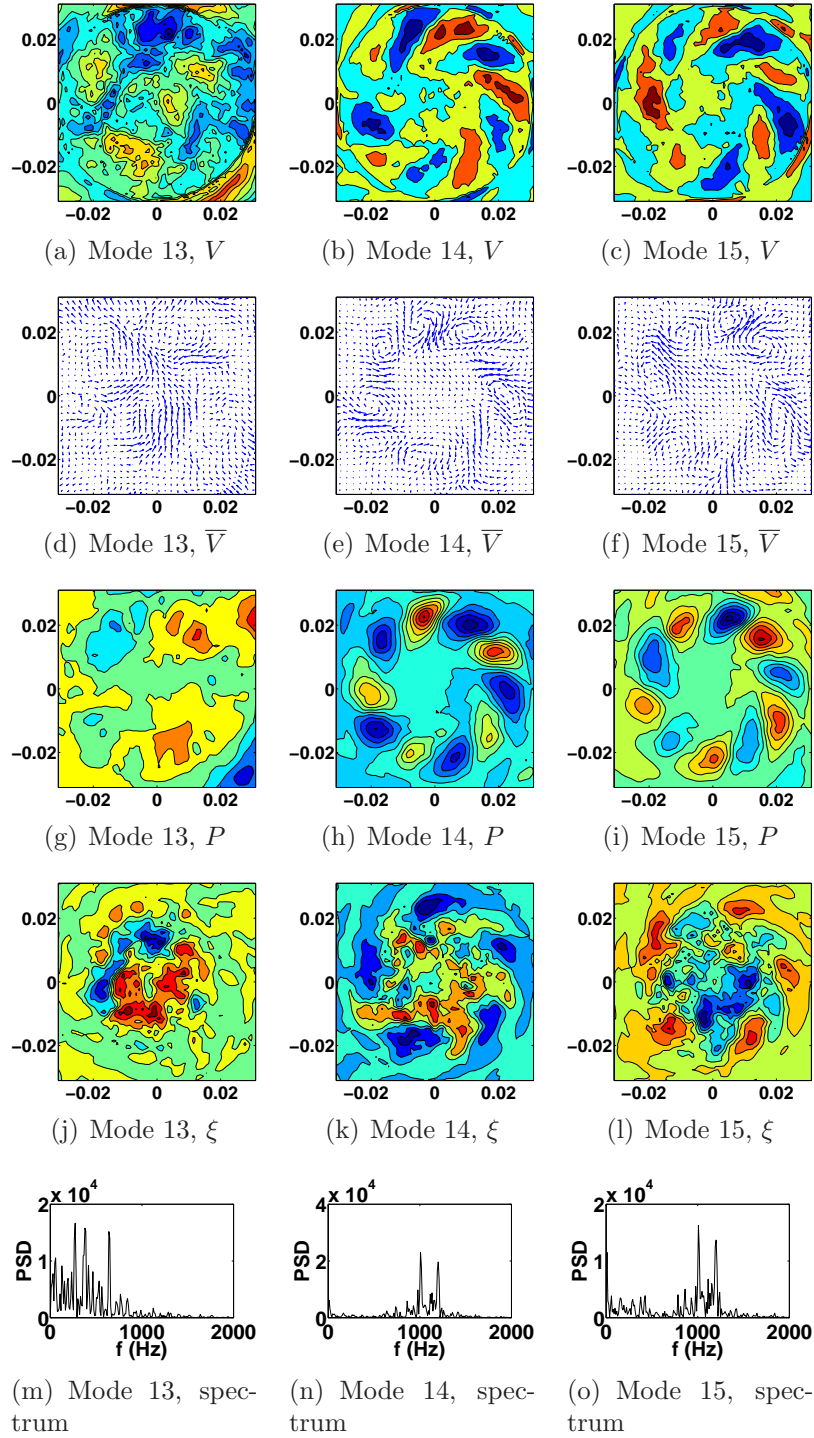
Figure 6.26: Inert flow. 2D POD modes 13-15 at $x = 5$ mm. The spectra refer to the Fourier analysis of the temporal coefficient associated with each mode.
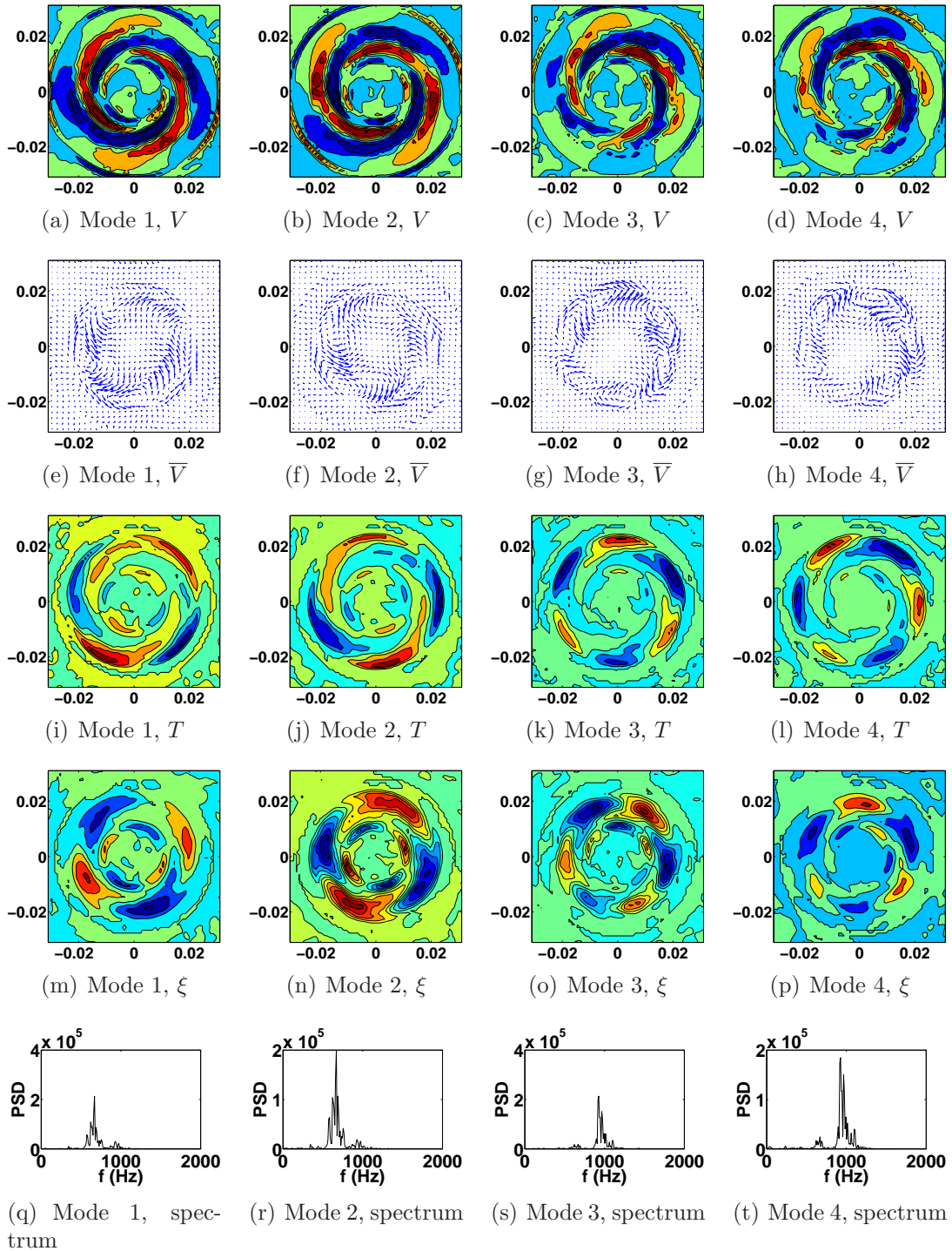
Figure 6.27: Reacting flow. 2D POD modes 1-4 at $x = 5$ mm. The spectra refer to the Fourier analysis of the temporal coefficient associated with each mode.
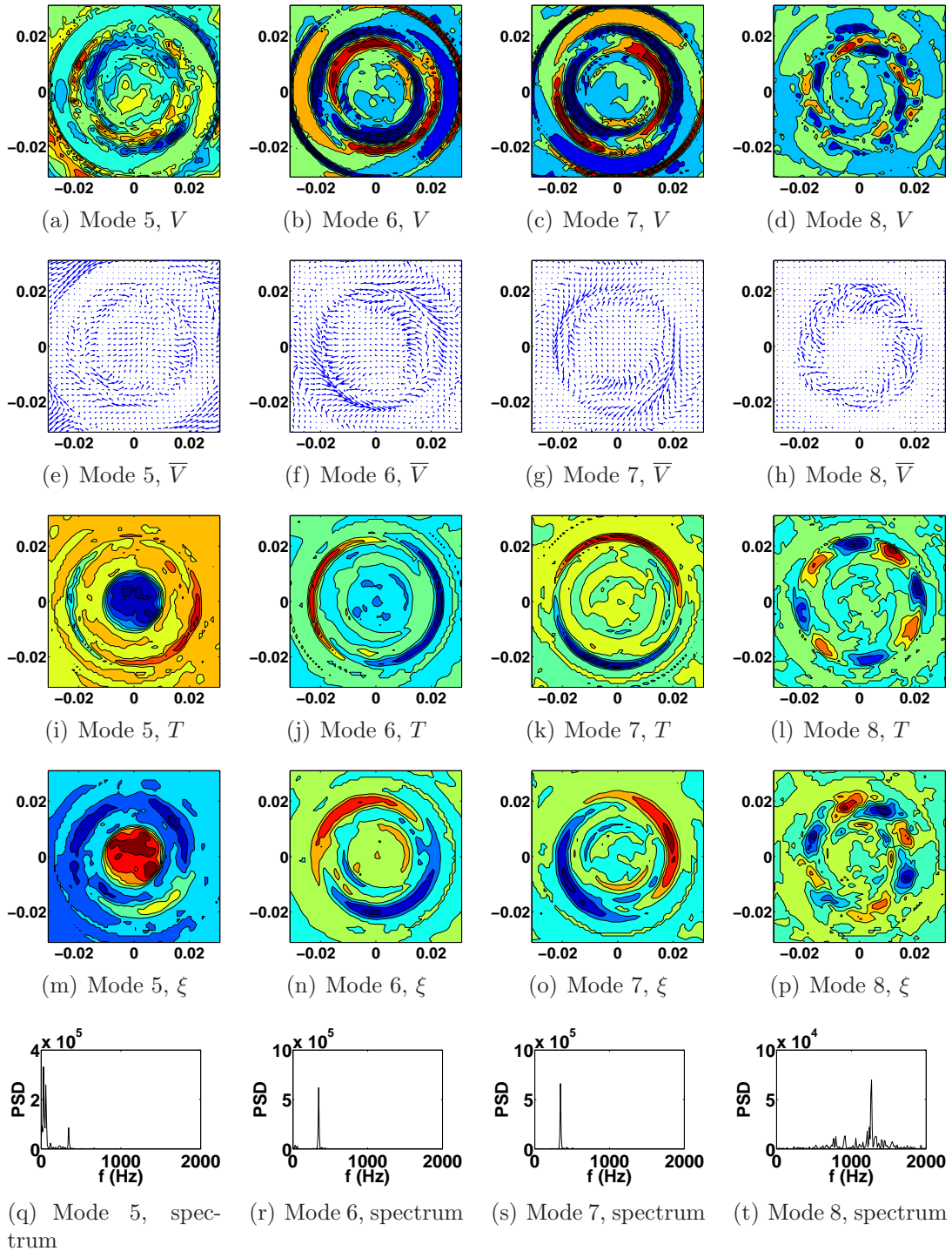
Figure 6.28: Reacting flow. 2D POD modes 5-8 at $x = 5$ mm. The spectra refer to the Fourier analysis of the temporal coefficient associated with each mode.

(a) Mode 9, V (b) Mode 10, V (c) Mode 11, V (d) Mode 12, V

(e) Mode 9, $\overline{V}$ (f) Mode 10, $\overline{V}$ (g) Mode 11, $\overline{V}$ (h) Mode 12, $\overline{V}$

(i) Mode 9, T (j) Mode 10, T (k) Mode 11, T (l) Mode 12, T

(m) Mode 9, ξ (n) Mode 10, ξ (o) Mode 11, ξ (p) Mode 12, ξ

(q) Mode 9, spectrum   (r) Mode 10, spectrum   (s) Mode 11, spectrum   (t) Mode 12, spectrum
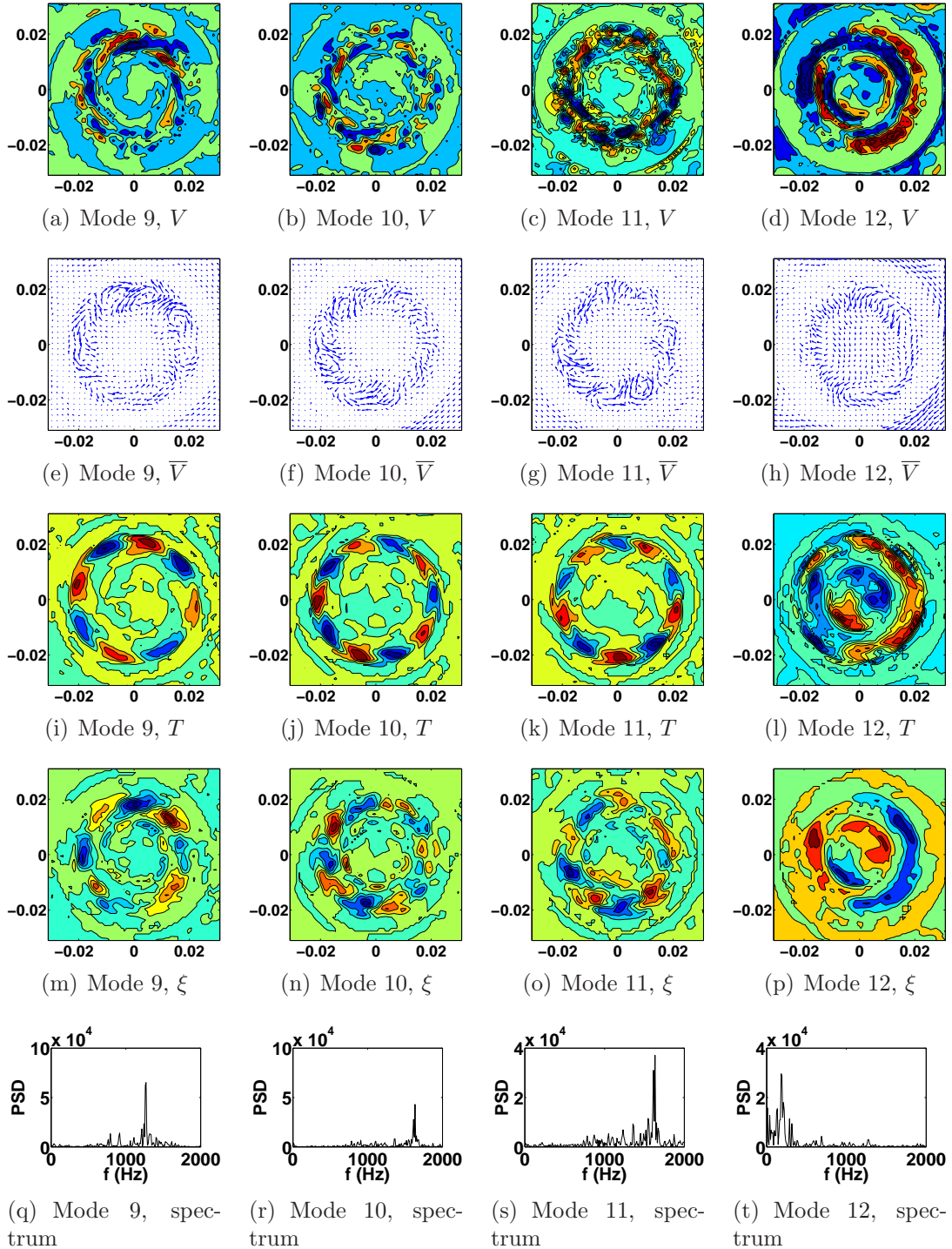
Figure 6.29: Reacting flow. 2D POD modes 9-12 at $x = 5$ mm. The spectra refer to the Fourier analysis of the temporal coefficient associated with each mode.

175

(a) Mode 13, V (b) Mode 14, V (c) Mode 15, V

(d) Mode 13, $\overline{V}$ (e) Mode 14, $\overline{V}$ (f) Mode 15, $\overline{V}$

(g) Mode 13, T (h) Mode 14, T (i) Mode 15, T

(j) Mode 13, ξ (k) Mode 14, ξ (l) Mode 15, ξ

(m) Mode 13, spec-trum   (n) Mode 14, spec-trum   (o) Mode 15, spec-trum
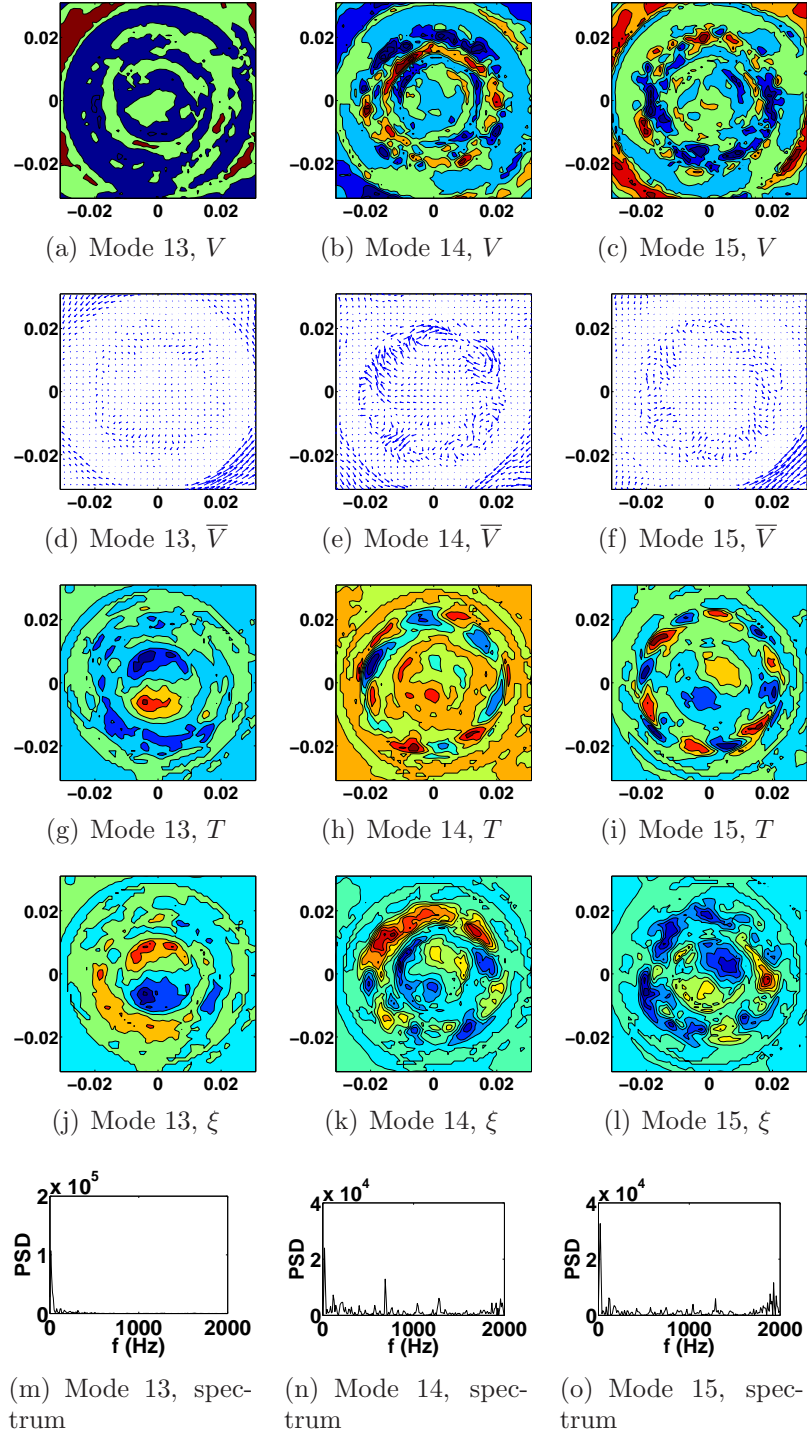
Figure 6.30: Reacting flow. 2D POD modes 13-15 at $x = 5$ mm. The spectra refer to the Fourier analysis of the temporal coefficient associated with each mode.

176
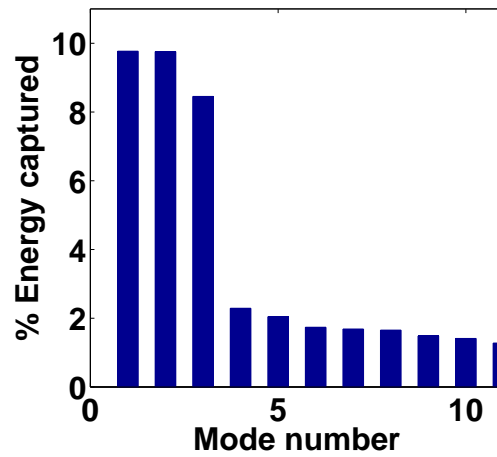
(a)
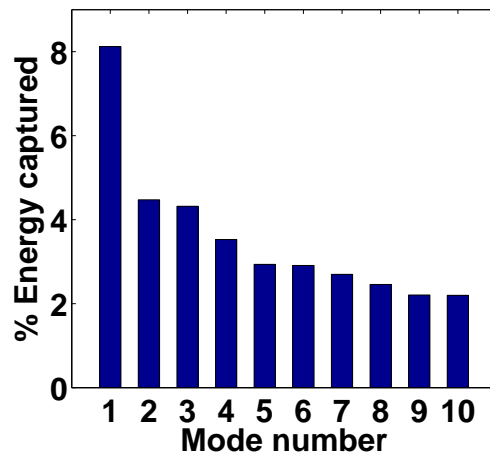
(b)

Figure 6.31: 3D POD analysis. Contribution to the total fluctuation energy of each mode: (a) inert case; (b) reacting case.

(a) Mode 1, U   (b) Mode 1, Q   (c) Mode 1, ξ

(d) Mode 2, U   (e) Mode 2, Q   (f) Mode 2, ξ
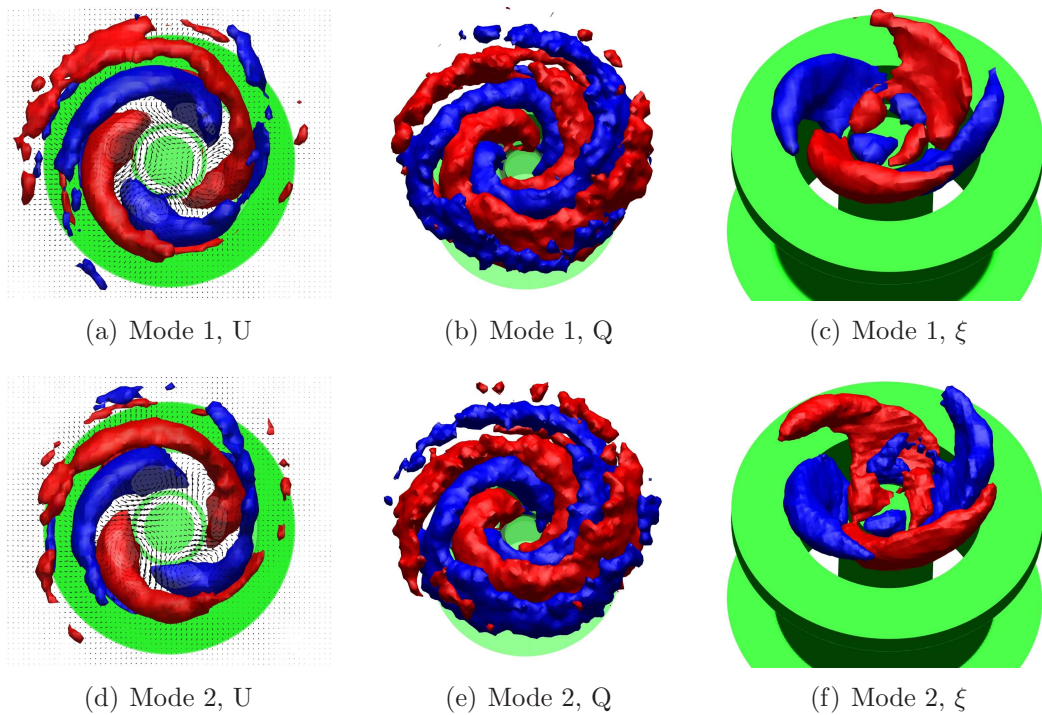
Figure 6.32: Inert flow. 3D POD mode 1 (a, b, c) and mode 2 (d, e, f). (a, d) Isosurfaces of the axial velocity fluctuations with the vectop map at x = 5 mm superimposed. (b, e, g) $Q-$criterion coloured by the axial velocity fluctuations. (c, f) Isosurfaces of the mixture fraction fluctuations. The negative fluctuations are plotted in blue, the positive ones in red.
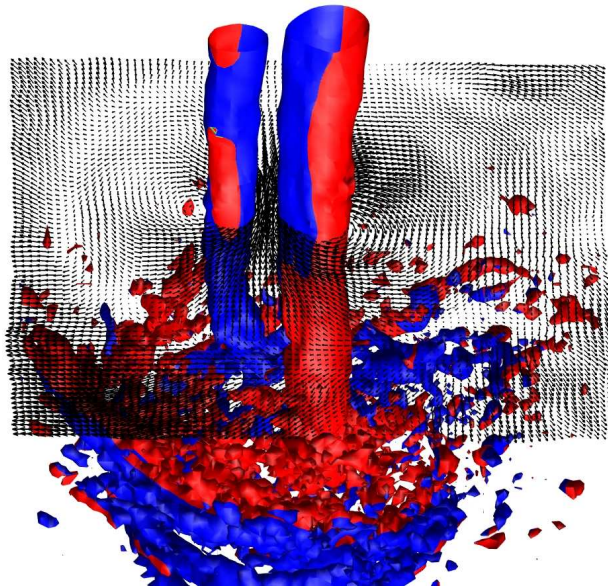
Figure 6.33: Inert flow. 3D POD mode 3 visualized using the Q-criterion coloured by the axial velocity fluctuations. The negative fluctuations are plotted in blue, the positive ones in red.

(a)

(b)
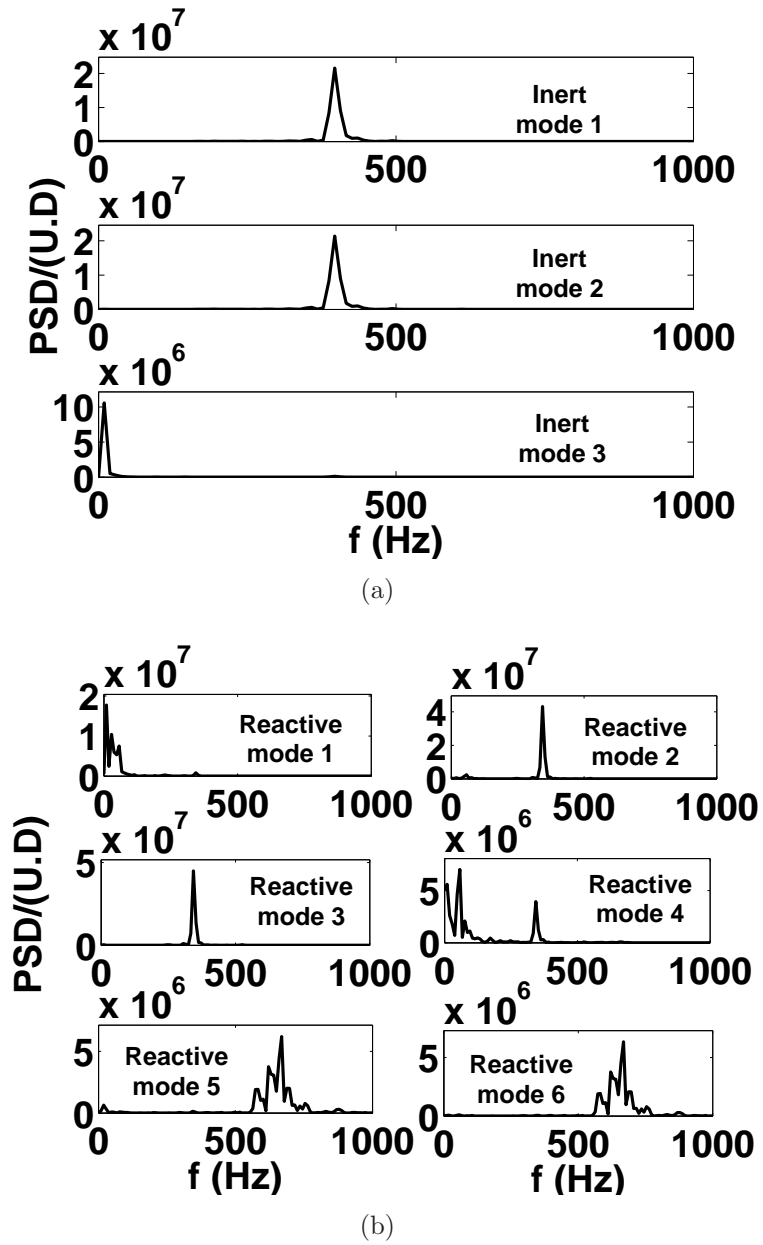
Figure 6.34: 3D POD analysis. Spectral analysis of the POD temporal coefficients $a_i(t)$: (a) inert case; (b) reacting case.
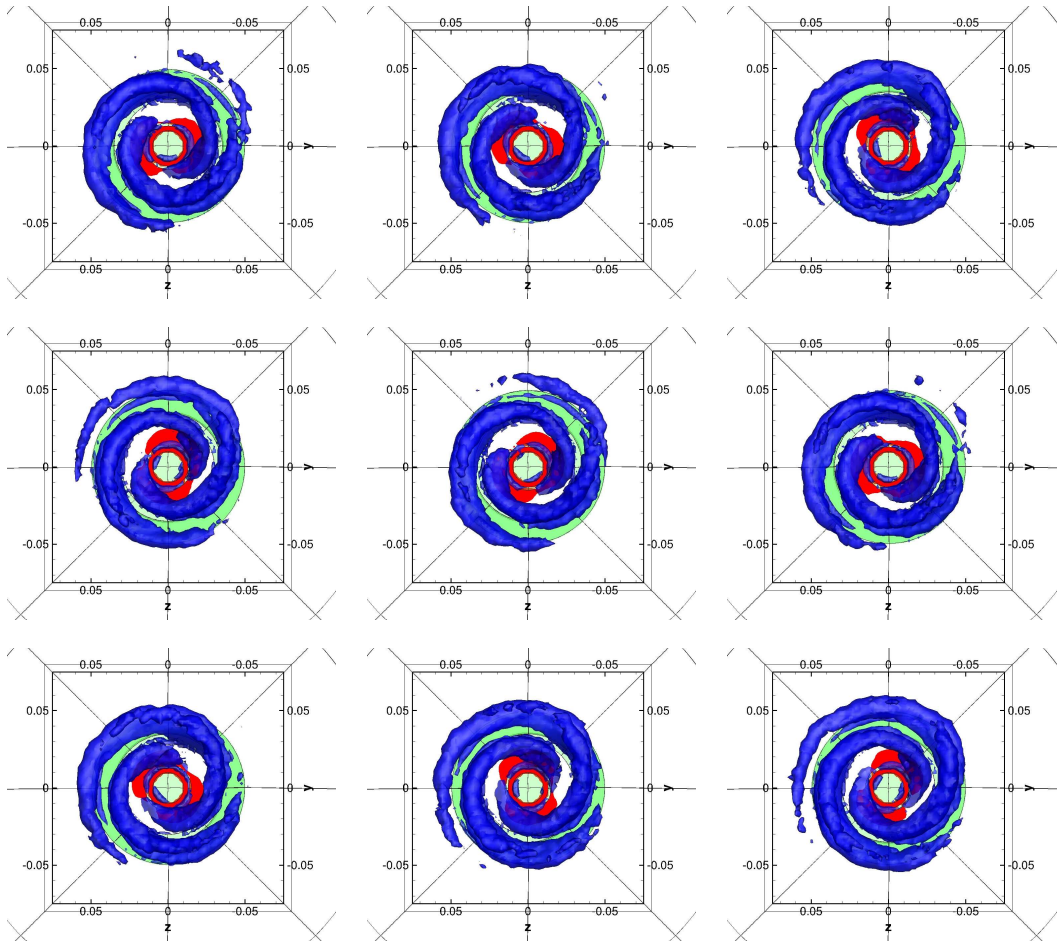
Figure 6.35: Inert flow. Reconstruction of several snasphots over one period of rotation based on the 3D POD modes 1 and 2. Visualization of (a) Q-criterion isosurfaces (blue color) and (b) mixture fraction contours (red color, corresponding to areas where $\xi \geq 0.35$), applied to the instantaneous reconstructed flow fields.
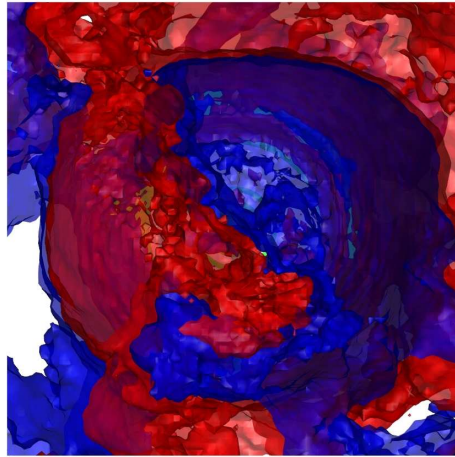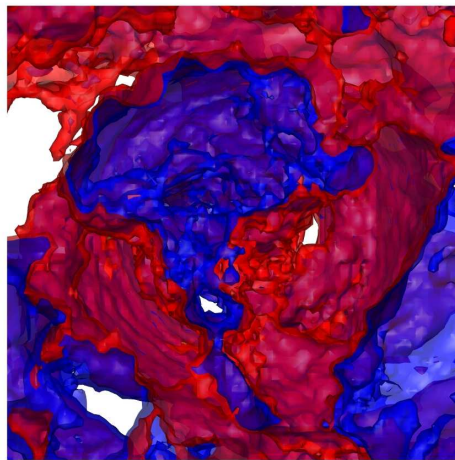
(a) Mode 1, U

(b) Mode 4, U

Figure 6.36: Reactive flow. 3D POD (a) mode 1 and (b) mode 4. Negative (blue) and positive (red) isosurfaces of axial velocity fluctuations. View from above the burner exit.

(a) Mode 2, Q-U

(b) Mode 2, Q-T

(c) Mode 2, ξ

(d) Mode 3, Q-U

(e) Mode 3, Q-T

(f) Mode 3, ξ
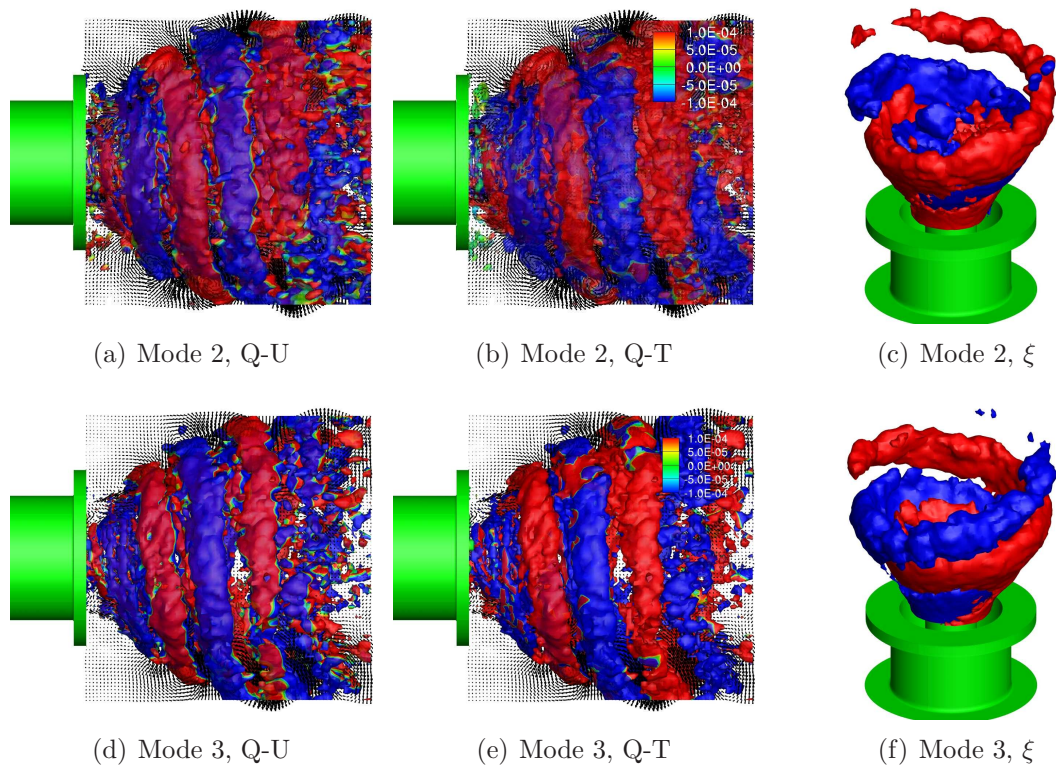
Figure 6.37: Reactive POD mode 2 (a, b, c) and mode 3 (d, e, f). (a, d) $Q-$criterion applied to the corresponding mode coloured by the axial velocity fluctuations. (b, e) $Q-$criterion coloured by the temperature fluctuations. (c, f) Isosurfaces of the mixture fraction fluctuations. The negative fluctuations are plotted in blue, the positive ones in red.

(a) Mode 5, Q-U

(b) Mode 5, Q-T

(c) Mode 5, ξ

(d) Mode 6, Q-U

(e) Mode 6, Q-T

(f) Mode 6, ξ
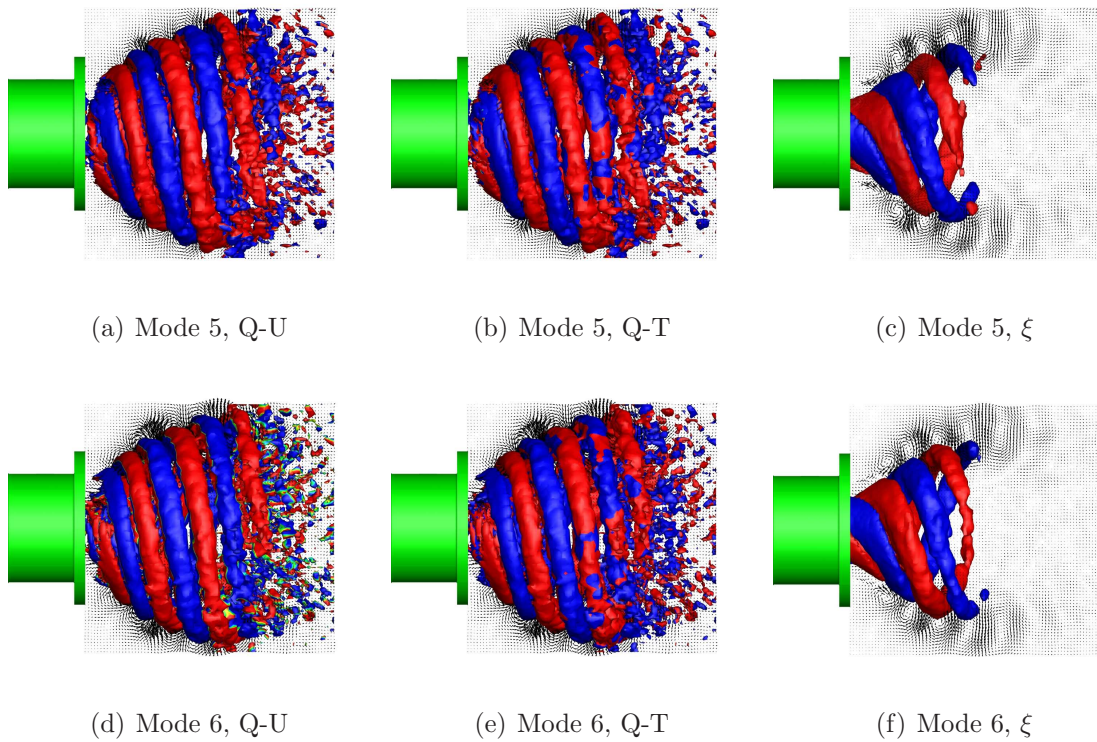
Figure 6.38: Reactive POD mode 5 (a, b, c) and mode 6 (d, e, f). (a, d) $Q-$criterion coloured by the axial velocity fluctuations. (b, e) $Q-$criterion coloured by the temperature fluctuations. (c, f) Isosurfaces of the mixture fraction fluctuations. The negative fluctuations are plotted in blue, the positive ones in red.
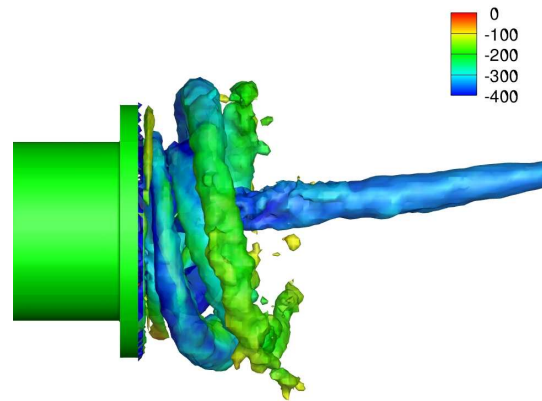
(a)
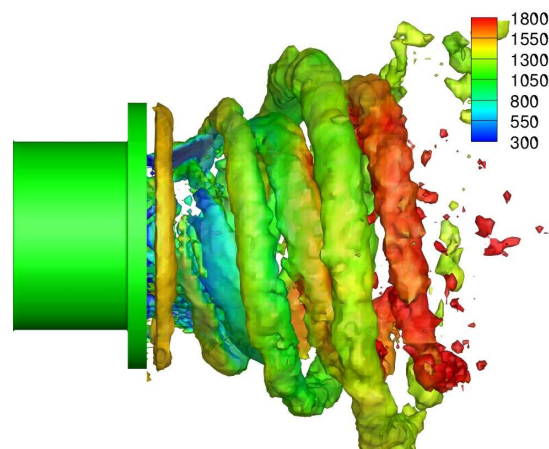
(b)

Figure 6.39: Visualization of the vortex core using the $Q-$criterion applied to a reconstructed snapshot based on modes 1 to 6, coloured by the reconstructed pressure for the inert case (a) and the temperature for the reacting case (b).

Chapter 7

Conditional Moment Closure/Large Eddy Simulation of a lifted non-premixed swirl flame

7.1 Introduction

The confined turbulent swirling non-premixed TECFLAM S09c flame is now investigated using Large Eddy Simulation coupled to the full equations of the Conditional Moment Closure model. The previous chapter has shown that the fluid mechanics of the flame can be succesfully predicted by using a LES-flamelet formulation as long as an appropriate mesh is used and that the right boundary conditions are applied at the numerical inlet (located inside the burner). In Ref. [51], instantaneous chemiluminescence emissions of the flame has been reported and an example is reproduced in Fig. 7.1. The image reveals the area where flame reactions and heat release take place. From the picture, it is evident that the flame is not attached to the nozzle. A lift-off height of 20-30 mm has been reported in Ref. [51]. While the LES-flamelet formulation has ineluctably predicted an attached flame, the CMC model has the capacity to extinguish the CMC cells in which the computational domain has been divided, as it was demonstrated in
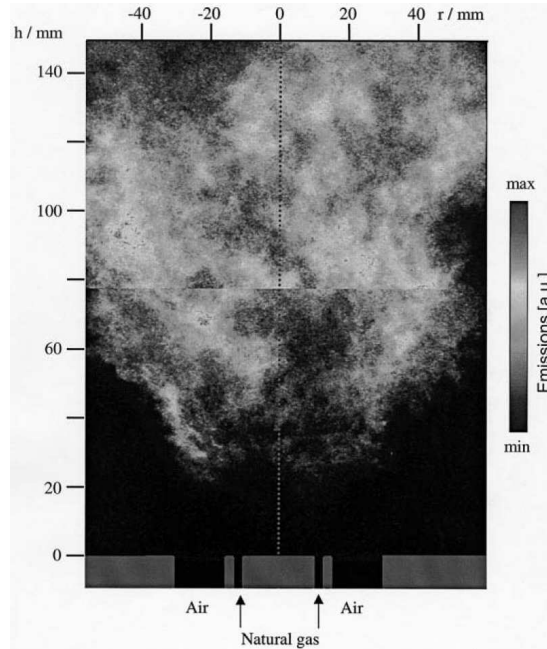
Figure 7.1: Chemiluminescence emission from the TECFLAM flame. From Ref. [51]

Chapter 5. The CMC model coupled to LES and its ability to track the variations of the local scalar dissipation rate had computed strong fluctuations in the reactive scalars distributions against mixture fraction, leading occasionally to the prediction of localized extinctions. Provided that the right boundary conditions are used for the CMC equations, the LES-CMC formulation has therefore, in principle, the ability to reproduce the lift-off observed experimentally in the non-premixed TECFLAM. This is explored in this chapter.

7.2 Method

7.2.1 Models and codes

A first order LES-CMC formulation has been used for this simulation. The codes and models used are fully described in Chapter 3. As for the LES/0D-CMC of the TECFLAM presented in Chapter 6, the CMC equations are computed using
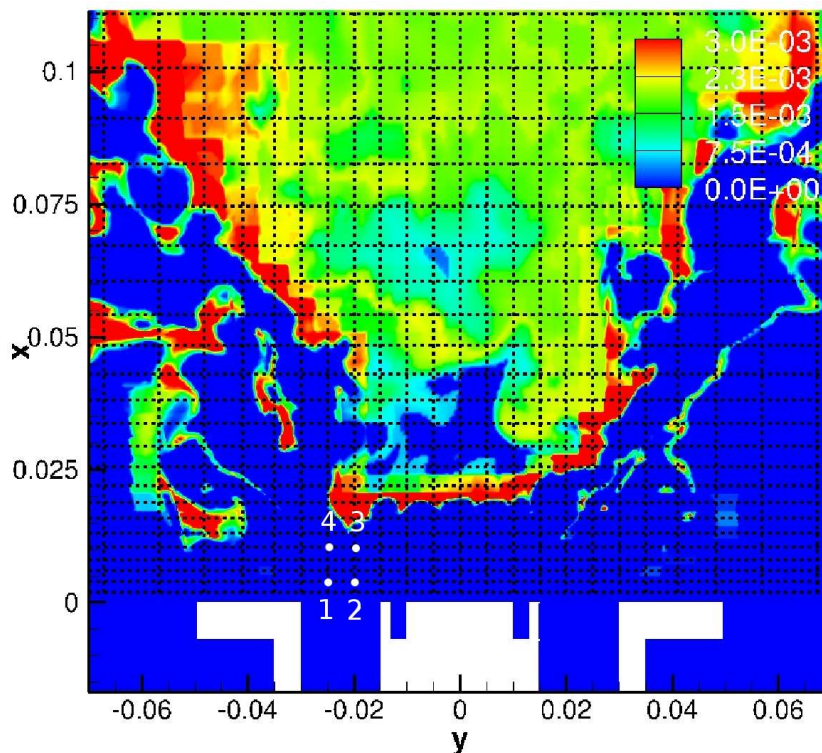
Figure 7.2: CMC grid superimposed on the instantanous OH mass fraction. Each CMC cell has its center located at an intersection of the black dashed lines. Points 1-4 are at locations (x,r)=(0.13D,0.83D), (0.13D,0.67D), (0.35D,0.67D), (0.35D,0.83D) respectively (in mm, with $D = 30$ mm); r is the distance from the centreline and x the axial distance from the bluff body.

the reduced chemistry mechanism ARM2.

7.2.2 Boundary conditions and numerical methods

This new large eddy simulation has been performed on the same grid as the one presented in Chapter 6 for the flamelet model (Fig. 6.2). The LES grid contains 7.8M cells. In this simulation, the CMC equations are solved at each LES iteration on a structured grid of $25 \times 25 \times 30 = 18750$ cells, with 30 cells being used in the axial direction. The CMC grid is shown in Fig. 7.2. From the figure, it is obvious that the CMC cells are clustered around the burner exit in an attempt to follow the dynamics of the air and fuel streams interaction. The inlet for the CMC grid

is located at the exit of the burner ($x = 0$ mm). Inert (i.e. unburnt) distributions of Q_α are injected at the top of the burner for all CMC cells located at a radius smaller than the outer radius of the air pipe ($r < 30$ mm). This corresponds to an area comprising the air and fuel pipes exit plus the top of bluff body. Putting "frozen" Q_α along the top surface of the bluff body mimics flame quenching there. Zero gradients in physical space of all conditional averages have been imposed elsewhere on the edges of the CMC grid. The initial condition for this new LES simulation is the solution computed with the LES/0D-CMC formulation. For the CMC equations, the initial solution used is the burning "flamelet" obtained for $N_0 = 20$ 1/s and presented in the previous Chapter (Fig. 6.4(b)).

The time-step used was still 5.0×10^{-6} s, which ensures a maximum CFL number varying around 0.35 during the whole simulation and a stable computation. The simulations were carried out on 24 quad-core processors at 2.53 GHz with 24 GB of RAM per core, producing 1.0 ms of simulated time in approximately 252 min. Hence solving the CMC equations at each LES iteration increases the computation time by a factor of 2.7 as compared to the LES-flamelet computation.

7.3 Results and Discussion

7.3.1 Instantaneous distributions

The flow and mixing fields experience changes when the CMC equations are solved. The CRZ predicted by the LES/3D-CMC formulation (Figs. 7.3(a) and 7.3(b)) is larger than its 0D-CMC counterpart (Fig. 6.7 of Chapter 6). The CRZ occupies most of the space on the top of the bluff body, resulting in even larger and deeper recirculations inside the air pipe than the ones reported in Chapter 6. As a result, even more fuel enters into the air pipe (see the instantaneous mixture fraction field in Fig. 7.3(c)) and the stoichiometric mixture fraction isoline is found to enter deeper inside the air pipe (Fig. 7.3(b)). The larger CRZ results in the main jet expanding more radially. The shape of the stoichiometric mixture fraction isosurface is also modified. The fuel rich zone of the flame has shrunk to a narrower space located around the fuel jet exit. The fact that the fuel jet is more strongly deflected towards the combustion chamber walls leads to a

(a) Axial velocity

(b) Axial velocity (zoom)

(c) Mixture fraction
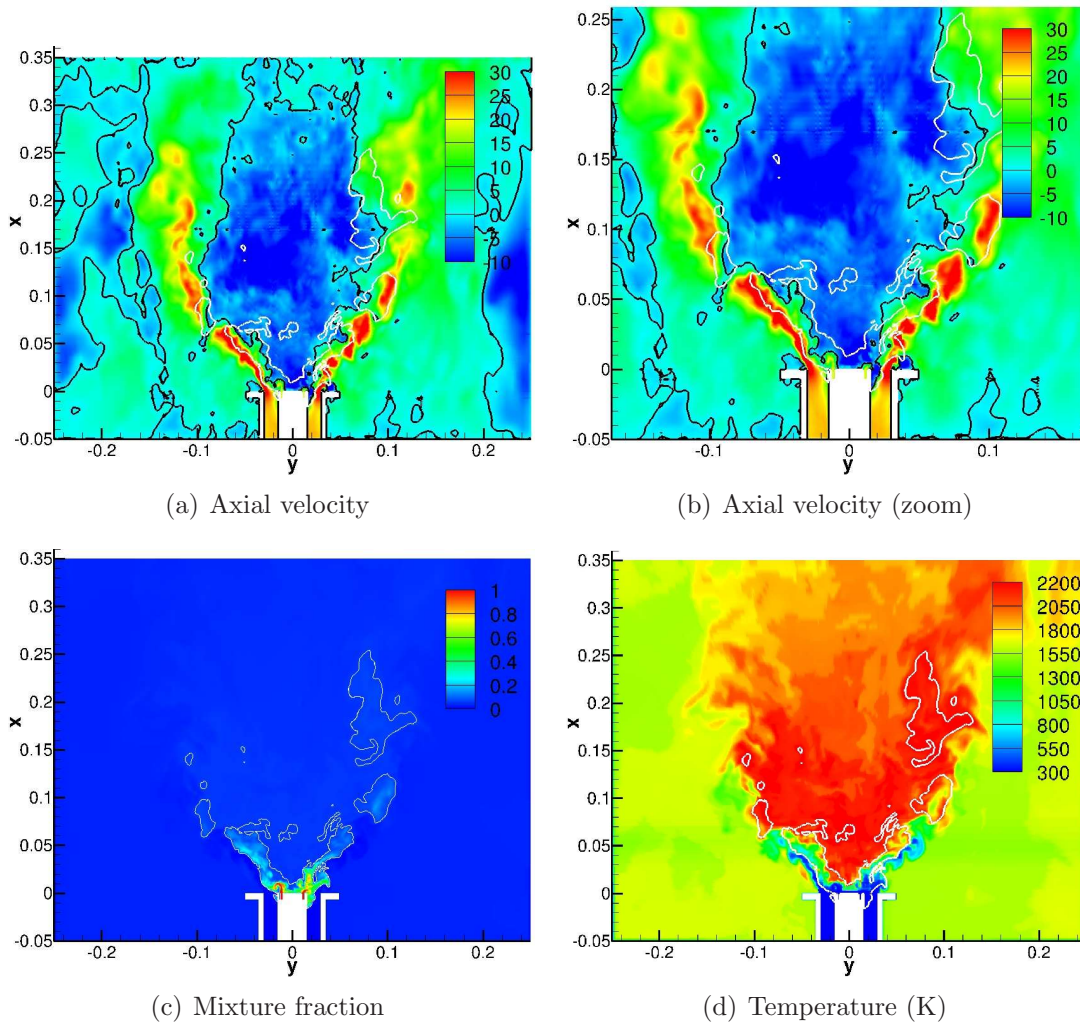
(d) Temperature (K)

Figure 7.3: Typical instantaneous contours of (a, b) the axial velocity, (c) the mixture fraction and (d) the temperature taken at the same instant. The white line represents the stoichiometric iso-surface.

quicker mixing between the fuel and air jets in the shear layers. This explains why the stoichiometric mixture fraction isosurface in the LES/3D-CMC simulation is shorter than its 0D-CMC counterpart, leading to a shorter flame.

In Figs. 7.3(d) and 7.4 the instantaneous contours of the temperature, Y_{OH}, Y_{CO_2}, Y_{NO} and Y_{CO} at the same instant have been ploted. They give an insight on the general shape of the flame. The distribution of these quantities will be commented later in the light of their mean and RMS radial profiles.

7.3.2   Velocity and mixture fraction fields

Figures 7.5, 7.6 and 7.7 show respectively the time-averaged radial profiles of the axial velocity, tangential velocity and mixture fraction. The time-averaging has been conducted over 45 ms and the flow had already been developing for 15 ms from the LES/0D-CMC solution before starting the averaging. Here we focus on the red curves, which correspond to the LES/3D-CMC simulation. The blue curves represent the LES-flamelet (0D-CMC) predictions already presented in Chapter 6, which have been reproduced here for comparison. From these graphs, it is evident that solving the full CMC equations has not improved the flow field prediction compared to the LES/0D-CMC simulation. The 3D-CMC predictions for the mean axial and tangential velocities, which were already good with the flamelet model, have not changed too much for distances up to at least $1D$ (30 mm). Further downstream, for $x \geq 2.33\ D$ (70 mm) the 3D-CMC predictions of the flow field are less good than their 0D-CMC counterparts, but remaining satisfactory. The limited deterioration of the time-averaged velocity prediction for positions far from the burner exit may be due to poor statistical convergence. In fact, the slow computation of the LES/3D-CMC simulation does not allow to gather the same amount of data as for the LES-flamelet simulation presented in Chapter 6. The expansion of the main stream is amplified by the LES/3D-CMC formulation. This results in the axial velocity peak being shifted to higher radial positions for axial positions above $x = 2.33\ D$ (70 mm). The main stream in the 3D-CMC computation is also found to be wider than predicted by the flamelet computation, which results in a decrease of the average peak velocity in the main stream due to mass conservation. The strength of the reverse flow in the Central

(a) Y_{OH}

(b) Y_{CO_2}

(c) Y_{NO}

(d) Y_{CO}
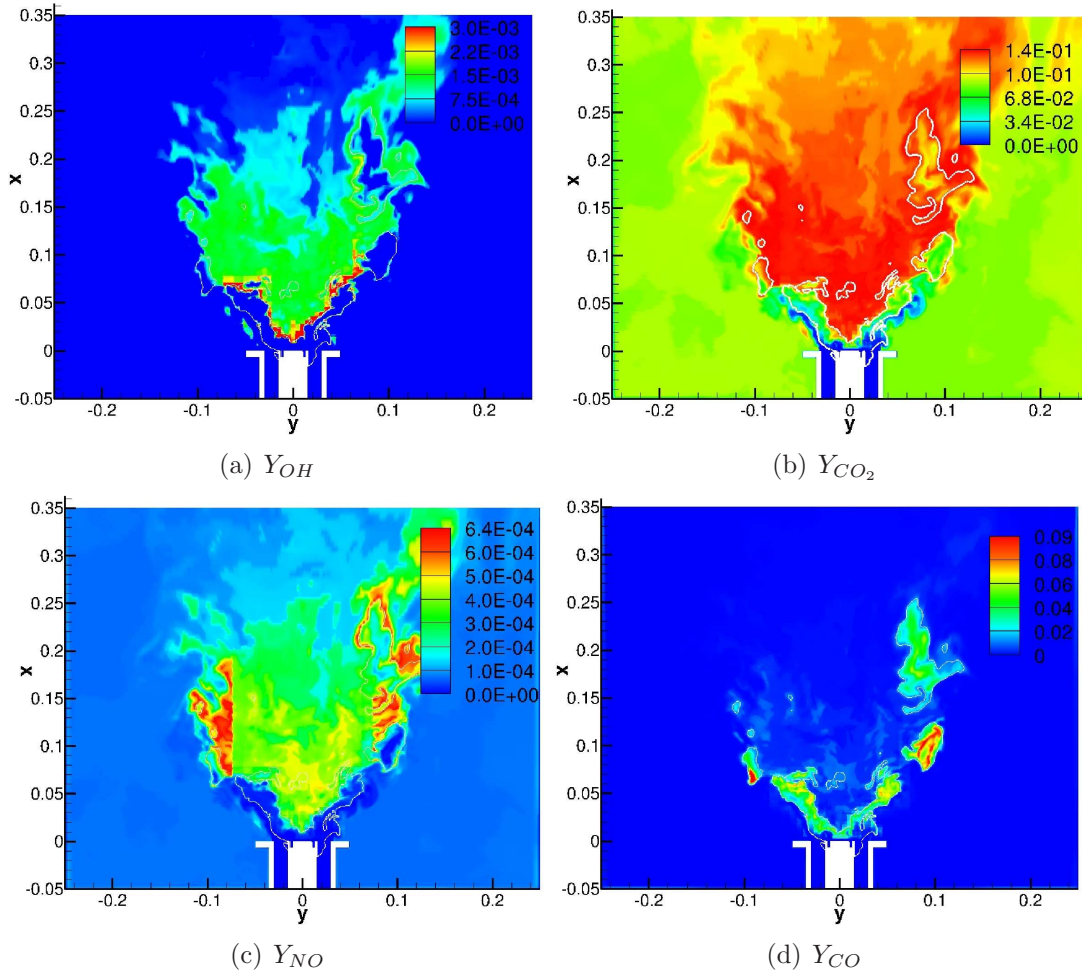
Figure 7.4: Typical instantaneous contours of the mass fraction of (a) OH, (b) CO2, (c) NO and (d) CO taken at the same instant. The white line represents the stoichiometric iso-surface.

Recirculation Zone is still underpredicted at each axial position, with no significant change between the 0D-CMC and 3D-CMC predictions (Fig. 7.5). This underprediction is limited close to the burner exit and tends to extend further as we go downstream. Unlike the flow field, the mixing field has been clearly improved by solving the CMC equations (Fig. 7.7). At $x \leq 0.333\ D$ (20 mm), the mixture fraction peak is predicted at the right radial position in both the 0D-CMC and 3D-CMC formulations. Moreover, the values of the mean mixture fraction peak now match closely the experimental ones, with only a slight underprediction of 5 % at $x = 10$ mm, to be compared to the overprediction of 16.5 % from the 0D-CMC simulation. The mean mixture fraction values along the centreline have also been improved but remained overpredicted by a factor of 2. At $x = 0.667\ D$ (20 mm), the radial profile of the mean mixture fraction matches well the experimental data in terms of both trend and magnitude. For positions above 40 mm ($x \geq 1.33\ D$), the maximum values of the mean mixture fraction, while leveling, become overpredicted as compared to experimental results in both the 0D-CMC and 3D-CMC formulations. Nevertheless solving the CMC equations results in a noticeable improvement in terms of magnitude of the mean mixture fraction, while the positions of its peaks are shifted slightly too far towards the outer part of flow. Overall the LES/3D-CMC results show that the mixing is accelerated as compared to the LES/0D-CMC. This observation is to be related to the previous comments made on the instantaneous flow and mixing fields in Section 7.3.1. The fuel jet is now bent towards the air stream at almost a perpendicular angle. As a consequence, the mixing of the air and fuel is accelerated in the shear layers. It can also be noticed that similar general behaviours were observed in the simulation of the non-swirl Delft-III piloted flame in Chapter 5: solving the CMC equations resulted in variations of the local density strong enough to have modified the flow and mixing fields predicted by the steady flamelet. While these density fluctuations did not result in an improvement of the flow field, the mixing field was however significantly closer to the experimental one.

Looking now at the RMS quantities (in Fig. 7.8 for the axial velocity, Fig. 7.9 for the tangential one, and Fig. 7.10 for ξ), there is no clear difference between the 0D-CMC and 3D-CMC results for positions close to the burner exit ($x \leq 1\ D$),
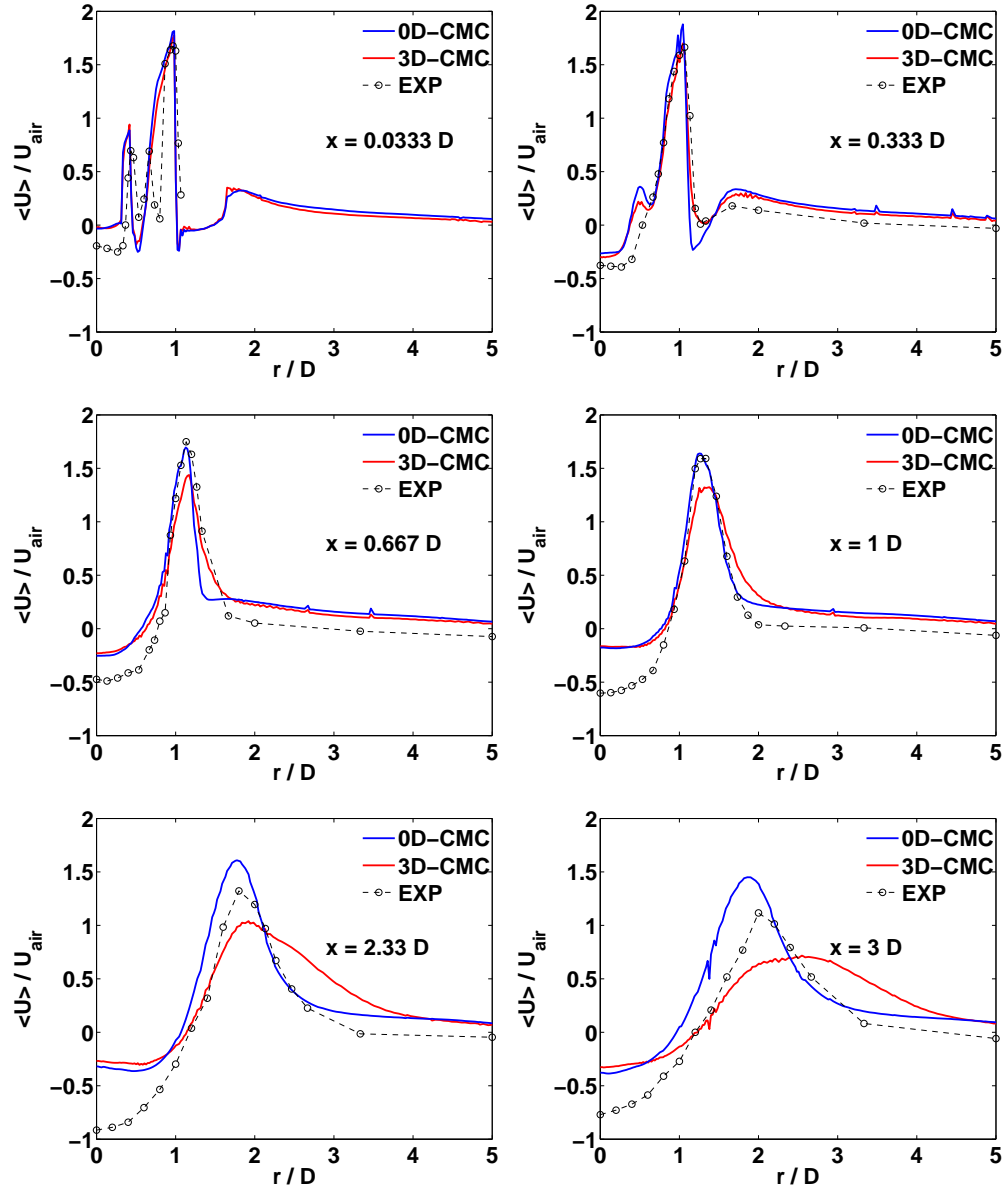
Figure 7.5: Radial profiles of the mean axial velocity at the indicated axial position. Experimental data from Ref. [51].
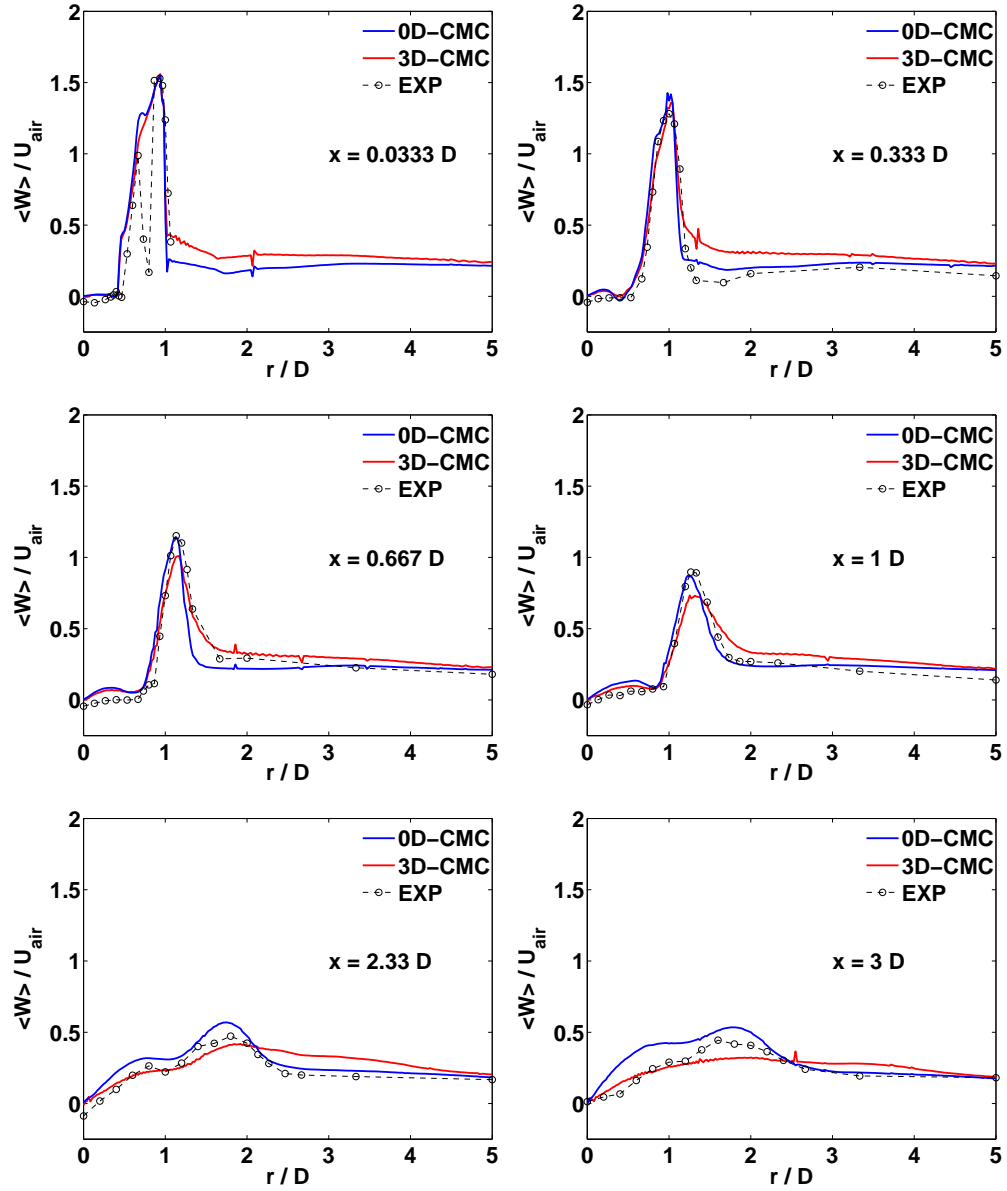
Figure 7.6: Radial profiles of the mean tangential velocity at the indicated axial position. Experimental data from Ref. [51].
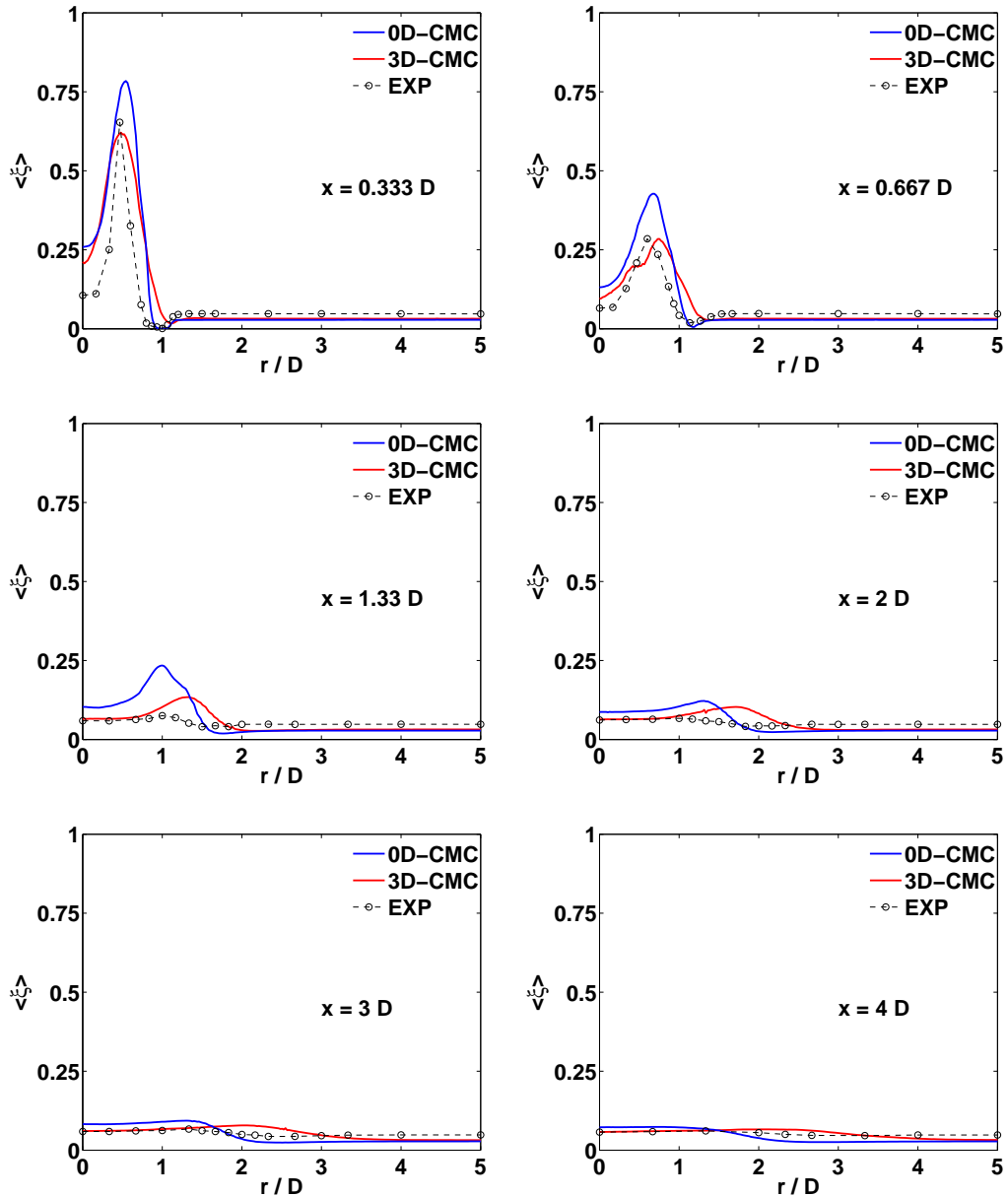
Figure 7.7: Radial profiles of the mean mixture fraction at the indicated axial position. Experimental data from Ref. [51].

and this for both the axial and tangential velocity RMS. Both present a limited underprediction of the RMS of the axial velocity, while the RMS of the tangential velocity is better predicted. Further downstream ($x \geq 1\ D$), the magnitude of the RMS of the axial velocity has increased and is closer to the experimental ones. The tangential RMS velocity are now slightly underpredicted. If we look at the RMS of the mixture fraction from the 3D-CMC simulation, they are found to be lower than their 0D-CMC values. Overall, the peak RMS values of velocities and mixture fraction are shifted towards the outer part of the flow in the 3D-CMC calculations.

7.3.3 Reaction zone and lift-off

The pictures in Fig. 7.11 represent the instantaneous isosurface of the stoichiometric mixture fraction plotted at the same instant as the snapshots in Fig. 7.4. From these figures, it is evident that the $\xi_{st}-$isosurface enters the air pipe and is attached to its inner wall. The mechanism responsible for the presence of the fuel inside the air pipe has been extensively described in Chapter 6. If we now look at Fig. 7.11(a), it is evident that, while the $\xi_{st}-$contour enters the burner, the flame does not and is lifted at a height of around 20 mm i.e 2/3 D. This is consistent with the experimental lift-off height of 20 mm reported in Ref. [51]. Figure 7.2 is a zoom of the Y_{OH} contour around the burner exit from which the flame lift-off height is also evident.

Studying again Fig. 7.11(a), we observed that Y_{OH} varies strongly in space at locations where the flow is burning (see also Fig. 7.4(a) with the white line corresponding to the stoichiometric mixture fraction) as well as in time. The highest values of Y_{OH} are found in a space located between the flame root (around $x = 2/3\ D$) and a height of around 2.5 D (75 mm). Further downstream, zones of high Y_{OH} as well as dark zones can be found. These comments are consistent with the observations reported in Ref. [51] through the record of the experimental chemiluminescence emissions. $\xi_{st}-$contour has also been coloured by the temperature in Fig. 7.11(b), Y_{NO} in Fig. 7.11(c) and Y_{CO} in Fig. 7.11(d) and these figures will be commented later in the text.
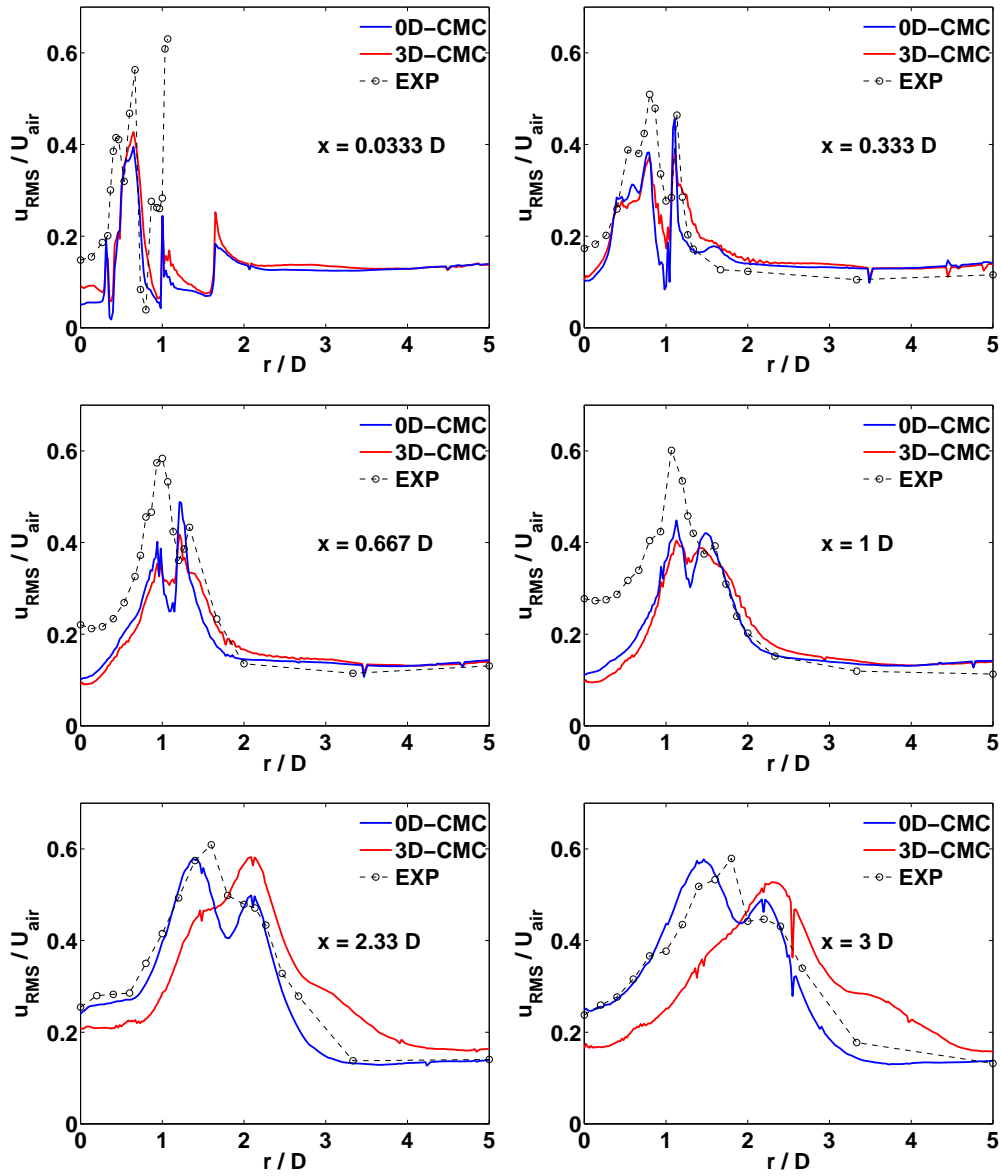
Figure 7.8: Radial profiles of the RMS of the axial velocity at the indicated axial position. Experimental data from Ref. [51].
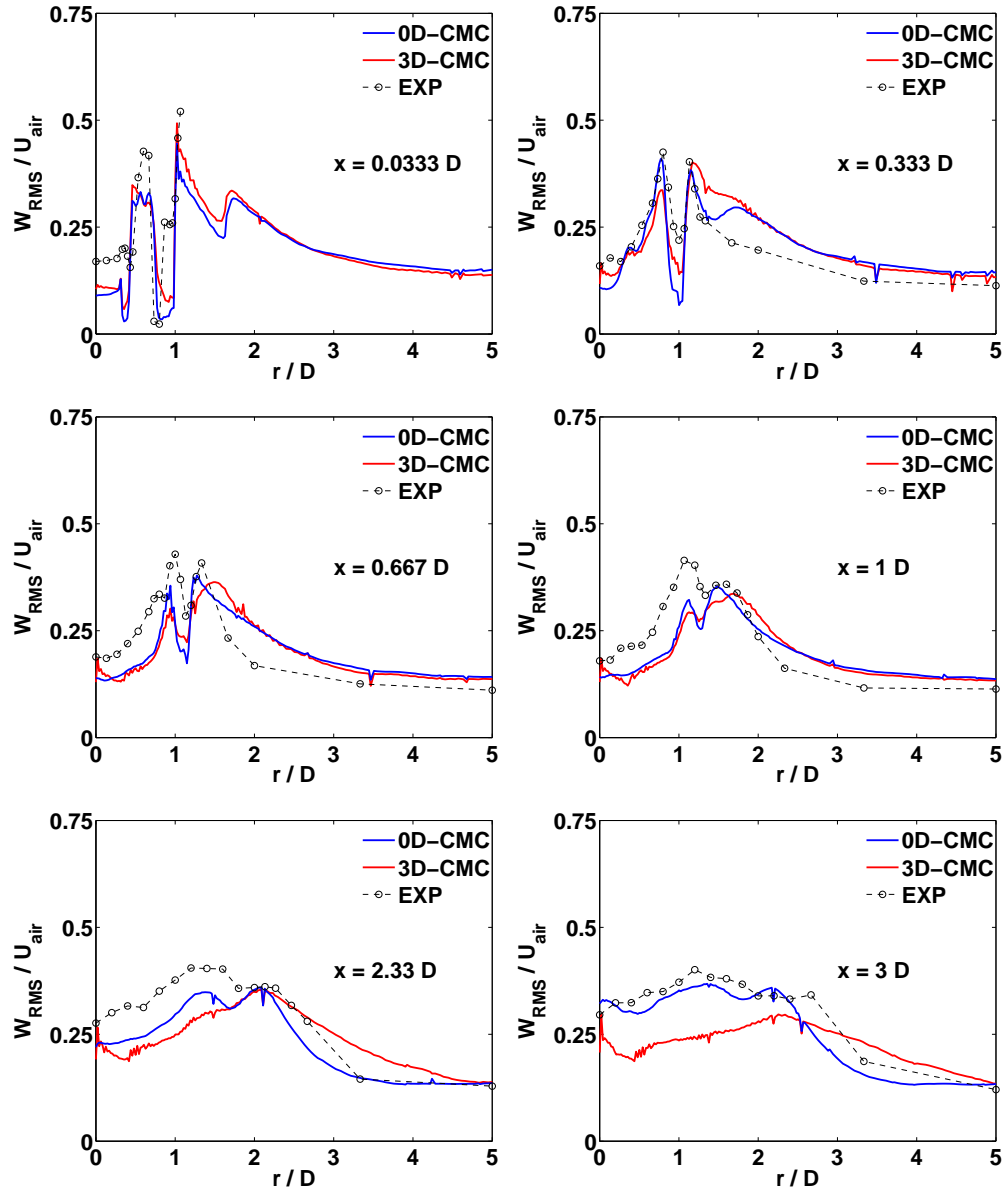
Figure 7.9: Radial profiles of the RMS of the tangential velocity at the indicated axial position. Experimental data from Ref. [51].
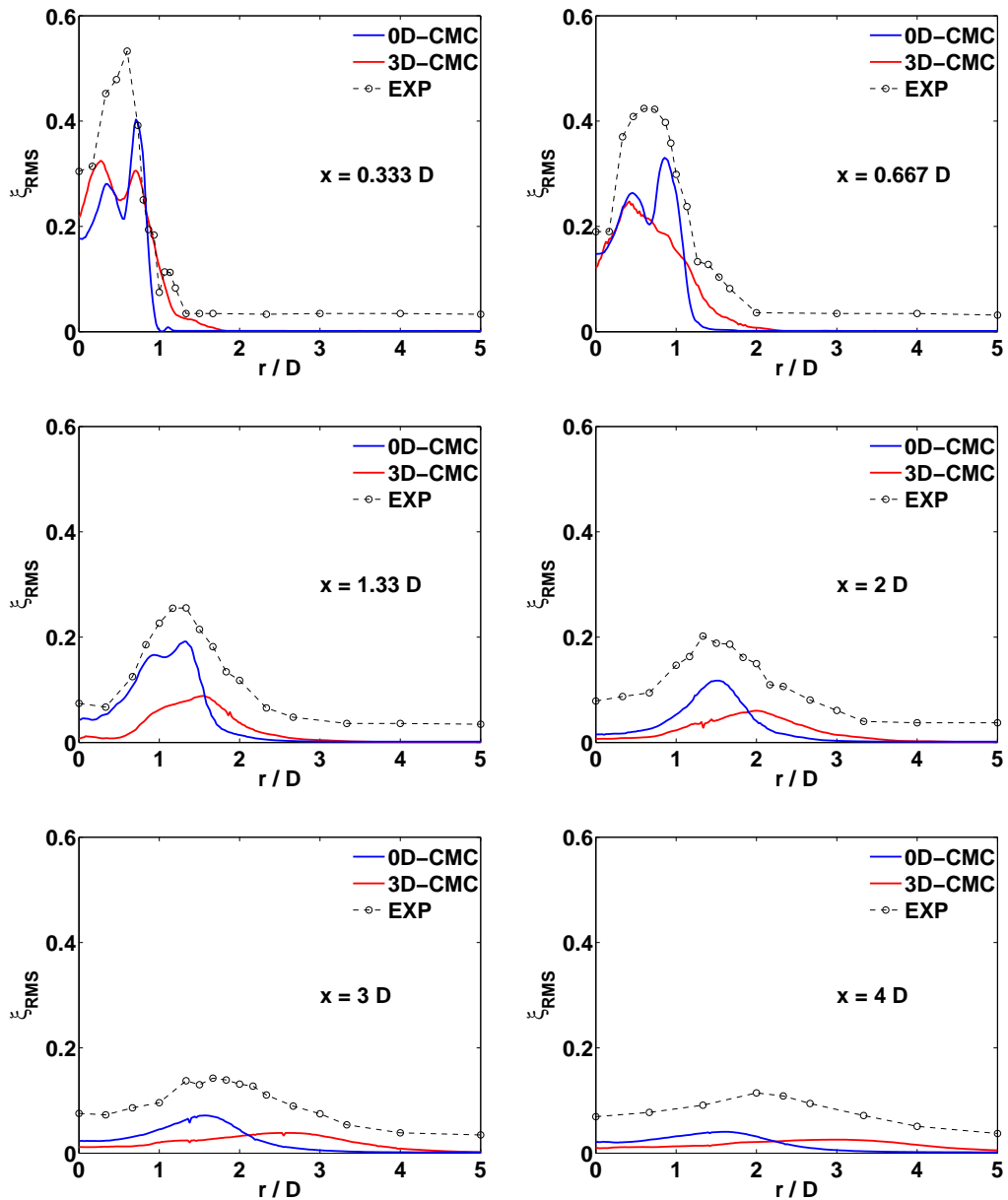
Figure 7.10: Radial profiles of the RMS of the mixture fraction at the indicated axial position. Experimental data from Ref. [51].
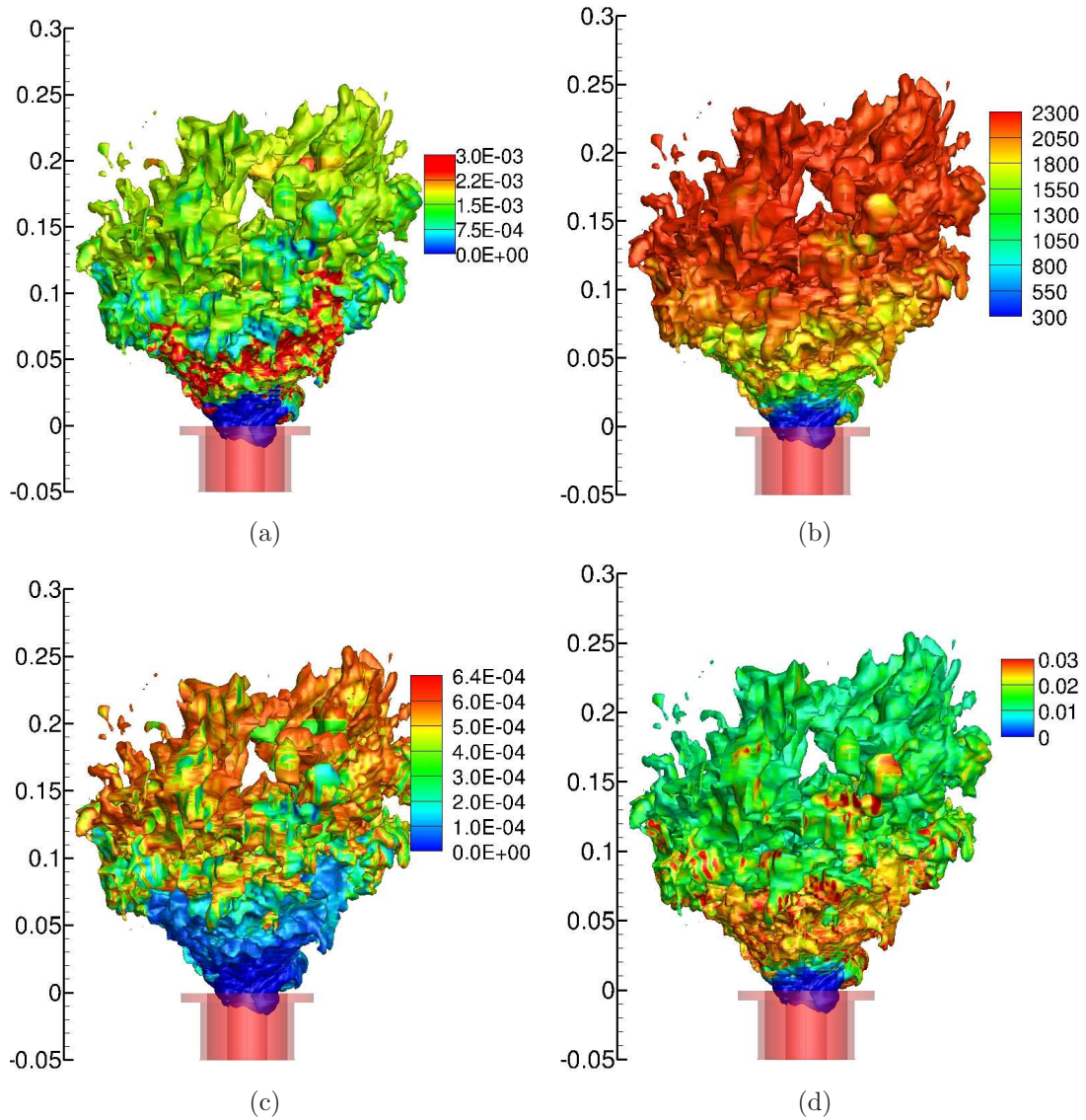
Figure 7.11: Typical instantaneous contours of the stoichiometric mixture fraction coloured by (a) OH mass fraction, (b) the temperature (K), (c) NO mass fraction and (d) CO mass fraction.

7.3.4 Flame dynamics and lift-off

Conditional distributions In order to understand the phenomenon responsible for the flame lift-off, the conditional profiles of $\widetilde{T|\xi}$ and $\widetilde{Y_{OH}|\xi}$ have been plotted in Figs. 7.12 and 7.14 at different instants and positions in the flow, while $\widetilde{Y_{CO}|\xi}$ and $\widetilde{Y_{NO}|\xi}$ are reported in Figs. 7.13 and 7.15. The corresponding $\widetilde{N|\eta}$ have also been plotted to correlate the fluctuations of the conditional distributions to the fluctuations from the mixing field and thus understand the dynamics of the flame. The distributions of several CMC cells located at two different radial positions above the burner exit have been analyzed. A first set of CMC cells distributions has been plotted in Figs. 7.12 and 7.13. They are located at $r = 0.83\ D$ (25 mm) from the centreline, which is along the center of the air annulus exit. Another set of CMC cells distributions is plotted in Figs. 7.14 and 7.15. They correspond to a radial position of $r = 0.67\ D$ (20 mm) from the centreline, which corresponds to a radial position of the inner side of the air pipe.

The CMC cells investigated in the first row of these figures have their center located at $x_c(2) = 4$ mm. They are located just above the CMC cells used to inject the CMC boundary conditions ($x_{c_{BCs}} = 2$ mm) i.e. an inert distribution in $\xi-$space. They are therefore the first cells resolved by the CMC code. We first look at the distributions in mixture fraction space represented in the first row of Figs. 7.12 and 7.13. The corresponding CMC cell has its center located at $x_c = 0.13\ D = 4$ mm and $r_c = 0.83\ D$, and is represented by Point 1 in Fig. 7.2. This point is located just above the middle of the air annulus exit. We note that the conditional temperature remains below 400 K, while the temperature of 300 K is injected at the CMC boundary conditions (BCs). We now look at the distributions in mixture fraction space represented in the first row of Figs. 7.14 and 7.15. The corresponding CMC cell has its center located at $x_c = 0.13\ D = 4$ mm and $r_c = 0.67\ D$ (Point 2 in Fig. 7.2). We note that some of the distributions correspond to burning events, the maximum temperature reaching time to time values as high as 1200 K. The intermittent ignitions occur in spite of overall high values of the scalar dissipation rate. In fact, $\widetilde{N|\eta}$ is found to exceed the scalar dissipation rate extinction limit of the steady flamelet (176 1/s) much often than

at the previous CMC cell location ($r = 0.83\ D$).

Further downstream, at $x = 0.35\ D = 10$ mm, the CMC cell distributions are plotted in the second rows of Figs. 7.12 and 7.13 ($r_c = 0.83\ D$), and Figs. 7.14 and 7.15 ($r_c = 0.67\ D$). The CMC cell located on the side of the inner wall, with $r_c = 0.67\ D$, is denoted by Point 3 in Fig. 7.2. Analysis of its conditional distributions shows that it experiences both fully burning and totally extinguished events. Between these two extreme cases, the conditional profiles of the temperature, Y_{OH} and pollutants mass fractions (Y_{CO} and Y_{NO}) fluctuate throughout a wide range of distributions. The CMC cell located at $r_c = 0.83\ D$ (Point 4 in Fig. 7.2) starts only to experience some burning events in its conditional distributions.

For axial positions $x \geq 0.63\ D$ (19 mm), the CMC cells at $r = 0.67\ D$ show fully burning distributions. As we go further downstream, the temporal variations of $\widetilde{N|\eta}$ become smaller and smaller, leading to limited fluctuations of the $\widetilde{Y_\alpha|\xi}$ distributions, before finally reaching a steady state. The CMC cells at $r = 0.83\ D$ experience a similar behaviour, but for axial positions $x \geq 0.86\ D$ (26 mm).

Time series To investigate further the dynamics of the flame lift-off, Fig. 7.16 shows time-series of the peak conditional scalar dissipation rate (i.e. at $\eta = 0.5$), $\widetilde{T|\xi_{st}}$, $\widetilde{Y_{OH}|\xi_{st}}$, $\widetilde{Y_{NO}|\xi_{st}}$ and $\widetilde{Y_{CO}|\xi_{st}}$, at various locations downstream and at radial locations corresponding again to the middle of the air annulus ($r = 0.83D$, left) and its inner side ($r = 0.67D$, right).

If we first look at the time series corresponding to the radial position of the air annulus center ($r = 0.83D$, Fig. 7.16 left), we see that $\widetilde{N|\eta}_{max}$ fluctuates strongly with time at positions close to the burner exit, crossing occasionally the 0D-CMC extinction limit of 176 1/s for $x/D = 0.2$ (axial position of 6 mm). A peak value of 400 1/s is observable. As we go further downstream, the scalar dissipation rate tends to relax and at $x/D = 1$ (axial position of 30 mm) it remains below 20 1/s.

Let us now analyse the curves of $\widetilde{Y_\alpha|\xi_{st}}$ against time. The curve of $\widetilde{Y_{OH}|\xi_{st}}$ shows that the flamelets corresponding to the CMC cells are not fully burning for axial positions below (at least) $x = 1D$ (30 mm). Between the inert distribution injected at the CMC BCs ($x/D = 0.07$, $x = 2$ mm) and the fully burning state, the flow experiences a series of intermediate states. These different states
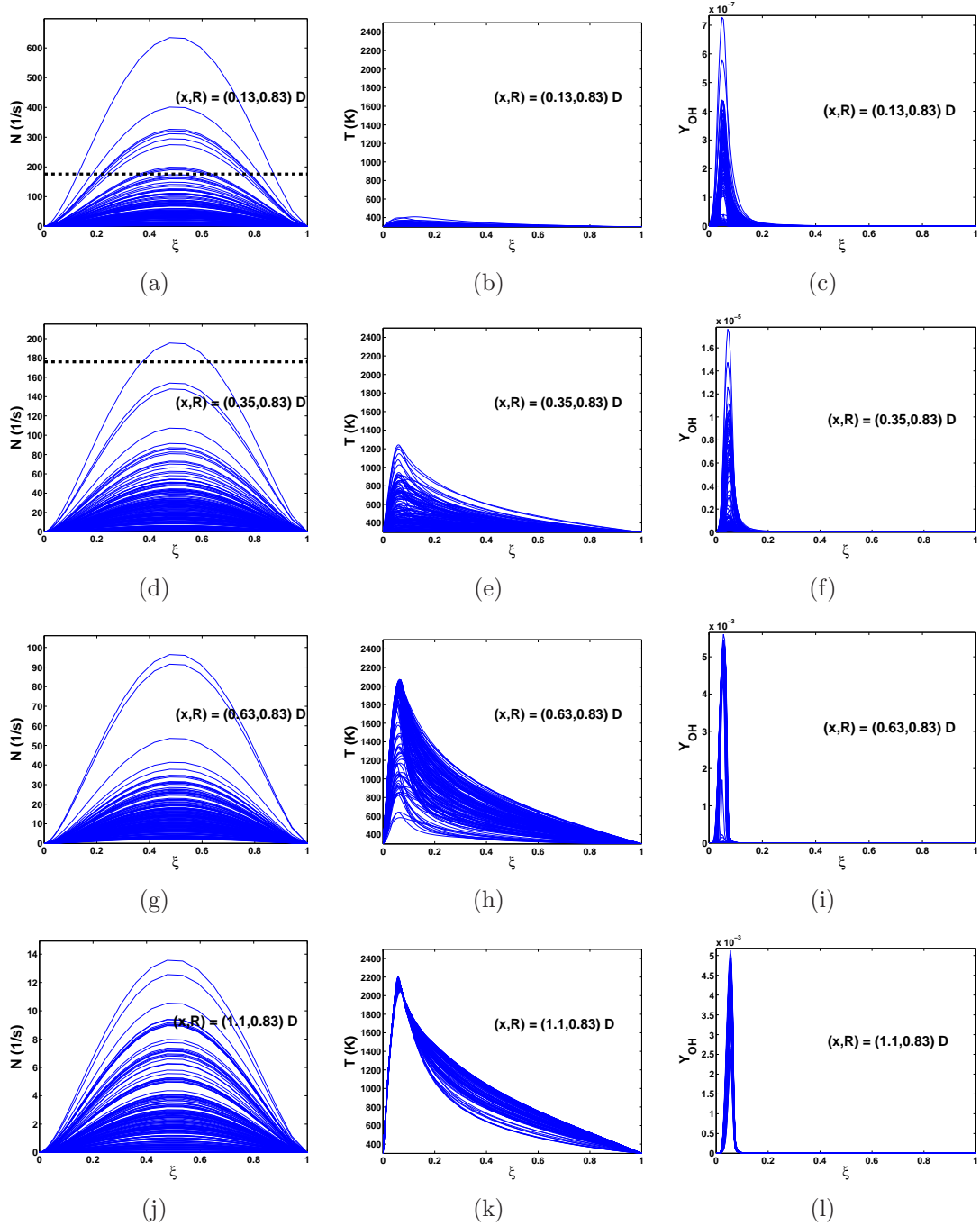
Figure 7.12: Instantaneous conditional ("CMC") profiles at several consecutive instants of N (scalar dissipation rate), T and OH mass fractions at the indicated axial positions and at $r = 0.83\ D$ (25 mm).
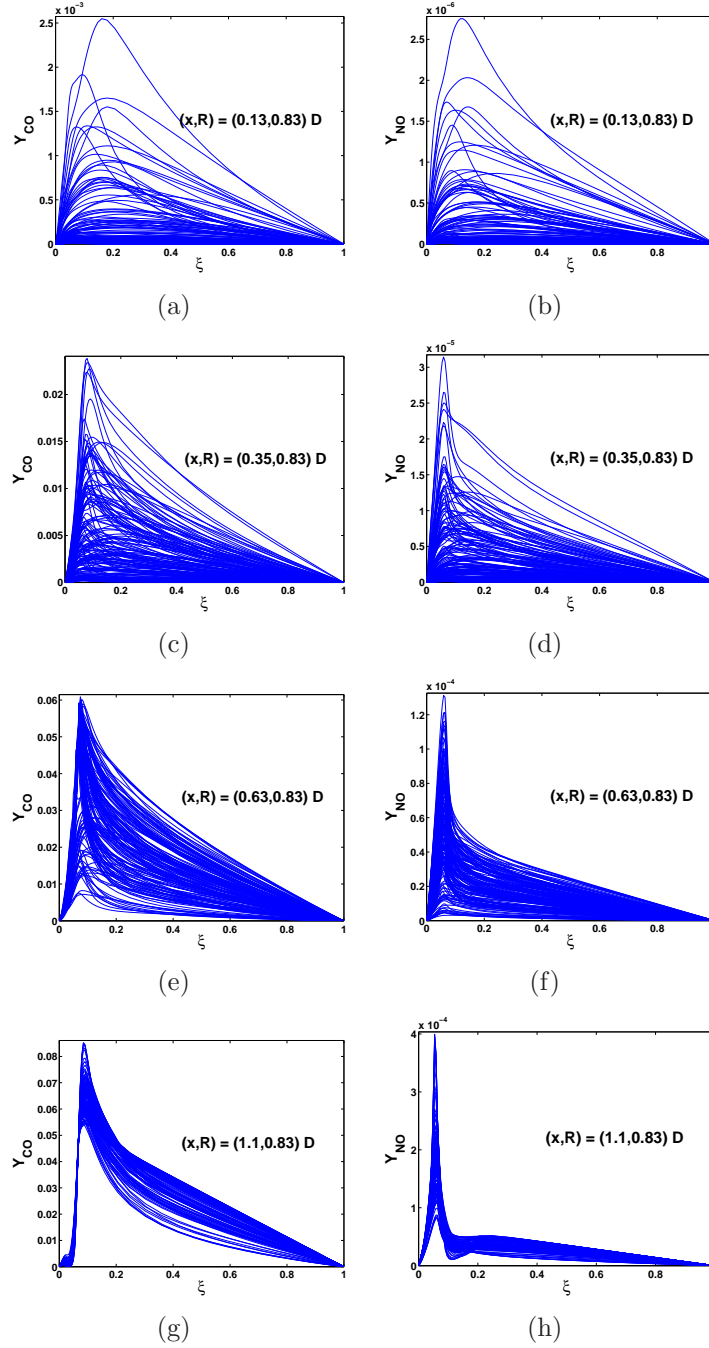
Figure 7.13: Instantaneous conditional ("CMC") profiles at several consecutive instants of CO and NO mass fractions at the indicated axial positions and at $r = 0.83\ D$ (25 mm).
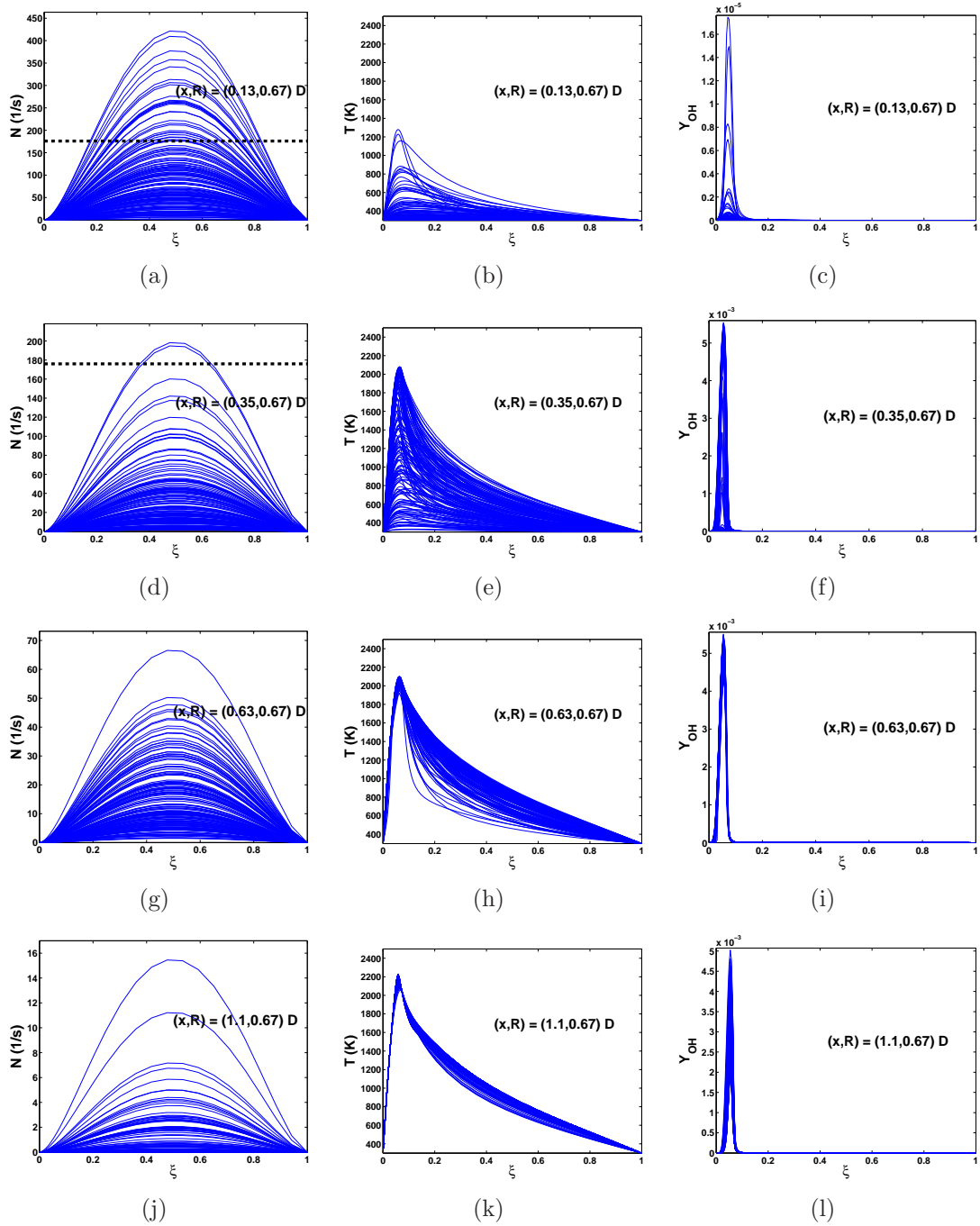
Figure 7.14: Instantaneous conditional ("CMC") profiles at several consecutive instants of N (scalar dissipation rate), T and OH mass fractions at the indicated axial positions and at $r = 0.67\ D$ (20 mm).
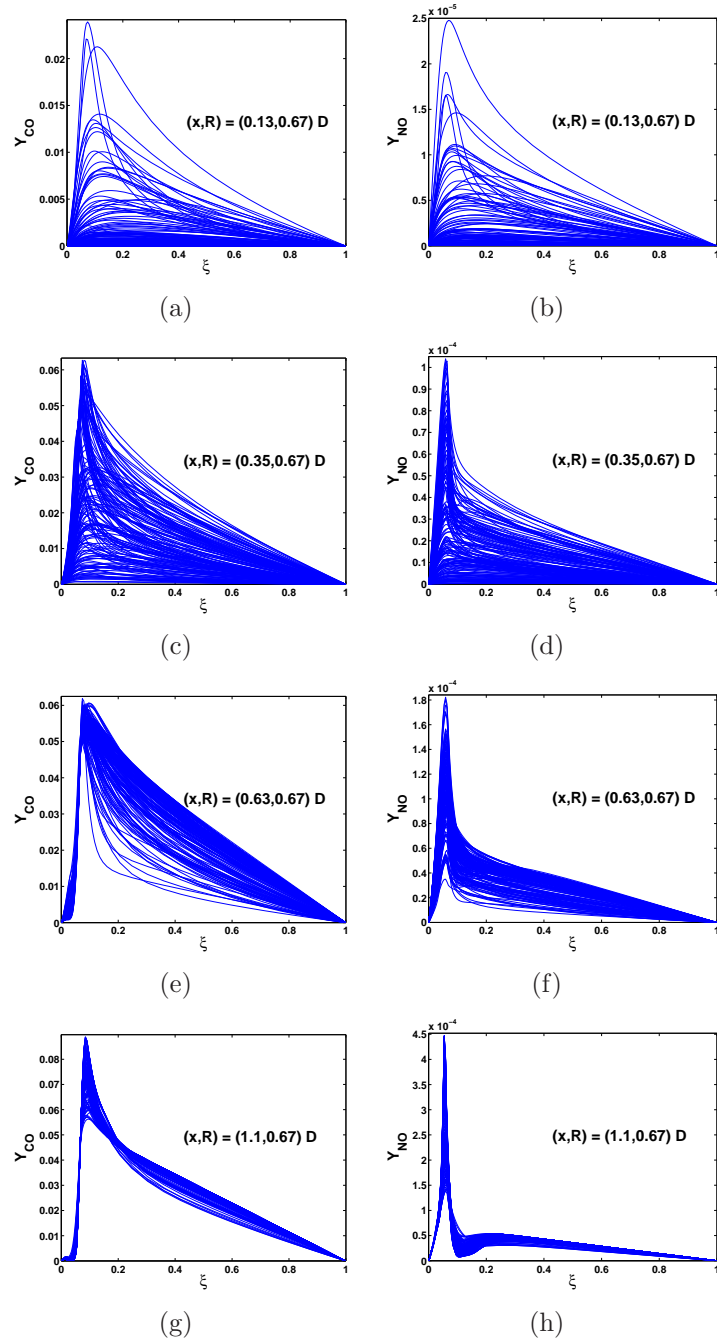
Figure 7.15: Instantaneous conditional ("CMC") profiles at several consecutive instants of CO and NO mass fractions at the indicated axial positions and at $r = 0.67\ D$ (20 mm).

correspond to the ignition process of the flamelet and their analysis provides insights on the flame lift-off dynamics. At $x/D = 0.2$ (6 mm), the stoichiometric temperature remains mainly the one of the inert flamelet injected at BCs (i.e. 300 K), with some small overshoots reaching occasionally a temperature of 700 K. $\widetilde{Y_{OH}|\xi_{st}}$, $\widetilde{Y_{NO}|\xi_{st}}$ and $\widetilde{Y_{CO}|\xi_{st}}$ remain equal or very close to zero, showing that the flow is not burning at this position.

At $x/D = 0.4$ (12 mm), $\widetilde{T|\xi_{st}}$ shows significant fluctuations, with overall a clear increase of the stoichiometric temperature, which reaches values as high as 1750 K. However, $\widetilde{Y_{OH}|\xi_{st}}$ remains overall close to zero, with the exception of a clear overshoot at time $t = 0.0425$ s. The flamelet at $x/D = 0.5$ (15 mm) shows the same general behaviour as the one at $x/D = 0.4$ (12 mm), but the temperature has now increased further and reaches occasionally 2000 K. The number of overshoots of $\widetilde{Y_{OH}|\xi_{st}}$ against time has also considerably increased, but they are not sufficient to fully ignite the flamelet. For radial positions around $r = 0.83D$ (corresponding to the radius of the air annulus middle), the area located from $x/D = 0.2$ to $x/D = 0.5$ (i.e. from $x = 6$ mm to $x = 15$ mm) corresponds to the pre-heat zone of the flame. In this area, NO emissions are found to remain low, while CO emissions can occasionally reach value corresponding to a fully burning flamelet. From this observation, it can be concluded that the flame lift-off height has a value between 15 mm to 30 mm at radial positions of $r = 0.83D$ i.e. above the air annulus middle, which is again consistent with the lift-off height of 20 mm reported experimentally [51].

If now we investigate the time series from the CMC cells located above the inner wall of the air pipe ($r = 0.67D$, Fig. 7.16 right), we can see the same general behaviour that leads to the full ignition of the flame. However, the process is found to occur faster at these locations than at the previous ones. For instance, the flamelets are found to be already fully burning at $x/D = 0.5$ (15 mm). As a consequence, the pre-heat zone is located at lower axial positions ($0.2 \le x/D \le 0.4$, or in mm: $6 \le x \le 12$) and the flame lift-off height at this radial position is reduced.

The reason for this faster ignition process as we go closer to the radial position of the air annulus inner wall is to be found in the dynamics of the flow and the stabilization process of this flame. As no pilot is present in this flame, the ignition
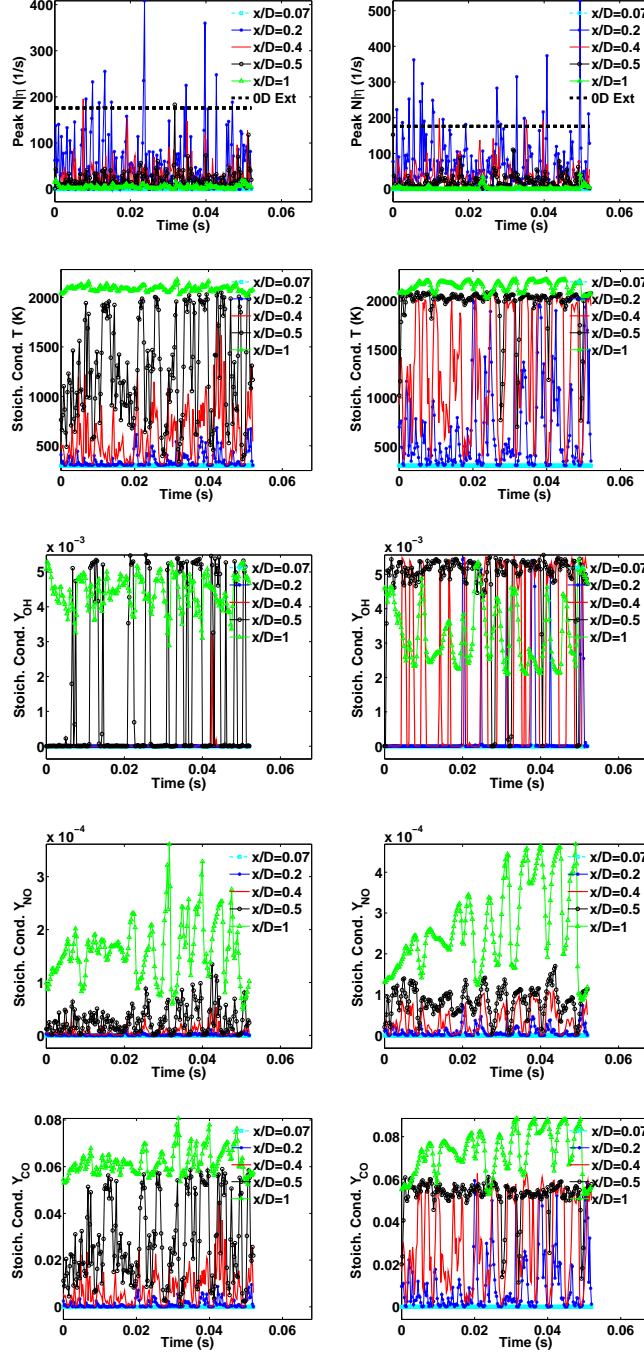
Figure 7.16: Time series of $\widetilde{N|0.5}$, $\widetilde{T|\xi_{st}}$, $\widetilde{Y_{OH}|\xi_{st}}$, $\widetilde{Y_{NO}|\xi_{st}}$ and $\widetilde{Y_{CO}|\xi_{st}}$ at $r = 0.83D$ (left) and at $r = 0.67D$ (right) at the indicated x. The black dotted lines on the top two graphs refer to the extinction value of the scalar dissipation rate (176 1/s).

of the cold flamelets injected at the burner exit has to be done by convection and diffusion of burning flamelets from neighbouring cells. Animations of the mass fraction of the reactive scalars (see sequence of snapshots in Fig. 7.17 for the temperature and in Fig. 7.18 for Y_{OH}) show the same process of fluid ignition as seen from its integrated point of view i.e. through the unconditional values of the reactive scalars. This process is mainly due to the action of the CRZ coupled to the dynamics of the burner flow created by the Rotating Vortex Cores described in Chapter 6. The CRZ carries upstream some burning flamelets towards the top of the bluff body. At some point, these burning flamelets may encounter the inert flamelet from and carried away by the air flow. This results in the slow ignition process of the local CMC cells as observed at $r = 0.83D$ in the left part of Fig. 7.16. On top of that, POD analysis in Chapter 6 has revealed that PVC-like structures create strong recirculations that occur periodically at a given position along the air annulus inner wall and just above it. When the flame is burning, these recirculations tend to periodically suck the burning flamelets above the bluff body towards the air pipe, decreasing the axial distance necessary for the inert mixture to fully ignite.

7.3.5   Temperature, species and pollutants prediction

Figure 7.3(d) shows an instantaneous contour of the temperature (in Kelvin) and Fig. 7.11(b) shows the stoichiometric mixture fraction instantaneous contour coloured by the temperature. From Fig. 7.11(b), the flame lift-off is evident with the temperature of the flame increasing gradually as one moves downstream. Figure 7.11(c) shows the same instantaneous contour coloured this time by Y_{NO}. From this figure, it is clear that the area of maximum NO mass fraction correspond to the area of maximum temperature i.e. at the top of the flame. As for the Delft flame emissions in Chapter 5, a temperature threshold is evident, the emissions of NO remaining very low for temperature below about 1800 K. In Fig. 7.11(d), the stoichiometric contour has now been coloured by Y_{CO}. While CO mass fraction close to the burner exit is zero as a consequence of the flame lift-off, the area of high CO mass fraction is located between the root of the flame (around $x = 20$ mm) and a height of around 80 mm. The CO mass fraction is
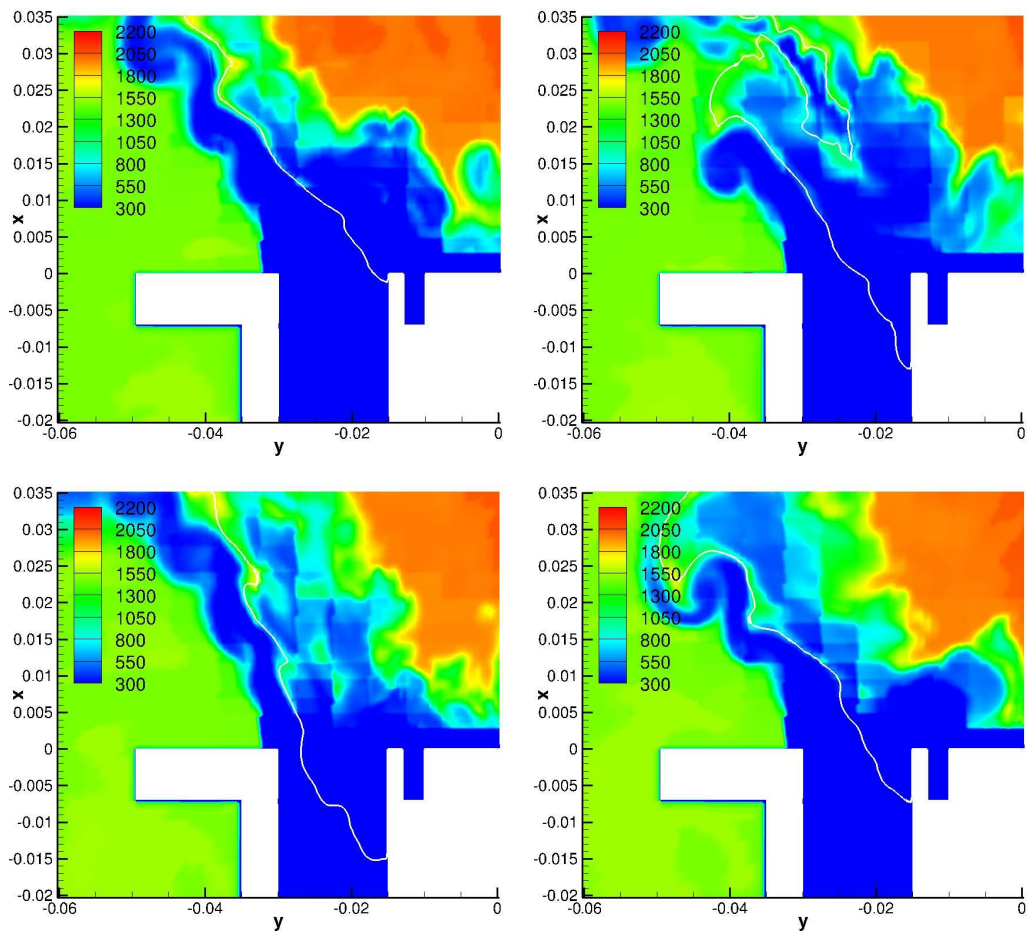
Figure 7.17: Sequence of instantaneous contours of the temperature at different instants separated by 1 ms (from left to right). The white lines represent the stoichiometric isolines.
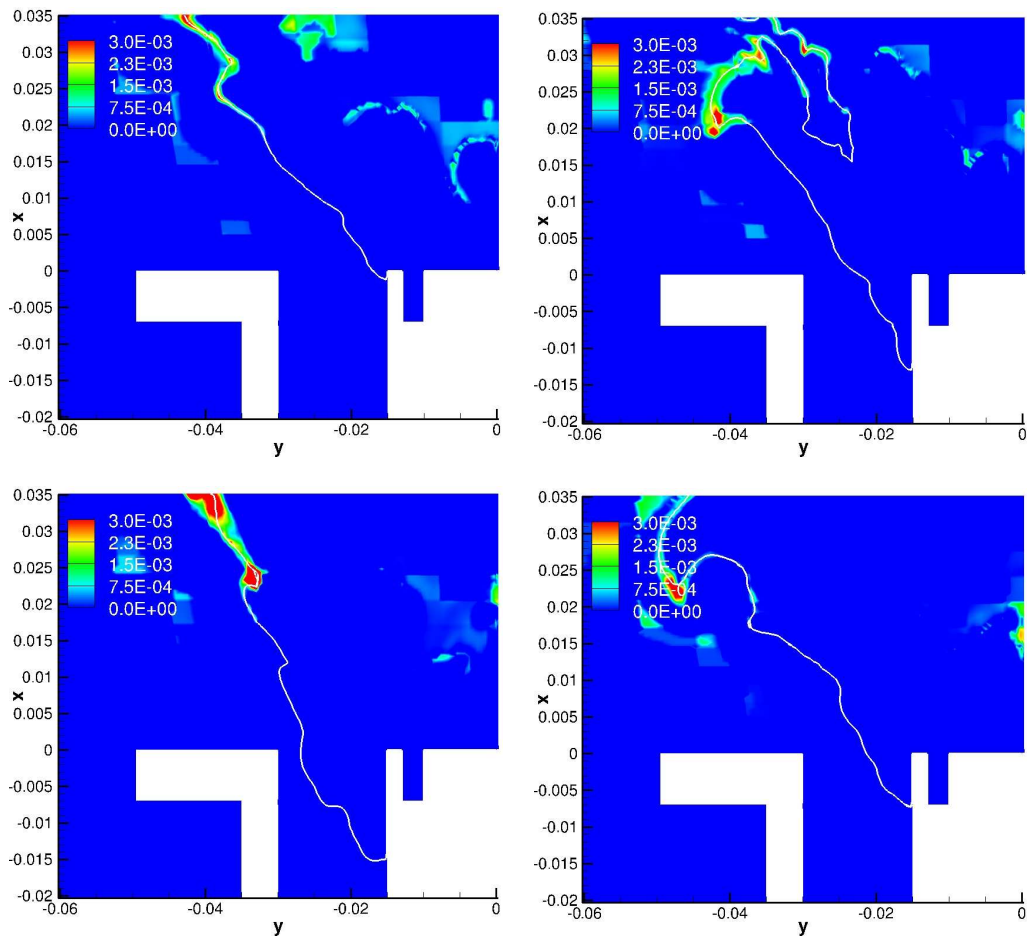
Figure 7.18: Sequence of instantaneous contours of Y_{OH} at different instants separated by 1 ms (from left to right). The white lines represent the stoichiometric isolines.

then found to decrease as we go further downstream. Instantaneous contours of CO_2, NO and CO emissions are also presented in Figs. 7.4(b), 7.4(c) and 7.4(d) respectively. High levels of CO_2 are found to develop inside the CRZ. Relatively high levels of NO emissions are also produced in the CRZ, while CO emissions are mainly localized along the stoichiometric mixture fraction isoline.

The radial profiles of the mean temperature are plotted in Fig. 7.19. They show that there has been an improvement in the prediction of the temperature for positions located between the CRZ and the ORZ. In fact, the LES/0D-CMC formulation had predicted a peak of temperature inside the shear layer where the fuel and air jets mix up for axial positions below 1.33 D (40 mm). The LES/3D-CMC formulation, because of its ability to capture the flame lift-off, do not predict this peak of temperature. The model captures accurately the temperature inside the CRZ and main stream close to the burner for positions up to 20 mm, but overpredict the temperature between the main stream and the combustion chamber walls. As we go further downstream, the temperature becomes more and more overpredicted at each radial position of the flow. The absence of modelling for the cooling system present in the TECFLAM configuration that maintains the walls at 300 K is probably responsible for the general overprediction of the temperature far from the burner exit. The radial profiles of the temperature RMS match well the experimental values in terms of trend and magnitude close to the burner, before becoming increasingly underpredicted as we go further downstream.

The radial profiles of the mean Y_{CH4}, Y_{O2}, Y_{H_2O}, Y_{CO_2} and Y_{CO} are presented respectively in Figs. 7.21, 7.23, 7.25, 7.27 and 7.29. A general observation of the species predictions is that a good match with the experimental data is reached at positions close to the burner exit. In the flow between the main stream and the combustion chamber walls (i.e at high radial positions), the discrepancies in terms of magnitude are generally significant, while both the trend and magnitude predictions worsen as we go further downstream. The radial profiles of the RMS of these quantities (Figs. 7.22, 7.24, 7.26, 7.28 and 7.30 respectively) are generally predicted satisfactorily in terms of trends, but become increasingly underpredicted as we go further dowsntream. Regarding the pollutants prediction, no experimental data was reported for NO. The radial profile of the mean Y_{CO}
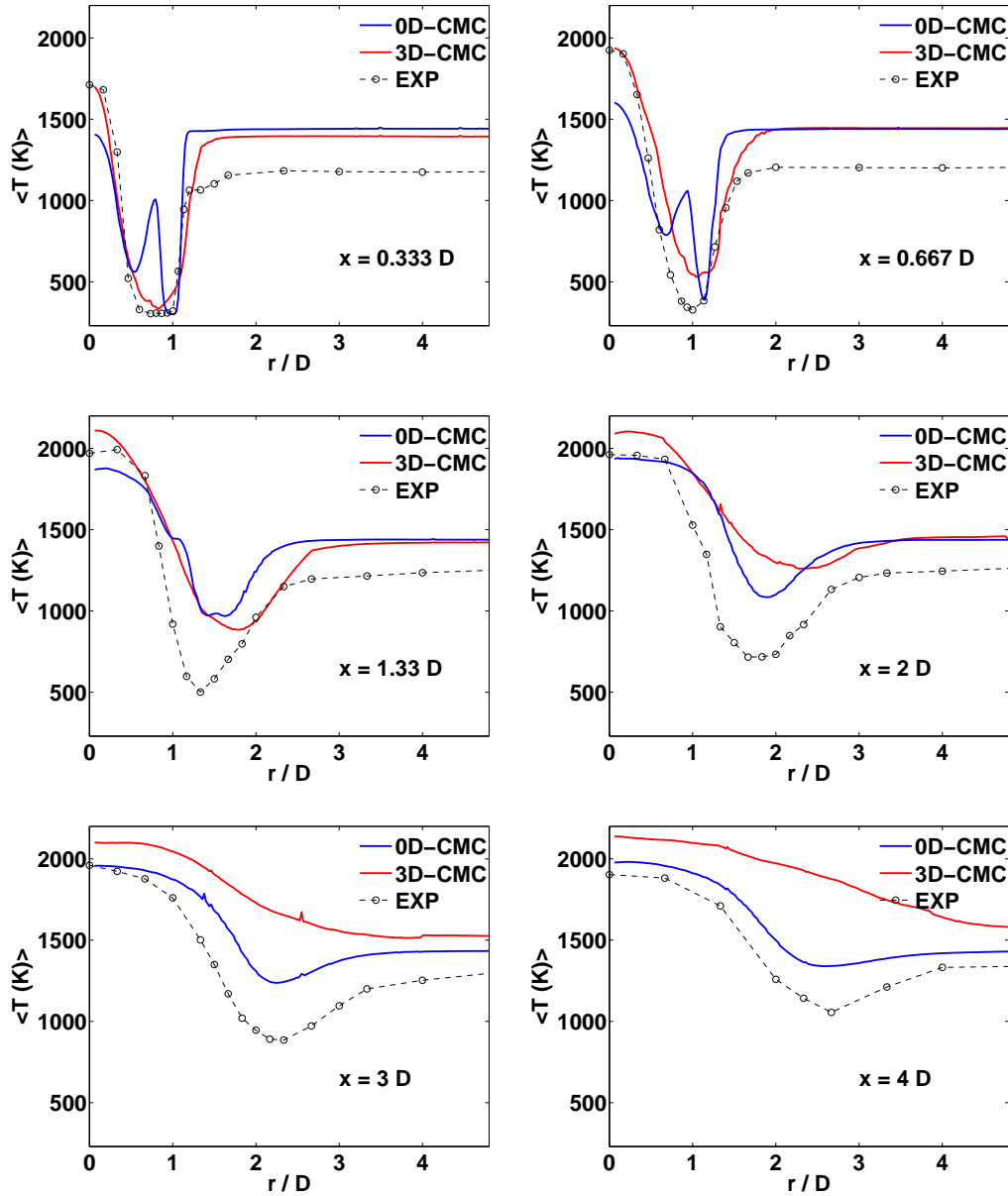
Figure 7.19: Radial profiles of the mean temperature at the indicated axial position. Experimental data from Ref. [51].
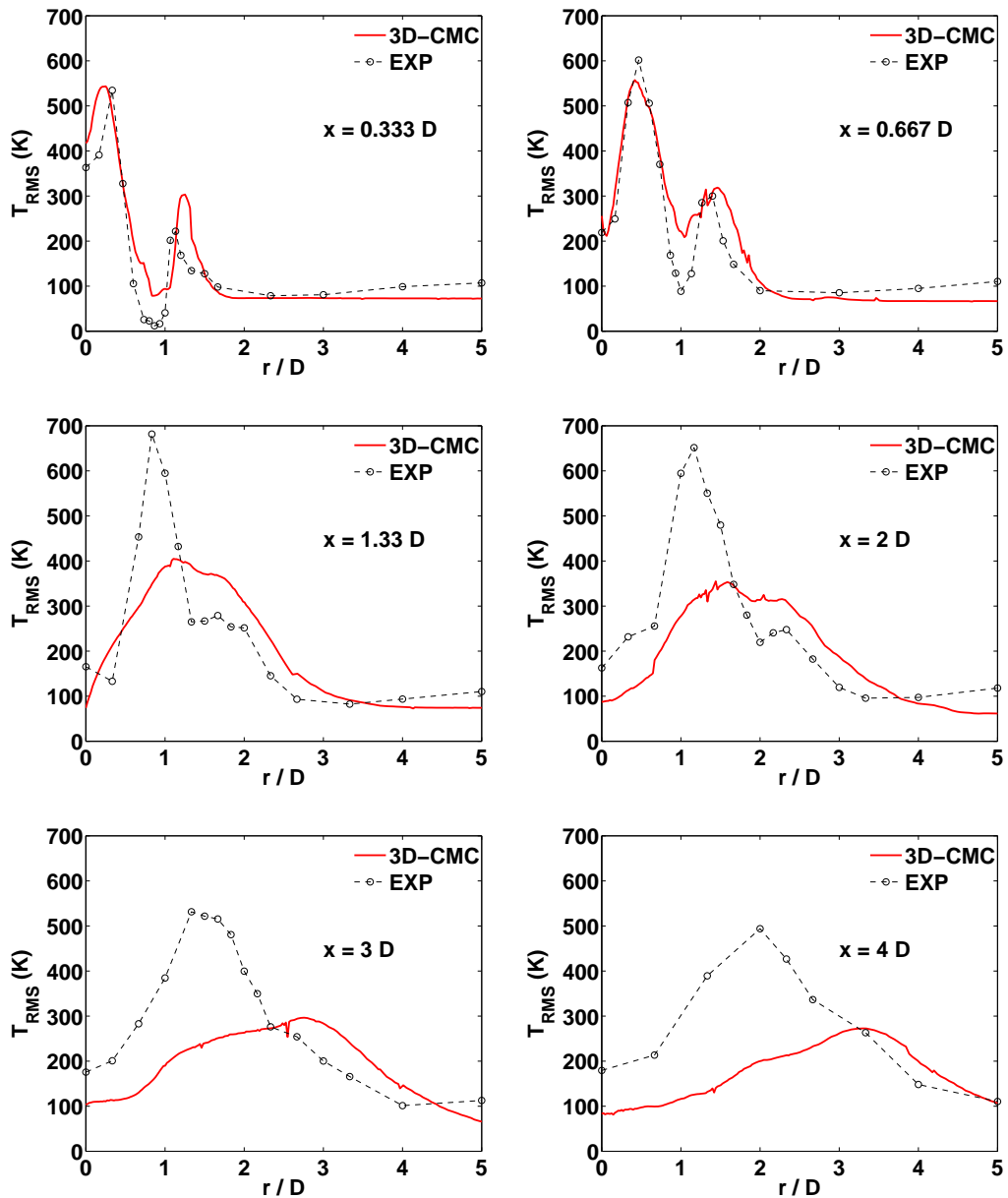
Figure 7.20: Radial profiles of the RMS of the temperature at the indicated axial position. Experimental data from Ref. [51].

(Fig. 7.29) matches well the experimental data for positions close to the burner exit before becoming increasingly overpredicted further dowstream.

7.4 Summary of main findings

The LES - first order CMC formulation has been applied to the confined non-premixed TECFLAM S09 flame. Solving the full CMC equations in time and space results in strong variations of the reactive scalars (temperature and species) distributions against the mixture fraction. As a result these distributions are significantly different from the prescribed distributions used for the flamelet model in Chapter 6. The conditional fluctuations in mixture fraction space result in strong variations of the local density. In particular, close to the burner exit the numerical formulation predicts the occurrence of a flame lift-off, with a lift-off height of around 20 mm, consistent with the experimental data. The flamelet distributions computed by the CMC model remain inert around the burner exit, modifying the local density compared to the LES/0D-CMC prediction. Consequently, the fluid mechanics of the flame is modified: the CRZ becomes larger and the radial expansion of the jet stream accelerates in the downstream part of the flow. The fuel jet is bent further towards the air stream, increasing the air-fuel mixing. This phenomenon is responsible for a clear improvement in the mixing field prediction, showing that the right mixing mechanisms have been captured by the LES/3D-CMC formulation. However the main jet opening is found to be too quick far from the burner exit. Regarding the flame lift-off process, the CMC model coupled to LES is able to capture the stabilization process of the flame: the CRZ is responsible for carrying back to the root of the flame some burning flamelets. These flamelets then encounter the inert flamelets injected at the air pipe exit and ignite them. The dynamics of the ignition process at the flame root is strongly affected by the aerodynamics of the burner. As described in Chapter 6, the presence of vortex cores rotating inside this type of burner is responsible for the periodic occurrences of recirculations along the inner wall of the air annulus. These recirculations attract further the neighbouring burning flamelets towards the flame root, accelerating the ignition process of the inert flamelets injected at the air pipe exit and hence improving the stability mechanisms of the lifted
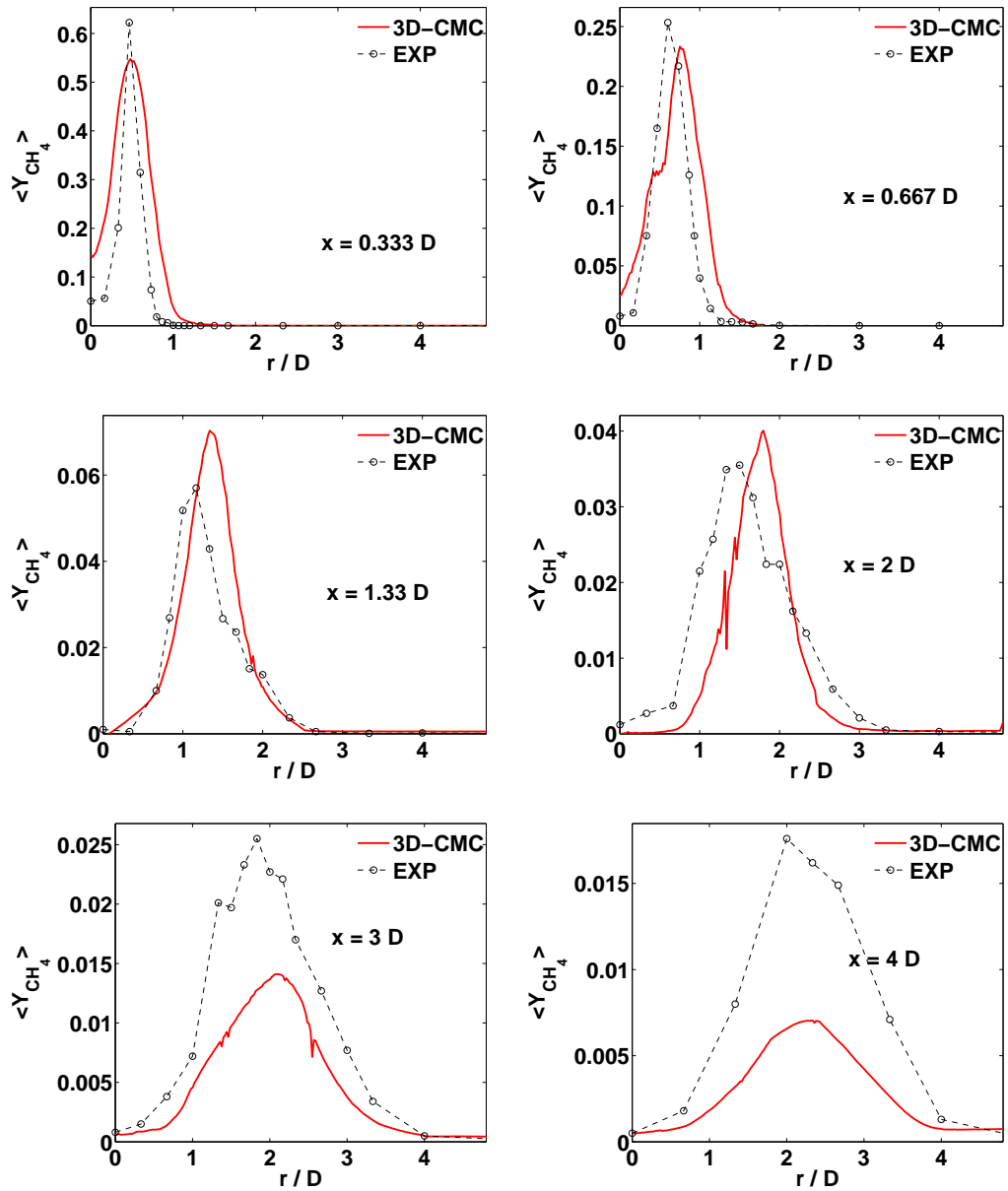
flame.

Figure 7.21: Radial profiles of the mean Y_{CH_4} at the indicated axial position. Experimental data from Ref. [51].
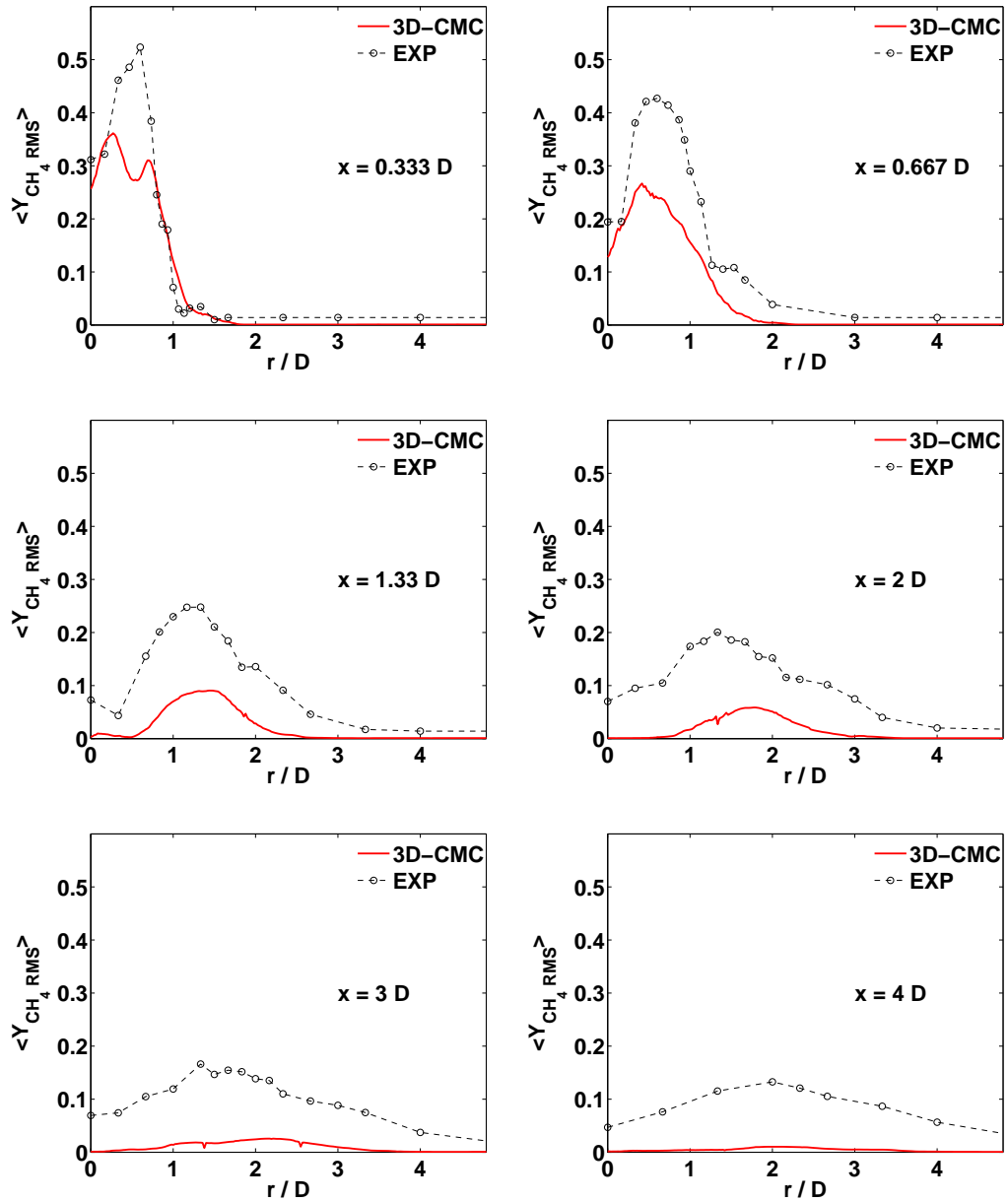
Figure 7.22: Radial profiles of the RMS of Y_{CH_4} at the indicated axial position. Experimental data from Ref. [51].
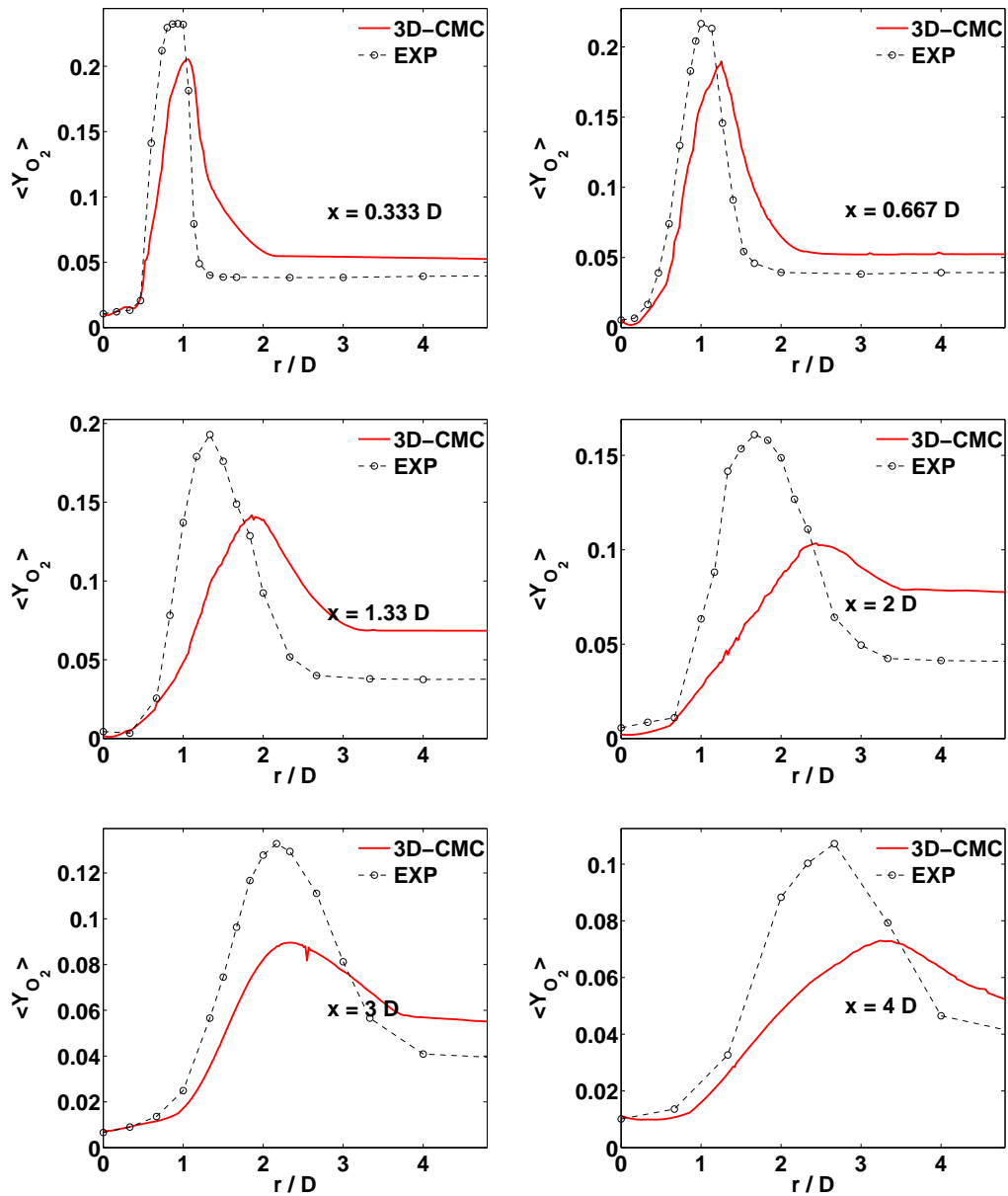
Figure 7.23: Radial profiles of the mean Y_{O_2} at the indicated axial position. Experimental data from Ref. [51].
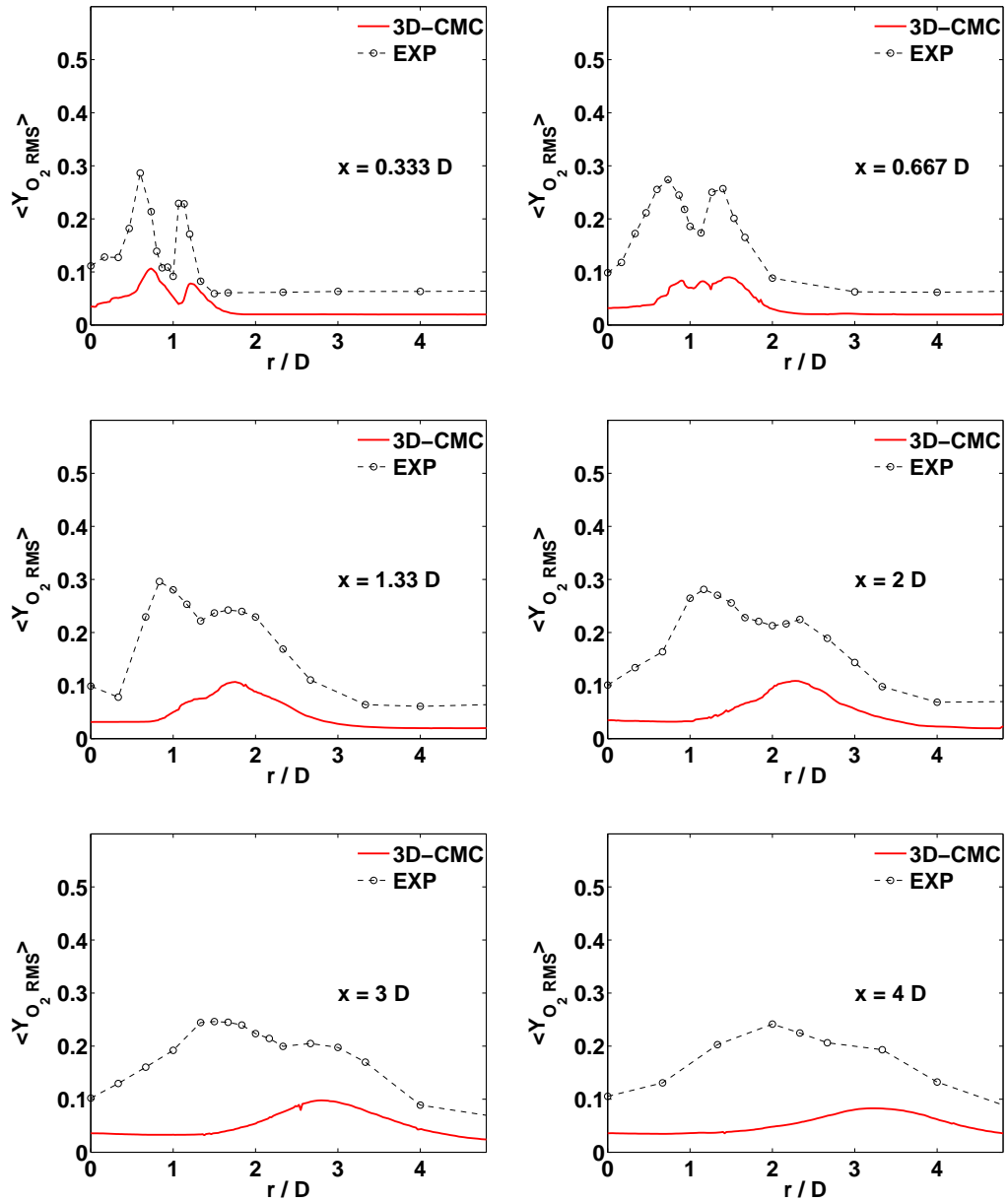
Figure 7.24: Radial profiles of the RMS of Y_{O_2} at the indicated axial position. Experimental data from Ref. [51].
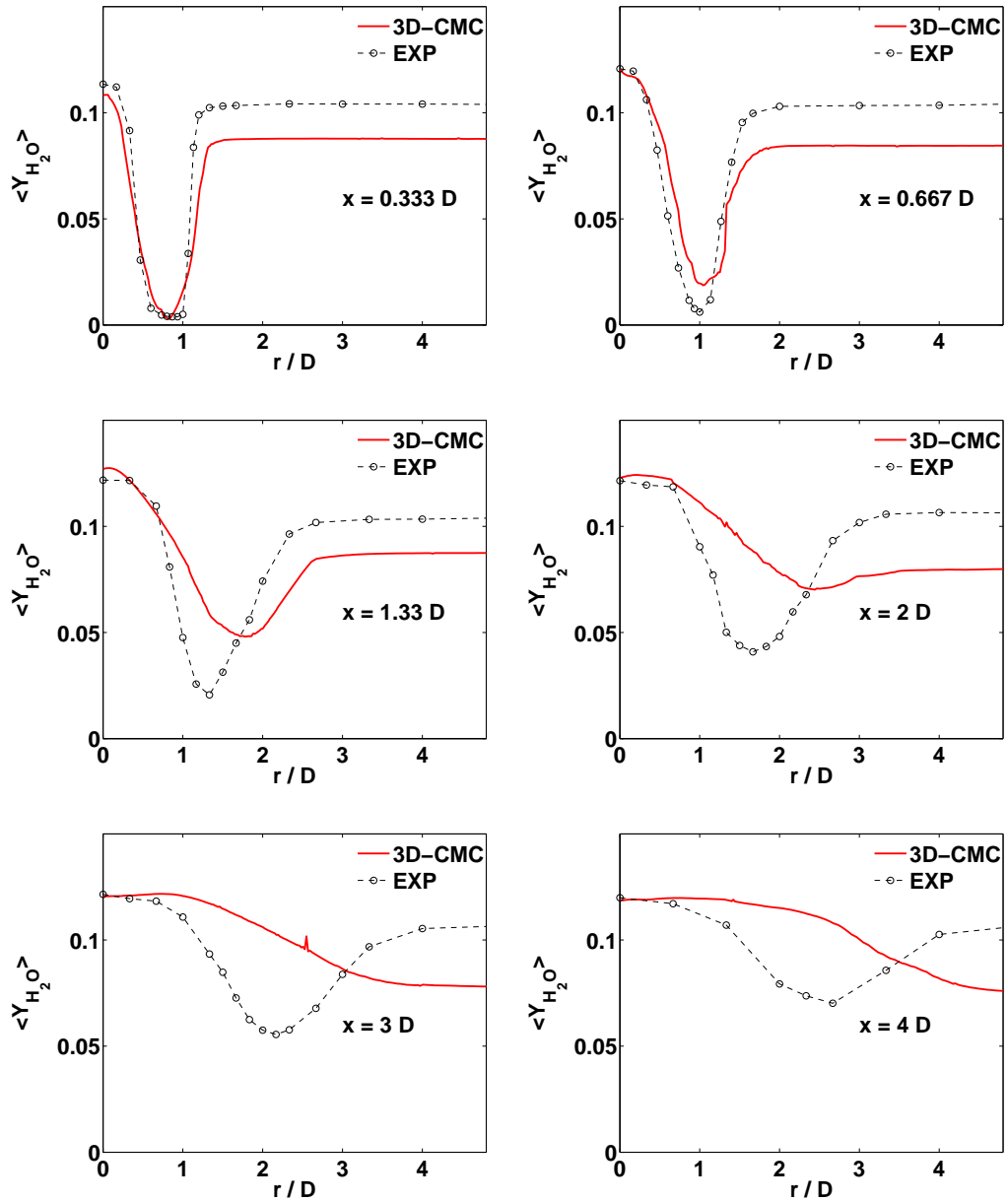
Figure 7.25: Radial profiles of the mean Y_{H_2O} at the indicated axial position. Experimental data from Ref. [51].
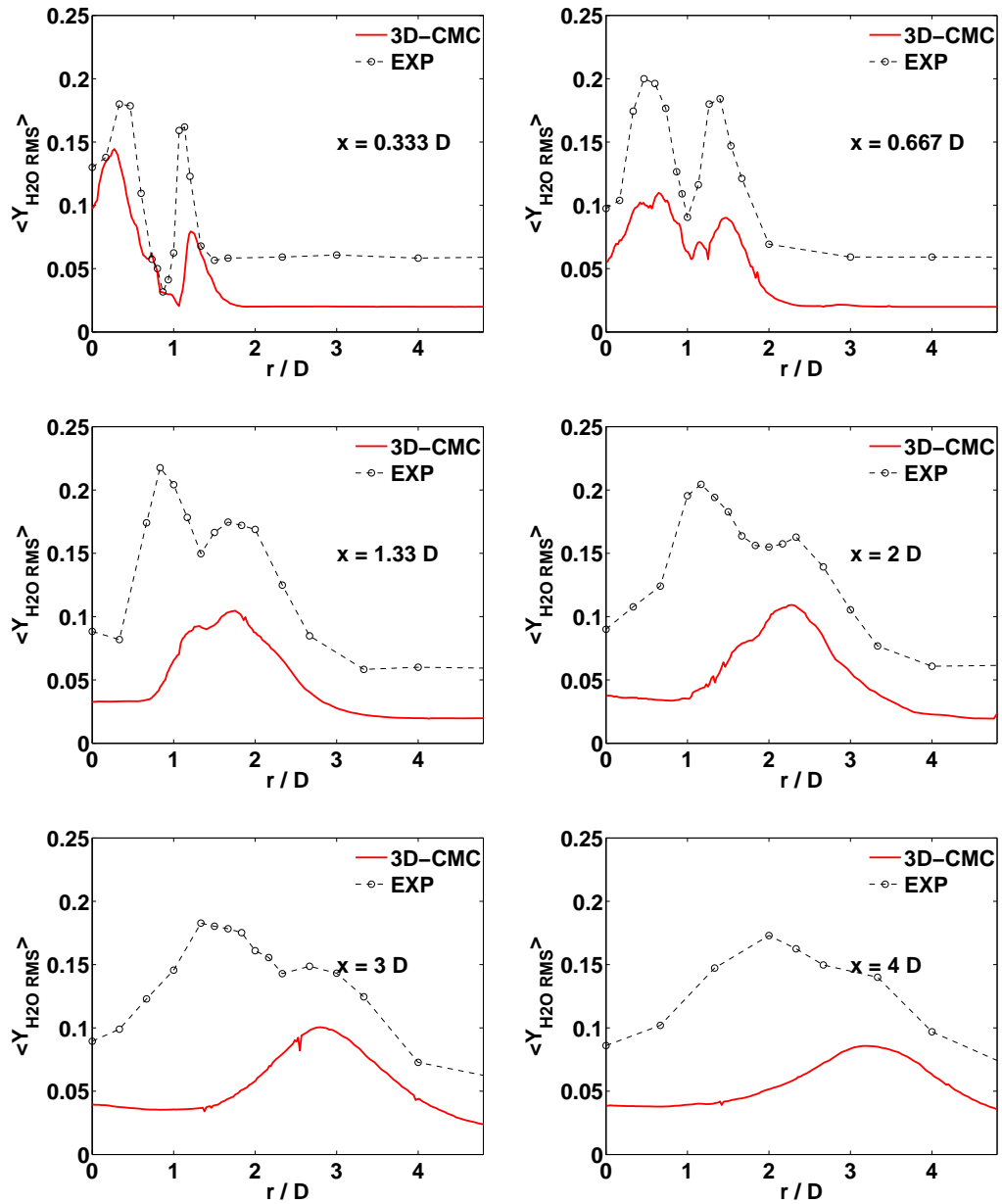
Figure 7.26: Radial profiles of the RMS of Y_{H_2O} at the indicated axial position. Experimental data from Ref. [51].
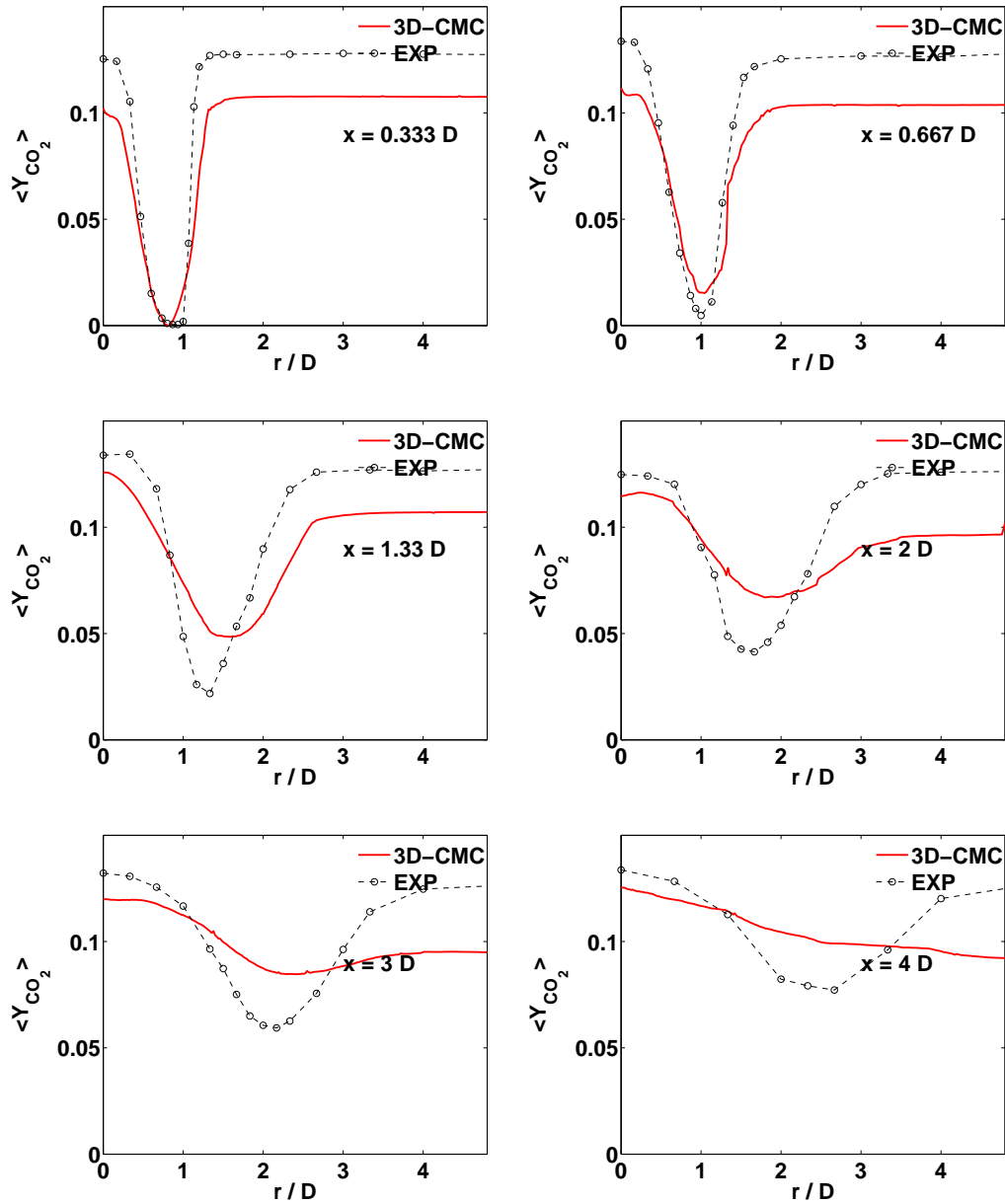
Figure 7.27: Radial profiles of the mean Y_{CO_2} at the indicated axial position. Experimental data from Ref. [51].
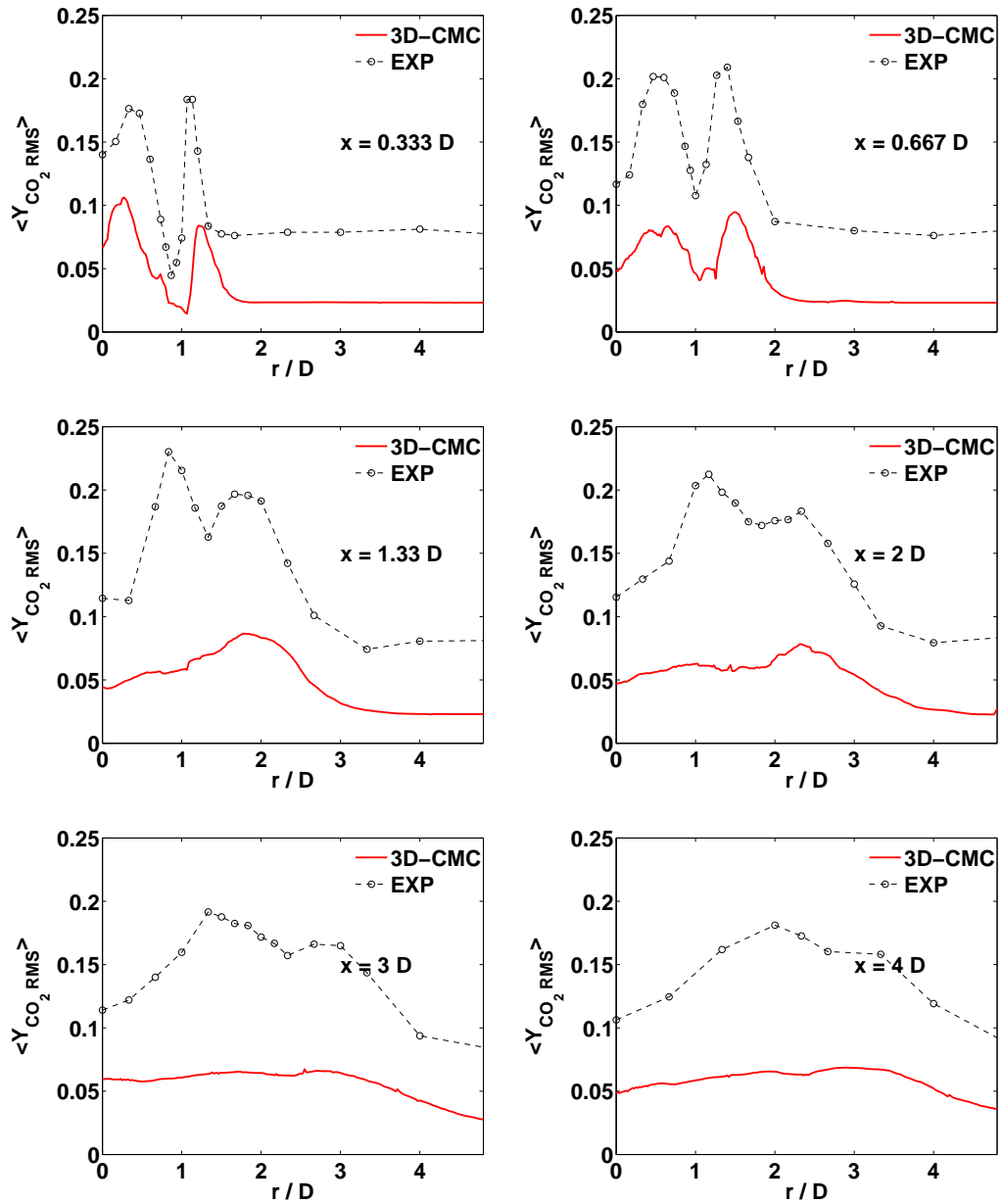
Figure 7.28: Radial profiles of the RMS of Y_{CO_2} at the indicated axial position. Experimental data from Ref. [51].
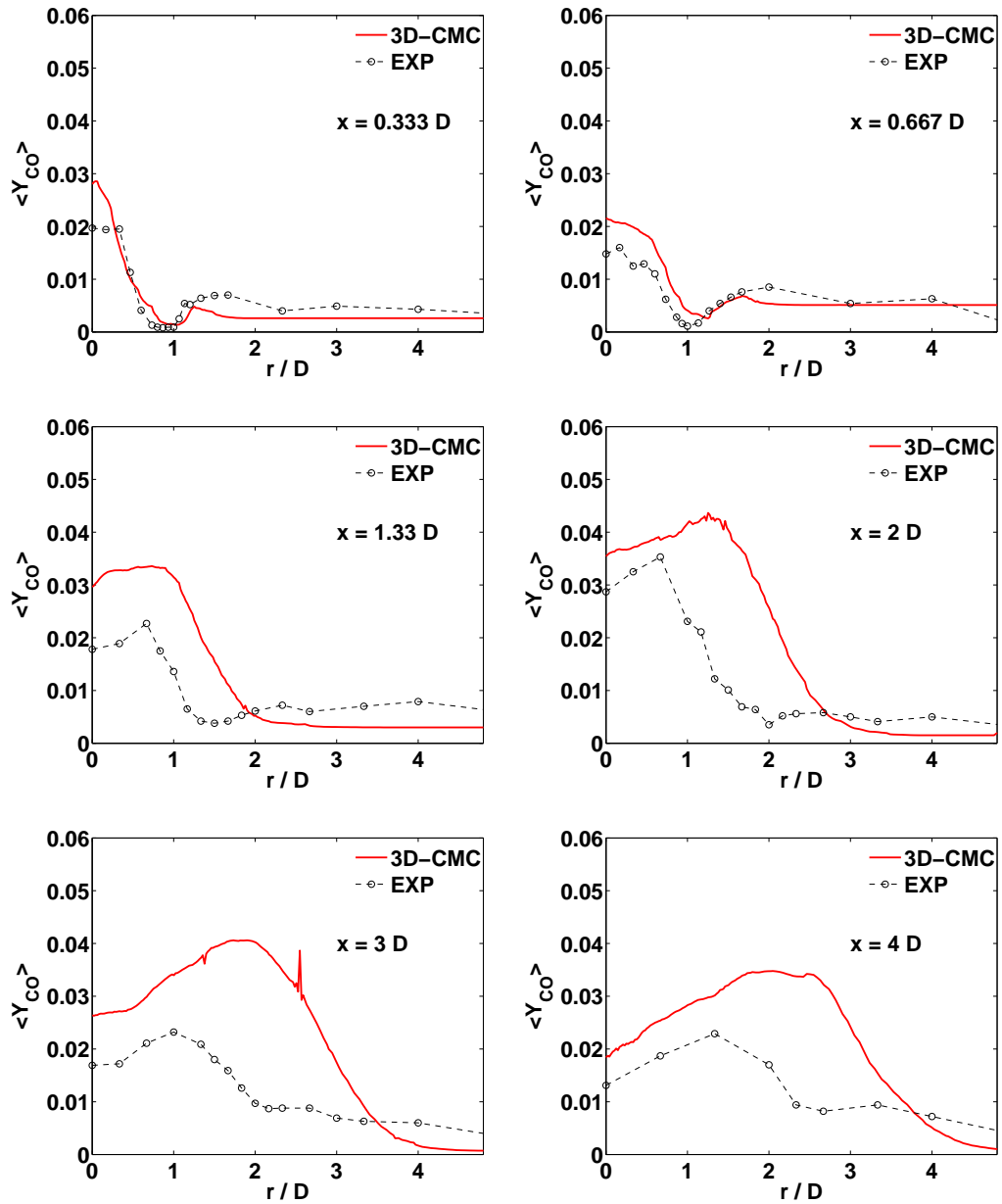
Figure 7.29: Radial profiles of the mean Y_{CO} at the indicated axial position. Experimental data from Ref. [51].
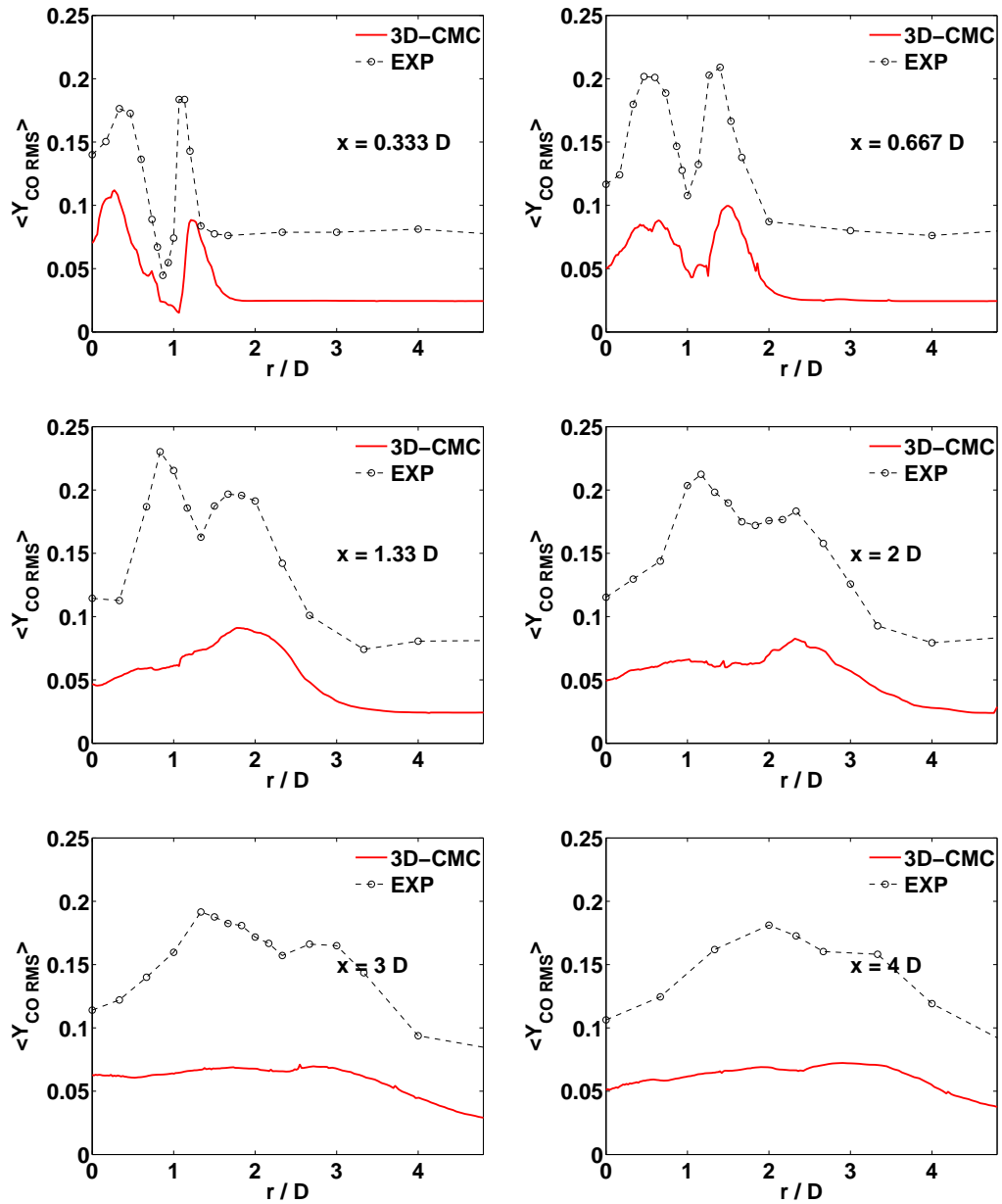
Figure 7.30: Radial profiles of the RMS of Y_{CO} at the indicated axial position. Experimental data from Ref. [51].

Chapter 8

Conclusions

8.1 Overview of the PhD work

In the present PhD work, several numerical simulations were conducted in order to further our understanding of the flame stabilization in swirl combustors. In the literature review presented in Chapter 2, a few key aspects of swirl flames requiring further investigations were identified. These aspects of swirl flames can be divided into two categories: the aerodynamics and combustion. The first two studies presented in this thesis are regarded as preliminary investigations. They focused on two academic configurations without swirl, but containing some important features present in swirl combustors. The first work (Chapter 4) analysed inert forced bluff body flows and the associated vortex shedding, while the second work (Chapter 5) analysed a piloted non-premixed flame and its succession of localized extinctions and re-ignitions reproduced by the LES-CMC code. The next two chapters represented an in-depth investigation of an academic non-premixed swirl flame. In Chapter 6 the aerodynamics of this swirl flame and its inert flow were investigated, with further insights developed on the Precessing Vortex Core-like structures developing inside the burner and their influence on the flow and flame dynamics. Finally, in Chapter 7, the use of a LES-CMC formulation allowed the analysis of the flame lift-off observed in experiments. The interaction between the aerodynamics and the combustion were investigated, in particular the effect of the Central Recirculation Zone and the PVCs in the burner. Throughout the thesis, we have made used of the Proper Orthogonal Decomposition method to

organize and analyze the datasets from the LES simulations. In this chapter, we give a summary of the main findings presented in this thesis and provide guidelines for further research.

8.2   LES of forced bluff body flows

In Chapter 4, isothermal air flows behind an axisymmetric conical bluff body, enclosed in a circular pipe of larger diameter that undergoes a sudden expansion, and with the incoming flow being forced at different single frequency (40 Hz, 160 Hz, 320 Hz) and with large amplitude, have been explored with Large-Eddy Simulations. This flow may be thought of as a model problem for combustors undergoing selft-excited oscillations.

- The Large-Eddy Simulations reproduced accurately the experimental findings in terms of phase-averaged mean and R.M.S. velocities, vortex formation, and spectral peaks.

- At low forcing frequencies, the recirculation zone was found to pulsate with the incoming flow, at a phase lag that depended on spatial location. No clear vortex shedding was observed.

- At high forcing frequencies, double vortex rings were shed from both the bluff body and inlet pipe edges at the pulsating frequency. The recirculation zone, as a whole, pulsated less.

- The phase-averaged turbulent fluctuations showed large temporal and spatial variations and were higher than the turbulent fluctuations of the unforced flow at the same position.

- The velocity spectra showed peaks at various harmonics of the pulsating frequency, whose relative magnitudes varied with location.

- Proper Orthogonal Decomposition analysis of the pulsating flow at 160 Hz, in particular snapshot reconstruction based on pairs of POD modes, led to the interpretation that the harmonics observed in the flow were associated

with some weak extra vortex sheddings occuring at harmonics of the forced frequency.

- Most of the fluctuating energy of the flow came from the deterministic part of the flow i.e. the part of the flow pulsating at the forced frequency.

- In this POD analysis, the pairs of POD modes roughly represented the convection inside the combustion chamber of the double vortex rings shed at the pulsating frequency or one of its harmonics.

8.3 CMC/LES of the Delft-III natural gas non-premixed jet flame

In Chapter 5, Large-Eddy Simulation (LES), coupled with a first order 3D Conditional Moment Closure (CMC) sub-grid model and the GRI3 detailed chemical mechanism, have been used to explore the structure of the Delft III piloted turbulent non-premixed flame. A LES coupled with a prescribed first order CMC solution has also been computed for comparison with the LES-CMC solution.

- The LES-CMC formulation reproduced the experimental observations well in terms of time-averaged statistics for velocity, mixture fraction, CO and temperature, with an exception of NO, which is overpredicted.

- Solving the CMC equations and updating the local density at each LES iteration resulted in a clear improvement of the mixture fraction radial profiles predictions, while no clear improvement was observed for the velocity predictions, which remain good.

- Localised extinctions, which led to the succession of burning and extinguished stoichiometric fluid along the flame front, were successfully captured.

- The sequence of localized extinctions and re-ignitions mainly occured close to the nozzle, consistent with experimental observations.

- The localized extinctions observed close to the nozzle regularly occured for values of the scalar dissipation rate below the quasi-steady extinction value. In fact, a significant proportion of the localized exctinctions observed close to the burner have to be understood as a lack of ignition of the inert flamelets injected at the flow inlet.

8.4   Investigation of the aerodynamics of a non-premixed swirl flame using LES

In Chapter 6, large-eddy simulation was used to solve the flow and mixing fields of the confined turbulent non-premixed TECFLAM S09c flame and its inert flow. For the reactive computation, LES was coupled with a prescribed first order CMC solution, as a preliminary attempt to model this swirl flame. This formulation was relatively fast compared to the LES coupled with the full CMC equations resolved at each LES iteration. Statistical analysis such as spectral analysis, correlations, and Proper Orthogonal Decomposition could then be performed with a very good statistical convergence. As a result, a comprehensive analysis of swirl flow aerodynamics was developed in this chapter.

- The LES-flamelet formulation, despite the fact that it could not capture localized extinctions, was found to reproduce the experimentally-observed formation of a Central Recirculation Zone via the Vortex Breakdown mechanism. The results agreed well with available experimental data for velocity and mixture fraction.

- Autocorrelation and spectral analysis revealed the presence of a periodic component inside the air inlet pipe and around the central bluff body, for both the inert and reactive flows.

- The fundamental frequency of this periodic motion increased by a factor of 1.6 in the reacting case.

- The coupled use of POD with LES allowed to identify the vortical structures of the flow and their associated frequency.

- The POD computation was based on a combination of several flow quantities such as the pressure or the mixture fraction in addition to the three velocity components. This resulted in a better identification of the important structures of the flow and brought to light the correlation between the vortex precession and the flow mixing.

- POD of the LES datasets revealed that large single and double helical longitudinal vortices, similar to a PVC, were formed along the air inlet inner wall, whose axes rotated around the burner. These vortices became highly curved inside the combustion chamber.

- The rotation of the vortical structures around the central bluff body were characterized by at least one pair of POD modes in both the inert and reacting cases.

- Spectral analysis of the corresponding temporal modes revealed that these vortices are responsible for the periodic component observed around the burner.

- Further pairs of modes, sometimes interpreted as harmonics of the fundamental pair of modes, were also present in the flow. The combustion process was found to trigger several other pairs of modes, resulting in a more complex dynamics of the flow.

- In the reactive flow, the vortices were more elongated and they extended much further inside the combustor compared to the inert case. This confirmed the observations from the spectra and autocorrelations of the axial velocity where the periodic component was observed much further inside the combustion chamber for the reactive flow.

- A long low-pressure column was also observed in the inert swirl flow along the centreline of the combustion chamber, while this structure was damped by the combustion.

8.5 CMC/LES of a lifted non-premixed swirl flame

In Chapter 7, the confined turbulent swirling non-premixed TECFLAM S09c flame was investigated using Large Eddy Simulation coupled to the full equations of the first order Conditional Moment Closure model.

- Consistently with the results observed in Chapter 5, solving the CMC equations at each LES iteration resulted in a clear improvement of mixture fraction radial profiles predictions, in particular close to the burner. However, the full CMC formulation also resulted in a slight overprediction of the jet expansion prediction far from the burner exit.

- Overall the results compared well with the experimental data in terms of mixture fraction and velocity.

- The temperature was well predicted close to the burner, but discrepancies increased further downstrean or closer to the chamber wall. In term of CO mass fraction, the prediction was satisfactory for axial positions lower than 1 diameter of the bluff body. Y_{CO} was then overall overpredicted.

- The LES-CMC code was able to capture the flame lift-off evident experiementally. The stabilization process of the flame was also captured by the numerical formulation: the CRZ carries back to the root of the flame some burning fluid, which then ignites the reactants injected at the air pipe exit.

- The recirculations created by the PVC-like structures described in Chapter 6 seemed to influence greatly the stability mechanisms of the lifted flame, the dynamics of which could be captured by the CMC code.

8.6 Guidelines for further studies

In this section, we suggest few topics for further investigations.

- In this thesis, LES coupled to the CMC model has been used to provide more insights on the transient events occuring in reactive flows. In particular, the CMC model has been found to be capable of reproducing localized extinctions and flame lift-off, which is a great improvement compared to the capability of a flamelet model. From a statistical point of view, it was found in the simulations of both a piloted non-premixed flame and a non-premixed swirl flame that solving the CMC equations resulted in strong enough variations of the local density to modify the velocity and mixture fraction fields. In both cases, the application of the advanced combustion model showed a clear improvement of the mixture fraction prediction, while the axial velocity prediction generally showed a slight worsening. An analysis and understanding of this behaviour is well worth of further investigation.

- In the simulations presented in this thesis, only some white noise was added to the top-hat profiles used for the numerical inlet velocities. It would be worth injecting some turbulent fluctuations at the numerical inlets to reproduce the turbulence of the flow in the burner and investigate its effects on the flame structure. For instance, the Kelvin-Helmholtz instabilities observed in Chapter 5 might not have remained visible at such axial distances from the burner exit if turbulent fluctuations had been added to the numerical inlet velocities.

- Another aspect of the thesis work is the comprehensive analysis of the flow based on Proper Orthogonal Decomposition. Several variables were used to perform POD analysis in an attempt to bring to light correlations between the flow, mixing and combustion dynamics. However, the results obtained were always interpreted from an aerodynamic point of view. As a result, it could be worth performing POD of LES datasets based on the scalar dissipation rate and Y_{OH} simultaneously in order to analyze further the dynamics of localized extinctions and flame lift-off. POD analysis based simultaneously on the velocity components and Y_{OH} could also reveal more information on the interaction between the flow aerodynamics and the combustion.

- In the study of the TECFLAM burner in Chapter 6, the dynamics of the hydrodynamic structures (i.e. their rotation or precession) was always characterized by (at least) a pair of modes. The spectral analysis of these modes generally showed a single frequency peak and the interpretation of the modes was therefore straightforward. However, for the vortex shedding observed in the bluff body pulsating flows (Chapter 4), the POD analysis has shown some of its limitations. In fact, the Proper Orthogonal Decomposition method, while enforcing the spatial orthogonality of the modes, computed an evolution of the modes based on multiple frequencies. The method did not separate each harmonic of the flow into a specific mode. As a consequence, we suggest that other analytical methods should be tried, such as the Dynamic Mode Decomposition [98]. With this method, the orthogonality is enforced in the frequency space rather than in the physical space, which could lead to an easier interpretation of the different modes in certain cases.

References

[1] S.F. AHMED, R. BALACHANDRAN, T. MARCHIONE, AND E. MAS-
TORAKOS. Spark ignition of turbulent nonpremixed bluff-body flames.
Combustion and Flame, **151**:366–385, 2007. 41, 46, 48

[2] Y.M. AL-ABDELI AND A.R. MASRI. Turbulent swirling natural gas
flames: Stability characteristics, unsteady behavior and vortex breakdown.
Combustion Science and Technology, **179**[1]:207–225, 2007. 15

[3] C. A. ARMITAGE, R. BALACHANDRAN, E. MASTORAKOS, AND R. S.
CANT. Investigation of the nonlinear response of turbulent premixed flames
to imposed inlet velocity oscillations. *Combustion and Flame*, **146**:419–436,
2006. 20, 41

[4] R. BALACHANDRAN. *Experimental Investigation of the Response of Tur-
bulent Premixed Flames to Acoustic Oscillations*. PhD thesis, University of
Cambridge, 2005. xiv, 42, 43, 44, 51

[5] R. BALACHANDRAN, B. O. AYOOLA, C. F. KAMINSKI, A. P. DOWL-
ING, AND E. MASTORAKOS. Experimental investigation of the nonlinear
response of turbulent premixed flames to imposed inlet velocity oscillations.
Combustion and Flame, **143**:37–55, 2005. 19, 41, 43, 64

[6] R. BALACHANDRAN, A. P. DOWLING, AND E. MASTORAKOS. Non-linear
response of turbulent premixed flames to imposed inlet velocity oscillations
of two frequencies. *Flow, Turbulence and Combustion*, **80**:455–487, 2008.
19, 41, 64

236

[7] R.S. Barlow, A.N. Karpetis, J.H. Frank, and J.Y. Chen. Scalar profiles and NO formation in laminar opposed-flow partially premixed methane/air flames. *Combustion and Flame*, **127**[3]:2102–2118, 2001. 26, 114

[8] F. Biagioli. Stabilization mechanism of turbulent premixed flames in strongly swirled flows. *Combustion Theory and Modelling*, **10**[3]:389–412, 2006. 2

[9] F. Biagioli, F. Guthe, and B. Schuermans. Combustion dynamics linked to flame behaviour in a partially premixed swirled industrial burner. *Experimental Thermal and Fluid Science*, **32**[7]:1344–1353, 2008. 17, 24

[10] RW Bilger. Turbulent jet diffusion flames. *Progress in Energy and Combustion Science*, **1**[2]:87–109, 1976. 31

[11] R.W. Bilger, S.B. Pope, K.N.C. Bray, and J.F. Driscoll. Paradigms in turbulent combustion research. *Proceedings of the Combustion Institute*, **30**[1]:21–42, 2005. 2, 23, 24

[12] S. Böckle, J. Kazenwadel, T. Kunzelmann, and C. Schulz. Laser-diagnostic multi-species imaging in strongly swirling natural gas flames. *Applied Physics B: Lasers and Optics*, **71**[5]:741–746, 2000. 127

[13] S. Böckle, J. Kazenwadel, T. Kunzelmann, D. Shin, C. Schulz, and J. Wolfrum. Simultaneous single-shot laser-based imaging of formaldehyde, oh, and temperature in turbulent flames. *Proceedings of the Combustion Institute*, **28**[1]:279–286, 2000. 127

[14] S. Böckle, J. Kazenwadel, T. Kunzelmann, D.I. Shin, and C. Schulz. Single-shot laser-induced fluorescence imaging of formaldehyde with xef excimer excitation. *Applied Physics B: Lasers and Optics*, **70**[5]:733–735, 2000. 127

[15] G. Borghesi, F. Biagioli, and B. Schuermans. Dynamic response of turbulent swirling flames to acoustic perturbations. *Combustion Theory and Modelling*, **13**[3]:487–512, 2009. 16, 17, 21, 22, 24

[16] N. Branley and WP Jones. Large eddy simulation of a turbulent non-premixed flame. *Combustion and flame*, **127**[1-2]:1914–1934, 2001. 30

[17] Jones W.P Branley N. Large eddy dimulation of a non-premixed turbulent swirling flame. 1999. 4th International Symposium on Engineering Turbulence Modelling and Measurements, Corsica, France. 127

[18] G. Broze and F. Hussain. Nonlinear dynamics of forced transitional jets: periodic and chaotic attractors. *Journal of Fluid Mechanics*, **263**:93–132, 1994. 19, 66

[19] RS Cant and E. Mastorakos. *An introduction to turbulent reacting flows*. Imperial College Pr, 2008. 2

[20] R.R. Cao and S.B. Pope. The influence of chemical mechanisms on PDF calculations of nonpremixed piloted jet flames. *Combustion and Flame*, **143**[4]:450–470, 2005. 114

[21] R.C. Chanaud. Observations of oscillatory motion in certain swirling flows. *Journal of Fluid Mechanics*, **21**[01]:111–127, 1965. xiv, 14

[22] H. Chen, S. Chen, and R.H. Kraichnan. Probability distribution of a stochastically advected scalar field. *Physical review letters*, **63**[24]:2657–2660, 1989. 32

[23] H. Choi, W.-P. Jeon, and J. Kim. Control of flow over a bluff body. *Annual Review of Fluid Mechanics*, **40**:113–139, 2008. 19

[24] D. R. Cole and M. N. Glauser. Applications of stochastic estimation in the axisymmetric sudden expansion. *Physics of Fluids*, **10**:2941–2949, 1998. 9, 46

[25] A.W. Cook and J.J. Riley. A subgrid model for equilibrium chemistry in turbulent flows. *Physics of fluids*, **6**:2868–2870, 1994. 30

[26] G. De Paola, E. Mastorakos, Y. M. Wright, and K. Boulouchos. Diesel engine simulations with multi-dimensional conditional moment closure. *Combustion Science and Technology*, **180**[5]:883–899, 2008.

5th Mediterranean Combustion Symposium, Monastir, Tunisia, Sep 09-13, 2007. 31

[27] J.E. DE VRIES. *Study on turbulent fluctuations in diffusion flames using laser-induced fluorescence.* PhD thesis, Delft University of Technology, 1994. xviii, xix, xx, 88, 102, 103, 104, 105, 107, 112, 119, 120, 121, 122, 123, 124, 125

[28] S. R. N. DE ZILWA, I. EMIRIS, J. H. UHM, AND J. H. WHITELAW. Combustion of premixed methane and air in ducts. *Proceedings of the Royal Society of London A*, **457**:1915–1949, 2001. 10, 16

[29] A. DEJOAN AND M. A. LESCHZINER. Large eddy simulation of periodically perturbed separated flow over a backward-facing step. *International Journal of Heat and Fluid Flow*, **25**:581–592, 2004. 9, 19, 45

[30] W. J. DEVEPORT AND E. P. SUTTON. An experimental study of two flows through an axisymmetric sudden expansion. *Experiments in Fluids*, **14**:423–432, 1993. 9

[31] AP DOWLING. A kinematic model of a ducted flame. *Journal of Fluid Mechanics*, **394**:51–72, 1999. 17

[32] C. DUWIG AND L. FUCHS. Large eddy simulation of vortex breakdown/flame interaction. *Physics of Fluids*, **19**:075103, 2007. 38

[33] C. DUWIG AND P. IUDICIANI. Extended proper orthogonal decomposition for analysis of unsteady flames. *Flow, turbulence and combustion*, **84**[1]:25–47, 2010. 38

[34] C. DUWIG, M. SALEWSKI, AND L. FUCHS. Simulations of a turbulent flow past a sudden expansion: A sensitivity analysis. *AIAA Journal*, **46**:408–419, 2008. 9

[35] B.O. ENFLO AND C.M. HEDBERG. *Theory of nonlinear acoustics in fluids.* Kluwer Academic Pub, 2002. 62

[36] D. Fabre, F. Auguste, and J. Magnaudet. Bifurcations and symmetry breaking in the wake of axisymmetric bodies. *Physics of Fluids*, **20**:051702, 2008. 8

[37] M. Fairweather and RM Woolley. Conditional moment closure calculations of a swirl-stabilized, turbulent nonpremixed methane flame. *Combustion and Flame*, **151**[3]:397–411, 2007. 1, 2, 25

[38] A. Garmory and E. Mastorakos. Capturing localised extinction in sandia flame f with les-cmc. *Proceedings of the Combustion Institute*, **33**[1]:1673–1680, 2011. 33, 90, 101, 112

[39] M. Germano, U. Piomelli, P. Moin, and W. H. Cabot. A dynamic subgrid-scale eddy viscosity model. *Physics of Fluids*, **3**:1760–1765, 1991. 29

[40] D. Greenblatt and I. J. Wygnanski. The control of flow separation by periodic excitation. *Progress in Aerospace Sciences*, **36**:487–545, 2000. 9, 19, 45

[41] B. Guo, T. A. G. Langrish, and D. F. Fletcher. Simulation of turbulent swirl flow in an axisymmetric sudden expansion. *AIAA Journal*, **39**:96–102, 2001. 9

[42] AK Gupta. *Swirl flows.* Technomic Publishing Co., Lancaster, PA, 1984. 1, 3, 5, 10, 11, 13, 15, 16, 17, 21

[43] P. Habisreuther, C. Bender, O. Petsch, H. Buchner, and H. Bockhorn. Prediction of pressure oscillations in a premixed swirl combustor flow and comparison to measurements. *Flow, Turbulence and Combustion*, **77**:147–160, 2006. 20

[44] C. Heeger, RL Gordon, MJ Tummers, T. Sattelmayer, and A. Dreizler. Experimental analysis of flashback in lean premixed swirling flames: upstream flame propagation. *Experiments in Fluids*, pages 1–11, 2010. 136, 143

[45] SIMONE HOCHGREB AND NICK COLLINGS. Combustion and ic engines. *Lecture notes, Dept. of Engineering, Cambridge University, Cambridge, UK*, 2008. 20, 21

[46] R. F. HUANG AND C. L. LIN. Velocity field of a bluff-body wake. *Journal of Wind Engineering and Industrial Aerodynamics*, **85**:31–45, 2000. 8, 9

[47] J. C. R. HUNT, A. A. WRAY, AND P. MOIN. Eddies, streams, and convergence zones in turbulent flows. Proceedings of the Summer Program N89-24555, Center for Turbulence Research, NASA Ames Research Centre, 1988. 63

[48] F. HUSSAIN AND J. JEONG. On the identification of a vortex. *Journal of Fluid Mechanics*, **285**:69–94, 1995. 63, 97

[49] S. JAMES, J. ZHU, AND M. S. ANAND. Large-eddy simulations as a design tool for gas turbine combustion systems. *AIAA Journal*, **44**:674–686, 2006. 30

[50] S. JAMES, J. ZHU, AND M. S. ANAND. Large-eddy simulations as a design tool for gas turbine combustion systems. *AIAA Journal*, **44**:674–686, 2006. 47

[51] O. KECK, W. MEIER, W. STRICKER, AND M. AIGNER. Establishment of a confined swirling natural gas/air flame as a standard flame: temperature and species distributions from laser Raman measurements. *Combustion Science and Technology*, **174**[8]:117–151, 2002. xxi, xxii, xxiv, xxv, xxvi, xxvii, 127, 129, 148, 150, 156, 157, 158, 159, 160, 161, 186, 187, 194, 195, 196, 197, 198, 199, 200, 208, 214, 215, 218, 219, 220, 221, 222, 223, 224, 225, 226, 227

[52] A. KEMPF, W. MALALASEKERA, K.K.J. RANGA-DINESH, AND O. STEIN. Large eddy simulations of swirling non-premixed flames with flamelet models: a comparison of numerical methods. *Flow, Turbulence and Combustion*, **81**[4]:523–561, 2008. 1, 10, 12, 15, 23, 24

[53] IS Kim and E. Mastorakos. Simulations of turbulent lifted jet flames with two-dimensional conditional moment closure. *Proceedings of the Combustion Institute*, **30**[1]:911–918, 2005. 25, 31

[54] I.S. Kim and E. Mastorakos. Simulations of turbulent non-premixed counterflow flames with first-order conditional moment closure. *Flow, Turbulence and Combustion*, **76**[2]:133–162, 2006. 31

[55] J.C. Kim, H.G. Sung, D.K. Min, and V. Yang. Large eddy simulation of the turbulent flow field in a swirl stabilized annular combustor. In *47 th AIAA Aerospace Sciences Meeting Including the New Horizons Forum and Aerospace Exposition (Disc 1)*. American Institute of Aeronautics and Astronautics, 1801 Alexander Bell Drive, Suite 500, Reston, VA, 20191-4344, USA,, 2009. 16, 21, 24

[56] S.H. Kim and K.Y. Huh. Use of the conditional moment closure model to predict NO formation in a turbulent CH4/H2 flame over a bluff-body. *Combustion and Flame*, **130**[1-2]:94–111, 2002. 25

[57] S.H. Kim, K.Y. Huh, and L. Tao. Application of the elliptic conditional moment closure model to a two-dimensional nonpremixed methanol bluff-body flame. *Combustion and Flame*, **120**[1-2]:75–90, 2000. 2

[58] M. Kiya, H. Ishikawa, and H. Sakamoto. Near-wake instabilities and vortex structures of three-dimensional bluff bodies: a review. *Journal of Wind Engineering and Industrial Aerodynamics*, **89**[14-15]:1219–1232, 2001. 8, 9, 45

[59] A.Y. Klimenko. Note on the conditional moment closure in turbulent shear flows. *Physics of Fluids*, **7**:446, 1995. 111

[60] A.Y. Klimenko and R.W. Bilger. Conditional moment closure for turbulent combustion. *Progress in energy and combustion science*, **25**[6]:595–687, 1999. 2, 31

[61] A.Y. KLIMENKO AND RW BILGER. Conditional moment closure for turbulent combustion. *Progress in Energy and Combustion Science*, **25**[6]:595–688, 1999. 32

[62] E. KONSTANTINIDIS AND S. BALABANI. Flow structure in the locked-on wake of a circular cylinder in pulsating flow: Effect of forcing amplitude. *International Journal of Heat and Fluid Flow*, **29**:1567–1576, 2008. 19

[63] R.M. KOPECKY AND K.E. TORRANCE. Initiation and structure of axisymmetric eddies in a rotating stream. *Computers and Fluids*, **1**:289–300, 1973. 24

[64] C. KULSHEIMER AND H. BUCHNER. Combustion dynamics of turbulent swirling flames. *Combustion and flame*, **131**[1-2]:70–84, 2002. 17

[65] C. KULSHEIMER AND H. BUCHNER. Combustion dynamics of turbulent swirling flames. *Combustion and Flame*, **131**:70–84, 2002. 20, 64

[66] T. LANDENFELD, A. KREMER, EP HASSEL, J. JANICKA, T. SCHÄFER, J. KAZENWADEL, C. SCHULZ, AND J. WOLFRUM. Laser-diagnostic and numerical study of strongly swirling natural gas flames. In *Symposium (International) on Combustion*, **27**, pages 1023–1029. Elsevier, 1998. 127

[67] A. H. LEFEBVRE. *Gas Turbine Combustion.* Taylor and Francis, 1998. 1

[68] T. C. LIEUWEN. Physics of premixed combustion-acoustic wave interactions. In T. C. LIEUWEN AND V. YANG, editors, *Combustion Instabilities in Gas Turbine Engines*, **210** of *Progress in Astronautics and Aeronautics*, pages 315–366. AIAA, 2005. 16

[69] O. LUCCA-NEGRO AND T. O'DOHERTY. Vortex breakdown: a review. *Progress in Energy and Combustion Science*, **27**[4]:431–481, 2001. 11, 13, 126, 131

[70] J. MANTZARAS AND T.H. VAN DER MEER. Coherent Anti-Stokes Raman Spectroscopy measurements of temperature fluctuations in turbulent natural gas-fueled piloted jet diffusion flames. *Combustion and Flame*, **110**[1-2]:39–53, 1997. 88

[71] T. Marchione, S. F. Ahmed, and E. Mastorakos. Ignition of turbulent swirling n-heptane spray flames using single and multiple sparks. *Combustion and Flame*, **156**:166–180, 2009. 41

[72] C. N. Markides, G. De Paola, and E. Mastorakos. Measurements and simulations of mixing and autoignition of an n-heptane plume in a turbulent flow of heated air. *Experimental Thermal and Fluid Science*, **31**[5]:393–401, APR 2007. 4th Mediterranean Combustion Symposium, Lisbon, PORTUGAL, OCT 06-10, 2005. 31

[73] A.R. Masri, R.W. Dibble, and R.S. Barlow. The structure of turbulent non-premixed flames revealed by raman-rayleigh-lif measurements. *Progress in Energy and Combustion Science*, **22**:307–362, 1996. 6

[74] W. Meier, O. Keck, B. Noll, O. Kunz, and W. Stricker. Investigations in the tecflam swirling diffusion flame: Laser raman measurements and cfd calculations. *Applied Physics B: Lasers and Optics*, **71**[5]:725–731, 2000. 127

[75] B. Merci, B. Naud, and D. Roekaerts. Flow and mixing fields for transported scalar PDF simulations of a piloted jet diffusion flame (Delft Flame III). *Flow, Turbulence and Combustion*, **74**[3]:239–272, 2005. 89

[76] B. Merci, D. Roekaerts, and B. Naud. Study of the performance of three micromixing models in transported scalar PDF simulations of a piloted jet diffusion flame (Delft Flame III). *Combustion and Flame*, **144**[3]:476–493, 2006. 89

[77] J. J. Miau, T. S. Leu, T. W. Liu, and J. H. Chou. On vortex shedding behind a circular disk. *Experiments in Fluids*, **23**:225–233, 1997. 8

[78] K. Midgley, A. Spencer, and J.J. McGuirk. Unsteady flow structures in radial swirler fed fuel injectors. *Journal of engineering for gas turbines and power*, **127**:755, 2005. 13

[79] G. J. NATHAN, S. J. HILL, AND R. E. LUXTON. An axisymmetric fluidic nozzle to generate jet precession. *Journal of Fluid Mechanics*, **370**:347–380, 1998. 46

[80] S. NAVARRO-MARTINEZ, A. KRONENBURG, AND F.D. MARE. Conditional moment closure for large eddy simulations. *Flow, Turbulence and Combustion*, **75**[1]:245–274, 2005. 31, 89, 111

[81] P.A. NOOREN, M. VERSLUIS, T.H. VAN DER MEER, R.S. BARLOW, AND J.H. FRANK. Raman-Rayleigh-LIF measurements of temperature and species concentrations in the Delft piloted turbulent jet diffusion flame. *Applied Physics B: Lasers and Optics*, **71**[1]:95–111, 2000. xviii, 88, 91

[82] P.A. NOOREN, H.A. WOUTERS, T.W.J. PEETERS, D. ROEKAERTS, U. MAAS, AND D. SCHMIDT. Monte Carlo PDF modelling of a turbulent natural-gas diffusion flame. *Combustion Theory and Modelling*, **1**[1]:79–96, 1997. 89

[83] J. PAIK AND F. SOTIROPOULOS. Numerical simulation of strongly swirling turbulent flows through an abrupt expansion. *International Journal of Heat and Fluid Flow*, **31**[3]:390–400, 2010. 128

[84] J. C. PAN, M. D. VANGSNESS, AND D. R. BALLAL. Aerodynamics of bluff-body stabilised confined turbulent premixed flames. *Journal of Engineering for Gas Turbines and Power*, **114**:783–789, 1992. 9, 10

[85] S. V. PATANKAR. *Numerical Heat Transfer and Fluid Flow*. Hemisphere, 1st edition, 1980. 30

[86] TWJ PEETERS, PPJ STROOMER, JE DE VRIES, D. ROEKAERTS, AND CJ HOOGENDOORN. Comparative experimental and numerical investigation of a piloted turbulent natural-gas diffusion flame. In *SYMPOSIUM INTERNATIONAL ON COMBUSTION*, pages 1241–1241. COMBUSTION INSTITUTE, 1994. 88, 89

[87] B. PIER. Local and global instabilities in the wake of a sphere. *Journal of Fluid Mechanics*, **603**:39–61, 2008. 8

[88] C.D. PIERCE AND P. MOIN. A dynamic model for subgrid-scale variance and dissipation rate of a conserved scalar. *Physics of Fluids*, **10**:3041–3044, 1998. 30

[89] H. PITSCH. Large-eddy simulation of turbulent combustion. *Annual Review of Fluid Mechanics*, **38**:453–482, 2006. 23, 24

[90] T. POINSOT AND D. VEYNANTE. *Theoretical and Numerical Combustion.* Edwards, 2001. 28

[91] S. B. POPE. *Turbulent Flows.* Cambridge University Press, London, 2000. 28

[92] J.W.S. RAYLEIGH. *The theory of sound.* Macmillan, 1896. 17

[93] A.M.A. ROCHA, J.A. CARVALHO, AND P.T. LACAVA. Gas concentration and temperature in acoustically excited Delft turbulent jet flames. *Fuel*, **87**[15-16]:3433–3444, 2008. 23

[94] D. ROEKAERTS, B. MERCI, AND B. NAUD. Comparison of transported scalar PDF and velocity-scalar PDF approaches to 'Delft flame III'. *Comptes Rendus Mecanique*, **334**[8-9]:507 – 516, 2006. 89

[95] M.R. ROOMINA AND R.W. BILGER. Conditional moment closure (CMC) predictions of a turbulent methane-air jet flame. *Combustion and Flame*, **125**[3]:1176–1195, 2001. 26

[96] S. ROUX, G. LARTIGUE, T. POINSOT, U. MEIER, AND C. BERAT. Studies of mean and unsteady flow in a swirled combustor using experiments, acoustic analysis, and large eddy simulations. *Combustion and Flame*, **141**[1-2]:40–54, 2005. xiv, 10, 14, 24

[97] Z. RUSAK AND S. WANG. Review of theoretical approaches to the vortex breakdown phenomenon. *AIAA Pap*, pages 96–2126, 1996. 12, 13

[98] P.J. SCHMID. Dynamic mode decomposition of numerical and experimental data. *Journal of Fluid Mechanics*, **656**[1]:5–28, 2010. 235

[99] P. Schmitt, T. Poinsot, B. Schuermans, and KP Geigle. Large-eddy simulation and experimental study of heat transfer, nitric oxide emissions and combustion instability in a swirled turbulent high-pressure burner. *Journal of Fluid Mechanics*, **570**:17–46, 2007. xiv, 17, 18, 20, 21, 23, 25

[100] B. Schuermans, V. Bellucci, F. Guethe, F. Meili, P. Flohr, and C.O. Paschereit. A detailed analysis of thermoacoustic interaction mechanisms in a turbulent premixed flame. *Proceedings of ASME Turbo Expo*, 2004. 17

[101] S. J. Shanbhogue, S. Husain, and T. Lieuwen. Lean blowoff of bluff body stabilized flames: Scaling and dynamics. *Progress in Energy and Combustion Science*, **35**:98–120, 2009. 10

[102] H. J. Sheen, W. J. Chen, and J. S. Wu. Flow patterns for an annular flow over an axisymmetric sudden expansion. *Journal of Fluid Mechanics*, **350**:177–188, 1997. 10

[103] A. R. Shenoy and C. Kleinstreuer. Flow over a thin circular disk at low to moderate Reynolds numbers. *Journal of Fluid Mechanics*, **605**:253–262, 2008. 8

[104] X Shi. Numerical simulation of vortex breakdown. *Proc. Collo. on VN*, **25**:69–80, 1985. 24

[105] L. Sirovich. Turbulence and the dynamics of coherent structures. I-Coherent structures. *Quarterly of applied mathematics*, **45**:561–571, 1987. 36

[106] Gregory P. Smith, David M. Golden, Michael Frenklach, Nigel W. Moriarty, Boris Eiteneer, Mikhail Goldenberg, C. Thomas Bowman, Ronald K. Hanson, Soonho Song, William C. Gardiner, Jr., Vitali V. Lissianski, and Zhiwei Qin. Gri-mech 3.0 web-site,. 90, 129

[107] P. G. Spazzini, G. Iuso, M. Onorato, N. Zurlo, and G. M. Di Cicca. Unsteady behavior of back-facing step flow. *Experiments in Fluids*, **30**:551–561, 2001. 9

[108] A. Spencer, J.J. McGuirk, and K. Midgley. Vortex breakdown in swirling fuel injector flows. *Journal of Engineering for Gas Turbines and Power*, **130**:021503, 2008. 13

[109] Turns S.R. *An introduction to combustion*. McGraw Hill, 1996. 6

[110] P.P.J. Stroomer. *Turbulence and OH Structures in Flames*. PhD thesis, Delft University of Technology, 1995. 88

[111] PPJ Stroomer, JE De Vries, and T.H. van der Meer. Effects of small-and large-scale structures in a piloted jet diffusion flame. *Flow, Turbulence and Combustion*, **62**[1]:53–68, 1999. 88, 112

[112] N. Syred. A review of oscillation mechanisms and the role of the precessing vortex core (PVC) in swirl combustion systems. *Progress in Energy and Combustion Science*, **32**[2]:93–161, 2006. xiv, 11, 12, 13, 14, 15, 126, 137, 142, 146

[113] N. Syred and J.M. Beer. The damping of precessing vortex cores by combustion in swirl generators. *Astronautica Acta*, **17**[4/5]:78, 1972. 13

[114] N. Syred and J.M. Beer. The damping of precessing vortex cores by combustion in swirl generators. *Astronautica Acta*, **17**[4/5]:78, 1972. 13

[115] N. Syred and J.M. Beer. Combustion in swirling flows- A review. *Combustion and Flame*, **23**:143–201, 1974. 11

[116] A. M. K. P. Taylor and J. H. Whitelaw. Velocity characteristics in the turbulent near wakes of confined axisymmetric bluff bodies. *Journal of Fluid Mechanics*, **139**:391–416, 1984. 9, 10, 48

[117] A. Triantafyllidis and E. Mastorakos. Implementation issues of the conditional moment closure model in large eddy simulations. *Flow, Turbulence and Combustion*, **84**:481–512, 2010. 31, 35

[118] A. Triantafyllidis, E. Mastorakos, and R. L. G. M. Eggels. Large eddy simulations of forced ignition of a non-premixed bluff-body methane flame with conditional moment closure. *Combustion and Flame*, **156**:2328–2345, 2009. 2, 30, 31, 46, 48, 52, 90

[119] M. Tutkun, P. B. V. Johansson, and W. K. George. Three-component vectorial proper orthogonal decomposition of axisymmetric wake behind a disk. *AIAA Journal*, **46**:1118–1134, 2008. 8

[120] C.O.U. Umeh, Z. Rusak, E. Gutmark, R. Villalva, and D.J. Cha. Experimental and Computational Study of Non-Reacting Vortex Breakdown in a Swirl-Stabilized Combustor. In *47 th AIAA Aerospace Sciences Meeting Including the New Horizons Forum and Aerospace Exposition(Disc 1)*. American Institute of Aeronautics and Astronautics, 1801 Alexander Bell Drive, Suite 500, Reston, VA, 20191-4344, USA,, 2009. 10, 11, 12, 13

[121] A. Valera-Median, N. Syred, and A. Griffiths. Characterization of Large Coherent Structures in a Swirl Burner under Combustion Conditions. In *47 th AIAA aerospace sciences meeting including the new horizons forum and aerospace exposition*. American Institute of Aeronautics and Astronautics, 1801 Alexander Bell Drive, Suite 500, Reston, VA, 20191-4344, USA,, 2009. 1, 10, 11, 13, 15

[122] P. Wang, X. S. Bai, M. Wessman, and J. Klingmann. Large eddy simulation and experimental studies of a confined turbulent swirling flow. *Physics of Fluids*, **16**:3306–3324, 2004. 9

[123] S. Wang, V. Yang, G. Hsiao, S.-Y. Hsieh, and H. C. Mongia. Large-eddy simulations of gas-turbine swirl injector flow dynamics. *Journal of Fluid Mechanics*, **583**:99–122, 2007. 20

[124] S. Wang, V. Yang, G. Hsiao, S.Y. Hsieh, and H.C. Mongia. Large-eddy simulations of gas-turbine swirl injector flow dynamics. *Journal of Fluid Mechanics*, **583**:99–122, 2007. 1, 10, 24

[125] YM WRIGHT, G DE PAOLA, K BOULOUCHOS, AND E MASTORAKOS. Simulations of spray autoignition and flame establishment with two-dimensional CMC. *Combustion and flame*, **143**[4]:402–419, DEC 2005. 31

[126] K. B. M. Q. ZAMAN AND A. K. M. F. HUSSAIN. Vortex pairing in a circular jet under controlled excitation. Part 1. General jet response. *Journal of Fluid Mechanics*, **101**:449–491, 1980. 66